



**HAL**  
open science

# Contributions de l'endommagement radoucissant à la zone de rupture autour des tunnels profonds dans les roches quasi-fragiles

Edoardo Trivellato

► **To cite this version:**

Edoardo Trivellato. Contributions de l'endommagement radoucissant à la zone de rupture autour des tunnels profonds dans les roches quasi-fragiles. Mécanique des matériaux [physics.class-ph]. Université Paris-Est, 2018. Français. NNT : 2018PESC1170 . tel-02914682

**HAL Id: tel-02914682**

**<https://pastel.hal.science/tel-02914682>**

Submitted on 12 Aug 2020

**HAL** is a multi-disciplinary open access archive for the deposit and dissemination of scientific research documents, whether they are published or not. The documents may come from teaching and research institutions in France or abroad, or from public or private research centers.

L'archive ouverte pluridisciplinaire **HAL**, est destinée au dépôt et à la diffusion de documents scientifiques de niveau recherche, publiés ou non, émanant des établissements d'enseignement et de recherche français ou étrangers, des laboratoires publics ou privés.



# **Softening damage contributions to the failure zone around deep tunnels in quasi-brittle rocks**

Thèse présentée pour l'obtention du grade de

*Docteur de l'Université Paris-Est*

*Spécialité : Géotechnique*

Soutenue le 18 décembre 2018 à Champs-sur-Marne par

**Edoardo TRIVELLATO**

Devant le jury composé de

Dr. Chloé ARSON	Georgia Institute of Technology	Rapporteur
Dr. Mountaka SOULEY	INERIS	Rapporteur
Pr. Jian-Fu SHAO	Polytech Lille	Examineur
Pr. Jean SULEM	École des Ponts ParisTech	Examineur
Pr. Kwai Kwan WONG	École Nationale des travaux publics de l'Etat	Examineur
Pr. Amade POUYA	École des Ponts ParisTech	Directeur de thèse
Dr. Darius SEYEDI	Andra	Co-encadrant de thèse
Dr. Minh-Ngoc VU	Andra	Co-encadrant de thèse



**Softening damage contributions to the failure zone  
around deep tunnels in quasi-brittle rocks**

Thèse présentée pour l'obtention du grade de

*Docteur de l'Université Paris-Est*

Spécialité : *Géotechnique*

Soutenue le 18 décembre 2018 à Champs-sur-Marne par

Edoardo TRIVELLATO



*To my grandpa,*

*Ultimo*



“Andando Giovanni con Raffaello [...], restarono l’uno e l’altro stupefatti della freschezza, bellezza e bontà di quell’opere [...]. Queste grottesche (che grottesche furono dette dell’essere state entro alle grotte ritrovate) [...] entrarono di maniera nella mente e nel cuore di Giovanni, che datosi a questo studio, non si contentò d’una sola volta o due disegnarle e ritrarle.”

Giorgio Vasari, *Vita di Giovanni da Udine*

“Une rampe droite et escarpée servait anciennement de communication entre les hautes et basses Catacombes [...] : j’y fis établir un grand escalier avec des pilastres toscans qui [...] sont de forts piliers de soutènement élevés sous un ciel dangereux.”

Louis-Étienne Héricart de Thury, *Description des Catacombes de Paris*

“More and more the villages, towns, and “cities” of Earth died and were swallowed by the Cities [...]. There were some eight hundred Cities on Earth, average population, ten million. Each City became a semiautonomous unit [...]. It became a steel cave, a tremendous, self-contained cave of steel and concrete.”

Isaac Asimov, *The Caves of Steel*



# Acknowledgements

This doctoral thesis was realized through a research collaboration between CERMES group in Laboratoire Navier, at École des Ponts ParisTech, and the R&D division at Andra, the French National Radioactive Waste Management Agency.

First of all, I would like to express all my gratitude to my thesis supervisor, Amade Pouya. I thank him for the selection of my candidacy, for his unconditional availability, his careful supervision, his optimism and passion, giving new propositions to fulfil every possible gap during this project. I sincerely thank the co-supervisors of this work, Darius Seyedi and Minh-Ngoc Vu: they always managed to address my path during the development of this research. Thanks for their advices, their guidance and the time dedicated during our periodical meetings. At the same time, I gratefully mention the Andra R&D division, for having supported this project and the related publications and communications.

I would like to acknowledge Chloé Arson and Mountaka Souley, to have accepted the revision of this manuscript. Sincere thanks also the other examiners who agreed to be part of the jury for my defence: Jian-Fu Shao, Jean Sulem and Henry Wong.

Three years of research would not be completely successful without the good workplace: I want to thank all my present and former colleagues in CERMES, an excellent research group, a warm and friendly environment.

Choosing a PhD is not a hazardous event: it must be pondered and desired. For this reason, I would like to mention and greatly thank Cristina Jommi and Stefano Muraro, who I feel lucky to consider friends. They triggered and guided my road as a (very!) junior researcher between the Delft University of Technology and Politecnico di Milano. I will always be grateful to this latter institution, for its educational program, for the formation received, for five incredible years.

The adventure of a PhD candidate takes place, of course, in a greater journey, where I am surrounded by all those who I can call family, spread nowadays more than once, throughout Italy, Paris and somewhere else. Thanks to everyone I met during this path and who is still part of it: thanks to Corrado, Martina, Patrizio, Valeria and all my hometown's team. All the best for every choice we could ever undertake in our future. Thanks to Agustín, for his trust and friendship, during three unforgettable years at École des Ponts, to Carolina, Chiara and the members of my initial *équipe parisienne*.

Eventually, I would like to thank, as intensely as possible, my parents, Roberto and Raffaella, for their unconditional support, their encouragements and teachings, their help in each and every choice which makes me feel, today, a fortunate PhD candidate, and much more.



# Abstract

The French National Radioactive Waste Management Agency (Andra) manages an Underground Research Laboratory (URL) at the Meuse / Haute-Marne Center to study the feasibility of a deep geological repository in the Callovo-Oxfordian claystone (COx). The galleries follow the major and minor principal stress directions. Some galleries show a quasi-isotropic stress state in their cross-section, while others show a greater anisotropy.

These works study the short-term failure and fracturing phenomena induced by the underground structures' excavation. Brittle softening damage is considered as a fundamental failure mechanism. The major part of scientific literature reports an estimation of this area from an elastic post-treatment or based on elastic-plastic analyses. If the first method does not consider the stresses' redistribution due to dissipative phenomena, elastic-plastic approaches sometimes seem insufficient to explain the geometry of these zones in some cases of deep excavations in quasi-brittle rocks (Pouya et al 2016). Two phenomena are studied, through numerical simulations by 2d Finite Elements: the development of a diffused failures, around the galleries' cross-section, and the fractures occurrence at their perimeter, along the excavation. While a plane strain analysis is suitable for the first problem, the second one is studied in axial symmetry.

For the first part of the research, two isotropic unloading processes, in softening elastic-plasticity or elastic-damage, reproduce a global instability related to the first modelling, whereas localized failure occurs with the second one. The latter model, upgraded to consider intrinsic anisotropies in terms of elasticity, resistance and damage dissipative law, allows a consistent estimation of the short-term failure zone, with values of convergences in accordance to the data, for a gallery considered as a case study. Then, the transition of material's failure from a brittle to ductile behaviour, with the confinement, is also simulated, according to different boundary conditions of a second gallery. The short-term damaged zones well reproduce the shape and extension of failure systems and the values of the instantaneous convergences are comparable to in-situ measurements (Trivellato et al 2018).

The second research axis concerns the elongation and mutual spacing of fractures, simplified as a system of finite and parallel discontinuities. Numerically, they are assimilated to *joint elements* (Goodman 1976). The cohesive fracture model, based on damage, (Pouya and Bemani 2015) was chosen for these elements. In presence of a single potential fracture, an unstable initiation is observed, possibly followed by a stable evolution, of reduced length. Then, models with a sequences of several joints were used to analyse the fracture periodicity. This work also allowed the study of different numerical techniques simulating the advancement of an excavation front. According to a precise choice of parameters, fractures' lengths are comparable to the

geological and geophysical surveys. Similarly, the activation of one potential fracture among different discontinuities was calculated, showing a periodic occurrence (Trivellato et al 2018).

This dissertation constitutes a new approach to reproduce the immediate effects of deep excavations in the Callovo-Oxfordian claystone. They study a short-term failure due to the material's brittleness, under low confinement. Damage is adopted as the only dissipation mechanism and is integrated by the effects of material's intrinsic anisotropy as well as its brittle-ductile post-peak transition. Results obtained by every research axis appear favourable to employ these models as complements to excavation studies. In perspective, the integration of plasticity / creep effects, as well as a poro-elastic framework accounting for hydraulic effects, may be considered.

**Keywords** : damage, softening claystone, deep galleries, diffused failure, fractures, numerical modelling.

## Résumé

L'Agence nationale pour la gestion des déchets radioactifs (Andra) gère un laboratoire souterrain de recherche au Centre de la Meuse/Haute-Marne (CMHM), pour étudier la faisabilité d'un stockage géologique profonde dans l'argilite du Callovo-Oxfordien (COx). Les galeries suivent les deux contraintes horizontales principales majeure et mineure. Tandis que certaines galeries possèdent un état de contraintes presque isotrope dans leur section, les autres montrent une anisotropie plus importante.

Ces travaux étudient les phénomènes de rupture et fracturation à court terme, induits par l'excavation autour des ouvrages. L'endommagement fragile est considéré comme mécanisme fondamental de rupture. En effet, on retrouve dans la littérature scientifique une estimation de cette zone à partir d'un post-traitement du champ des contraintes en élasticité ou basée sur un calcul élasto-plastique. Si la première méthode ne considère pas la redistribution des contraintes due aux phénomènes dissipatifs, les approches élasto-plastiques semblent parfois insuffisantes pour expliquer la géométrie de cette zone dans certains cas des excavations en roches quasi-fragiles (Pouya et al 2016). Deux phénomènes sont étudiés, avec des simulations numériques aux Eléments Finis 2d : le développement d'une rupture diffusé, autour de la section des galeries, et l'apparition des fractures le long de l'excavation. Alors qu'une modélisation en déformations planes simule le premier cas, le deuxième est étudié en axisymétrie.

Pour la première approche, deux décharges isotropes, en élasto-plasticité ou élasto-endommagement radoucissant, démontrent une instabilité globale liée au premier modèle, alors que des ruptures localisées se produisent avec le deuxième. Ceci, enrichi pour considérer les anisotropies d'élasticité, de résistance et d'endommagement du matériau, permet une bonne estimation de la zone de rupture à court terme, avec des valeurs des convergences conformes aux données, pour une galerie testée comme cas d'étude. Ensuite, la transition de la rupture du matériau de fragile à ductile, avec le confinement, est aussi prise en compte, avec les différentes conditions aux limites d'une deuxième galerie. Les zones endommagées à court terme estiment correctement la forme et l'extension de la rupture et les valeurs des convergences instantanées sont comparables aux mesures (Trivellato et al 2018).

Le deuxième axe de recherche concerne la prédiction de la longueur des fractures, simplifiées comme des discontinuités finies et parallèles, ainsi que leur espacement. Numériquement, ces sont assimilées aux *éléments joints* (Goodman 1976). Le modèle de la fracture cohésive (Pouya et Bemani 2015) a été choisi pour ces éléments. Avec une seule discontinuité, on observe une initiation *instable* de la fracture, possiblement suivi par une évolution *stable*, d'une longueur réduite. Plusieurs séquences des joints ont été employés pour calculer la périodicité des fractures. Ces travaux ont permis aussi l'étude de différentes méthodes numériques qui simulent

l'avancement d'un front d'excavation. Selon un choix précis des paramètres, on calcule des longueurs de fracturation comparables aux mesures, ainsi que la possibilité d'obtenir l'activation d'une seule fracture parmi plusieurs (Trivellato et al 2018).

Ces travaux de thèse constituent une nouvelle approche de prédiction des effets du creusement sur l'argilite du Callovo-Oxfordien. Ils étudient une rupture à court terme due au comportement fragile sous faible confinement. Le mécanisme de dissipation en endommagement est intégré par les effets à la fois de l'anisotropie intrinsèque du matériau et de sa transition fragile-ductile. Les résultats obtenus par les deux axes de recherche favorisent l'utilisation de ces modèles comme compléments aux études des excavations. En perspective, leur intégration avec les effets de la plasticité/fluage du matériau, ainsi qu'avec la poro-élastique en comptant les effets hydrauliques, peut être envisageable.

**Mots-clés** : endommagement, argilite radoucissante, galeries profondes, rupture diffusée, fractures, modélisation numérique.

# Contents

<i>Abstract</i> .....	i
<i>Résumé</i> .....	iii
<i>Contents</i> .....	v
<i>List of Symbols</i> .....	vii
<i>List of Figures</i> .....	xiii
<i>List of Tables</i> .....	xix
<b>Chapter 1 : Introduction and Context of the Research</b> .....	1
1.1    Motivations and background.....	4
1.1.1    Observations and studies at the Andra Underground Research Laboratory .....	7
1.1.2    The Callovo-Oxfordian claystone formation .....	16
1.2    Some aspects of failure around deep excavations .....	22
1.2.1    2d stress solution for tunnel cross section in case of elasticity .....	25
1.2.2    A 2d stress solution for tunnel cross section in case of elasticity - perfect plasticity .....	28
1.2.3    Two simple cases of failure localization around a circular borehole .....	33
<b>Chapter 2 : Numerical and Theoretical Framework with Softening Models</b> .....	37
2.1    Presentation of the <i>FE</i> code and constitutive laws formulation.....	40
2.1.1    Elastic-plastic softening model .....	46
2.1.2    Elastic-damage softening model .....	48
2.2    Main differences between plasticity and damage in softening.....	55
2.3    An anisotropic upgrade of the <i>elastic-damage</i> softening model .....	70
<b>Chapter 3 : General Damage-Based Modelling on Drifts Section</b> .....	77
3.1    Failure analysis with a 2d <i>global</i> damage model .....	80
3.2    Modelling the anisotropic failure response .....	83
3.3    Transverse-isotropic elasticity .....	93
3.4    Non-monotonic failure anisotropy in two dimensions .....	97
<b>Chapter 4 : Shear Damage-Based Modelling on Drifts Section</b> .....	107
4.1 <i>Shear-damage</i> elastic model for 2d plane strain problem.....	110
4.2    Preliminary results with monotonic failure anisotropy .....	115
4.3    Fourth-order modelling of non-monotonic failure anisotropy .....	120
4.4    Modelling the softening brittle-ductile transition.....	125
4.5    Final results for plane strain damage around the URL drifts .....	130

<b>Chapter 5 : Discrete Modelling of Chevron Fractures</b> .....	141
5.1 Problem definition with constitutive and numerical modelling .....	144
5.2 <i>Single-fracture</i> numerical analyses .....	151
5.3 <i>Multi-fractures</i> numerical analyses with drifting simulations.....	156
5.3.1 Excavation method 1.....	156
5.3.2 Excavation method 2.....	158
5.3.3 Excavation method 3.....	161
<b>General Conclusions and Perspectives</b> .....	165
Plane section modelling of the failure zone .....	167
Discrete modelling of fractures occurrence.....	171
<b>References</b> .....	173
<b>Appendices</b> .....	183
A – Details on the <i>FEM</i> codes.....	183
B – Anisotropies in failure criteria and damage-elasticity .....	185
B.1 Drucker-Prager failure criterion based on a second (II) order rotation tensor.....	185
B.2 Mohr-Coulomb type failure criterion based on a second (II) order rotation tensor .....	187
B.3 Mohr-Coulomb type failure criterion based on a fourth (IV) order rotation tensor .....	191
B.4 Elastic-damage stiffness tensor with no damage expansion along $z$ .....	196

# List of Symbols

*Units are reported on the right, as (mainly) adopted in the manuscript.*

*Units are omitted in case of generic quantities or variables or coefficients, geometric and rotation spaces or vectors or matrices, mathematical functions.*

$x, y, z$ : Cartesian coordinates system; horizontal, vertical, axial	[m], [m], [m]
$r, \theta, z$ : cylindrical coordinates system; radial, orthoradial, axial	[m], [°] or [rad], [m]
$Z$ : in-situ depth	[m]
$g$ : gravity coefficient	[-]
$\bullet(X)$ : generic quantity $\bullet$ at the point $X$ in a coordinates system	
$\bullet_{(0)}$ : initial conditions of $\bullet$	
$\bullet(i)$ : quantity $\bullet$ along a certain direction $i$	
$\bullet(t)$ : quantity $\bullet$ as a function of $t$	( $t$ defined in the following)
$\tilde{\bullet}$ : modified quantity with respect to $\bullet$	
$\dot{\bullet}$ : rate or time-derivative of quantity $\bullet$	
$N$ : number of elements in a FE mesh	
$n$ : number of nodes in a FE mesh or integer scalar quantity / coefficient	
$\Delta$ : notation of algebraic increment of a quantity or quantity fraction coefficient	
$\zeta$ : tolerance value in numerical processes	
$A$ : real scalar quantity / coefficient	
$\mathbf{a}$ : vector or matrix	
$a_i$ : $i$ -th component of the vector $\mathbf{a}$	
$a_{ij}$ : $i$ -th, $j$ -th component of the matrix $\mathbf{a}$	
$\mathbf{A}$ : tensorial quantity (vector or matrix)	
$A_i$ : $i$ -th component of the vector (or tensor) $\mathbf{A}$	
$A_{ij}$ : $i$ -th, $j$ -th component of the matrix (or tensor) $\mathbf{A}$ or indicial notation if 2 <sup>nd</sup> order tensor	
$A_{ijkl}$ : indicial notation if 4 <sup>th</sup> order tensor	
$\delta_{ij}$ : indicial notation for the identity matrix	
$\mathbf{I}_{(3 \times 3)}$ : 3-dimensional identity matrix	
$\mathbf{n}$ : normal unit vector	
$\mathbf{t}$ : tangential unit vector	
$\alpha$ : generic angle or rotation angle between coordinates systems	[°]
$r_a$ : radius of a circular gallery (or minor semi-axis if elliptical)	[m]
$r_a'$ : major semi-axis of an elliptical gallery	[m]
$r_p$ : radius of the circular failure zone around a gallery	[m]

$\Gamma$ : plane identified by coordinates $x$ and $y$ , gallery cross-section	
$p_0$ : internal homogeneous pressure in a circular gallery	[MPa]
$\sigma_T$ : homogeneous tensile stress to simulate an excavation process	[MPa]
$\sigma_v$ : vertical in-situ stress component	[MPa]
$\sigma_H$ : major horizontal in-situ stress component	[MPa]
$\sigma_h$ : minor horizontal in-situ stress component	[MPa]
$\sigma_{ij}$ : stress tensor component / indicial notation	[MPa]
$\boldsymbol{\sigma}$ : stress tensor	[MPa]
$s_{ij}$ : deviatoric stress tensor component / indicial notation	[MPa]
$\mathbf{s}$ : deviatoric stress tensor	[MPa]
$q$ : deviator in triaxial compression	[MPa]
$\sigma_\infty$ : in-situ stress in 2-dimensional isotropic conditions	[MPa]
$\sigma_{p,rr}$ : radial stress component at the (plastic) failure limit	[MPa]
$\mathbf{T}_i$ : local stress state at $i$	[MPa]
$\sigma_n$ : normal stress component	[MPa]
$\tau$ : tangential stress component	[MPa]
$I_1$ : stress tensor first invariant	[MPa]
$J_2$ : deviatoric stress tensor second invariant	[MPa]
$\varepsilon_{ij}$ : deformations tensor component / indicial notation	[-]
$\boldsymbol{\varepsilon}$ : deformations tensor	[-]
$e_{ij}$ : deviatoric deformations tensor component / indicial notation	[-]
$\mathbf{e}$ : deviatoric deformations tensor	[-]
$\varepsilon_{ij}^E$ : elastic deformations tensor component / indicial notation	[-]
$\boldsymbol{\varepsilon}^E$ : elastic deformations tensor	[-]
$\varepsilon_{ij}^P$ : plastic deformations tensor component / indicial notation	[-]
$\boldsymbol{\varepsilon}^P$ : plastic deformations tensor	[-]
$\ \boldsymbol{\varepsilon}^P\ $ : norm of the plastic deformations $\ \boldsymbol{\varepsilon}^P\ $	[-]
$\mathbf{U}$ : displacements vector	[mm]
$U_x$ : horizontal displacement	[mm]
$U_y$ : vertical displacement	[mm]
$\ \mathbf{U}\ $ : displacements norm	[mm]
$\rho$ : material density	[kg/m <sup>3</sup> ]
$e$ : void ratio	[-]
$\mathbf{C}$ : elastic stiffness matrix	[MPa]
$C_{ijkl}$ : indicial notation for $\mathbf{C}$	[MPa]
$\mathbf{C}^{-1}$ : elastic compliance matrix	[MPa <sup>-1</sup> ]
$C^{-1}_{ijkl}$ : indicial notation for $\mathbf{C}^{-1}$	[MPa <sup>-1</sup> ]

$b$ : Biot coefficient	[MPa <sup>-1</sup> ]
$E$ : Young modulus	[MPa]
$E_{MAT}$ : matrix Young modulus	[MPa]
$E_{HOM}$ : homogenised Young modulus	[MPa]
$E_x$ : horizontal Young modulus	[MPa]
$E_y$ : vertical Young modulus	[MPa]
$E_z$ : axial Young modulus	[MPa]
$E_{oed}$ : oedometric modulus	[MPa]
$K$ : elastic bulk modulus	[MPa]
$\nu$ : Poisson's ratio	[-]
$\lambda$ : first Lamé coefficient	[MPa]
$\mu$ : shear modulus (or second Lamé coefficient)	[MPa]
$\mu_{MAT}$ : matrix shear modulus	[MPa]
$\mu_{HOM}$ : homogenised shear modulus	[MPa]
$w$ : material water content	[-]
$\gamma_w$ : water specific gravity	[kN/m <sup>3</sup> ]
$K_w$ : material permeability to water	[m <sup>2</sup> ]
$k_w$ : material hydraulic conductivity to water	[m/s]
$p_w$ : water pore pressure in the material	[MPa]
$q_w$ : water flow per unit area	[m/s]
$c_v$ : 1-dimensional consolidation coefficient	[m <sup>2</sup> /s]
$H$ : drainage length in a 1-dimensional consolidation process	[m]
$T$ : normalized time in a 1-dimensional consolidation process	[-]
$\varphi$ : friction angle	[°]
$C$ : effective cohesion	[MPa]
$K_P$ : passive earth pressure coefficient	[-]
$f$ : failure criterion	
$\sin\alpha$ : Drucker-Prager friction coefficient (related to $\varphi$ )	[-]
$K$ : Drucker-Prager cohesion coefficient (related to $\varphi$ and $C$ )	[MPa]
$\chi$ : generic internal variable	
$g(\chi)$ : generic yielding law	
$A$ : plastic coefficient	[-]
$\zeta$ : plastic internal variable	[-]
$D$ : damage internal variable	[-]
$D_m$ : threshold value of $D$ for residual conditions	[-]
$g(D)$ : damage law function	
$p_C$ : hydrostatic/lateral confinement in triaxial conditions (cell pressure)	[MPa]

$\omega$ : angle between the normal to the material stratification and the horizontal ( $x$ )	[°] or [rad]
$\mathbf{m}$ : unit vector parallel to the material stratification	
$\sigma_0$ : uniaxial compressive strength	[MPa]
$\sigma_0(p_C)$ : triaxial compressive strength, for a certain $p_C$	[MPa]
$\varepsilon_0$ : axial deformation corresponding to $\sigma_0$	[-]
$\sigma_r$ : uniaxial residual compressive strength	[MPa]
$\varepsilon_r$ : axial deformation corresponding to $\sigma_r$	[-]
$\sigma_{0,\omega}$ : uniaxial compressive strength for an inclination $\omega$	[MPa]
$\sigma_0(p_C)_{,\omega}$ : triaxial compressive strength, for a certain $p_C$ , for an inclination $\omega$	[MPa]
$C_{\text{sph}}$ : spherical coefficient defining $\sigma_{0,\omega}$	
$C_{\text{dev}}$ : deviatoric coefficient defining $\sigma_{0,\omega}$	
$\sigma_R$ : uniaxial tensile strength	[MPa]
$\beta$ : deformation softening coefficient /cohesive fracture softening coefficient	[-]
$\eta_r$ : stress softening ratio	[-]
$\eta$ : complementary to $\eta_r$	[-]
$\mathbf{M}$ : second order anisotropy tensor	
$h$ : anisotropy scaling factor related to $\mathbf{M}$	[-]
$\mathbf{H}$ : fourth order anisotropy tensor	
$h_n$ : anisotropy normal scaling factor related to $\mathbf{H}$	[-]
$h_s$ : anisotropy shear scaling factor related to $\mathbf{H}$	[-]
$d(z,t)$ : axial <i>excavation function</i> (excavation along the coordinate $z$ )	
$z_0$ : axial offset coordinate in an excavation process	[m]
$H_a$ : total gallery length in an excavation process	[m]
$L_N$ : geometric coefficient in $d(z,t)$ related to finite elements size	[mm]
$e_0$ : initial thickness of a discontinuity / fracture opening	[mm]
$d$ : distance between two discontinuities	[m]
$\bar{s}$ : distance between two fractures	[m]
$\bar{L}$ : fracture propagation length	[m]
$\mathbf{u}$ : relative displacements vector between the surfaces of a fracture	[m]
$u_n$ : relative normal displacement between the surfaces of a fracture	[m]
$u_t$ : relative tangential displacement between the surfaces of a fracture	[m]
$s$ : binary contact parameter between the surfaces of a fracture	[-]
$\mathbf{K}$ : stiffness matrix of an intact discontinuity	[MPa/m]
$K_{nn}$ : normal component of $\mathbf{K}$	[MPa/m]
$K_{tt}$ : shear component of $\mathbf{K}$	[MPa/m]
$\kappa$ : $K_{tt}$ to $K_{nn}$ ratio	[-]

$\mathbf{k}_0$ : fracture residual stiffness matrix	[MPa/m]
$k_{0n}$ : normal component of $\mathbf{k}_0$	[MPa/m]
$k_{0t}$ : shear component of $\mathbf{k}_0$	[MPa/m]
$G$ : fracturing energy dissipation rate	[MPa·m]
$G_C$ : critical value of $G$	[MPa·m]

*Virtual time-dependent quantities defined for numerical transient processes. They have no physical correspondence and units are omitted.*

$t$ : virtual temporal variable
$\Delta t$ : numerical increment of $t$
$t_0$ : initial value of $t$ in a numerical transient process
$t_f$ : final value of $t$ in a numerical transient process
$V$ : virtual velocity in a numerical transient process



# List of Figures

## Chapter 1

<b>Figure 1.1</b> : overview of DGR in the concept of <i>Cigéo</i> project.....	5
<b>Figure 1.2</b> : identification of four zones affected by mechanical perturbation due to excavation .....	6
<b>Figure 1.3</b> : plan of the Andra URL at the Centre Meuse-Haute Marne and principal stress directions [93].....	8
<b>Figure 1.4</b> : excavation methods for the URL drifts reported in Figure 1.3.. .....	9
<b>Figure 1.5</b> : support systems for GCS (a) and GED (b) drifts. ....	9
<b>Figure 1.6</b> : 3d scan analyses around inside galleries at Andra URL. ....	10
<b>Figure 1.7</b> : estimated fractures density, moving radially from GCS drift’s wall.....	10
<b>Figure 1.8</b> : conceptual model for extensional and shear ( <i>Chevron</i> ) fractures’ pattern for the drift GCS (a) together with detected fracture planes on the radial direction (b). ....	10
<b>Figure 1.9</b> : 3d conceptual models for fractures patterns around drifts at the URL, together with the 2d simplification of the system EDZ-EdZ. ....	12
<b>Figure 1.10</b> : (a), development of shear bands around GCS drift according to the total deviatoric strain at 60 days from excavation [66] and (b), contours of the cumulated plastic multiplier at the end of the excavation [57]. ....	13
<b>Figure 1.11</b> : horizontal (blue) and vertical (orange) convergences evolution in GCS drift, excavated along $\sigma_H$ (a), and in GED drift, excavated along $\sigma_h$ (b).....	13
<b>Figure 1.12</b> : Mine-by test concept for GCS. ....	14
<b>Figure 1.13</b> : instantaneous and differed displacements around GCS from mine-by tests, modified from [93]. ....	14
<b>Figure 1.14</b> : horizontal displacements prediction in drift GCS, reported in Guayacán–Carrillo and compared to the original results from Armand et al. ....	15
<b>Figure 1.15</b> : simplified chart of the Paris East Basin and location of the Andra URL at the CMHM.....	16
<b>Figure 1.16</b> : vertical section of the local geology at the site of the Andra CMHM.....	17
<b>Figure 1.17</b> : stress-strain behaviour under different lateral stresses, $p_C$ and principal stresses plot at failure with a Hoek–Brown failure criterion interpolation.....	19
<b>Figure 1.18</b> : TXc tests showing a transition from the fragile post-peak response under uniaxial conditions ( $p_C = 0$ ) to the almost perfect yielding under high confining pressure ( $p_C = 20$ MPa).....	19
<b>Figure 1.19</b> : illustration of the proposed analyses’ concept for failure description and numerical modelling .....	21
<b>Figure 1.20</b> : failure modes, as reported in Vardoulakis et al. [109]. ....	22
<b>Figure 1.21</b> : axial-splitting in sandstone (a) and shear failure in limestone (b), reported in Crook et al. [28]. ....	23
<b>Figure 1.22</b> : qualitative comparison of the shape of the excavation damaged zone between (a) numerical prediction and (b) X-ray tomography scan after hollow cylinder testing.....	23
<b>Figure 1.23</b> : failure envelope for brittle failure, showing four failure mechanisms: no damage, shear failure, spalling, and unravelling. ....	24
<b>Figure 1.24</b> : axial symmetry of a 3d borehole problem (a) and plane of reference for the analysis of stress-strain fields on a gallery cross-section (b). ....	26
<b>Figure 1.25</b> : analytical elastic solution for cylindrical stress components acting in the cross section gallery.....	27
<b>Figure 1.26</b> : axial symmetry of a 3d borehole problem (a) and plane of reference for the study of the stress field with a circular failure extension on a gallery cross-section (b). ....	29
<b>Figure 1.27</b> : $\sigma_{\theta\theta}$ and $\sigma_{rr}$ along a radial direction for internal pressures of 1 MPa (continuous lines) and 0.5 MPa (dotted lines). ....	31
<b>Figure 1.28</b> : $\sigma_{\theta\theta}$ , $\sigma_{rr}$ and $\sigma_{zz}$ along a radial direction for internal pressures of 1 MPa (continuous lines) and 0.5 MPa (dotted lines). ....	33
<b>Figure 1.29</b> : localisation of failure at the point A due to an anisotropic in-situ stress on the section plane $\Gamma$ . ....	34

**Figure 1.30** : localisation of failure at the point A due to different local values of UCS  $\sigma_0$  around the perimeter. .... 34

## Chapter 2

<b>Figure 2.1</b> : procedures composing the step-by step resolution of the $\sigma : \epsilon$ relation for a classical constitutive law in <i>Utilizer.f90</i> .....	41
<b>Figure 2.2</b> : general structure of the FE processor <i>POROFIS</i> : code core, i/o files and related subroutines. ....	42
<b>Figure 2.3</b> : materials assignment and mesh creation in GiD, followed by insertion of a discontinuities network based on the original mesh through <i>DISCRAC</i> .....	43
<b>Figure 2.4</b> : same stress-strain curve under monotonic uniaxial loading and different unloading-reloading paths with elastic-plasticity (P) or elastic-damage (D) mechanical model.....	44
<b>Figure 2.5</b> : Plastic coefficient A in Eq. 2.14a, as a function of softening parameters $\beta$ and $\eta_r$ . ....	47
<b>Figure 2.6</b> : variation of the damage function $g(D)$ with damage, for the same representative values for the parameter $\beta$ . ....	49
<b>Figure 2.7</b> : numerical implementation steps for a circular gallery excavation for plane strains simulations. ....	50
<b>Figure 2.8</b> : geometry for the first FE numerical model of a circular gallery excavation. ....	51
<b>Figure 2.9</b> : extension of plastic deformations (a) and axial stress $\sigma_{zz}$ (b), for a total unloading ( $p_0 = 0$ ), in perfect elastic-plasticity .....	52
<b>Figure 2.10</b> : extension of the damage variable (a) and axial stress $\sigma_{zz}$ (b), for a total unloading ( $p_0 = 0$ ) in perfect elastic-damage .....	53
<b>Figure 2.11</b> : values of the axial stress $\sigma_{zz}$ , for $p_0 = 0$ , along a radial direction of Figure 2.9b and Figure 2.10b. ....	53
<b>Figure 2.12</b> : three meshes adopted to perform the mesh sensitivity analyses in elastic-perfect-plastic conditions. ...	54
<b>Figure 2.13</b> : extension of the plastic deformations for the three meshes reported in Figure 2.12.....	54
<b>Figure 2.14</b> : plastic radius evolution for the three meshes reported in Figure 2.12. ....	54
<b>Figure 2.15</b> : triaxial stress-strain data, reported in [117] (a) and [9] (b).....	56
<b>Figure 2.16</b> : <i>POROFIS</i> validation of the elastic-softening models based on triaxial test data from [10]. ....	56
<b>Figure 2.17</b> : plastic deformations (a) and damage variable $D$ (b) for an isotropic gallery excavation with elastic-plastic and elastic-damage materials, respectively.....	57
<b>Figure 2.18</b> : plastic deformations (a) and damage variable $D$ (b) for the same numerical models reported in Figure 2.17.....	58
<b>Figure 2.19</b> : evolution of the plastic radius $r_p$ during the unloading (normalized) of the opening in Figure 2.18a. ....	59
<b>Figure 2.20</b> : Post-peak behaviour and related to the shear band thickness for a specimen under uniaxial compression evolution ([66], [99]).....	61
<b>Figure 2.21</b> : uniaxial response of specimen compression simulated in <i>POROFIS</i> .....	61
<b>Figure 2.22</b> : possible bifurcated configuration of failure zone in $n$ branches, around a cylindrical structure, on a cross-section plane.....	62
<b>Figure 2.23</b> : elastic-perfect brittle behaviour as a particular case for of the uniaxial compressive behaviour in Figure 2.4 ( $\beta = 0$ ).....	63
<b>Figure 2.24</b> : elliptical-shaped gallery deformation at the elastic limit, derived from an initial circular gallery perimeter .....	63
<b>Figure 2.25</b> : initial and boundary conditions on the same geometry of Figure 2.8, with an anisotropic 2d in the gallery cross section. ....	65
<b>Figure 2.26</b> : plastic deformations in (a) and damage variable $D$ in (b) for a complete unloading of the circular gallery. ....	65
<b>Figure 2.27</b> : circular geometry adopted for numerical simulations further presented. ....	66
<b>Figure 2.28</b> : plastic deformations in (a) and damage in (b) for a complete unloading of the circular gallery.....	66
<b>Figure 2.29</b> : 8 lobes – shaped failure zone after complete unloading. ....	68
<b>Figure 2.30</b> : spiral shear bands in artificial sandstone. ....	68

<b>Figure 2.31:</b> scheme of hydraulic boundary conditions for a specimen in a 1d consolidation problem. ....	69
<b>Figure 2.32:</b> in (a) conceptual model and geometrical characteristic of the 2d excavation-induced zone referring to the observation for GCS drift. In (b), indication of the type of fractures included in the EDZ and EdZ on the same 2d numerical model. ....	71
<b>Figure 2.33:</b> scheme of the implemented anisotropic damage expansion in the reference coordinates. ....	72
<b>Figure 2.34:</b> mesh size sensitivity analyses in softening plasticity. ....	74
<b>Figure 2.35:</b> mesh size sensitivity analyses in softening damage with the $2d_{ED}$ model. ....	74
<b>Figure 2.36:</b> extension of the failure radius in softening plasticity (a) and softening $2d_{ED}$ model (b). ....	75

## Chapter 3

<b>Figure 3.1 :</b> 2d conceptual model for the system EDZ-EdZ for a drift excavated along stress $\sigma_H$ at the Andra URL. ....	80
<b>Figure 3.2 :</b> numerical model, initial conditions (a) and excavation boundary conditions (b) for the numerical analyses presented in the current section. ....	81
<b>Figure 3.3 :</b> contour plot for the damage $D$ , at the end of the excavation, with its the horizontal extension. ....	81
<b>Figure 3.4 :</b> contour plots for horizontal ( $U_x$ ) displacement (a) and vertical ( $U_y$ ) displacements field (b). ....	82
<b>Figure 3.5 :</b> total horizontal (red line) and vertical displacements (blue line), measured at the GCS drift's perimeter, with a focus on the initial values likely to correspond to the excavation-induced response. ....	82
<b>Figure 3.6 :</b> increasing of D expansion with the decreasing of $\sigma_{zz(0)}$ imposed as axial boundary/initial conditions (a) $\sigma_{zz(0)} = -10$ MPa; (b) $\sigma_{zz(0)} = -8$ MPa; (b) $\sigma_{zz(0)} = -5$ MPa. ....	83
<b>Figure 3.7 :</b> reference scheme of the excavation problem in a 2d stress state simplification with the global (Cartesian) and local (polar) coordinates systems. ....	84
<b>Figure 3.8 :</b> conceptual model for the implementation of the anisotropic Drucker-Prager failure criterion. ....	84
<b>Figure 3.9 :</b> simulation of confined compression tests with $\sin\alpha = 0.28$ , $K = 5.3$ MPa and $h = 0.3$ . ....	86
<b>Figure 3.10 :</b> numerical results simulating a confined compression at $p_c = 12$ MPa with the anisotropic Druger-Prager criterion. ....	88
<b>Figure 3.11 :</b> initial/boundary conditions (a) and excavation procedure (b) with $r_a = 2.6$ m. ....	89
<b>Figure 3.12 :</b> contour plot for the damage $D$ , at the end of the excavation. ....	90
<b>Figure 3.13 :</b> contour plots for horizontal ( $U_x$ ) displacement (a) and vertical ( $U_y$ ) displacements field (b). ....	90
<b>Figure 3.14 :</b> 2d conceptual model for GED drift [9]. ....	90
<b>Figure 3.15 :</b> contour plot for the damage $D$ , at the end of the excavation. ....	91
<b>Figure 3.16 :</b> contour plots for horizontal ( $U_x$ ) displacement (a) and vertical ( $U_y$ ) displacements field (b). ....	91
<b>Figure 3.17 :</b> total horizontal and vertical convergences, measured at the GED drift's perimeter. ....	92
<b>Figure 3.18 :</b> conceptual model of an horizontally stratified geological formation to formalize and implement the anisotropic elasticity. ....	93
<b>Figure 3.19 :</b> contour plot for the damage $D$ , at the end of the excavation. ....	96
<b>Figure 3.20 :</b> contour plots for horizontal ( $U_x$ ) displacement (a) and vertical ( $U_y$ ) displacements field (b). ....	97
<b>Figure 3.21 :</b> conceptual 2d scheme for failure localisation of drifts GCS and GED. ....	98
<b>Figure 3.22 :</b> conceptual model for the implementation of the anisotropic 2d failure criterion in Eq. 3.30. ....	99
<b>Figure 3.23 :</b> plots of $\sigma_{\theta,\omega}$ (red) and $\sigma_{\theta(p_c),\omega}$ confined at 12 MPa (blue), for $\varphi = 20^\circ$ , $K = 15$ MPa, $h = 0.2$ . ....	101
<b>Figure 3.24 :</b> $\sigma_{\theta,\omega}$ for $\varphi = 20^\circ$ , $K = 15$ MPa, $h = 0.2$ . ....	101
<b>Figure 3.25 :</b> non-monotonic calibration strength in specimen confined at 12 MPa [91]. ....	102
<b>Figure 3.26 :</b> contour plot for the damage $D$ , GCS drift. ....	103
<b>Figure 3.27 :</b> contour plots for horizontal displacement (a) and vertical displacements field (b), GCS drift. ....	103
<b>Figure 3.28 :</b> contour plot for the damage $D$ , GED drift. ....	104
<b>Figure 3.29 :</b> contour plots for horizontal displacement (a) and vertical displacements field (b), GED drift. ....	104

## Chapter 4

<b>Figure 4.1</b> : bi-dimensional schemes of the extension of EDZ-EdZ around the studied drifts, along $\sigma_H$ and $\sigma_h$ , at the Andra URL.....	110
<b>Figure 4.2</b> : conceptual model of the damage mechanism occurring in the material at failure. ....	110
<b>Figure 4.3</b> : model stress-strain curve under monotonic uniaxial loading and damage unloading-reloading .....	112
<b>Figure 4.4</b> : damage extensions according to boundary and initial conditions in Table 4.1 of GCS in (a) and GED drifts in (b), after complete excavation. $\eta_r = 0.9$ .....	113
<b>Figure 4.5</b> : horizontal (a) and vertical (b) displacements fields according to boundary and initial conditions in Table 4.1 of GCS drift (Figure 4.4a). $\eta_r = 0.9$ .....	113
<b>Figure 4.6</b> : horizontal (a) and vertical (b) displacements fields according to boundary and initial conditions in Table 4.1 of GED drift (Figure 4.4b). $\eta_r = 0.9$ .....	113
<b>Figure 4.7</b> : damage extensions according to boundary and initial conditions in Table 4.1 for GCS in (a) and GED drifts in (b), after complete excavation. $\eta_r = 0.2$ .....	114
<b>Figure 4.8</b> : horizontal (a) and vertical (b) displacements fields according to boundary and initial conditions in Table 4.1 of GCS drift (Figure 4.7a). $\eta_r = 0.2$ .....	114
<b>Figure 4.9</b> : horizontal (a) and vertical (b) displacements fields according to boundary and initial conditions in Table 4.1 of GED drift (Figure 4.7b). $\eta_r = 0.2$ .....	114
<b>Figure 4.10</b> : uni- and triaxial compression tests (TXc) on COx specimens, focusing on the fragile response in uniaxial compressions. Modified after [8]. ....	116
<b>Figure 4.11</b> : monotonic interpretation of data in Table 3.10 (Section 3.4), according to the failure criterion in Eq. 4.8. ....	116
<b>Figure 4.12</b> : Figure 3.2 : numerical model, initial conditions (a) and excavation boundary conditions (b) for the numerical analyses presented. ....	117
<b>Figure 4.13</b> : damage extensions according to boundary and initial conditions in Table 4.1 of GCS drift. Coarse mesh reported in Figure 4.12 in (a) and fine mesh reported in Figure 3.11, Section 3.2. ....	117
<b>Figure 4.14</b> : horizontal (a) and vertical (b) displacements fields according to boundary and initial conditions in Table 4.1 of GCS drift, with the coarse mesh reported in Figure 4.12. ....	117
<b>Figure 4.15</b> : horizontal (a) and vertical (b) displacements fields according to boundary and initial conditions in Table 4.1 of GCS drift, with the fine mesh reported in Figure 3.11, Section 3.2. ....	118
<b>Figure 4.16</b> : damage extensions according to boundary and initial conditions in Table 4.1 of GED drift. Coarser mesh reported in Figure 4.12 in (a) and finer mesh reported in Figure 3.11, Section 3.2. ....	118
<b>Figure 4.17</b> : horizontal (a) and vertical (b) displacements fields according to boundary and initial conditions in Table 4.1 of GED drift, with the coarse mesh reported in Figure 4.12.....	118
<b>Figure 4.18</b> : horizontal (a) and vertical (b) displacements fields according to boundary and initial conditions in Table 4.1 of GED drift, with the fine mesh reported in Figure 3.11, Section 3.2. ....	119
<b>Figure 4.19</b> : conceptual model for the implementation of the new anisotropic 2d failure criterion. ....	120
<b>Figure 4.20</b> : scheme of failure localization at a coordinate $0 < \theta < \pi/2$ (in this case, $\pi/4$ ), symmetric to both axis $x$ and $y$ on the cross-section plane $\Gamma$ .....	122
<b>Figure 4.21</b> : numerical simulations validating the symmetric failure attainment calculated with the 2d anisotropic criterion modified by $\mathbf{H}$ .....	122
<b>Figure 4.22</b> : $\sigma_{\theta,\omega}$ modelled with $\mathbf{H}$ (red line) and $\mathbf{M}$ (dotted line). $\varphi = 20^\circ$ , $K = 15$ MPa. $h_n = h_s = 1.44$ with $\mathbf{H}$ . $h = 0.2$ with $\mathbf{M}$ . Linear representation in (a), radar representation in (b).....	123
<b>Figure 4.23</b> : $\sigma_{\theta,\omega}$ variation according to, separately, $h_n$ (a) and $h_s$ (b). $\varphi = 20^\circ$ , $K = 15$ MPa. ....	123
<b>Figure 4.24</b> : calibration of the Mohr-Coulomb type anisotropic criterion (i.e. Eq. 4.8) defined with $\tilde{\sigma}(\mathbf{H})$ .....	125
<b>Figure 4.25</b> : deviator stress vs. axial strain for TXc tests confined at 1 MPa (left) and 10 MPa (right). Modified from [14]. ....	126
<b>Figure 4.26</b> : stress-strain curves in TXc tests with different confining stresses [46]. ....	126
<b>Figure 4.27</b> : conceptual model for the subdivision of concentrically brittle-ductile transition zones in the area potentially subjected to damage. ....	127

<b>Figure 4.28</b> : values of softening parameters $\beta$ and $\eta_r$ (respectively, in (a) and (b)) calculated from TXc data recorded in various bibliographic references. ....	128
<b>Figure 4.29</b> : scheme of the approach to select $\sigma_{rr}$ representing every <i>transition zone</i> for the variation of softening parameters in the post-peak simulation of COx claystone behaviour. ....	129
<b>Figure 4.30</b> : diagrams for the definition of $\beta$ (a) and $\eta_r$ (b) in the transition zones defined in the geometry of numerical modelling for GCS drift. ....	130
<b>Figure 4.31</b> : diagrams for the definition of $\beta$ (a) and $\eta_r$ (b) in the transition zones defined in the geometry of numerical modelling for GED drift. ....	130
<b>Figure 4.32</b> : numerical model, initial conditions (a) and excavation boundary conditions (b) for the last 2d plane strain numerical analyses. ....	132
<b>Figure 4.33</b> : distribution of the damage variable $D$ for a complete unloading of the GCS drift with 3 <i>brittle-ductile</i> transition zones. ....	132
<b>Figure 4.34</b> : distribution of displacements' norm (a) and horizontal stress (b) for a complete unloading of the GCS drift with 3 <i>brittle-ductile</i> transition zones. ....	133
<b>Figure 4.35</b> : distribution of the damage variable $D$ for a complete unloading of the GCS drift with 6 <i>brittle-ductile</i> transition zones. ....	133
<b>Figure 4.36</b> : distribution of displacements' norm (a) and horizontal stress (b) for a complete unloading of the GCS drift with 6 <i>brittle-ductile</i> transition zones. ....	134
<b>Figure 4.37</b> : distribution of the damage variable $D$ for a complete unloading of the GED drift with 3 <i>brittle-ductile</i> transition zones. ....	134
<b>Figure 4.38</b> : distribution of displacements' norm (a) and vertical stress (b) for a complete unloading of the GED drift with 3 <i>brittle-ductile</i> transition zones. ....	135
<b>Figure 4.39</b> : distribution of the damage variable $D$ for a complete unloading of the GED drift with 6 <i>brittle-ductile</i> transition zones. ....	135
<b>Figure 4.40</b> : distribution of displacements' norm (a) and vertical stress (b) for a complete unloading of the GED drift with 6 <i>brittle-ductile</i> transition zones. ....	136
<b>Figure 4.41</b> : distribution of the damage variable $D$ for a complete unloading of the GCS drift with 6 <i>brittle-ductile</i> transition zones and $\beta = 0.4$ , everywhere assigned. ....	136
<b>Figure 4.42</b> : distribution of displacements' norm (a) and horizontal stress (b) for a complete unloading of the GCS drift with 6 <i>brittle-ductile</i> transition zones and $\beta = 0.4$ . ....	137
<b>Figure 4.43</b> : distribution of the damage variable $D$ for a complete unloading of the GED drift with 6 <i>brittle-ductile</i> transition zones and $\beta = 0.4$ ....	137
<b>Figure 4.44</b> : distribution of displacements' norm (a) and vertical stress (b) for a complete unloading of the GED drift with 6 <i>brittle-ductile</i> transition zones and $\beta = 0.4$ . ....	137

## Chapter 5

<b>Figure 5. 1</b> : conceptual model of the 3d geomechanical problem in (a) and proposed simplification of 2d axisymmetric modelling of discontinuities in (b) ....	144
<b>Figure 5. 2</b> : 3d scan structural survey for the interpretation of shear <i>Chevrons</i> ' structure, in (a), and excavation-induced fractures in drill core, in (b). ....	145
<b>Figure 5. 3</b> : multi-scale scheme for 2d axisymmetric simulations ....	146
<b>Figure 5. 4</b> : schematization of a cohesive zone model for crack evolution. ....	147
<b>Figure 5. 5</b> : damage degradation of the single joint cohesive zone. ....	147
<b>Figure 5. 6</b> : cohesive fracture's yield surface, in (a), modified from [76]. Damage law $g(D)$ , for different values of the yielding parameter $\beta$ . ....	149
<b>Figure 5. 7</b> : boundary/initial conditions (a) and excavation procedure (b) for 2d axisymmetric simulations in single fracture numerical analyses. ....	152
<b>Figure 5. 8</b> : initial unstable fracture opening (a), followed by a progressive <i>joint-by-joint</i> (stable) cracking (b). ....	153
<b>Figure 5. 9</b> : diagram of the fracture evolution in (a) and a zoom on every consecutive joint opening in (b) ....	154

<b>Figure 5. 10:</b> stress path for the joint element intersecting the drift's sidewall.....	154
<b>Figure 5. 11:</b> analogue fracture initiation, increasing the <i>cohesive zone</i> strength, in (a) and comparison between the cracking length evolutions for the two <i>single fracture</i> simulations in (b). ....	155
<b>Figure 5. 12:</b> horizontal displacement field in (a) and radial displacement of the drift's perimeter along $z$ in (b) ....	155
<b>Figure 5. 13:</b> initial conditions in (a) and modified geometries corresponding to the drift's advancements in (b), for the excavation method 1.....	157
<b>Figure 5. 14:</b> results of fracture's occurrence after the first excavation step, as reported in Figure 5. 13b.....	157
<b>Figure 5. 15:</b> numerical model for the excavation method 2, with boundary conditions in (a) and geometry's dimensions in (b).....	158
<b>Figure 5. 16:</b> excavation function $d(z, t)$ , as a function of space in (a) and of time in (b).....	159
<b>Figure 5. 17:</b> contour plot illustrating the binary values assumed by $d(z, t)$ during a drifting numerical process.....	160
<b>Figure 5. 18:</b> contour plot of damage on joint elements, adopting the excavation method 2, showing fractures' occurrences and spacing.....	161
<b>Figure 5. 19:</b> numerical model for the excavation method 3. In (a), geometry's dimensions and boundary conditions and, in (b), a schematization of the numerical procedure applied for the excavation. ....	162
<b>Figure 5. 20:</b> contour plots for opened fractures, in (a), and horizontal displacements, in (b), calculated with the excavation method 3.....	163

## Appendices

<b>Figure A.1 :</b> procedures composing the step-by step resolution of the $\sigma : \varepsilon$ relation for a classical constitutive law in <i>Utilizer.f90</i> .....	183
<b>Figure A.2 :</b> local-global-local iterative procedure for yielding correction with global verification of the consistency law.....	184
<b>Figure A.3 :</b> normal and tangential local coordinates system in <i>POROFIS</i> and <i>DISROC</i> , for the evaluation of the stress state at $i$ .....	184
<b>Figure B.1:</b> volume element scheme for the anisotropic Drucker-Prager failure criterion. ....	185
<b>Figure B.2:</b> volume element scheme for the anisotropic Mohr-Coulomb type failure criterion. ....	187
<b>Figure B.3:</b> $\sigma_{\theta, \omega}$ , as a function of $\omega$ , with $\varphi = 20^\circ$ , $K = 15$ MPa and $h = 0.2$ .....	189
<b>Figure B.4:</b> $\sigma_{\theta}(p_C = 12 \text{ MPa})_{, \omega}$ as a function of $\omega$ , with $\varphi = 20^\circ$ , $K = 15$ MPa and $h = 0.2$ .....	191
<b>Figure B.5:</b> volume element scheme for the IV order anisotropic Mohr-Coulomb type failure criterion. ....	191
<b>Figure B.6:</b> $\sigma_{\theta, \omega}$ , as a function of $\omega$ , with $\varphi = 20^\circ$ , $K = 15$ MPa and $h_n = h_s = 1.44$ . ....	194
<b>Figure B.7:</b> $\sigma_{\theta}(p_C = 12 \text{ MPa})_{, \omega}$ as a function of $\omega$ , with $\varphi = 20^\circ$ , $K = 15$ MPa and $h_n = h_s = 1.44$ .....	195
<b>Figure B.8:</b> 3d model for stratified formation behind the section $\Gamma$ for 2d plane strain excavation problem.....	196

# List of Tables

## Chapter 1

<b>Table 1.1</b> : average extensions of extensional and shear fraction around the drifts at Andra URL as function of the gallery radius $r_a$ .....	11
<b>Table 1.2</b> : mineralogical composition at the main level of the URL [121]. .....	16
<b>Table 1.3</b> : summary of basic properties of Callovo-Oxfordian claystone according to different literature databases. 18	

## Chapter 2

<b>Table 2.1</b> : set of parameters for the basic elastic-plastic and elastic-damage material laws in <i>POROFIS</i> . .....	44
<b>Table 2.2</b> : set of parameters adopted for the first elastic-plastic and elastic-damage numerical simulations with perfect yielding. ....	51
<b>Table 2.3</b> : extension of plastic radius for each of the results reported in Figure 2.13.....	55
<b>Table 2.4</b> : parameters obtained by elastic-plastic and elastic-damage softening calibration. ....	57
<b>Table 2.5</b> : initial stress state components for the geometry reported in Figure 2.25. ....	65
<b>Table 2.6</b> : parameters to reproduce a perfect-brittle yielding response for failure zone in Figure 2.28.....	66
<b>Table 2.7</b> : parameters employed for the failure zone calculus in Figure 2.29. ....	67
<b>Table 2.8</b> : parameters for the softening mesh size sensitivity analyses. ....	74
<b>Table 2.9</b> : extension of plastic radius for each of the results reported in Figure 2.34 and Figure 2.35.....	75

## Chapter 3

<b>Table 3.1</b> : boundary and initial stress components for the numerical analyses of EDZ shape and extension (inner heterogeneous failure) reported in Figure 3.1. ....	80
<b>Table 3.2</b> : numerical values for the parametrization of the $2d_{ED}$ model adopted in the following.....	81
<b>Table 3.3</b> : comparison between estimated intervals and computed values for short-term $U_x$ and $U_y$ . ....	82
<b>Table 3.4</b> : summary of $\sigma_{0,\omega}$ and $\sigma_0(p_c)_{,\omega}$ employed for calibration of the anisotropic Drucker-Prager criterion. ....	87
<b>Table 3.5</b> : parametrisation for stress-strain diagrams in Figure 3.10 and for the next numerical failure analysis around GCS drift.....	88
<b>Table 3.6</b> : $\sigma_{(0)}$ components for the next numerical failure analysis around GCS drift. ....	89
<b>Table 3.7</b> : calculated maximal values of $ U_x $ and $ U_y $ around GCS and GED perimeters. Comparison with in-situ surveys from extensometers.....	92
<b>Table 3.8</b> : elastic parameters accounting for transverse isotropy, adopted in the next numerical analysis. ....	96
<b>Table 3.9</b> : calculated maximal values of $ U_x $ and $ U_y $ around GCS perimeters, compared with in-situ surveys from extensometers. ....	97
<b>Table 3.10</b> : data for $\sigma_0(p_c)_{,\omega}$ with $p_c = 12$ MPa [91], on specimens sampled with different inclinations and approximately the same initial water content.....	101
<b>Table 3.11</b> : model parameters for the anisotropic failure criterion in Eq. 3.30, calibrated in Figure 3.25.....	103
<b>Table 3.12</b> : numerical values for components $\sigma_{xx,(0)}$ , $\sigma_{yy,(0)}$ as reported in Figure 3.21. ....	103

## Chapter 4

<b>Table 4.1</b> : $\sigma_{(0)}$ components for the next numerical excavation analysis around GCS and GED drifts.....	112
<b>Table 4.2</b> : values of linear elastic and softening parameters adopted for the $2d_{ESD}$ model .....	115
<b>Table 4.3</b> : GCS drift, mesh-size sensitivity on displacements at the perimeter. ....	119

<b>Table 4.4</b> : GED drift, mesh-size sensitivity on displacements at the perimeter. ....	120
<b>Table 4.5</b> : calibration of the Mohr-Coulomb type anisotropic criterion defined with $\tilde{\sigma}(\mathbf{H})$ . ....	125
<b>Table 4.6</b> : contour plots of the analyses' results, according to the boundary conditions and imposed division of transition zones. ....	131
<b>Table 4.7</b> : summary of sub-horizontal and sub-vertical displacements calculated around GCS and GED drifts' perimeter ( $r = r_a$ ) . ....	138

## Chapter 5

<b>Table 5. 1</b> : description of $\sigma_{(0)}$ for GCS drift. ....	146
<b>Table 5. 2</b> : $\sigma_{(0)}$ as initial/boundary conditions for 2d axisymmetric simulations. ....	151
<b>Table 5. 3</b> : failure and damage yielding parameters for the first <i>single fracture</i> numerical simulation. ....	153
<b>Table 5. 4</b> : failure parameters for joint elements ....	160
<b>Table 5. 5</b> : parameters for the numerical excavation procedure ....	160

## **Chapter 1**

# **Introduction and Context of the Research**



In this first chapter, the study motivations and industrial application of these thesis' works are initially presented. The geomechanical problem to be investigated is explained, together with the choice of a modelling approach based on damage mechanics. A description of the real scale facilities (the *Underground Research Laboratory* managed by Andra), constituting the reference for mathematical and numerical simulations of the problem follows. Some significant researches concerning the modelling of the excavation effects in the geological formation of Callovo-Oxfordian claystone are then reported, together with a presentation of the material characteristics. The first section is concluded with the work's outline explaining the organisation of the manuscript and the logic paths followed to simplify the geomechanical problem for mathematical and numerical purposes.

The second section provides a brief summary of some literature benchmarks considered pertinent to provide a scientific framework for the topic of failure around deep boreholes. Then, to provide an analytical complement for the problem of stresses redistribution around circular openings, the elastic solution is reported together with a simple example considering a perfect yielding failure. The section is concluded showing two typical example of failure localization around a deep circular gallery.

## 1.1 Motivations and background

Energy supply by nuclear power plants constitutes, nowadays, one of the main technologies adopted in this industrial sector. The treatment and isolation of the radioactive waste generated by activities based on nuclear energy have become fundamental concerns. In principle, more intensive emissions of radionuclides from radioactive waste would require more isolated disposal facilities. In France, about the 90% of total wastes (Low- and Intermediate-Level, Short-Lived wastes, LIL-SL, and Very Low-Level wastes, VLL) are disposed in existing, sub-surficial locations. At the national level, the principal issue is the disposal management of the minor part of nuclear waste, constituting, nonetheless, more than 90% of the total radionuclides emissions: the High-Level and Intermediate-Level, Long-Lived wastes (HL and IL-LL) [5]. Among other countries, France has identified the *deep geological repository* (DGR) as a suitable and safe technique to conceive and implement deep disposal facilities for radioactive waste correspondent to HL and IL-LL types. DGR is based on the individuation of favourable geological formations characterized by structural, hydro-mechanical and geochemical properties to isolate as best the radionuclides dispersion and assure the most efficient construction and operation of disposal facilities. These type of formations are identified as *host media*, or *host rocks*, because of their geological features (e.g. claystones and shales). In France, the mission of the site identification and feasibility studies for a DGR concept is in charge to the French national radioactive waste management agency, *Andra* (*Agence Nationale pour la gestion des déchets radioactifs*). The agency has individuated the deep geological formation of Callovo-Oxfordian claystone as an appropriate host rock constituting the final barrier for the disposal of HL and IL-LL wastes. Characteristics such as very low permeability and reduced molecular diffusion constitutes favourable elements for this choice ([8], [31] and [121]).

Medium-term reversibility, for about 100 years, and safety after the repository closure, for thousands of years, are key requirements related to the conception of a geological repository. Andra has conceived the project *Cigéo* (*Centre Industriel de Stockage Géologique / Industrial center for geological disposal*) to forward these demands ([3], [31]): it will be composed of horizontal cells connected to access galleries and containing the radioactive wastes as illustrated in Figure 1.1. Once the feasibility study phase started, Andra began, in 2000, the construction of the Underground Research Laboratory (URL) at the agency Centre in the Meuse-Haute Marne department (CMHM). Excavated in the Callovo-Oxfordian formation, at about 500 m depth, the laboratory is a network of drifts to characterize the chemo-thermo-hydro-mechanical properties and behaviors of the confinement claystone, as well as test, demonstrate the feasibility, optimise the concept of the future DGR.

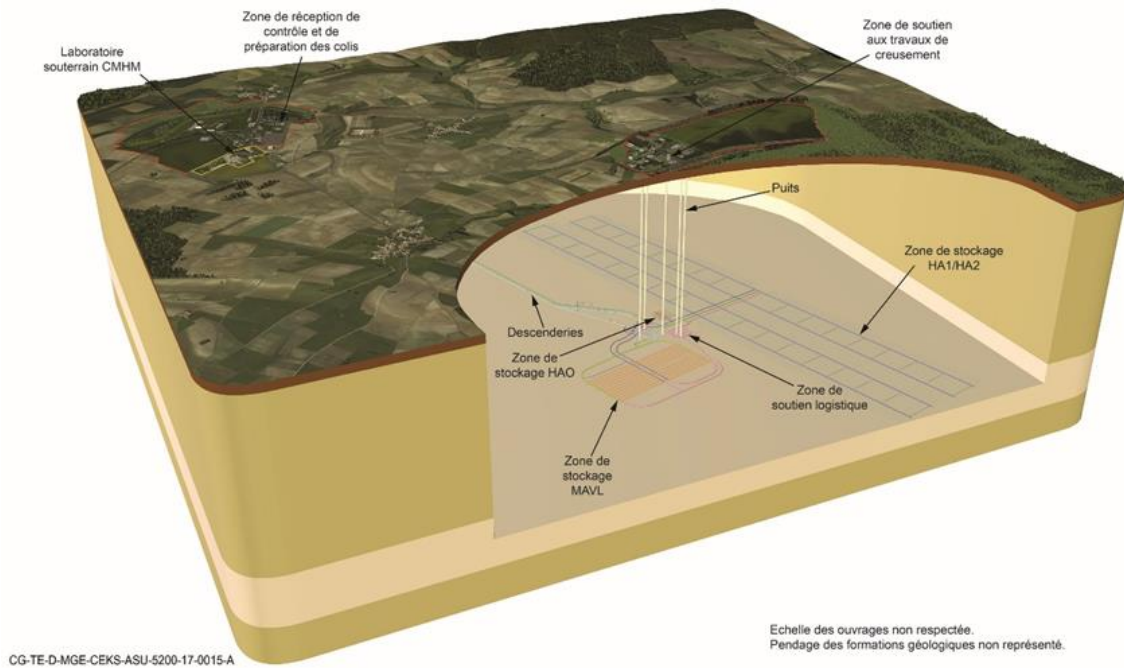


**Figure 1.1** : overview of DGR in the concept of *Cigéo* project (image is property of Andra).

Drifts are intended as real-scale experiments to characterize the response of the rock according to the excavation method, structure geometry, supports system and orientations with respect to the principal stresses' directions (e.g. [7], [8], [91]). In geological formations such as the Callovo-Oxfordian claystone, the excavation of deep tunnels creates a surrounding area characterized by cracking and diffused failure, whose shape and extension are the main issues for the repository safety. The terminology to define this zone has undergone several changes with progresses in geomechanics. Generally, researchers divide the overall zone in different concentric parts depending on the induced modifications on the hydraulic and transmission properties of the material ([71], [103]). In the proximity of the gallery perimeter, the formation of several interconnected macro-fractures leads to irreversible changes of these properties. Moving outward, the influence of the excavation decreases, together with the induced damage interconnections. Further, only temporary and reversible modifications of the material properties occur. Thus, in the area where failure occurs, variations of the excavation fractures' entity and interconnections corresponds to different modifications of initial properties. These zones can be all referred as *Excavation Damage Zones*, *EDZs*, according to the classification review published by Perras and Diederichs [71]. Collecting different related works, the authors provide a scheme distinguishing four concentric levels of EDZs, from the excavation perimeter:

1. Construction Damage Zone (CDZ): it includes inevitable excavation consequences and additional damage effects induced by the construction method. These second effects may be adjusted according to the excavation / support techniques.

2. Highly Damaged Zone (HDZ): it includes inevitable damage causing geometry, structure, and/or induced stress changes, independent of excavation method. Highly interconnected macro-fractures are typically observed.
3. Excavation Damage Zone (EDZ): it corresponds to the transition from a connected damaged area to a partially connected or isolated damage area. In these areas, irreversible micro-damage phenomena occur.
4. Excavation Influence Zone (EIZ): this is a stress-strain influence zone involving only reversible (elastic) changes. The outer limit, occurring at a large radial distance, is of minimal interest for a single excavation. On the contrary, in case of multiple, parallel excavations the interaction of adjacent EIZs should be considered.

In this work, for sake of simplicity in the notation, the ensemble of the three zones CDZ, HDZ and the inner EDZ is identified by the single acronym *EDZ* (*D* = Damaged). A unique notation identifying the area characterized by irreversible changes in the material were already proposed by Emsley et al. [35] and also adopted by Tsang et al. [103]. The transition zone, moving from the inner limit of the EDZ to the EIZ (irreversible to reversible changes) is identified with the acronym *EdZ* (*d* = disturbed). Many efforts are addressed by Andra to understand the phenomena leading to the formation of an *EDZ-EdZ* system around the drifts in the Callovo-Oxfordian claystone at the Underground Research Laboratory.

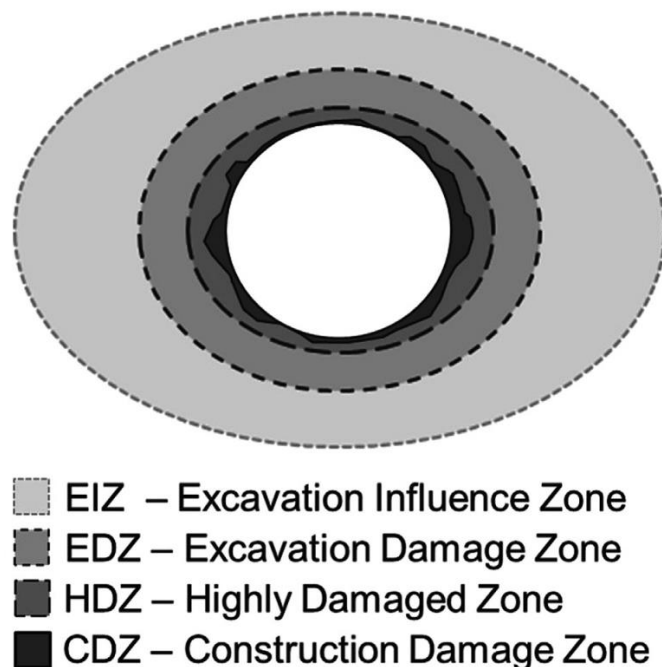


**Figure 1.2** : identification of four zones affected by mechanical perturbation due to excavation, as reported in Perras and Diederichs [71].

These efforts have undergone several scientific campaigns, at different levels, from laboratory micro-scale to in-situ experiments and monitoring, with the cooperation of different research groups (e.g. [91], [93]). This thesis project aims to provide a contribution on these efforts. Numerical analyses on computational models at the underground structure scale constitute the subject of this work and are presented and discussed in this manuscript. The approach adopted to model the EDZ-EdZ formation around deep galleries will account for a reduction of the host rock resistance when the reversible (elastic) conditions are overcome and material failure is attained. In general, the extension of this zone is estimated from a stress field calculated in elasticity or based on an elastic-plastic calculation ([3], [25]); if the first method does not take into account the redistribution of stresses due to irreversible phenomena, the conventional elastic-plastic modelling seems insufficient to explain the geometry of the failure zone encountered in some cases of deep structures in quasi-brittle rocks ([77], [78] and [102]). Observations suggest that *damage mechanics* phenomena, while the material resistance decreases (i.e. softening), are crucial to the development of these zones. Predictions of the material short-term failure will be performed by a purely mechanical mathematical and numerical modelling, based on damage mechanics. In the following, a description of the Andra URL, with relevant in-situ instrumentations and measurements is reported. Some related researches and thesis' projects, concerning geotechnical aspects of the feasibility study, are discussed. A presentation of the Callovo-Oxfordian claystone concludes the contents of this section.

### *1.1.1 Observations and studies at the Andra Underground Research Laboratory*

The Andra Underground Research Laboratory (URL), which construction began in 2000, is formed by a network of main drifts, service galleries and two vertical access shafts, accessible by the surface facilities at the CMHM. Drifts are characterized by diameter extensions varying from 4 to 9 m. Micro-tunnels are also present, whose diameters do not exceed 1 m. According to its research purposes, it is still an ongoing work with advancing tunnel fronts and operating experiments and installations. An initial drift was excavated at a depth  $Z = 455$  m from one of the vertical access shafts. Then, the main level of the galleries network forming the URL was set at  $Z = 490$  m, within the Callovo-Oxfordian claystone. At this level, the formation presents an in-situ stress state  $\sigma_{(0)}$  without significant spatial variations. Its components have been estimated as follows (e.g. [31], [113]):

- Vertical stress,  $\sigma_v = \rho g Z \approx 12.7$  MPa;
- Major horizontal stress,  $\sigma_H \approx 16.2$  MPa;
- Minor horizontal stress,  $\sigma_h \approx 12.4$  MPa.

The pore pressure at the main level (-490 m) is around 4.7 MPa. It is underlined that the components reported above correspond to average values obtained from several estimation campaigns. Here, drifts are horizontally excavated and have been designed to follow, in most cases, the directions of the two principal horizontal stress components,  $\sigma_H$  and  $\sigma_h$ , respectively oriented at N155°E and N65°E ([8], [9] and [31]). A recent plan of the URL [93] is illustrated in Figure 1.3: the drifts' network is formed by a series of galleries with perpendicular connections. According to the in-situ stresses previously reported, drifts can be divided in two groups:

- Horizontal drifts with a quasi-isotropic, 2d stress state on their cross-section (i.e.  $\sigma_v$  and  $\sigma_h$ );
- Horizontal drifts with an anisotropic, 2d stress state on the same section (i.e.  $\sigma_v$  and  $\sigma_H$ ).

Excavations of drifts (4 to 9 m of diameter) were generally performed with two standard devices: the pneumatic hammering machine, the road header machine and TBM, shown respectively in Figure 1.4a, Figure 1.4b and Figure 1.4c. Because of the anisotropy of the in-situ stress state components, a main target for mathematical and numerical modelling, generally related to excavation response in the material, consists in the prediction of an EDZ-EdZ system validated by observations for both groups of drifts, where the hydro-mechanical conditions of a boundary value problem change. In particular, two instrumented drifts, already considered by previous / ongoing researches (e.g. [41], [57], [67], [97] and [105]) will be adopted to validate the modelling propositions: GCS drift, (*Galerie de Conception Souple / Flexible*), lined by yieldable concrete wedges; and GED drift (*Galerie Expérimentale Deux*), supported by sliding arches installed every meter. Both are conceived to have a flexible support, yieldable according to rock deformations ([7], [60]) (e.g., Figure 1.5a and Figure 1.5b).

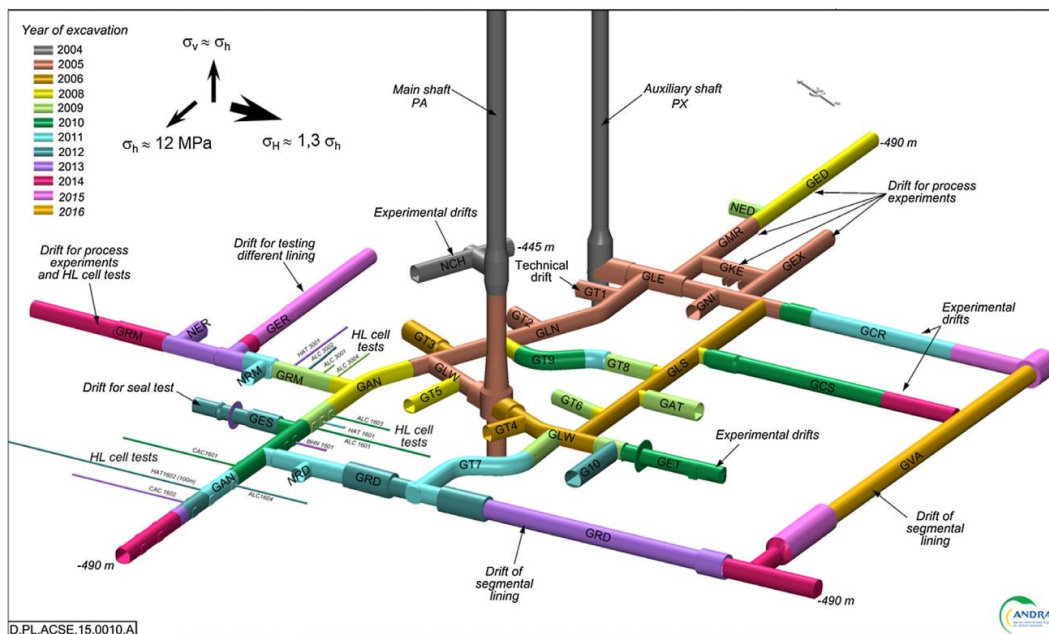
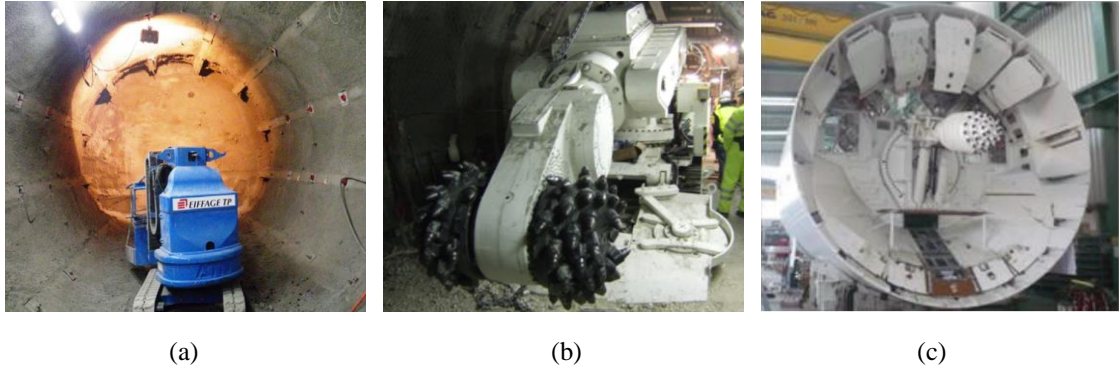


Figure 1.3 : plan of the Andra URL at the Centre Meuse-Haute Marne and principal stress directions [93].



**Figure 1.4** : excavation methods for the URL drifts reported in Figure 1.3. From (a) to (c), pneumatic hammering [17], road header [93] and road header under shield machine [42].



**Figure 1.5** : support systems for GCS (a) and GED (b) drifts. (from [42] and [93]). Supports are mainly composed of radial bolts (HA25 of 3 m length), with a ~15 cm of fibres shotcrete and welded mesh.

Extensive surveys have been executed to investigate the fractured zone around galleries, as the GCS and GED drifts. Geological insights from 3d scan, at the front and sides, allowed to map the excavation-induced structures within the claystone and to produce statistical data on the fracture pattern ([7], [9]). In the next page, the scan procedure with some interpretation of discontinuities formed around galleries' perimeters is reported in Figure 1.6. Resin-injection tests have also been executed, on radial core-drillings: the setup adopted for these experiments is detailed Armand et al. and Noiret et al. ([9], [60]). Figure 1.7 reports the estimated fractures density and Figure 1.8 a 3d model of the fractures pattern, for the drifting direction parallel to  $\sigma_H$ . In-situ observations from similar tests conducted on micro-tunnels confirms a certain repeatability of fractures' patterns in relation to the borehole diameter. In general, two types of fractures can be distinguished: *shear fractures* (mode II) and *tensile fractures* (mode I). Shear fractures are preponderant and expand longer and deeper in the rock, with low dip discontinuities. They are often called *Chevron* or *herringbone* fractures, due to the resulting geometrical structure [9]. Extensional fractures (*spalling*) are concentrated near the drift's wall with a more heterogeneous dip and strike [92].

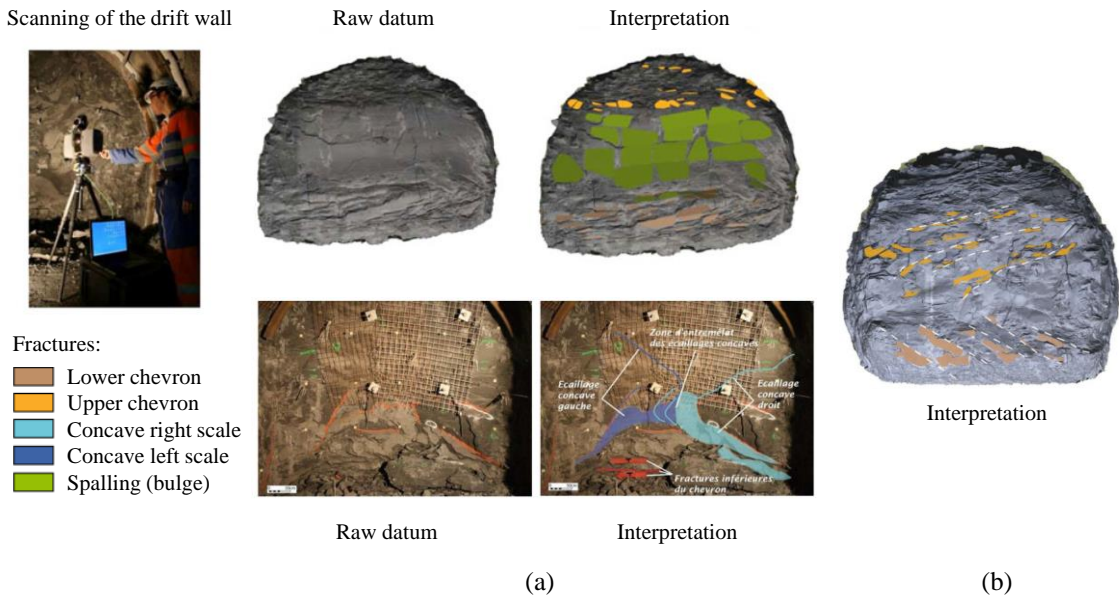


**Figure 1.6** : 3d scan analyses around inside galleries at Andra URL. Results for a front gallery along  $\sigma_H$  (up) and  $\sigma_h$  (low) in (a). Results at the gallery lateral wall along  $\sigma_H$  in (b) (modified from [9], [66]).

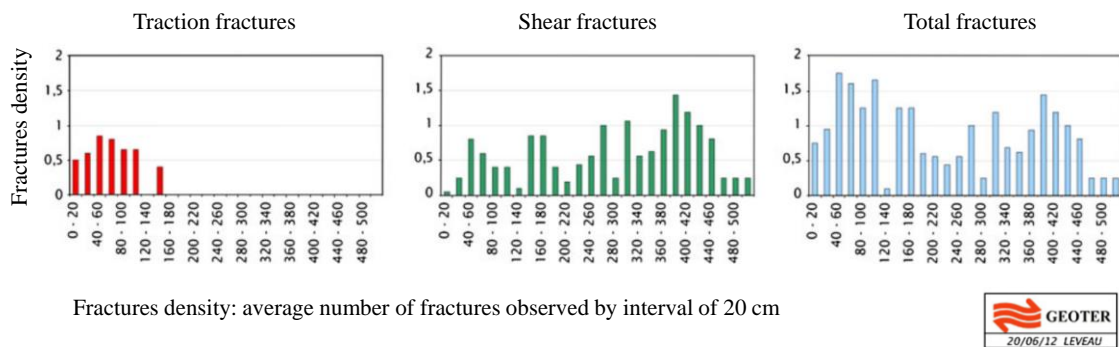


**Figure 1.7** : estimated fractures density, moving radially from GCS drift's wall (modified from [9]).

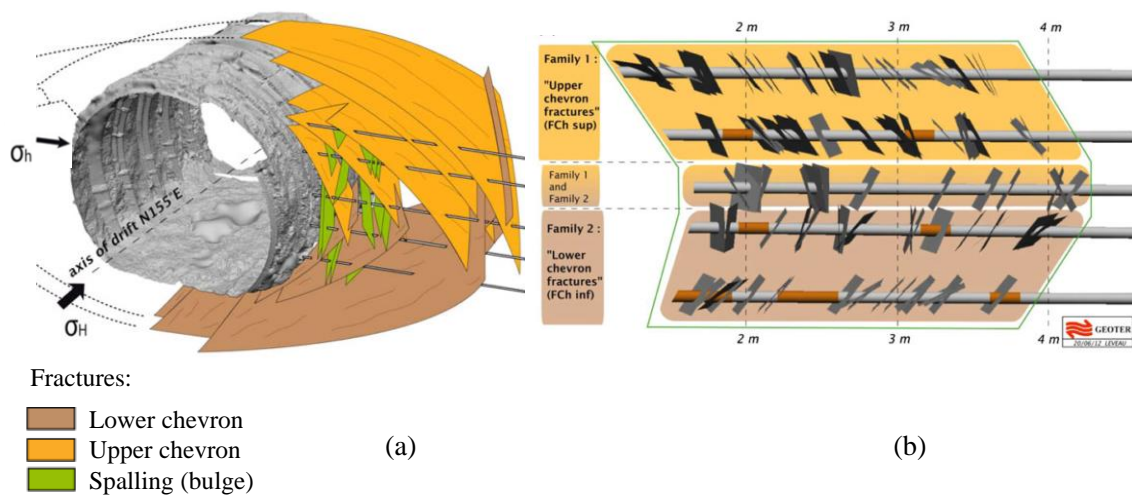


**Figure 1.8** : conceptual model for extensional and shear (*Chevron*) fractures' pattern for the drift GCS (a) together with detected fracture planes on the radial direction (b) (modified from [9]).

According to Figure 1.7, the average density is around 6 fractures per meter in the sidewall of the GCS drift, but it varies greatly along the radial direction. The number of fractures is greater between 0.30 and 1.80 m, corresponding to the heterogeneous area of highly interconnected fractures, in mode *I* and *II* (EDZ). Density increases again between 3.20–4.60 m from the wall, in the area where discontinuities appear more homogeneous, forming the Chevron structures (EdZ). Here, two families of fractures may be noticed, having the same strike, perpendicular to the axis of the drift, but an opposite dip, as illustrated in Figure 1.8. From this model, it can be remarked that these families distinguish a *lower* system of Chevron fractures from an *upper* system, both generated by normal shear. In the horizontal plan, lower Chevrans are curved while, in the vertical at the middle of the face tunnel, the strike of fractures is perpendicular to drift axis. On the borders of drift's faces and walls, the strike is oblique, oriented toward the unexcavated zone, while their dip is oriented toward the excavation. Upper Chevrans have the same curve in horizontal plane, but their dip is oriented toward the unexcavated zone. The *spalling* or *bulge* structures, localized in the middle of the drift's face (Figure 1.8a), corresponds to a fractures system generated by extension [9]. For drifts parallel to the direction of  $\sigma_h$ , shear Chevron fractures generated ahead of the tunnel front during excavation, with a fracture dip is around  $45^\circ$ . Extension of the Chevron zone ahead of the excavation face is between 0.5 and 1 drift diameter ( $\sim 4$  m). They develop beyond the drifts, with a dip oriented at a lower angle ( $10\text{--}30^\circ$ ) with respect to the wall. This fracture system was identified only in drill cores from the sidewall. For these drifts, unloading tensile fractures are identified all around the excavations (sidewall, ceiling and floor). Most fractures are parallel to the drift wall, partially connected together [9]. More than fractures' initiation, their development around the excavations is related, among other reasons, to the orientations of the principal in-situ stresses and to material anisotropies. The shape of the areas including fractures differs between the two directions, because of the different initial stress state. For drifts excavated along  $\sigma_H$ , the initial stress state is quasi-isotropic in the cross section plane, but the extent of the system EDZ-EdZ is higher on the horizontal direction. Therefore, short-term evolution of this zone may be mainly driven by the intrinsic claystone anisotropy. On the other hand, along  $\sigma_h$ , anisotropy of the in-situ stresses should play a key role in the vertical development of the EDZ-EdZ. Table 1.1 reports the average extension, related to the gallery's radius  $r_a$ , of fractured zones for both excavation directions.

**Table 1.1** : average extensions of extensional and shear fraction around the drifts at Andra URL as function of the gallery radius  $r_a$ , according to Armand et al. [9].

Drift direction parallel to:	Extensional fractures			Shear fractures		
	ceiling	floor	lateral	ceiling	floor	lateral
$\sigma_H$	$0.2 \cdot r_a$	$0.2 \cdot r_a$	$0.4 \cdot r_a$	-	-	$1.6 \cdot r_a$
$\sigma_h$	$0.6 \cdot r_a$	$0.8 \cdot r_a$	$0.2 \cdot r_a$	$1.2 \cdot r_a$	$1.6 \cdot r_a$	-

Based on data from in-situ surveys, Figure 1.9 reports the conceptual models for the fractures structures previously described, for drifts along  $\sigma_H$  (Figure 1.9a) and  $\sigma_h$  (Figure 1.9b). Extension and shape for the estimated EDZ-EdZ area, including the fractures families, on the cross section of the two types of drift, is also illustrated in two dimensions.

It may be confirmed that the formation of this fractured area is essentially due to the drifting action, causing immediate and short-term mechanical perturbations in the surrounding material. Irreversible phenomena corresponding to damage and plastic effects concur, together, to the material yielding, eventually, to the coalescence of discontinuities causing fractures. Nonetheless, some post-excavation analyses do not exclude desaturation effects (e.g. tunnel ventilation) at the drifts perimeter and, in the long-term, deformations due to creep [66]. Two examples of modelling proposition for a 2d prediction of the EDZ-EdZ are reported in the following, according to the works of and Pardoen & Collin [69], in Figure 1.10a, and Mánica et al. [57], in Figure 1.10b. On the left, a cross-anisotropic elastic-visco-plastic material is adopted and the total deviatoric strain 60 days after the excavation are displayed. Strain localisation develops preferentially in the horizontal thanks to a variable material cohesion providing an anisotropic failure criterion, aiming to predict the Chevrons' main structure occurring around the GCS drift. The modelling for strains localisation is detailed in the related thesis' works [66]. On the right, an estimation of the damaged zone for the same gallery is plotted by the cumulative plastic multiplier contours [57]. Even in this case, according to the authors, anisotropy of the geological formation should be accounted in the elastic-visco-plastic model.

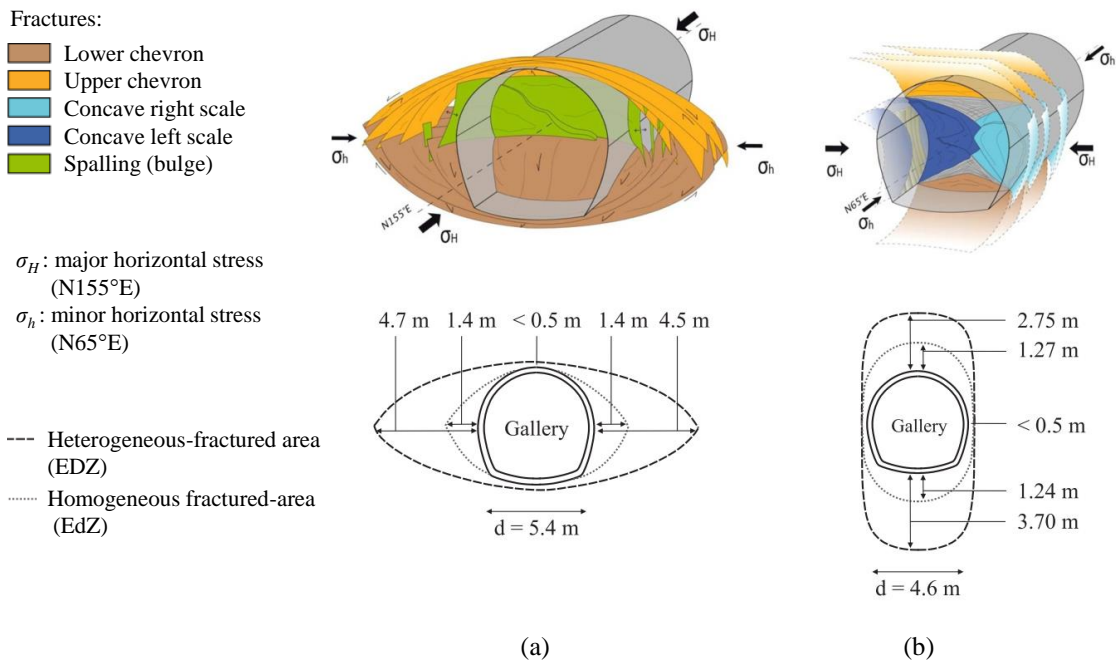


**Figure 1.9** : 3d conceptual models for fractures patterns around drifts at the URL, together with the 2d simplification of the system EDZ-EdZ. In (a), models for the drift GCS along  $\sigma_H$  and, in (b), for the drift GED, along  $\sigma_h$  (modified from [66]).

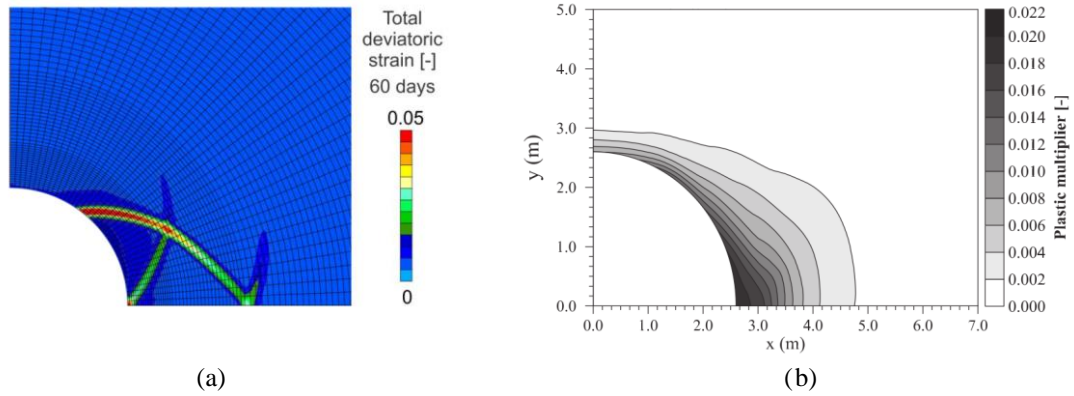


**Figure 1.10** : (a), development of shear bands around GCS drift according to the total deviatoric strain at 60 days from excavation [66] and (b), contours of the cumulated plastic multiplier at the end of the excavation [57].

Another type of geological surveys, adopted in this work to validate the proposed models, is constituted by in-situ measures and estimations of drifts' convergences and displacements occurring in the rock massive around the excavations. An exhaustive modelling exercise to reproduce short and long-term convergences around drifts at the Andra URL is reported in the thesis' works of Guayacán-Carrillo [42]. Convergence measurements show an anisotropic closure, which depends on the drifts' orientations and confirms the observations already provided for the failure zones evolution. In particular, a different horizontal to vertical average convergence ratio can be derived for drifts along both directions. This ratio is about 0.5 to for drifts following the direction of  $\sigma_H$  and 4 for those excavated along  $\sigma_h$  [8]. Vertical and horizontal convergences measured in GCS and GED drift are reported in Figure 1.11 and show a displacement rate significantly higher during about 100 days after the excavation and the installation of the acquisition systems. Nonetheless, it can be remarked a residual convergence rate which is not null, in general, for measures in Figure 1.11a. In Figure 1.11b, vertical convergence shows a residual rate further than 1000 days after the excavation: here, vertical convergence coincides with the principal direction of failure evolution.

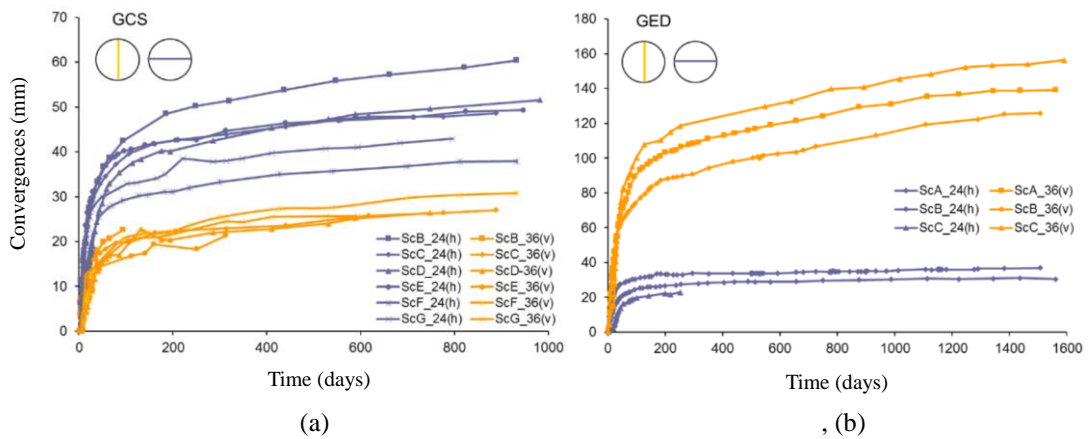


**Figure 1.11** : horizontal (blue) and vertical (orange) convergences evolution in GCS drift, excavated along  $\sigma_H$  (a), and in GED drift, excavated along  $\sigma_h$  (b). Modified from [42].

It is underlined that convergences measurements, previously shown, derive from instrumentation placed after the tunnel face passage at the investigation sections. Thus, it is often important not to neglect hydro-mechanical effects induced in the medium ahead of the front gallery, before the excavation front transition. Indeed, when describing the fractures pattern for the main drifts' directions, it has been specified that fractures may be generated already ahead of the tunnel front during excavation. For this reason, the mine-by test technique has been employed at the URL to investigate hydro-mechanical effects induced in the COx claystone before the tunnel face transition ([8], [91] and [93]). In particular, many data from hydro-mechanical mine-by tests for drift GCS are available, as pore over-pressures and displacements induced in the material located in the area including / surrounding the forthcoming excavation. Installations were conducted from a service tunnel parallel and 30 m distant from GCS, according to the set-up reported in Figure 1.12. Figure 1.13 shows a reanalyse of total horizontal displacements,  $U_x$ , from mine-by tests extensometers at different radial distances from the wall of GCS drift. The data processing allowed to separate the instantaneous part of displacements (Figure 1.13a) from the time-dependent (Figure 1.13b).

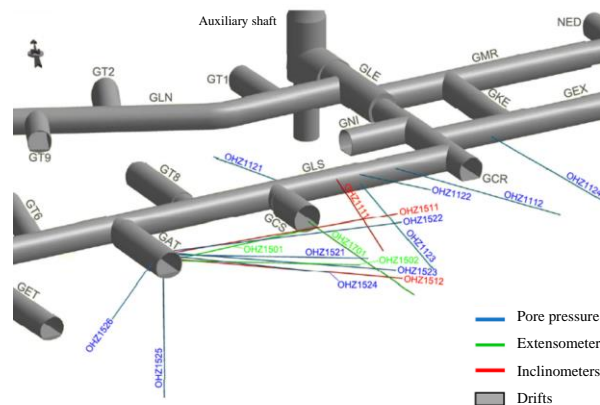


Figure 1.12 : Mine-by test concept for GCS, modified from [93].

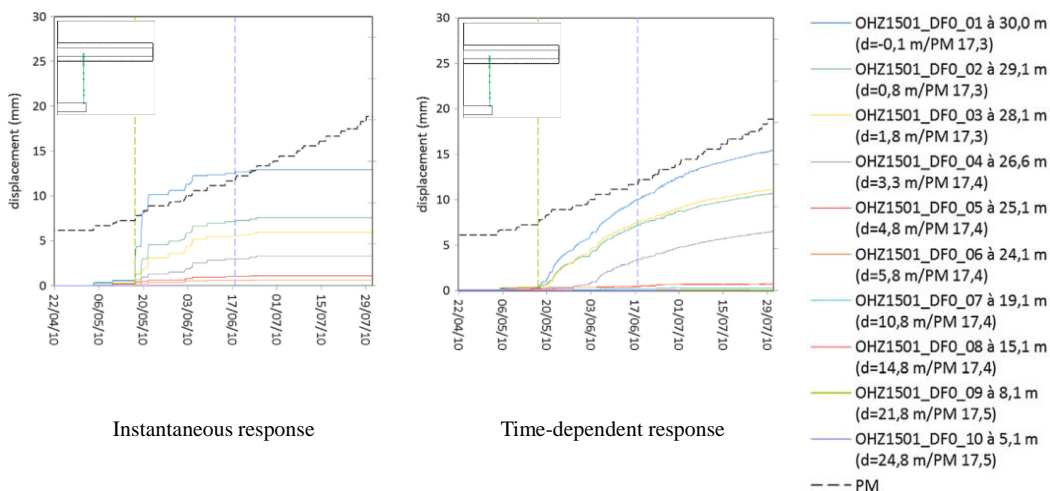
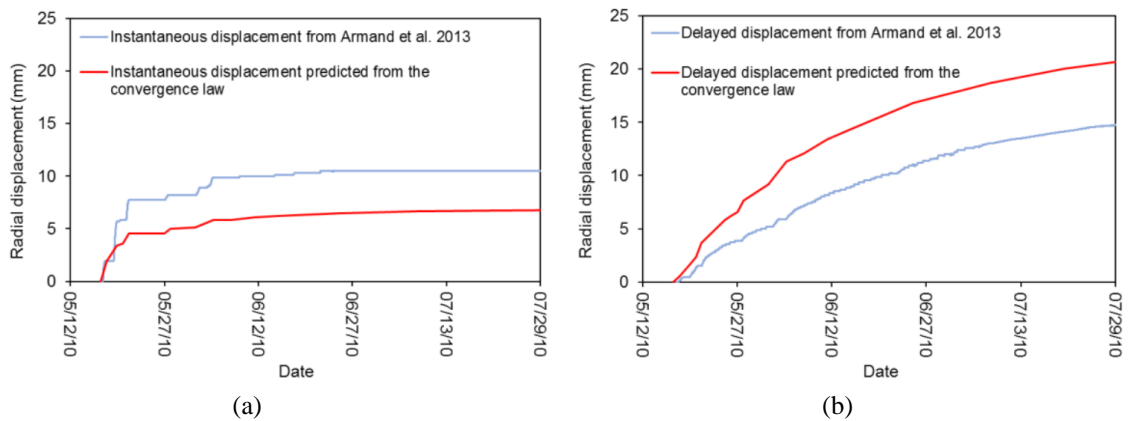


Figure 1.13 : instantaneous and differed displacements around GCS from mine-by tests, modified from [93]. Data are originally published in [8].



**Figure 1.14** : horizontal displacements prediction in drift GCS, reported in Guayacan–Carrillo and compared to the original results from Armand et al. [8]. Instantaneous in (a) and differed displacements in (b).

In both diagrams of Figure 1.13, the dotted line *PM* identifies the excavation chronogram while the two vertical dotted lines indicates the transition of the front at the instrumented section (green dotted line) and the successive front location corresponding to zero rate of instantaneous displacement (purple dotted line). Two significant observations enrich the database already provided by convergences in Figure 1.11: firstly, the survey point closest to the drift’s wall (OHZ1501\_DF0\_01 in Figure 1.13a) detects a displacement of about 4 mm occurring in the section before the tunnel front transition. Then, according to the excavation chronogram detailed in Noiret [60], the purple dotted line indicates a distance of about 2 times the drift’s diameter, from the considered section, where no further instantaneous displacement are esteemed. According to the reanalyses of rough data, Figure 1.13b confirms the existence of time-dependent displacements immediately after the front transition at the instrumented section: in particular, an almost constant rate of time-dependent displacement can be remarked during the advancing of the front up to 2 time the tunnel diameter, with a successive decreasing. As mentioned before, extensive analyses to model instantaneous and differed displacements in the Andra URL drifts is comprehended in the thesis’ works of Guayacan-Carrillo [42]. Figure 1.14 reports the horizontal displacements reproduction, by modelling, for the instrumented point closest to the drift’s perimeter previously illustrated in Figure 1.13 (instantaneous displacements in Figure 1.14a and differed one in Figure 1.14b).

In the following, the last content of this current section is presenting a characterization of the Callovo-Oxfordian formation. Eventually, the conclusion of the section will report the general outline of this manuscript, specifying the main contents of each chapter.

### 1.1.2 The Callovo-Oxfordian claystone formation

The geological area of the Paris East Basin, formed by an accumulation of sedimentary deposits, includes the argillaceous formation of Callovo-Oxfordian claystone (COx). A simplified geological map of arising formations in the North-Eastern France, together with the location of the Andra URL at the Centre Meuse-Haute Marne, is reported in Figure 1.15 [122]. In Meuse/Haute-Marne department, the formation has a variable depth (around 420 and 550 m) and it is interbedded between Dogger limestone (below) and Oxfordian limestone formations (above). The local geological stratification is reported in Figure 1.16. Callovo-Oxfordian claystone is included among the well-known *soft rock / hard soils* formations widely studied in the European contest for nuclear waste repository, as the Boom Clay, in Belgium, and Opalinus Clay, in Switzerland (e.g. [13], [50]). The mineralogical composition of COx includes mainly illite and smectite clay minerals, quartz, and carbonate [84]. At the main level of the research laboratory (-490 m), clay minerals composition in COx is almost constant with 55 % I/S (illite–smectite interstratified minerals), 30% illite and 15% kaolinite and chlorite. The overall mineralogy is reported in Table 1.2 [121].

**Table 1.2** : mineralogical composition at the main level of the URL [121].

<i>Tectosilicates</i>	20%
<i>Carbonates</i>	20 – 25%
<i>Clay minerals</i>	50 – 55%
<i>Subordinate pyrites and iron oxides</i>	3%

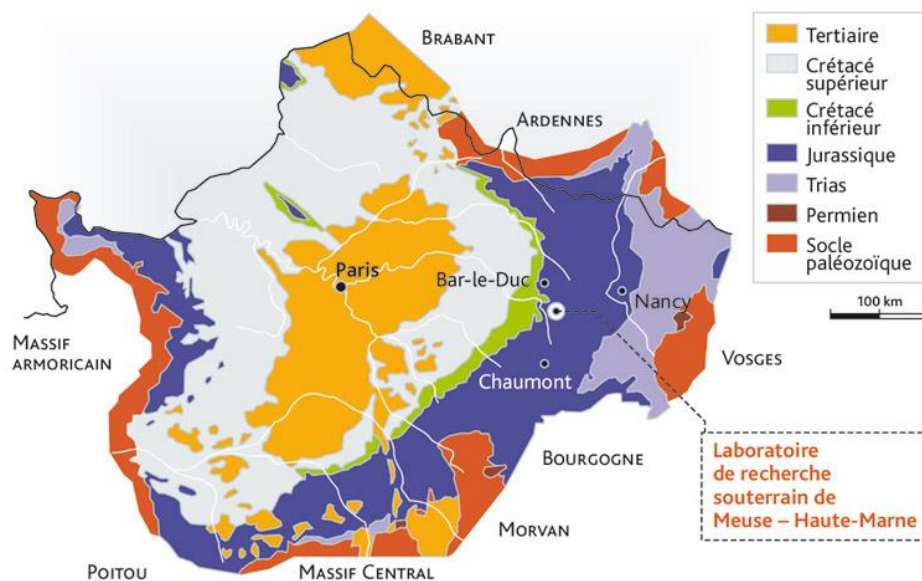


**Figure 1.15** : simplified chart of the Paris East Basin and location of the Andra URL at the CMHM (IRSN [122], courtesy of Stéphane Jungers).

Microstructural analyses reveal a mean pore diameter of about 20 nm ([26], [87]), leading to very low permeability values. The average claystone porosity at -490 is equal to  $18 \pm 1\%$  (e.g. [8]) and natural water contents of core samples ranges between 5 and 8% (e.g. [42]). An anisotropic behaviour is featured by the material, mainly due to its mode of deposition: a layered structure is observed due to the sedimentary nature of the formation. Over time, such a geological structure develops further its vertical cross-anisotropy due to the increasing overburden vertical stress [113]. Eventually, Callovo-Oxfordian claystone presents a double anisotropy, on the hydro-mechanical properties and on in-situ stress state. For instance, different Young moduli's values exist changing from the parallel to the perpendicular direction relatively to the horizontal bedding planes. Uniaxial compressive strength of the material also depends on the considered orientation to the main loading direction. In the next page, Table 1.3 collects some typical values of material properties concerning microstructure and hydraulic and mechanical parameters.

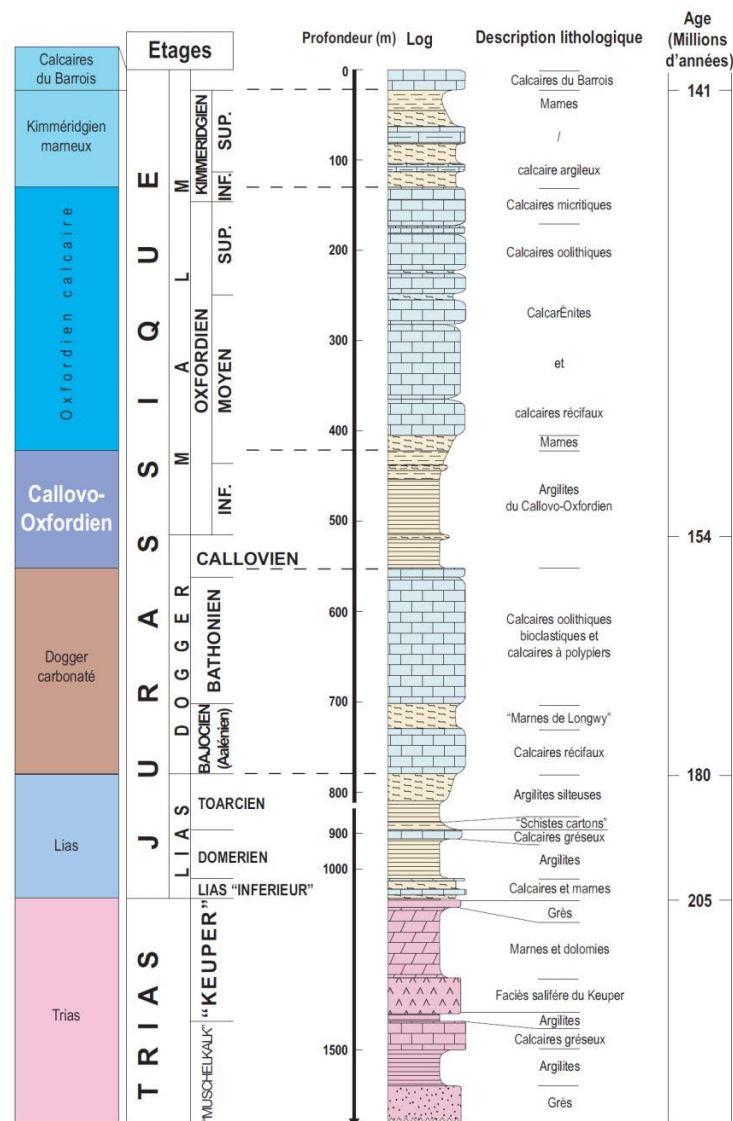


Figure 1.16 : vertical section of the local geology at the site of the Andra CMHM [121].

**Table 1.3** : summary of basic properties of Callovo-Oxfordian claystone according to different literature databases ([8], [26], [37], [87], [114] and [121]). Single values must be considered as average estimations.

<i>Microstructure properties</i>	Mean pore diameter [nm]	20
	Void ratio, $e$ [-]	0.22
	Density, $\rho$ [kg/m <sup>3</sup> ]	2300 - 2400
<i>Mechanical and hydraulic properties</i>	Young modulus, $E$ [MPa]	3500 - 8000
	Poisson's ratio, $\nu$ [-]	0.2 - 0.35
	Biot's coefficient, $b$ [-]	0.6
	Friction angle, $\varphi$ [°]	20
	Cohesion, $C$ [MPa]	3 - 7
	Uniaxial compressive strength, $\sigma_0$ [MPa]	17 - 25
	Uniaxial tensile strength, $\sigma_R$ [MPa]	1.5
	Water content, $w$ [-]	0.05 - 0.08
	Permeability, $K_w$ [m <sup>2</sup> ]	$5 \cdot 10^{-20}$ - $5 \cdot 10^{-21}$

In general, Young moduli's anisotropy may vary from 1.2 up to 2, defined as the parallel to perpendicular values ratio, with respect to the horizontal material stratification [8]. The variation of material failure resistance, in term of uniaxial compressive strength,  $\sigma_0$ , as function of the bedding orientation, gives the variability reported in Table 1.3. Also the tensile strength shows a weak dependency on the material orientation.

The stress-strain and failure behaviour of the Callovo-Oxfordian claystone has been widely studied, taking into account coupled thermic and hydraulic phenomena, at the material point scale as well as the drifts' one (e.g. [8], [12] and [57]). For the short-term response, triaxial compression (TXc) and extension (TXe) tests have been performed to analyse the COx deformation behaviour together with the failure resistance. Examples of these aspects are, respectively, reported in Figure 1.17a and b, showing results of TXc tests. A linear response is observed under low deviatoric stress, before the resistance peak, particularly for reduced values of confining pressures,  $p_C$ . A discussion focusing on the variation of material stiffness (i.e. the Young modulus), remarked in different literature sources, is provided in Chapter 2. In particular, the imposed rate of axial strains, in triaxial shear stage, seems a fundamental parameter to be checked while testing, to assure if the estimated stiffness parameters correspond to an undrained or drained response [12]. Brittle failure of the samples is observed under low  $p_C$  values, which is confirmed by the formation of inclined shear bands. This implies a strong reduction of material resistance in final, or *residual*, conditions. An increase of the confinement  $p_C$  determines, naturally, higher resistance values in triaxial conditions,  $\sigma_0(p_C)$ . This is a common observation in laboratory testing on geomaterials.

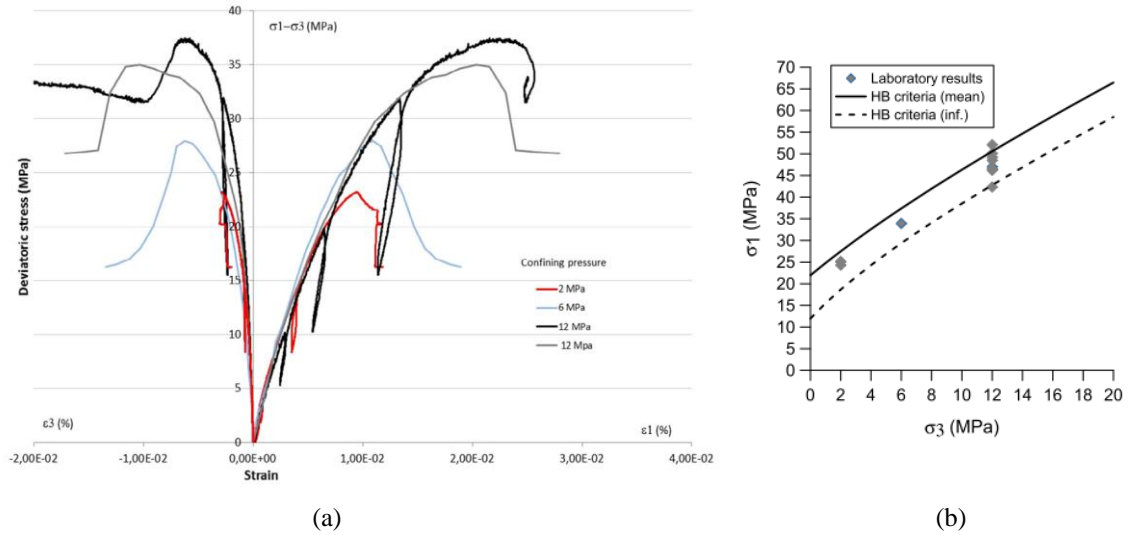


**Figure 1.17** : stress-strain behaviour under different lateral stresses,  $p_C$  and principal stresses plot at failure with a Hoek-Brown failure criterion interpolation [10].

Meanwhile, a higher confinement corresponds to a change in the claystone post-failure behaviour, which reveals to be more and more ductile, with respect to the very fragile response in uniaxial conditions. The stress-strain diagrams in Figure 1.18 show an example of this yielding behaviour transition under five different  $p_C$  values. The same numerical simulations mentioned above will focus also on this aspect. In the fourth chapter, a discussion on the physical aspects of material yielding and their implications on the employment of the proposed numerical model predicting the excavations' behaviour will be provided. Eventually, it has been observed that the claystone presents a rather brittle behaviour under tensile loading [42]. Concerning the long-term aspects, creep of the COx has already been investigated and included in some proposed models based on elastic-plasticity, for the behaviour prediction to excavations. Useful references for the description and analyses of time-dependent behaviour of the material can be found in the works of Guayacán-Carrillo et al. ([41] and [42]), Mánica et al. [57] and Zhang et al. [117].

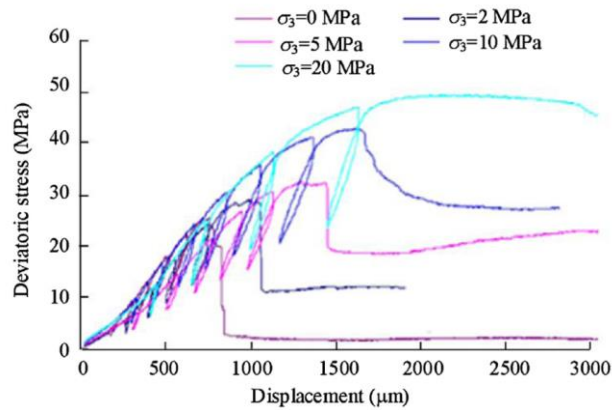


**Figure 1.18** : TXc tests showing a transition from the fragile post-peak response under uniaxial conditions ( $p_C = 0$ ) to the almost perfect yielding under high confining pressure ( $p_C = 20$  MPa) [8].

As anticipated, an outline of the manuscript is reported hereby. Previously, the context of deep geological repository (DGR) for nuclear waste has been presented. Then, Andra facilities at the Centre Meuse-Haute Marne have been presented, together with real-scale observations and current modelling proposals for the host rock behaviour to excavations. A presentation of the material has followed. The second part of Chapter 1 recalls some significant benchmarks for failure analyses around boreholes, with published works related to other DGR contexts for nuclear waste. Then, two existing analytical solutions are introduced: firstly, in elasticity, then, considering perfect failure conditions (in plasticity). The rest of the manuscript is structured as follows:

- Chapter 2: presentation of the main Finite Element (FEM) code adopted and basic material models. Simulation of circular excavations in perfect and softening yielding conditions. Discussion on the post-failure predictions, changing from plasticity to damage yielding. Upgrade of the elastic-damage model to be employed for successive numerical analyses.
- Chapter 3: adoption of the upgraded model to validate the short-term failure for a drift along  $\sigma_H$  at the Andra URL. Focus of the axial stress' influence on 2d numerical simulations in plane strain hypothesis. First implementation of anisotropies for the failure criterion and the elastic stiffness tensor. Prediction of failure at the URL main level, around two perpendicular drifts, for different boundary conditions. Revision of the failure criterion to neglect the axial stress in the resistance calculation and numerical testing.
- Chapter 4: second modification of the stiffness tensor, based on a damage dissipation affecting the shear component of the elastic-damage matrix. Further improvement of the anisotropic failure criterion and proposition of the final elastic-damage model for drifts' analyses following both the main horizontal stresses ( $\sigma_H$  and  $\sigma_h$ ) at Andra URL. Introduction of the *brittle-ductile transition* of the COx post-failure behaviour and considerations on drained or undrained testing conditions for stiffness parameters' choice. Final numerical simulations for 2d failure around circular openings.
- Chapter 5: simplification of fractures patterns around drifts at Andra URL and approximation to a 2d axisymmetric problem for numerical purposes. Presentation of the damage-based cohesive model for the interfaces and numerical FEM discretisation with *joint elements*. Numerical testing analysing a *single-fracture* opening. Then, introduction of *multi-fractures* simulations and numerical implementation of the excavation process. Discussion on the results obtained, focusing on the fractures length and mutual distance of occurrence.
- General conclusions and outlooks to the thesis' works, with perspectives for possible forthcoming researches.

Numerical modelling proposed throughout the whole manuscript is logically arranged following two main *research axis*. This subdivision depends on the choice for the 2d analyses approach of a typical 3d problem in geomechanics and geotechnical engineering, as illustrated in Figure 1.19. This double approach has physical and numerical correspondences, described in the following.

- From Chapter 2 to Chapter 4, 2d plane strain simulations of failure in the cross-section of circular galleries are presented. They contribute to the short-term modelling of the system EDZ-EdZ, for drifts at the Andra URL, along  $\sigma_H$  and  $\sigma_h$  (i.e. different boundary conditions). Finite Element (FEM) approach constitutes the suitable tool for the numerical investigation of generation and evolution of the EDZ-EdZ, intended as a *continuous*, “diffused” failure system.
- In Chapter 5, 2d axisymmetric simulations describing fracturing around galleries are presented. Here, short-term failure is intended as a *discontinuous* system. Boundary conditions correspondent to in-situ stresses, will remain, in general, constant. This second part of numerical analyses differs also on some of the numerical tools. As previously introduced, linear elements (*joint elements*, e.g. [39]), reproducing discontinuities in a FEM-based displacements field, will be included. At the same time, these works offer the chance to study different numerical implementations simulating a tunnelling excavation.

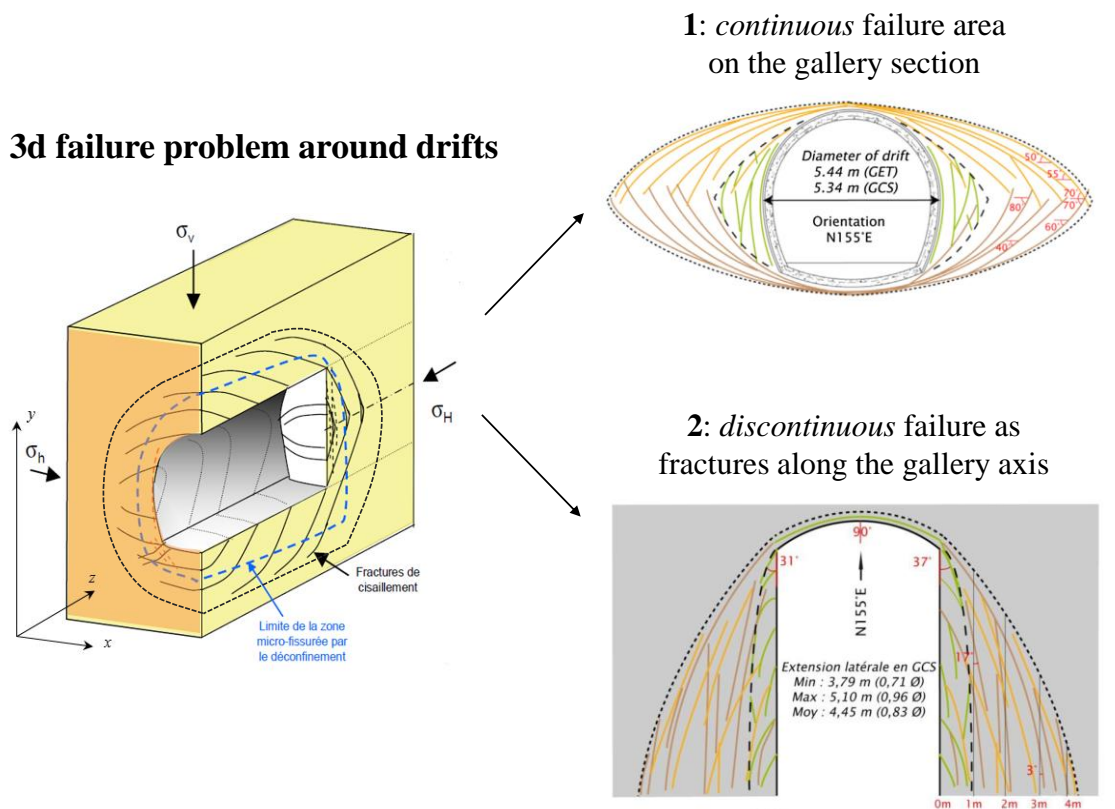


**Figure 1.19** : illustration of the proposed analyses' concept for failure description and numerical modelling (original figures modified from [60] and [93]).

## 1.2 Some aspects of failure around deep excavations

Failure around boreholes, tunnels and drifts constitutes a wide theoretical topic in geomechanics and, sometimes, an engineering challenge for practitioners. A brief summary, with some significant references, is discussed in the following.

Phenomenological, analytical and numerical analyses focusing on boreholes stability and failure reunite research works and applications lasting for decades. In particular, localized failures around openings, often defined *breakouts* or *exfoliations*, constitute a serious matter for the progress of a drilling process. Significant deviatoric stresses acting in the section plane, at great depth, enhance the stress concentrations around the borehole and lead to its deterioration. As reported in Vardoulakis et al. [109], failure is not a strict material property but depends on the stress path and boundary conditions of the system. According to the authors, two types of failure modes can be identified: *extension rupture* and *shear banding*. Figure 1.20 provides a scheme of these possible failure modes. Multiple failure possibilities introduce the concept of *bifurcation* of the solution. In case of the breakouts, an *instable* phenomenon occurs. These concepts are recalled in Chapter 2, when significant aspects on numerical results shown in Section 2.2 will be discussed. Nonetheless, a deep focus on these topics exceeds the scopes of this thesis. Rigorous mathematical formulation for instability analyses and determination of the critical bifurcation stress, around a circular borehole, are detailed in the exhaustive work of Vardoulakis & Papanastasiou [109]. Related numerical applications, concerning the localization and post-bifurcation treatment by regularization methods (e.g., Cosserat continuum) can be found in Papanastasiou & Vardoulakis [63] and, recently, in Papanastasiou & Zervos [65]. Similar analyses, based on observed failure mechanisms, are reported in Crook et al. [28]: local instability often occurs as a borehole breakout (cross-sectional elongation of the initial geometry) and evolves, later, towards a more stable elliptical shape. Observations of the two mechanisms are illustrated in Figure 1.21.

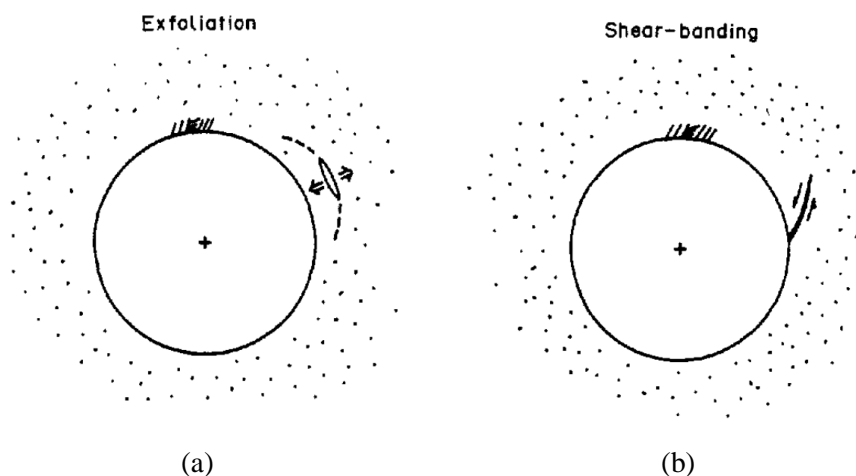


**Figure 1.20** : failure modes, as reported in Vardoulakis et al. [109]. Exfoliation (a), shear-banding (b).

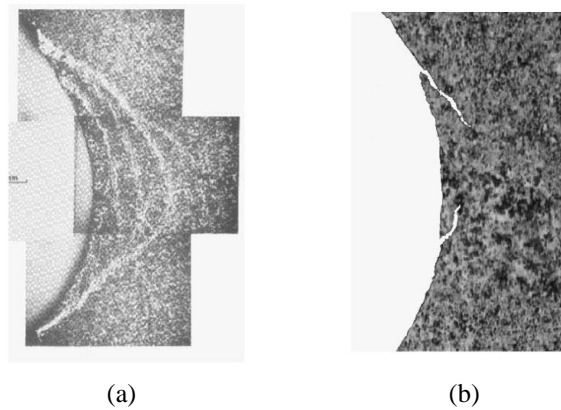


**Figure 1.21** : axial-splitting in sandstone (a) and shear failure in limestone (b), reported in Crook et al. [28]. A correspondence can be noticed with the conceptual schemes in Figure 1.20 and similarities with failure patterns around drifts in Andra URL can be remarked.

At the laboratory scale, analogue failure modes have been observed in hollow cylinder tests on Opalinus Clay and Boom Clay (Labiouse et al. [49], Labiouse & Vietor [50]), under specific hydro-mechanical controlled boundary conditions. As previously mentioned, these materials are considered as host geological formations for other feasibility studies of nuclear waste DGR in Europe, respectively at the sites of Mont Terri (Switzerland) and Mol (Belgium). In particular, bedding plane splitting and buckling in the indurated and brittle Opalinus Clay occurred (in analogy with Figure 1.20a and Figure 1.21a), while a predominance of shear failure along conjugated planes was observed in the more ductile Boom Clay (similarly to Figure 1.20b and Figure 1.21b). It is worth underling that the failure area, referred as *Excavation Damaged Zone* in the mentioned publications ([49] and [50]), corresponds to the system denoted as EDZ-EdZ, in this manuscript. For the case of Boom Clay, numerical simulations, based on hollow cylinder experiments, revealed a damage zone geometrically similar to in-situ evidences at the Andra URL. The elliptical failure obtained in numerical simulations agreed with laboratory testing, as reported in François et al. [36] and illustrated in Figure 1.22.

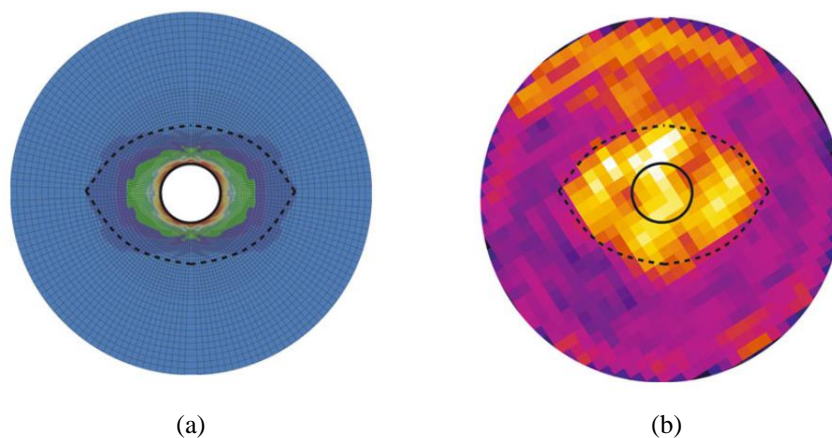


**Figure 1.22** : qualitative comparison of the shape of the excavation damaged zone between (a) numerical prediction and (b) X-ray tomography scan after hollow cylinder testing. Modified from François et al. [36].

As COx claystone, Boom Clay exhibits some anisotropic properties and, according to the authors, they contribute to the formation of an eye-shaped EDZ-EdZ. In Figure 1.22a, the numerical simulation, showing the shape and distribution of total deviatoric strains, provides a correct prediction of the failure extension in the medium, subjected to hollow cylinder testing.

Besides failure modes, failure extension around an excavation is a fundamental assessment required for the drifting process and the retaining structures. When dealing with DGR for nuclear waste storage, this concern becomes a priority to prevent radionuclides transport, along the system EDZ-EdZ, from the geological barrier used for isolation [71]. The stress-induced yield of hard rock at depth combines different mechanisms where tensile damage and confinement reduction also play important roles. To the extreme, tensile micro-cracking, influenced by low confinement conditions near excavations, leads to the material slabbing (e.g. [33], [38]). It corresponds to the same instable failure type previously introduced (*breakout*). For brittle rocks, as the Callovo-Oxfordian formation, the strength envelope can be represented by the multiphase diagram in Figure 1.23. This envelope is the result of the mechanics of tensile fracture accumulation and propagation corresponding to a reduction of the yield surface as confining stresses are relaxed. These mechanisms are well identified by a *damage-type* energy dissipation. As a certain damage threshold is exceeded, acoustic emissions are observed and micro-crack damage accumulates, leading to cracks interaction and, eventually, coalescing in a macro-scale shear failure, if the confinement level is sufficiently high (*shear-banding*). Moving to the low confinement zone (*Spalling Failure* in Figure 1.23), individual cracks can propagate differently, leading to macroscopic axial splitting or spalling normal to the minor principal stress (denoted  $\sigma_3$ ).

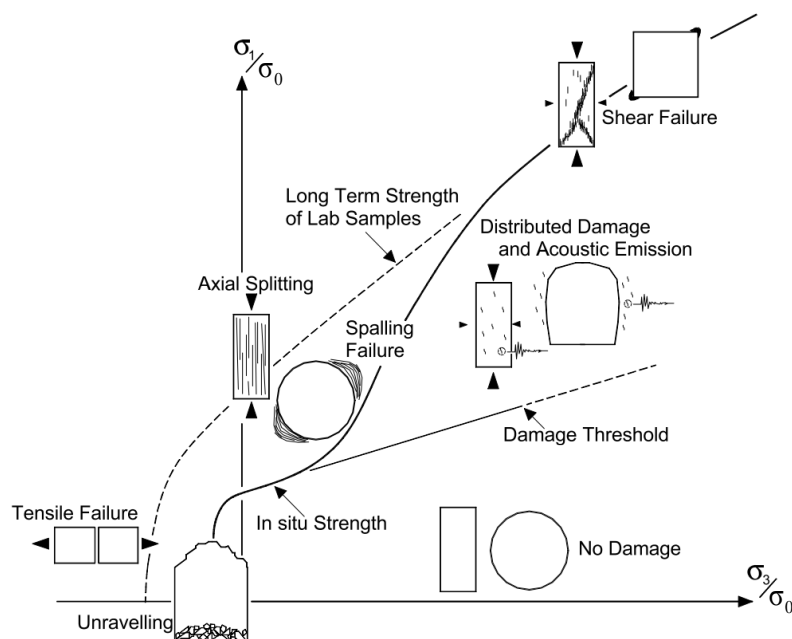


**Figure 1.23** : failure envelope for brittle failure, showing four failure mechanisms: no damage, shear failure, spalling, and unravelling. Axis are normalized to the UCS,  $\sigma_0$ . Modified after Diederichs [33].

As a result, the rock strength, in-situ, is likely lower than the correspondent prediction from laboratory tests, as fewer cracks (i.e. material damage) are required for failure [33]. If the effects of tensile damage and resistance, amplified by elevated sensitivity to low confinements, are neglected, erroneous predictions of rock yield can be performed. In this work's analyses, even if failure is traditionally evaluated considering the contribution of confinement in the criterion formulation, the damage-based mechanics is privileged and investigated, rather than a better-known approach in plasticity. *Continuum damage mechanics* (CDM) approaches have been already reported, in scientific literature, as successful analysis tools to take into account the inhomogeneous redistribution of material properties and stresses in the vicinity of the boreholes [86]. Hard rock formations such as Berea or Tablerock sandstone appear, sometimes, even more appropriate to exploit the potentiality of damage modelling, in particular for stress-driven failure at boreholes, due to stress concentrations, developing in breakouts (e.g. [28], [86]).

This review, concerning non-linearities and irreversible aspects of materials surrounding boreholes at different scales, had the objective to draw a general bibliographic context for the specific issues related to observations at the Andra URL. Without the intention to deeply focus on each mentioned reference, an attempt to collocate the thesis' subject in a determined geomechanics topic has been made. In the following, it seems suitable to include three subsections describing some basic mathematics to approach the problem of excavation in pre-compressed media. Thus, the stress' solutions around a circular cavity will be shown, firstly, in elasticity and, lastly, accounting for a simplified failure condition. In both cases, the analytical solutions are exposed. Then, simple conditions for localization of failure at a cavity wall will be presented.

### *1.2.1 2d stress solution for tunnel cross section in case of elasticity*

Assuming a linear elastic material, the analytical solution for the calculation of the stress field around a circular borehole exists. For sake of simplicity, a change from the Cartesian reference system to a cylindrical coordinate system is assumed, in general, for mechanical problems concerning circular boreholes, i.e. showing axial symmetries. A cylindrical gallery with the cross section perpendicular to the direction  $z$  is considered, as illustrated in Figure 1.24a. In Figure 1.24b, the cross section on the plane defined in Cartesian coordinates  $(x ; y)$  is reported together with the local reference in cylindrical coordinates,  $(r ; \theta)$ . The coordinate  $r = r_a$  identifies the gallery radius. In cylindrical coordinates, for stress fields around a circular borehole, the tensorial form of classical equilibrium equations without body forces, in Eq.1.1 are written according to Eq. 1.2a and b:

$$\nabla \cdot \boldsymbol{\sigma} = 0 \quad (1.1)$$

$$\frac{\partial \sigma_{rr}}{\partial r} + \frac{\sigma_{rr} - \sigma_{\theta\theta}}{r} = 0 \quad ; \quad \frac{1}{r} \frac{\partial \sigma_{\theta\theta}}{\partial \theta} + \frac{\partial \sigma_{r\theta}}{\partial r} + 2 \frac{\sigma_{r\theta}}{r} = 0 \quad (1.2a-b)$$

Cylindrical equilibrium in Eq. 1.2a and b includes the hypotheses of plane strain, i.e.  $\varepsilon_{zz} = 0$ . The solution of the stress components in elasticity, valid for the entire domain on  $(x ; y)$  or  $(r ; \theta)$  according to Figure 1.24b, can be obtained starting from Eq. 1.2a and b and applying the boundary conditions correspondent to the far-field conditions ( $r \rightarrow \infty$ ) and to the gallery perimeter ( $r = r_a$ ). The simplest formulation, accounting for a circular gallery with a retaining structure providing a support equal to  $p_0$ , refers to an isotropic pre-compressed medium (e.g. a deep rock formation). The tensor describing an isotropic in-situ stress state, for every point of the domain and considering the third direction correspondent to the axis of symmetry  $z$ , writes:

$$\boldsymbol{\sigma}(x, y, z) = \boldsymbol{\sigma}(r, \theta, z) = \sigma_{\infty,(0)} \cdot \mathbf{I}_{(3 \times 3)} \quad (1.3)$$

According to Eq. 1.3, the initial, or in-situ, stress tensor depends only on the initial stress component,  $\sigma_{\infty,(0)}$ , which multiplies the  $(3 \times 3)$  identity matrix. This boundary conditions, together with the condition imposed by the internal pressure at  $r = r_a$ , provides the solution of the radial and orthoradial stress components, derived from Eq. 1.2a and b. They write, respectively:

$$\sigma_{rr} = \sigma_{\infty,(0)} - (\sigma_{\infty,(0)} - p_0) \frac{r_a^2}{r^2} \quad (1.4)$$

$$\sigma_{\theta\theta} = \sigma_{\infty,(0)} + (\sigma_{\infty,(0)} - p_0) \frac{r_a^2}{r^2} \quad (1.5)$$

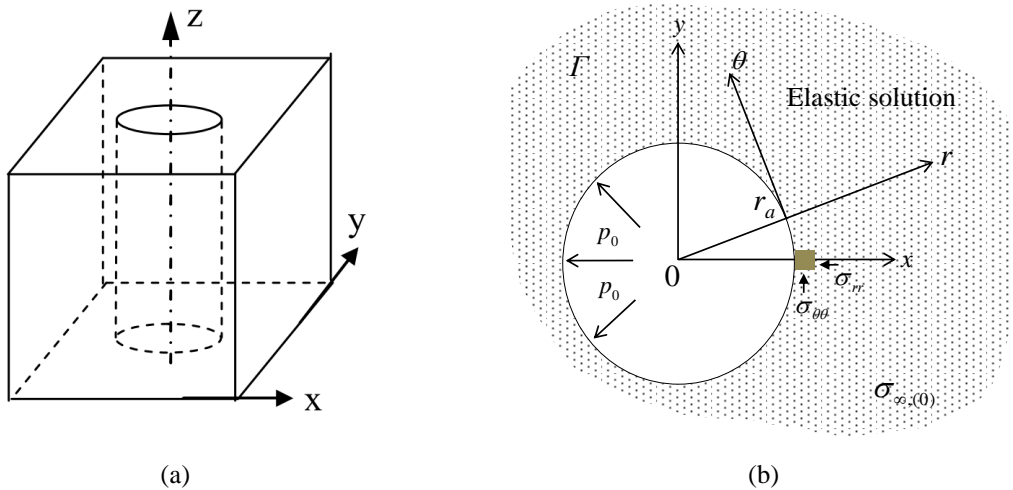


**Figure 1.24** : axial symmetry of a 3d borehole problem (a) and plane of reference for the analysis of stress-strain fields on a gallery cross-section (b).

Under the assumption of complete excavation with no support linings and focusing on the zone coincident with the tunnel perimeter, i.e.  $r = r_a$ , Eq. 1.4 and 1.5 can be significantly simplified:

$$\sigma_{rr}(r = r_a, p_0 = 0) = 0 \quad (1.6)$$

$$\sigma_{\theta\theta}(r = r_a, p_0 = 0) = 2\sigma_{\infty,(0)} \quad (1.7)$$

In particular, if a failure condition for the material was considered, Eq. 1.7 would represent the value to be compared to the uniaxial compressive strength (*UCS*),  $\sigma_0$  in this work. The elastic solution, for whatever radial direction, of the planar components  $\sigma_{rr}$  and  $\sigma_{\theta\theta}$ , is illustrated in Figure 1.25. To trace the graphic, it is assumed:

- Gallery radius  $r_a = 2.5$  m and no internal support, i.e.  $p_0 = 0$ .
- Initial isotropic stress  $\sigma_{\infty,(0)} = -12$  MPa.

It is necessary to clearly define the signs convention, defining when the state variables considered in analytical and numerical works, presented throughout the entire manuscript, assume a positive or negative value. According to a common practice of rock mechanics and oppositely to the soil mechanics reference, positive values for stresses and forces define, here, tensile actions. Negative values define, on the contrary, stresses and forces correspondent to compressive actions. For instance, for a stress tensor component  $\sigma_{ij}$ , one writes:

$$|\sigma_{ij}| = \begin{cases} +\sigma_{ij} & \text{if } \sigma_{ij} > 0 \\ -\sigma_{ij} & \text{if } \sigma_{ij} < 0 \end{cases} \quad (1.8a-b)$$

Concerning kinematic variables, positive strains and displacements assume positive values when corresponding to elongations along the coordinates' versus of the reference system adopted.

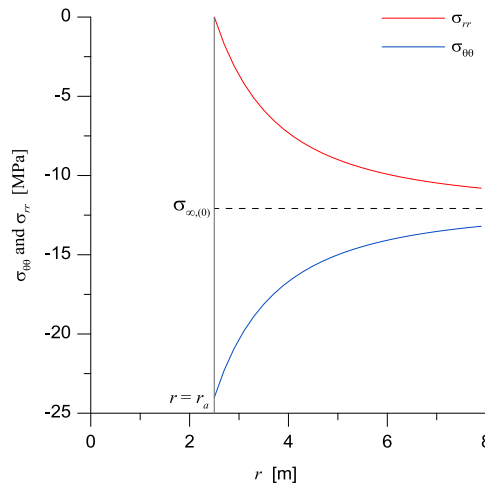


**Figure 1.25** : analytical elastic solution for cylindrical stress components acting in the cross section gallery with reference to Eq. 1.4 and 1.5.  $r_a = 2.5$  m and  $\sigma_{\infty,(0)} = -12$  MPa.

The solution reported above shows that, on a radial direction, whatever increment of one stress component corresponds to an equal decreasing of the other; formally:

$$\dot{\sigma}_{rr} = -\dot{\sigma}_{\theta\theta} \quad , \quad \forall r \quad (1.9)$$

The validity of Eq. 1.9 above is easily verified even in presence of an internal pressure  $p_0$  correspondent to a lining structure, according to Eq. 1.4 and 1.5. From a physical point of view, if the ensemble of the hypothesis above is true, the excavation of a circular tunnel induces an increasing of the deviatoric part,  $\mathbf{s}$ , of the initial stress tensor  $\boldsymbol{\sigma}_{(0)}$ . Thus, the material is subjected only to distorsional deformations (changes in shape), without development of spherical deformations (changes in volume). In particular, this is true not only for every point in the cross section, but also within the entire space  $(x; y; z)$  or  $(r; \theta; z)$ . This corresponds to the plane strain hypotheses ( $\varepsilon_{zz} = 0$ ) in the cylindrical equilibrium (Eq. 1.2a and b), which allows stating an eventual condition on the axial stress  $\sigma_{zz}$ , in purely elastic behaviour:  $\dot{\sigma}_{zz} = 0$ . With respect to an initial value, coincident with in-situ stress state or imposed as boundary condition in numerical modelling, no variation occurs in the initial value  $\sigma_{zz,(0)}$ . In particular, according to the system of Figure 1.24b, if no initial value for  $\sigma_{zz}$  is defined *a priori* as boundary condition,  $\sigma_{zz,(0)}$  is directly obtained by the plane strain condition:

$$\varepsilon_{zz} = \frac{\sigma_{zz}}{E} - \frac{\nu}{E}(\sigma_{rr} + \sigma_{\theta\theta}) = 0 \quad \rightarrow \quad \sigma_{zz,(0)} = \nu(\sigma_{rr,(0)} + \sigma_{\theta\theta,(0)}) \quad (1.10)$$

$E$  is the Young's modulus and  $\nu$  the Poisson ratio. Eq. 1.9 and the right condition of Eq. 1.10, together, show the validity of the boundary condition  $\dot{\sigma}_{zz} = 0$ . In many numerical analyses presented in the successive chapters, the initial condition  $\sigma_{zz,(0)}$  will be determined according to Eq. 1.10. In the following, failure conditions are introduced and modifications of the elastic solution will be analysed, under some simplicity assumptions.

### 1.2.2 A 2d stress solution for tunnel cross section in case of elasticity - perfect plasticity

With a linear elastic and perfect yielding behaviour, it is possible to evaluate the extension of the failure zone  $r_p$  as well as and the stress variables in every point of the radial direction. As commonly adopted in literature (e.g. [48]), failure is modelled by the development of plastic deformations. According to the same cylindrical symmetry in 3 dimensions, (Figure 1.26a), for every point of the 2d domain in Figure 1.26b, a cylindrical coordinate system may be assumed. Again, the coordinate perpendicular to the plane is the axial coordinate  $z$ . The following hypothesis are considered:

- Mohr-Coulomb failure criterion [51] not depending on  $\sigma_{zz}$ .

- Purely frictional material,  $\varphi > 0$  while  $C = 0$ .
- Perfect plasticity after the elastic limit.
- Isotropic stress state in the cross section described by  $\sigma_{\infty,(0)}$ .
- Plane strain conditions:  $\varepsilon_{zz} = 0$ .

According to a Mohr-Coulomb approach with no cohesion, the criterion in cylindrical coordinates writes:

$$\sigma_{\theta\theta} - \sigma_{rr} = (\sigma_{\theta\theta} + \sigma_{rr}) \sin \varphi \quad (1.11)$$

$\sigma_{\theta\theta}$  at failure must respect the equation:

$$\sigma_{\theta\theta} = \frac{(1 + \sin \varphi)}{(1 - \sin \varphi)} \sigma_{rr} = K_p \sigma_{rr} \quad (1.12)$$

$K_p$  is the passive earth pressure coefficient. For the radial equilibrium equation (Eq. 1.2a):

$$\frac{\partial \sigma_{rr}}{\partial r} + \sigma_{rr} \frac{(1 - K_p)}{r} = 0 \quad \rightarrow \quad \frac{\partial \sigma_{rr}}{\sigma_{rr}} = \frac{\partial r}{r} (K_p - 1) \quad (1.13a-b)$$

The partial differential equation is resolved as follows:

$$\ln \sigma_{rr} = (K_p - 1) \ln r + \ln A \quad \rightarrow \quad \sigma_{rr} = A r^{(K_p - 1)} \quad (1.14a-b)$$

With the coefficient A:

$$\sigma_{rr}(r = r_a) = p_0 \quad \rightarrow \quad A = \frac{p_0}{r_a^{(K_p - 1)}} \quad (1.15a-b)$$

Since it is necessary to satisfy the failure condition:

$$\sigma_{\theta\theta} = K_p \sigma_{rr} \quad (1.16)$$

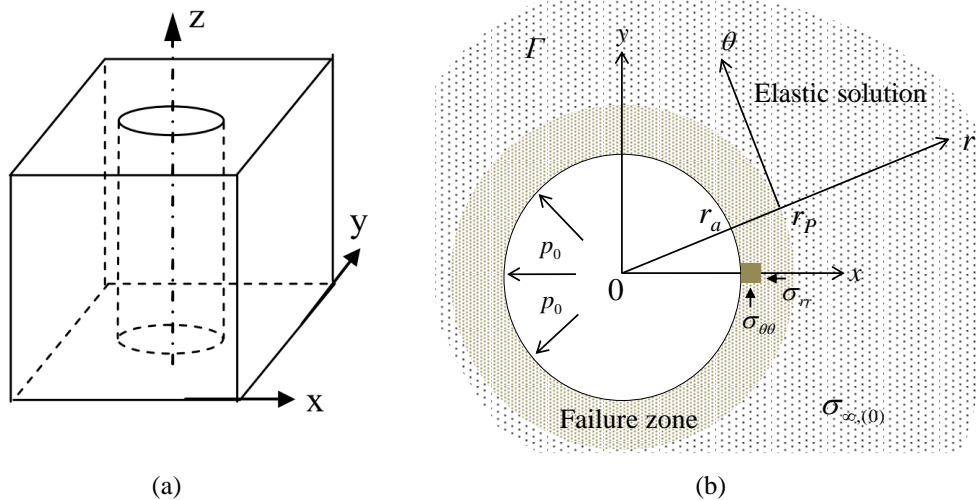


**Figure 1.26** : axial symmetry of a 3d borehole problem (a) and plane of reference for the study of the stress field with a circular failure extension on a gallery cross-section (b).

Eventually, for  $r_a \leq r \leq r_p$ , the two stress variables write:

$$\sigma_{rr} = p_0 \left( \frac{r}{r_a} \right)^{(K_p-1)} \quad \text{and} \quad \sigma_{\theta\theta} = K_p p_0 \left( \frac{r}{r_a} \right)^{(K_p-1)} \quad (1.17a-b)$$

If the classical elastic solution for  $\sigma_{\theta\theta}$  and  $\sigma_{rr}$  writes:

$$\sigma_{\theta\theta} = \sigma_{\infty,(0)} + (\sigma_{\infty,(0)} - p_0) \frac{r_a^2}{r^2} \quad (1.18)$$

$$\sigma_{rr} = \sigma_{\infty,(0)} - (\sigma_{\infty,(0)} - p_0) \frac{r_a^2}{r^2} \quad (1.19)$$

The elastic solution, in presence of a failure zone  $r_a \leq r \leq r_p$ , writes (for  $r > r_p$ ):

$$\sigma_{\theta\theta} = \sigma_{\infty,(0)} + (\sigma_{\infty,(0)} - \sigma_{P,rr}) \frac{r_p^2}{r^2} \quad (1.20)$$

$$\sigma_{rr} = \sigma_{\infty,(0)} - (\sigma_{\infty,(0)} - \sigma_{P,rr}) \frac{r_p^2}{r^2} \quad (1.21)$$

It is necessary to define the radial stress component at the failure plastic limit,  $\sigma_{P,rr}$ . If, in elasticity only, it is possible to write:

$$\sigma_{\theta\theta}(r = r_a) = 2\sigma_{\infty,(0)} - p_0 \quad (1.22)$$

$$\sigma_{rr}(r = r_a) = p_0 \quad (1.23)$$

In presence of a failure zone extending for  $r_a \leq r \leq r_p$ :

$$\sigma_{\theta\theta}(r = r_p) = 2\sigma_{\infty,(0)} - \sigma_{P,rr} \quad (1.24)$$

$$\sigma_{rr}(r = r_p) = \sigma_{P,rr} \quad (1.25)$$

According to the solution within the failure zone and to respect the criterion, at  $r > r_p$ :

$$\sigma_{\theta\theta}(r = r_p) = 2\sigma_{\infty,(0)} - \sigma_{P,rr} = K_p p_0 \left( \frac{r_p}{r_a} \right)^{(K_p-1)} \quad (1.26)$$

$$\sigma_{rr}(r = r_p) = \sigma_{P,rr} = p_0 \left( \frac{r_p}{r_a} \right)^{(K_p-1)} \quad (1.27)$$

$$\sigma_{\theta\theta} = K_p \sigma_{rr} \quad (1.28)$$

$\sigma_{P,rr}$  writes:

$$K_p \sigma_{rr} = K_p \sigma_{P,rr} = \sigma_{\theta\theta} = 2\sigma_{\infty,(0)} - \sigma_{P,rr} \quad \rightarrow \quad \sigma_{P,rr} = \frac{2}{1+K_p} \sigma_{\infty,(0)} \quad (1.29a-b)$$

The extension of the failure zone  $r_P$  can be also derived:

$$r_P = r_a \left( \frac{2}{1 + K_p} \frac{\sigma_{\infty,(0)}}{p_0} \right)^{\left( \frac{1}{K_p - 1} \right)} \quad (1.30)$$

In the following, the plot of  $\sigma_{\theta\theta}$  and  $\sigma_{rr}$  with  $r$  for a weak internal pressure (compression) of  $-1$  MPa is reported. It is superposed with the same plot for a further reduction of this internal confinement down to  $-0.5$  MPa, assuming an excavation in its final phase. According to the hypothesis, no cohesion is assumed. The friction angle  $\varphi = 20^\circ$  and  $\sigma_{\infty,(0)} = -12$  MPa. The tunnel radius corresponds to  $r_a = 2.5$  m. First of all, it is necessary to point out that the plot shows an unrealistic situation with respect to tunnelling conception and design in the engineering practice: a deep rock formation presents, in general, decent cohesion values  $C$  to provide a higher failure resistance than the one correspondent to the situation shown in Figure 1.27. Moreover, the internal retaining structures must be conceived to limit the gallery convergences: for instance, a preliminary design method will refer to the so called rock-support interaction diagram [20]. The intersection between the curve of the radial displacement (*Ground Response Curve*) with the support reaction line will determine the internal pressure  $p_0$  requested to maintain a convergence threshold. Then, once the tunnel support has been dimensioned, numerical simulations (e.g. Finite Element Method) can be performed to provide more detailed force-displacement and stress-strain analyses. On the other side, the plot is significant to evaluate some differences between the stress conditions in the failure zone and the elastic conditions still valid for  $r > r_P$ : here, each positive increment of the orthoradial stress corresponds to a negative increment of the radial one. As previously shown, the *axial* stress  $\sigma_{zz}$  remains constant to its initial value  $\nu(\sigma_{rr,(0)} + \sigma_{\theta\theta,(0)})$  or, in the principal (Cartesian) coordinate system,  $\nu(\sigma_{xx,(0)} + \sigma_{yy,(0)})$ . In the failure zone  $r_a \leq r \leq r_P$ , this is no longer valid:  $\Delta\sigma_{zz} \neq 0$ .

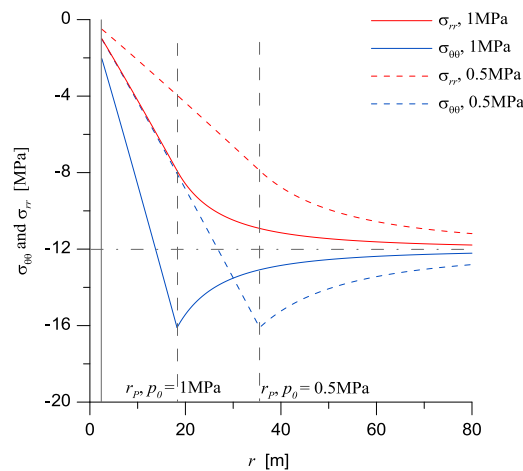


**Figure 1.27** :  $\sigma_{\theta\theta}$  and  $\sigma_{rr}$  along a radial direction for internal pressures of 1 MPa (continuous lines) and 0.5 MPa (dotted lines).

If an elastic-plastic behaviour at failure is assumed, the finite and incremental formulations of total strains write:

$$\boldsymbol{\varepsilon} = \boldsymbol{\varepsilon}^E + \boldsymbol{\varepsilon}^P \quad \text{and} \quad \dot{\boldsymbol{\varepsilon}} = \dot{\boldsymbol{\varepsilon}}^E + \dot{\boldsymbol{\varepsilon}}^P \quad (1.31a-b)$$

According to the general flow rule in plasticity for a strain component  $\varepsilon_{ij}^P$ , we can write the incremental form of the plastic strain along  $z$ :

$$\dot{\varepsilon}_{ij}^P = \dot{\lambda} \frac{\partial f}{\partial \sigma_{ij}} \quad \rightarrow \quad \dot{\varepsilon}_{zz}^P = \dot{\lambda} \frac{\partial f}{\partial \sigma_{zz}} \quad (1.32a-b)$$

Two of the hypothesis enounced in this paragraph are recalled: the failure criterion does not depend on  $\sigma_{zz}$  [51] and the excavation problem is treated in 2d plane strains,  $\varepsilon_{zz} = 0$ . For the first hypothesis, the plastic deformations component  $\dot{\varepsilon}_{zz}^P$  must be null and no plastic deformations along  $z$  are generated. Considering the second hypothesis, also the elastic deformation component along  $z$  must remain null. The elastic stress solution is still valid for  $\Delta\sigma_{zz}$ , according to Eq. 1.10, but  $|\Delta\sigma_{rr}| \neq |\Delta\sigma_{\theta\theta}|$ , meaning  $\Delta\sigma_{zz} \neq 0$ . In the failure zone, a finite increment of the orthoradial and radial stresses can be evaluated from Eq. 1.17a-b, for a fixed variation of the internal pressure:

$$\Delta\sigma_{rr} = \Delta p_0 \left( \frac{r}{r_a} \right)^{(K_p-1)} \quad \text{and} \quad \Delta\sigma_{\theta\theta} = K_p \Delta p_0 \left( \frac{r}{r_a} \right)^{(K_p-1)} \quad (1.33a-b)$$

As a consequence, for every reduction of the internal confinement  $p_0$ , both  $\sigma_{\theta\theta}$  and  $\sigma_{rr}$ , within the failure zone  $r_a \leq r \leq r_p$ :  $|\Delta\sigma_{rr}| < 0$  and  $|\Delta\sigma_{\theta\theta}| < 0$ . Considering Eq. 1.10, a finite increment of  $\sigma_{zz}$  respects the condition:

$$\frac{\Delta\sigma_{zz}}{E} - \frac{\nu}{E} \Delta p_0 (1 + K_p) \cdot \left( \frac{r}{r_a} \right)^{(K_p-1)} = 0 \quad \rightarrow \quad \Delta\sigma_{zz} = \nu \cdot \Delta p_0 (1 + K_p) \cdot \left( \frac{r}{r_a} \right)^{(K_p-1)} \quad (1.34a-b)$$

The equation above implies that, for a reduction of the internal pressure  $|\Delta p_0| < 0$ , within the failure zone  $r_a \leq r \leq r_p$ , a reduction of the *axial* stress component must correspond:  $|\Delta\sigma_{zz}| < 0$ . In Figure 1.28, the radial evolution of  $\sigma_{\theta\theta}$  and  $\sigma_{rr}$  (according to Figure 1.27) are superposed to the radial evolution of  $\sigma_{zz}$  for the same reduction of internal pressure, assuming a Poisson's ratio  $\nu = 0.2$ . The role of  $\sigma_{zz}$  in the failure analyses around tunnels and relative criterion formulations has been a debated topic, even in relatively dated publications (e.g. [81]). Considering a failure criterion also depending on  $\sigma_{zz}$ , plastic strains are possible along  $z$  and analytical solutions reported above are no longer valid. This will be discussed again in Section 2.1 with numerical analyses considering perfect elastic-plasticity and a Drucker-Prager failure criterion ( $f$  depending also on  $\sigma_{zz}$ ). Some discrepancies between plasticity and damage will be encountered, as well as important differences in the post-failure phase, if a softening yielding is considered instead of a material exhibiting perfect yielding.

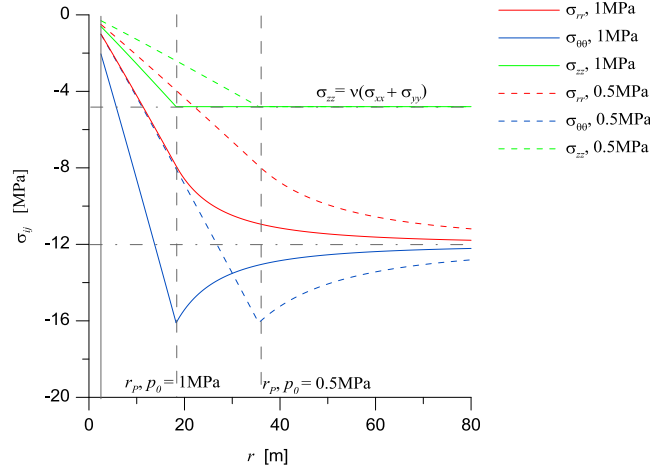


**Figure 1.28** :  $\sigma_{\theta\theta}$ ,  $\sigma_{rr}$  and  $\sigma_{zz}$  along a radial direction for internal pressures of 1 MPa (continuous lines) and 0.5 MPa (dotted lines).

In the final part of this discussion, two possibilities for the failure localisation around a circular borehole are shown. They cover a relevant interest because of their correspondences with in-situ evidences and the Andra URL. In the next chapters, numerical results presented, including softening post-failure analyses, often reproduce the failure initiation conditions shown in the following.

### 1.2.3 Two simple cases of failure localization around a circular borehole

According to the reference schemes for 2d, plane strain analyses proposed in Figure 1.24 and Figure 1.26, the homogeneous failure condition corresponds to a simultaneous verification of the failure criterion at every point of the perimeter  $r = r_a$ , i.e.  $f = 0$ ,  $\forall \theta$ . On the contrary, localization of failure occurs if the criterion is verified only at certain points around the gallery perimeter: failure is not simultaneous  $\forall \theta$  and, in general:  $f \leq 0$ ,  $\forall \theta$ .

A first case of failure localisation is a stress state, in the cross section, characterized by anisotropy and not defined by a unique component  $\sigma_{xx,(0)}$ . Referring to the scheme illustrated in Figure 1.29, the tensor correspondent to the initial stress state  $\boldsymbol{\sigma}_{(0)}$  in the cross section plane  $\Gamma$  is characterized by the principal vertical component higher than the horizontal, i.e.  $\sigma_{xx,(0)} < \sigma_{yy,(0)}$ . With no internal pressure, the radial and orthoradial stresses along these directions, write:

$$\sigma_{rr} = 0 \quad (1.35)$$

$$\sigma_{\theta\theta}(A) = 3\sigma_{yy,(0)} - \sigma_{xx,(0)} \quad \text{and} \quad \sigma_{\theta\theta}(B) = -\sigma_{yy,(0)} + 3\sigma_{xx,(0)} \quad (1.36a-b)$$

Eq. 1.35 is valid for every point at the perimeter. According to Eq. 1.36a-b, with  $\sigma_{xx,(0)} < \sigma_{yy,(0)}$ :

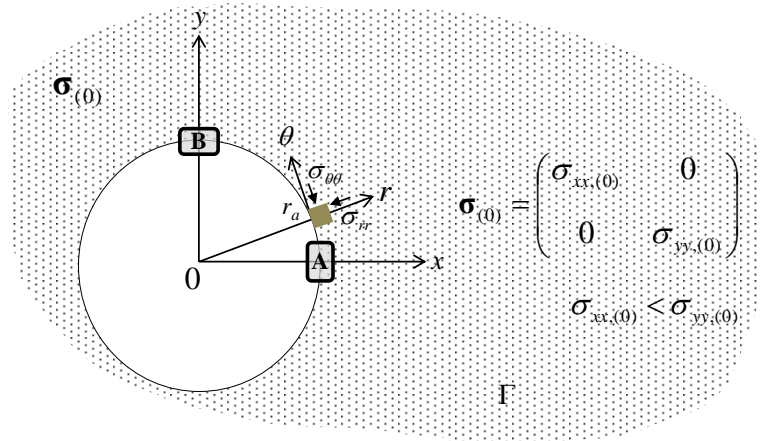


**Figure 1.29** : localisation of failure at the point A (and its symmetric along  $x$ ) due to an anisotropic in-situ stress on the section plane  $\Gamma$ .

$$\sigma_{\theta\theta}(A) > \sigma_{\theta\theta}(B) \tag{1.37}$$

It is evident that, if the same uniaxial compressive strength (UCS) can be offered by the material, the anisotropic  $\sigma_{(0)}$ , where anisotropy directions coincide with the principal ones, induces a delayed failure between points A and B (and their symmetric ones along these directions). In particular, failure initiation will localize firstly at A.

The second condition for localized failure is illustrated by Figure 1.30. In this case, the inhomogeneous response of the material at the perimeter is determined by the UCS,  $\sigma_0$ , due to an anisotropy characterizing the medium itself (e.g. for inherent anisotropy or induced by diagenesis). For a 2d, plane strain problem with an isotropic initial stress state on the plane  $\Gamma$ , described by the only value  $\sigma_{xx(0)}$ , the same component  $\sigma_{\theta\theta}$  exists,  $\forall \theta$  at  $r = r_a$ , with or without an internal pressure  $p_0$ . Nonetheless, since  $f(r = r_a) = 0$  when  $\sigma_{\theta\theta}(r = r_a) = \sigma_0$ , failure will firstly localize at the point A. In fact, here the material exhibits a lower value of UCS than, for instance, the same at the point B, on the vertical direction.

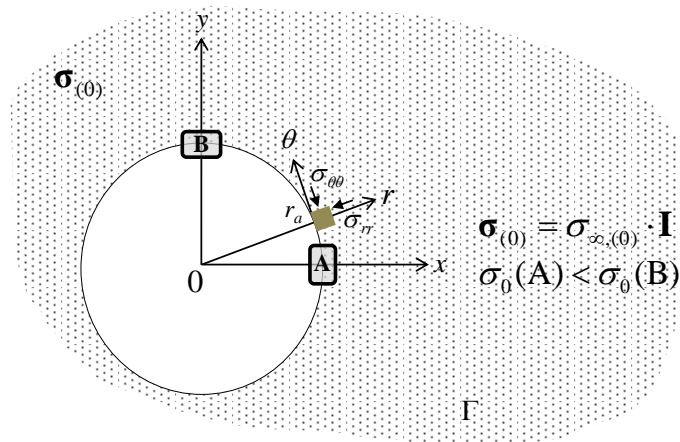


**Figure 1.30** : localisation of failure at the point A (and its symmetric along  $x$ ) due to different local values of UCS  $\sigma_0$  around the perimeter.

The analytical stress solutions and the simple analyses for failure localization previously reported conclude the second section of this chapter, dedicated to a general framework for the problem of boreholes failure. Chapter 2 is presenting the first numerical analyses for failure, comparing damage and plasticity yielding conditions. Particularly in Section 2.2, numerical results are described in detail, referring to some theoretical contents already mentioned before. These discussions constitute the fundamentals for damage-based numerical modelling of failure around drifts at the Andra URL, presented throughout the entire manuscript.

## Conclusion

This initial chapter intended to provide, at first, the industrial implications for this study, corresponding to the mission of Andra for the development of a DGR facility for nuclear waste disposal in France. The Andra Underground Research Laboratory (URL), the site for real scale feasibility studies, was presented together with related research and thesis works constituting a framework and reference for the current one. A characterisation of the Callovo-Oxfordian claystone properties has been included in the first section. This reported, eventually, the main outlines of the manuscript, describing the logical structure of the entire research work and the approaches chosen for modelling of the short-term failure around the excavations at the URL, based on damage mechanics.

A literature review for some significant contributions, covering a particular interest for the thesis' topic, has been included in the second section, together with some examples of similar excavation-induced effects on other geological formations selected as host media for nuclear waste disposal. A successive review and discussion on analytical solutions for the stress distributions around deep circular boreholes and an analyses of failure localisations concluded the second section.

After the presentation of the research motivations and background, the forthcoming chapter presents, at first, the code adopted to process FEM numerical models simulating failure around boreholes in 2d plane strain conditions. In general, Chapter 2 is intended to provide the theoretical motivations and basic implications for a mechanical modelling based on damage, in particular accounting for the material's reduction of strength during yielding.

## **Chapter 2**

# **Numerical and Theoretical Framework with Softening Models**



In this chapter, an initial presentation of the principal Finite Element code adopted, *POROFIS* (Pouya, 2015 [72]), is presented and some of its characteristics and structure are detailed. Then, mathematical formulations of constitutive models to describe the response of a softening medium induced by a circular gallery excavation are provided. A first application to validate similarities on an isotropic unloading of a 2d circular cavity in perfect yielding conditions together with mesh-size analyses is performed.

Subsequently, fragile characteristics of the Callovo-Oxfordian claystone post-failure response for low confinements are recalled before performing numerical analyses of unloading of circular cavities in isotropic and anisotropic conditions when softening occurs. Significant differences between results in brittle plasticity and brittle damage will be shown. A focus on the concept of instable damage propagation and enhanced bifurcation phenomena when failure occurs in damage condition will be discussed.

Eventually, an upgrade to the basic softening damage model will be introduced and physical motivations will be discussed. The model upgrade will constitute the basis of successive numerical analyses of failure propagation around galleries in Andra URL. New mesh-size sensitivity analyses, now accounting for softening conditions, will conclude the last Section of the current chapter.

## 2.1 Presentation of the *FE* code and constitutive laws formulation

Numerical simulations further presented in this chapter are performed adopting the Finite Element (FEM) code *POROFIS* ([72], <http://mecharock.net/>). As mentioned at the end of Section 1.2, results by FEM simulations presented also in Chapter 3 and Chapter 4 employ the code *POROFIS*. In Chapter 5, numerical analyses adopt *POROFIS* and, in parallel, the analogue FEM code software DISROC. *POROFIS* is a 2d Finite Element code derived from DISROC, which is developed by the software development company Fracsima (<http://www.fracsima.com/>). *POROFIS* is conceived for modelling coupled Thermo-Hydro-Mechanical (THM) and Chemical phenomena in POROUS FISSURED media. *POROFIS* is designed for research-oriented applications and includes a large variety of non-linear constitutive laws and coupling models for various THM phenomena. In general, it is possible to assign one or more materials in the pre-processing phase of the numerical simulation by choosing the constitutive laws already existing in *POROFIS*. For this work's purposes, the code structure allows the user to develop customized constitutive laws based on the pre-defined subroutines: the enrichment of constitutive laws is based on theoretical and physical assumptions which will be discussed in these sections and in the following chapters, passing through the two main research axis discussed in Section 1.2: 2d plane-strain numerical study for the continuous failure (*damaged*), zone around a circular gallery and 2d axisymmetric numerical study for the generation and evolution of fractures during the advancing of the excavation front. *POROFIS* is hence employed as a *processor* to solve the FEM problem according to assigned characteristics defined in the pre-processing phase: materials, boundary conditions (BCs), initial conditions (ICs) and spatial 2d discretisation (mesh). For every numerical simulation, the pre- and post-processing phases (visualisation and analyses of the results) are operated by means of the pre- and post-processor interface GiD (<https://www.gidhome.com/>).

For this research, two of the subroutines (modules) constituting the structure of *POROFIS* have been modified according to physical and numerical needs and assumptions for the different simulations: as the whole code, they are implemented in FORTRAN90 and included in two separated files: *Utilizer.f90* and *Hydmec.f90*. In the module *Utilizer.f90*, user-defined constitutive laws can be written and compiled in order to assign a new material in the numerical model. A general constitutive law – as those adopted in this work – is structured in *Utilizer.f90* in three main parts:

1. Definitions of the necessary variables for the failure criterion,  $f$ : resistance parameters and stress tensor components acting in the failure criterion. In general, every failure criterion employed is based on stress rather than strain. This first part ends with the explicit expression of the failure criterion and it is checked, for each element (at its Gauss point), if the current stress state overcomes  $f$ .

2. If, for one or more mesh elements,  $f = 0$  within a selected tolerance, the dissipation (yielding) law is written and solved in order to actualize the internal variable(s)  $\chi$  at the Gauss points of the dissipating elements.
3. The third and last part includes the resolution of the current stress-strain state according to the pre- or user-defined elastic stiffness tensor.

In Appendix A, Figure A.1, an example of the subroutine structure containing the FORTRAN implementation the basic constitutive laws, later presented in this section, is provided, with an indication of the three main parts described above. Such a subdivision of the entire constitutive law defining the  $\sigma : \epsilon$  relation, at each Gauss point, constitutes a practical advantage, if one (or more) of the three parts are intended to be singularly modified. It will be the case when the upgrades to the basic elastic-damage law are introduced, in particular accounting for the material anisotropies. These aspects will be detailed in Section 2.3 and Chapter 3 and Chapter 4. Figure 2.1 shows a diagram of the procedures composing the step-by step resolution of the  $\sigma : \epsilon$  relation for a Gauss point according to its structure in the module *Utilizer.f90*.

Another useful feature of the module *Utilizer.f90*, for user-defined purposes, consists in an internal subroutine which allows tracing a specific contour plot for one or more selected state variables ( $\sigma$ ,  $\epsilon$ ,  $\chi$ ,  $f$ , etc...) for the GiD post-processing phase. This is possible for a particular computation step as well as for multiple steps, in order to visualize the evolution of the selected problem variable(s).

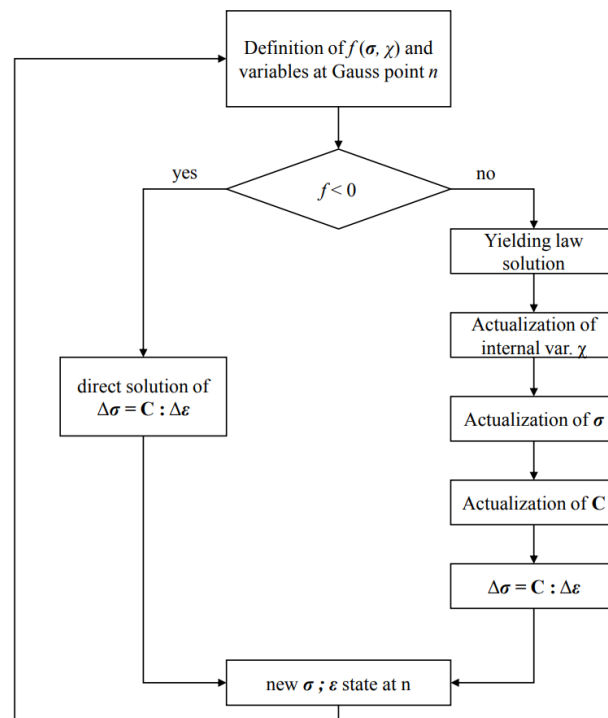


**Figure 2.1** : procedures composing the step-by step resolution of the  $\sigma : \epsilon$  relation for a classical constitutive law in *Utilizer.f90*.

The second accessible module, *Hydmec.f90*, allows - in relation to this work's purposes - to operate interventions on the step-by-step solution of the FE problem according to the specific needs of the simulation. For instance, in the 2d plane strain simulations, an internal subroutine included in *Hydmec.f90* allows to operate on the BCs of the gallery realisation phase. It takes into account a partial unloading of the pre-confining (in situ) stress state up to the limit elastic conditions, simulating a linear unloading, at the gallery wall, in isotropic or anisotropic conditions. In a similar way, another subroutine allows a time-dependent modifications of BCs along the gallery side for the 2d axisymmetric simulations in Chapter 5, to reproduce the advancement of an excavation front at a constant drift speed. These procedures will be detailed in the relative chapters and sections.

In the following, Figure 2.2 reports the general working scheme for a FEM problem in *POROFIS*. The processor itself, composed by a part of internal subroutines plus those accessible by the user, *Utilizer* and *Hydmec*. According to Figure 2.2, for a generic *Project* file created in GiD, these files are accepted by *POROFIS* as input:

- The *Project* input file itself, containing the mesh connectivity matrix, the nodes coordinates, the material types and the BCs;
- The *Project.param* file, containing the computation parameters for the numerical solution;
- If necessary, the *Project.rep* file, containing the final conditions (in term of state variables) of a previous stage, and used as initial conditions (ICs) for the simulation stage.

As reported in [72], *POROFIS* may account for potential discontinuities in the FEM model (e.g. rock interfaces, fractures, drying cracks) with hydro-mechanical couplings between a *matrix* (intact material) and discontinuities themselves. For instance, discontinuities in the displacement field may exist with the relative stress values that verify the constitutive laws at the integration (Gauss) points. Similarly, a network of potential discontinuities in a FEM model reproducing a clayey soil may generate fractures due to drying-out effects. Fruitful applications of *POROFIS* in cracking modelling may be found in the Phd thesis of Nguyen [61] and Vo [111].

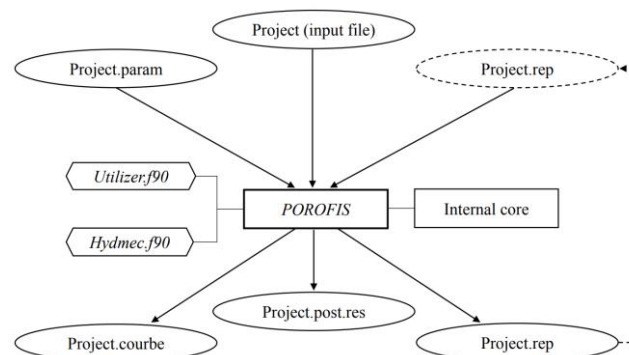


**Figure 2.2 :** general structure of the FE processor *POROFIS*: code core, i/o files and related subroutines (<http://www.fracsima.com/>).

Based on already known numerical approaches [39], *POROFIS* is able to process a FEM mesh containing a network of pre-oriented or random discontinuities adopting interfaces or *joint* elements. A numerical tool developed by Fracsima, *DISCRAC*, allows for this procedure, starting from a normal FEM mesh. In general, it is possible either to insert discontinuities directly in the geometry definitions, tracing them in the same way as a boundary element, or transform the sides of whatever number of surface elements in a network of discontinuities. A *joints-enriched finite element* numerical model (JFEM) is eventually obtained; an example of this pre-processing procedure is shown in Figure 2.3, where each side of surface (2d) triangular elements are transformed in potential discontinuities and assigned with the material *Fracture* (elastic, elastic-plastic or elastic-damage). In Chapter 5, numerical models with pre-defined discontinuities assimilated with joint elements will be employed. Moreover, *DISCRAC* assigns automatically new nodes for each joint element side, which can move independently, according to boundary conditions, materials, etc. This is necessary to overcome the FEM imposition of infinitesimal strain (i.e. a continuous and derivable displacement field).

For non-linear and dissipative behaviours, *POROFIS* performs, for each calculation increment, a local check at each Gauss point based on one Newton-Raphson iteration. This check is intended to verify, globally (for the entire mesh), if the displacements convergence and the failure criterion tolerance - according to the consistency law  $f = \dot{f} = 0$  - are respected. An accepted verification implies an advancement to the forward calculation step, while a rejected verification forces the code to execute again, locally, a new Newton-Raphson iteration. This procedure applies to surface elements as well as to interface *joint* elements. In Appendix A, Figure A.2, a scheme of the described computational procedure is reported.

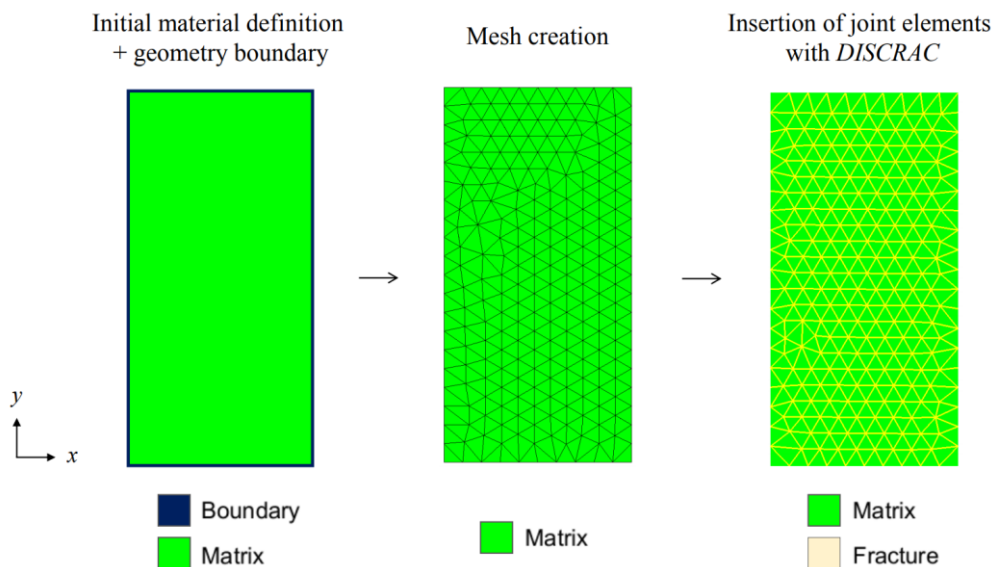


**Figure 2.3 :** materials assignment and mesh creation in GiD, followed by insertion of a discontinuities network based on the original mesh through *DISCRAC*.

After a general presentation of the principal numerical tool adopted, the two basic mechanical models for the material behaviour in the initial simulations are introduced. According to the statement in Section 1.1, their main task is the simulation of a fragile behaviour after failure, characterized by softening of the material: a progressive reduction of its resistance when the elastic limit is firstly reached. A linear decreasing of the uniaxial resistance occurs after the first failure at the elastic limit and it is followed by a residual constant resistance when a certain deformation threshold is reached. The same behaviour in uniaxial compression is treated within the frameworks of elastic-plasticity and elastic-damage, according to two formulations pre-defined in *POROFIS*, to obtain the same stress-strain curve under monotonic uniaxial loading, according to Figure 2.4 ([77]; [78]). Here, the fundamental difference in the reversible unloading-reloading path between plasticity and damage is shown: if dissipation in plasticity corresponds to an increase of irreversible (plastic) deformations (without any change in the material stiffness), damage dissipation reduces progressively the material stiffness (e.g. Young modulus  $E$ , for a uniaxial compression test), without any accumulation of irreversible deformations. For an unloading/reloading path,  $f \leq 0$  and  $\dot{f} = 0$ , Figure 2.4 shows that, while the branch P is parallel to the first elastic one, implying the formation of a residual plastic deformation  $\varepsilon^P$  if  $\sigma = 0$ , the branch D returns to the axis origin, corresponding to a Young modulus' reduction with respect to the initial one. This is equal to the ratio between the stress and strain at the elastic limit,  $\sigma_0$  and  $\varepsilon_0$ :

$$\frac{\sigma_0}{\varepsilon_0} = E \quad (2.1)$$

Young modulus in Eq. 2.1 is one of the models' parameters to be inserted as input for numerical simulations. The two elastic-softening models, as defined in *POROFIS*, include a total of 6 parameters to define, respectively, the elastic behaviour, the failure resistance and the yielding conditions, as reported in Table 2.1. Each parameter is described subsequently.

**Table 2.1** : set of parameters for the basic elastic-plastic and elastic-damage material laws in *POROFIS*.

Elasticity parameters	Failure parameters	Yielding (softening) parameters
Young modulus, $E$ [MPa] ; Poisson ratio, $\nu$ [-]	$\sin\alpha$ [-] ; $K$ [MPa]	$\beta$ [-] ; $\eta_r$ [-]

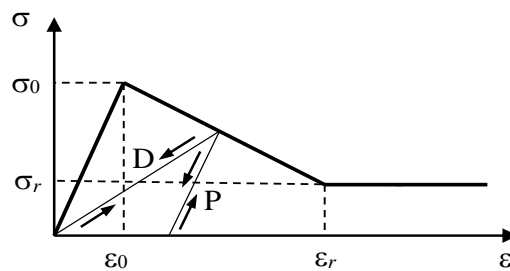


**Figure 2.4** : same stress-strain curve under monotonic uniaxial loading and different unloading-reloading paths with elastic-plasticity (P) or elastic-damage (D) mechanical model.

Parameters  $E$  and  $\nu$  reported in Table 2.1 establish the Hooke's linear elastic law according to Eq. 2.2 in the following, where  $\lambda$  and  $\mu$  are the Lamé coefficients. As a 2d FE code, *POROFIS* allows for plane strain, plane stress or axisymmetric simulations. Eq. 2.2 will be differently written in its tensorial and incremental form to distinguish between elastic-plasticity and elastic-damage.

$$\begin{bmatrix} \sigma_{xx} \\ \sigma_{yy} \\ \sigma_{zz} \\ \tau_{xy} \end{bmatrix} = \begin{bmatrix} \lambda + 2\mu & \lambda & \lambda & 0 \\ \lambda & \lambda + 2\mu & \lambda & 0 \\ \lambda & \lambda & \lambda + 2\mu & 0 \\ 0 & 0 & 0 & \mu \end{bmatrix} \begin{bmatrix} \varepsilon_{xx} \\ \varepsilon_{yy} \\ \varepsilon_{zz} \\ 2\varepsilon_{xy} \end{bmatrix} \quad (2.2)$$

Failure resistance for the softening models is implemented adopting the Drucker-Prager criterion, reported in Eq. 2.3 ([2]; [34]). According to the common practice for failure in geomaterials, shear resistance, expressed in Eq. 2.3 with the deviator stress second invariant  $J_2$ , is increased by the contribution of the mean stress. It is expressed with the total stress first invariant,  $I_1$ . It is underlined that the criterion is implemented oppositely than soil mechanics' signs convention: here, compression stresses are negative and tensile stresses are positive. Thus, while  $J_2$  is always positive,  $I_1$  assumes a negative value for a compressive mean stress state. Eq. 2.3 contains also the yielding law  $g(\chi)$ : the internal variable changes as function of the model's choice, according to either a plastic or a damage dissipation. As detailed in Section 1.2, a transition from uniaxial to triaxial loading constitutes the main condition for the most common failure mechanisms around galleries, moving from the cavity interface: in general, according to the signs' convention adopted,  $I_1 \leq 0$  for the material surrounding the cavity. For these conditions [2], the failure parameters in Table 2.1 are written according to Eq. 2.4a-b. The first is related to the friction angle only,  $\phi$  (Eq. 2.4a), the second to both  $\phi$  cohesion  $C$  (Eq. 2.4b).

$$\sqrt{3J_2} + \sin \alpha I_1 - K \cdot g(\chi) = 0 \quad (2.3)$$

$$\sin \alpha = \frac{2 \sin \phi}{3 - \sin \phi} \quad ; \quad K = \frac{6C \cos \phi}{3 - \sin \phi} \quad (2.4a-b)$$

In Table 2.1,  $\beta$  and  $\eta_r$  constitutes the last couple of parameters to be presented. They define the slope of the linear decrease of the uniaxial compressive strength between the elastic limit condition and the residual conditions ( $\sigma_0$  and  $\sigma_r$  in Figure 2.4). While  $\beta$  is function of the strains correspondents to these conditions,  $\eta_r$  corresponds to the ratio between the two limit stresses, according to Eq. 2.5a and b in the following:

$$\beta = \frac{\varepsilon_r - \varepsilon_0}{\varepsilon_0} \quad ; \quad \eta_r = \frac{\sigma_r}{\sigma_0} \quad (2.5a-b)$$

### 2.1.1 Elastic-plastic softening model

In the following, the incremental stress-strain law and the Drucker-Prager failure criterion as implemented in the pre-defined *POROFIS* constitutive model are reported, together with the consistency law:

$$\dot{\boldsymbol{\sigma}} = \mathbf{C} : (\dot{\boldsymbol{\varepsilon}} - \dot{\boldsymbol{\varepsilon}}^P) \quad (2.6)$$

$$f(\boldsymbol{\sigma}, \xi) = \sqrt{3J_2} + \sin \alpha I_1 - K(1 - \xi) \quad (2.7)$$

$$\dot{f} = \frac{\partial f}{\partial \boldsymbol{\sigma}} : \dot{\boldsymbol{\sigma}} + \frac{\partial f}{\partial \xi} : \dot{\xi} = 0 \quad (2.8)$$

$\mathbf{C}$  is the linear elastic isotropic tensor defined by  $E$  and  $\nu$  (Eq. 2.2). The failure criterion in Eq. 2.7 recalls Eq. 2.3, with  $g(\xi) = (1 - \xi)$  and  $\xi$ , defined as the plastic internal variable. At the elastic limit,  $f(\boldsymbol{\sigma}, \xi = 0) \leq 0$  and, for uniaxial compression (for instance, along the vertical direction  $y$ ), the stress tensor writes:

$$\boldsymbol{\sigma} = \begin{bmatrix} 0 & 0 & 0 \\ 0 & \sigma_{yy} & 0 \\ 0 & 0 & 0 \end{bmatrix} \quad (2.9)$$

From Eq. 2.7 and 2.8 at the elastic limit, it is possible to derive the limit condition for the vertical stress not to initiate material failure:

$$f(\boldsymbol{\sigma}, \xi = 0) = |\sigma_{yy}| + \sin \alpha \sigma_{yy} - K \leq 0 \quad (2.10)$$

According to compression conditions,  $\sigma_{yy} < 0$  while the uniaxial compressive strength (*UCS*,  $\sigma_0$ ) is always defined positive. It can be expressed only as function of the input failure parameters in Table 2.1 (Eq. 2.12):

$$\sigma_{yy} < 0 \rightarrow |\sigma_{yy}| = -\sigma_{yy} = \sigma_0 \quad (2.11)$$

$$\sigma_0 = \frac{K}{1 - \sin \alpha} \quad (2.12)$$

The yielding softening law corresponds to the incremental expression of the internal variable,  $\xi$  and it is function of the rate of the plastic deformation norm:

$$\|\dot{\boldsymbol{\varepsilon}}^P\| = \sqrt{\varepsilon_{ij}^P \varepsilon_{ji}^P} = \sqrt{(\varepsilon_{xx}^P)^2 + (\varepsilon_{yy}^P)^2 + (\varepsilon_{zz}^P)^2 + 2(\varepsilon_{xy}^P)^2} \quad (2.13)$$

The evolution of  $\xi$  is written in order to respect the shape of the uniaxial stress-strain curve in Figure 2.4 and distinguish the linear softening from the residual resistance conditions:

$$\begin{cases} \dot{\xi} = \frac{\eta}{(\eta + \beta)} \frac{E}{K} \frac{1}{\sqrt{3 \sin^2 \alpha + \frac{3}{2}}} \|\dot{\boldsymbol{\varepsilon}}^P\| = \mathbf{A} \cdot \|\dot{\boldsymbol{\varepsilon}}^P\| & |\xi| < \eta \\ \dot{\xi} = 0 & |\xi| \geq \eta \end{cases} \quad (2.14a-b)$$

If  $|\zeta| < \eta$  (linear softening branch), the consistency law in Eq. 2.8 is directly related to the rate of plastic deformations norm:

$$\dot{f} = \frac{\partial f}{\partial \boldsymbol{\sigma}} : \dot{\boldsymbol{\sigma}} + \frac{\partial f}{\partial \xi} \frac{\partial \xi}{\partial \|\boldsymbol{\varepsilon}^P\|} : \|\dot{\boldsymbol{\varepsilon}}^P\| = 0 \quad (2.15)$$

$\|\dot{\boldsymbol{\varepsilon}}^P\|$  is updated together with the current stress state  $\boldsymbol{\sigma}$  at each code iteration when failure occurs according to the plastic yielding law in Eq. 2.14a-b. Here, besides the parameters already introduced, we identify  $\eta$ : this is complementary to the ratio between  $\sigma_r$  and  $\sigma_0$ :  $\eta = 1 - \eta_r$ . It can be noticed that, if  $|\zeta| < \eta$ , the relation between the internal variable and the plastic strains norm is linear according to a constant *plastic coefficient*, denoted A in Eq. 2.14a. It reproduces the linear softening behaviour for  $\varepsilon_0 < \varepsilon \leq \varepsilon_r$ . Under residual constant conditions, no further plastic strains may be cumulated. For a very ductile material, the asymptotic tendency moves towards the condition of perfect yielding; according to the proposed parametrization it writes  $\eta_r \rightarrow 1$  and  $\beta \rightarrow \infty$ . On the other hand, for very brittle materials, both parameters will tend to 0. From a physical point of view, a ductile behaviour must correspond to a low rate of  $\|\dot{\boldsymbol{\varepsilon}}^P\|$ : after failure, the material dissipates slowly the elastic energy. On the contrary, a high  $\|\dot{\boldsymbol{\varepsilon}}^P\|$  rate corresponds to a brittle behaviour and a rapid dissipation of the elastic energy. Since the plastic coefficient A in Eq. 2.14a governs the rate of plastic deformations, it is evident that it must increase for  $\eta_r \rightarrow 0$  and  $\beta \rightarrow 0$ , while it must decrease for  $\eta_r \rightarrow 1$  and  $\beta \rightarrow \infty$ , as graphically explained in Figure 2.5. Recalling Eq. 2.10 and 2.12, if  $|\zeta| > 0$ ,  $\sigma_0$ , is variable and writes:

$$\sigma_0 = \frac{K(1 - \xi)}{1 - \sin \alpha} \quad (2.16)$$

Eq. 2.16 describes – under the simplification of uniaxial loading – the decreasing of the material UCS in the linear softening phase, among the limit values  $\sigma_0(\xi = 0)$  and  $\sigma_r = \eta_r \cdot \sigma_0$ .

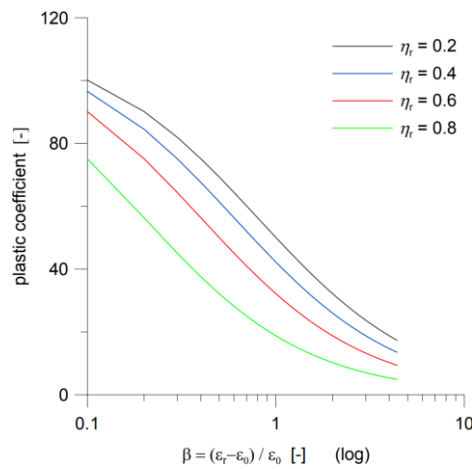


**Figure 2.5** : Plastic coefficient A in Eq. 2.14a, as a function of softening parameters  $\beta$  and  $\eta_r$ .

### 2.1.2 Elastic-damage softening model

As for the previous case, the elastic-damage model assumes linear isotropic elasticity and a linear plus residual softening phase as failure occurs. Eq. 2.17 below writes the incremental stress-strain constitutive law in presence of damage  $D$ , the model internal variable. In this case,  $D$  becomes the independent variable in the yielding function  $g(\chi) = g(D)$ , included in the Drucker-Prager failure criterion (Eq. 2.18). Each increment of damage  $D$  and the stress state  $\boldsymbol{\sigma}$  must respect the consistency law in Eq. 2.19. As mentioned previously and according to Figure 2.4, the dissipation mechanism (yielding) in this model do not include any irreversible deformation. The irreversible aspect of a purely damage-based modelling, as expressed in Eq. 2.17, consists in the progressive reduction of material stiffness when yielding, by the variation of  $D$  between 0 and 1. It is underlined that the Young modulus  $E$  only is reduced by  $D$  during the loading process, while the Poisson ratio  $\nu$  remains constant.

$$\dot{\boldsymbol{\sigma}} = (1 - D) \cdot \mathbf{C} : \dot{\boldsymbol{\varepsilon}} \quad (2.17)$$

$$f(\boldsymbol{\sigma}, D) = \sqrt{3J_2} + \sin \alpha I_1 - g(D)K \quad (2.18)$$

$$\dot{f} = \frac{\partial f}{\partial \boldsymbol{\sigma}} : \dot{\boldsymbol{\sigma}} + \frac{\partial f}{\partial g(D)} \frac{\partial g(D)}{\partial D} : \dot{D} = 0 \quad (2.19)$$

Following the same calculations reported for the elastic-plastic case, when  $f(\boldsymbol{\sigma}, D=0)$ , it is possible to demonstrate the validity of Eq. 2.12 to express  $\sigma_0$  at the elastic limit: thus, it is necessary to introduce the damage law:

$$\begin{cases} g(D) = \frac{(1-D)(\eta + \beta)}{\eta + \beta(1-D)} & 0 \leq D \leq \frac{\eta + \beta}{1 + \beta} = D_m \\ g(D) = \eta_r & D > \frac{\eta + \beta}{1 + \beta} = D_m \end{cases} \quad (2.20a-b)$$

Again, Eq. 2.20a and b reproduce the softening behaviour with a linear to constant transition, where  $D = D_m$  corresponds to the threshold value, as represented in elastic-plasticity by  $|\zeta| = \eta$ . In particular, by Eq. 2.20a, it can be derived that  $g(D)$  is equal to 1 when  $D = 0$ , while in Eq. 2.20b it assumes the value of the ratio  $\eta_r$  between  $\sigma_r$  and  $\sigma_0$ . Thus, the variable  $\sigma_0$  between the limit values  $\sigma_0(D=0)$  and  $\sigma_r = \eta_r \cdot \sigma_0$  write:

$$\sigma_0 = \frac{g(D)K}{1 - \sin \alpha} \quad (2.21)$$

The value assumed by  $\beta$  may differently influence  $g(D) \in [0 ; \eta_r]$ . According to Figure 2.6a and b, it can be noticed how the variation of  $g(D)$  remains linear or quasi-linear if  $\beta \leq 1$  ( $\varepsilon_r = 2 \cdot \varepsilon_0$ , Figure 2.4), while it is highly non-linear, for instance, for  $\beta = 10$ . In this case, the material may initially develop more damage without modifying significantly its *intact*  $\sigma_0$ .

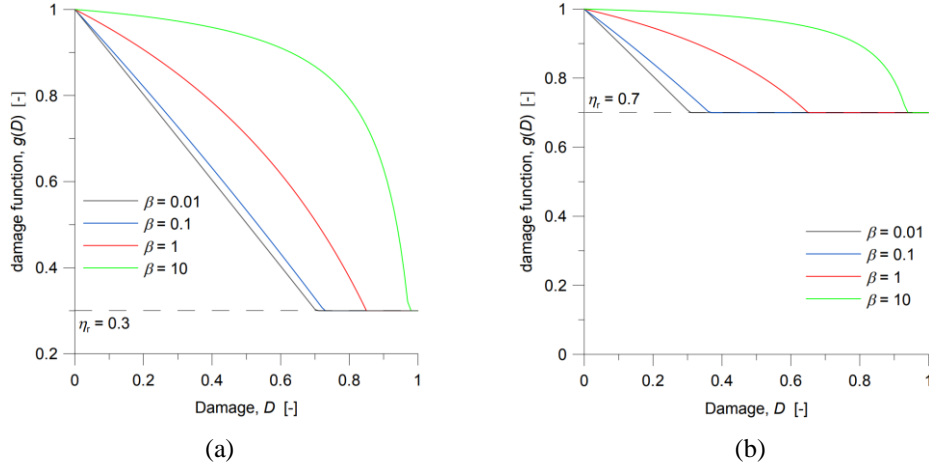


**Figure 2.6** : variation of the damage function  $g(D)$  with damage, for the same representative values for the parameter  $\beta$ . In (a), it is assumed  $\eta_r = 0.3$ , while in (b)  $\eta_r = 0.7$ .

The softening models, previously introduced, have been employed to perform some first FEM simulations in *POROFIS*, to calculate the isotropic unloading of a 2d circular cavity. These calculations are performed assuming plane strains condition. This approach is adopted for every simulation discussed in the current chapter, in Chapter 3 and Chapter 4. Under the hypothesis of a long tunnel without deviations, the assumption of plane strains is generally used in galleries concept and design practice (e.g. [3], [15], [20], [25], [40], [112]). According to the Cartesian reference system already adopted in Section 1.2 for stresses analytical solutions, we define with the axis  $z$  the *axial direction*, perpendicular to the tunnel cross section. This one lays on the plane  $(x ; y)$ . In such a reference system, the plane strains assumption writes  $\varepsilon_{zz} = 0$  and, for the 3d principal stress tensor in the Cartesian system, the following equation is verified:

$$\boldsymbol{\sigma} = \begin{bmatrix} \sigma_{xx} & 0 & 0 \\ 0 & \sigma_{yy} & 0 \\ 0 & 0 & \sigma_{zz} \end{bmatrix} = \begin{bmatrix} \sigma_{xx} & 0 & 0 \\ 0 & \sigma_{yy} & 0 \\ 0 & 0 & \nu(\sigma_{xx} + \sigma_{yy}) \end{bmatrix} \quad (2.22)$$

Stress initial and boundary conditions for the numerical analyses presented in this section respect the condition in Eq. 2.22. In particular, the initial stress state  $\boldsymbol{\sigma}_{(0)}$  is defined as isotropic within the tunnel section and, consequently, writes:

$$\boldsymbol{\sigma}_{(0)} = \begin{bmatrix} \sigma_{xx,(0)} & 0 & 0 \\ 0 & \sigma_{yy,(0)} & 0 \\ 0 & 0 & \nu(\sigma_{xx,(0)} + \sigma_{yy,(0)}) \end{bmatrix} = \sigma_{\infty,(0)} \begin{bmatrix} 1 & 0 & 0 \\ 0 & 1 & 0 \\ 0 & 0 & 2\nu \end{bmatrix} \quad (2.23)$$

$\sigma_{\infty,(0)}$  is the in-situ isotropic stress on  $(x ; y)$ . In presence of a yielding material with linear elasticity before failure, it is possible to optimize the calculation time and perform a partial unloading in only one calculation step. The stress values simulating the partial unloading will be set according to the imposed failure parameters,  $K$  and  $\sin\alpha$ , and boundary conditions. Then, when the elastic

limit is attained, *POROFIS* can process as input the previous elastic calculus (Figure 2.2) and perform a fixed number of iterations for the next partial unloading (when failure occurs). For a circular opening, the scheme is reported in Figure 2.7. At the beginning the material is undisturbed and the pressure at the internal boundary of the future gallery is equivalent to the in-situ stress state  $\sigma_{(0)}$  (numerically,  $-\sigma_{(0)}$  must be set if  $\sigma_{(0)}$  is defined positive). Then, a one-step unloading is applied at the tunnel wall to reach the elastic limit  $f \leq 0$ . This will be firstly attained around the gallery interface ( $r = r_a$ ). The second stage includes the multiple-steps unloading for the yielding phase, either in plasticity or in damage. The numerical excavation procedure in Figure 2.7 is applied for every 2d plane strain simulations of circular galleries excavations, both in case of an isotropic or an anisotropic  $\sigma_{(0)}$ . It is important to underline that the in-situ stress state may be anisotropic within the gallery section on the plane ( $x ; y$ ), meaning  $\sigma_{xx,(0)} \neq \sigma_{yy,(0)}$ . In this case, the internal pressure at each point  $i$  of the gallery perimeter is defined according to the Cauchy's stress theorem:

$$\mathbf{T}_i = \boldsymbol{\sigma}_{(0)} \cdot \mathbf{n} \quad , \quad \mathbf{n} = (\cos \alpha \quad \sin \alpha)^T \quad (2.24a-b)$$

In Eq. 2.24b,  $\alpha$  is the angle formed by the unit outward normal vector  $\mathbf{n}$  to the gallery perimeter at the point  $i$ . In the numerical model, each point  $i$  on the gallery perimeter corresponds to the side of a finite element. The local normal and tangential unit vectors are evaluated at the geometrical centre of its side. In Appendix A, Eq. A.1 and A.2 report the 2d local stresses evaluation, for a defined  $\boldsymbol{\sigma}_{(0)}$ , (according to the Cauchy's stress theorem). In Appendix A, Figure A.3, the local system for a certain inclination  $\alpha$  to the horizontal is detailed, according to the coordinates' reference as implemented in *POROFIS* and *DISROC*.

In Figure 2.8, the geometry and mesh for the isotropic unloading of a circular gallery are reported. In the GiD pre-processor, a squared domain with a 44 m side is defined for a circular tunnel with a 2 m internal radius,  $r_a$ . In Figure 2.8a, the geostatic stage is defined according to the scheme below, with  $-\sigma_{\infty,(0)} = -12$  MPa displacements boundary conditions are reported. A unique material *MATRICE* is defined for the entire geometry and meshed by the GiD meshing tool (Figure 2.8b). The minimum size for the surface elements at the tunnel wall is set equal to 25 cm.

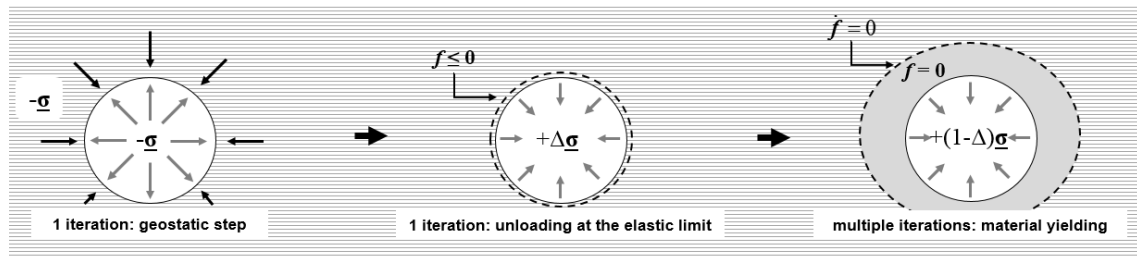


**Figure 2.7 :** numerical implementation steps for a circular gallery excavation for plane strains simulations.

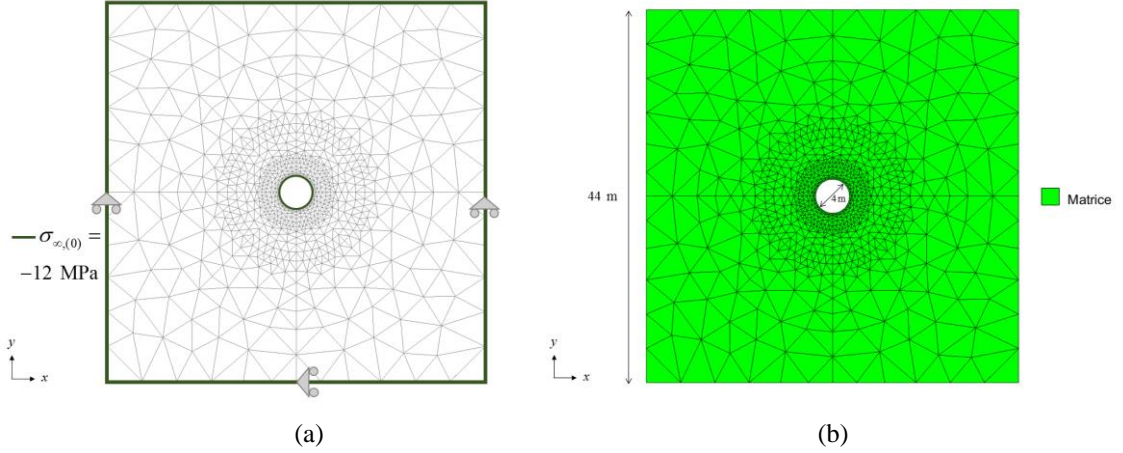


**Figure 2.8** : geometry for the first FE numerical model of a circular gallery excavation. Stress and displacements BCs in (a); domain dimensions and material assignment in (b).

When the geostatic stage (applying stress BCs in Figure 2.8a) is obtained, the first excavation up to the elastic limit is calculated, applying a positive radial (normal) stress at the circular perimeter,  $+\Delta\sigma_{\infty,(0)}$ . This stage is followed by the second unloading  $+(1-\Delta)\cdot\sigma_{\infty,(0)}$ , following the scheme in Figure 2.7. If, at the beginning of the calculus, the radial stress at the circular perimeter ( $r = r_a$ ) must be equal to  $-\sigma_{\infty,(0)}$ , at the end it is null for every orthoradial coordinate  $\theta$  :

$$-\sigma_{\infty,(0)} + \Delta\sigma_{\infty,(0)} + (1-\Delta)\sigma_{\infty,(0)} = 0 \rightarrow \sigma_{rr}(r = r_a) = 0 \quad (2.25)$$

In the following, contour plots of internal variables (respectively,  $\|\mathbf{\epsilon}^p\|$  and  $D$ ) are reported, in Figure 2.9a and Figure 2.10a, to compare the elastic-plastic case to the elastic-damage. The plots correspond to the last stage at  $p_0 = 0$  and parameters are listed in Table 2. 2. Both softening plastic and damage models reproduce a perfect yielding behaviour if  $\eta_r = 1$  is assumed, in Figure 2.4 and Eq. 2.5b. Since the object of this numerical simulations is a first comparison between the results provided by the two models, not every parameter among those in Table 2. 2 is necessarily representative for in-situ conditions or Callovo-Oxfordian claystone. Concerning the extension of the failure zone, either in plasticity or in damage, it can be noticed that, as expected, no significant differences in term of shape and extension are found: particularly, in both cases, a circular shape is obtained, with an approximate 2 m extension, equal to  $r_a$ . Nonetheless, even if Figure 2.9a and Figure 2.10a induce to conclude that no differences between the two models exist in perfect yielding conditions, Figure 2.9b and Figure 2.10b report the final contour plots of the axial stress component  $\sigma_{zz}$ : substantial differences can be noticed, moving from plasticity to damage.

**Table 2. 2** : set of parameters adopted for the first elastic-plastic and elastic-damage numerical simulations with perfect yielding.

$E$ [MPa]	$\nu$ [-]	$\sin\alpha$ [-]	$K$ [MPa]	$\beta$ [-]	$\eta_r$ [-]
6000	0.25	0.25	15.0	1.0	1.0

Figure 2.11 reports the values of  $\sigma_{zz}(r)$  for whatever radial direction beginning from  $r = r_a$ . It is numerically found that, if plastic deformations occur, the axial stress will increase its compression effect on the failure zone in the cross section. On the other side, if damage in the material occurs, the axial stress in compression will reduce within the same zone. Formally, we write, for  $r_a \leq r \leq r_p$ :

$$|\Delta p_0| < 0 \rightarrow |\Delta \sigma_{zz}| > 0, \text{ in plasticity} \quad (2.26)$$

$$|\Delta p_0| < 0 \rightarrow |\Delta \sigma_{zz}| < 0, \text{ in damage} \quad (2.27)$$

According to Eq. 2.27, damage failure implies a reduction of  $\sigma_{zz}$ , while, if calculated in perfect plasticity, its absolute value increases (Eq. 2.26). The local inversion of the general trend, around  $r = 0.4$  m, is simply due to local numerical effects depending on the mesh discretisation. It is reminded that the Drucker-Prager failure criterion depends also on the axial stress component (Eq. 2.3, 2.7 and 2.18) and, while yielding, plastic dissipation allows the development of plastic deformations along the axial direction  $z$ :

$$\dot{\varepsilon}_{zz}^P = \dot{\Lambda} \frac{\partial f}{\partial \sigma_{zz}} \neq 0 \quad (2.28)$$

On the contrary, with a criterion not depending on  $\sigma_{zz}$  (e.g. Mohr-Coulomb), no plastic deformations along  $z$  would be possible, as seen in Chapter 1, Section 1.2:

$$\dot{\varepsilon}_{zz}^P = \dot{\Lambda} \frac{\partial f}{\partial \sigma_{zz}} = 0 \quad (2.29)$$

The possibility to develop plastic deformations along  $z$ , in plane strain, gives  $\dot{\varepsilon}_{zz}^P = -\dot{\varepsilon}_{zz}^E$ . On the contrary, under the same hypothesis in elastic-damage, since no plastic deformations may be developed in any direction, the condition  $\varepsilon_{zz}^E = \dot{\varepsilon}_{zz}^E = 0$  is still valid.

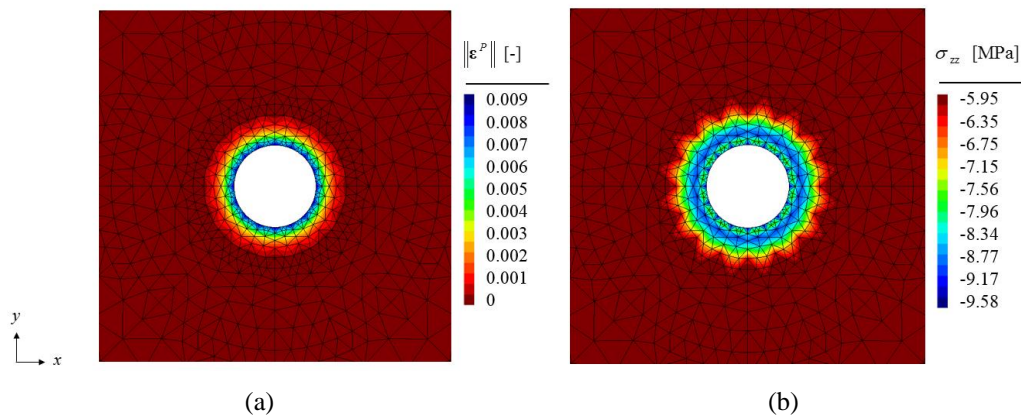


**Figure 2.9** : extension of plastic deformations (a) and axial stress  $\sigma_{zz}$  (b), for a total unloading ( $p_0 = 0$ ), in perfect elastic-plasticity

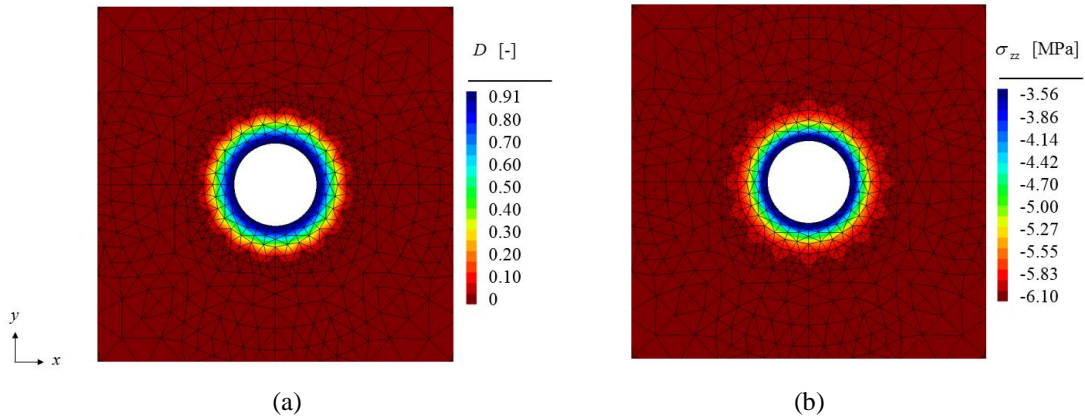


**Figure 2.10** : extension of the damage variable (a) and axial stress  $\sigma_{zz}$  (b), for a total unloading ( $p_0 = 0$ ) in perfect elastic-damage.

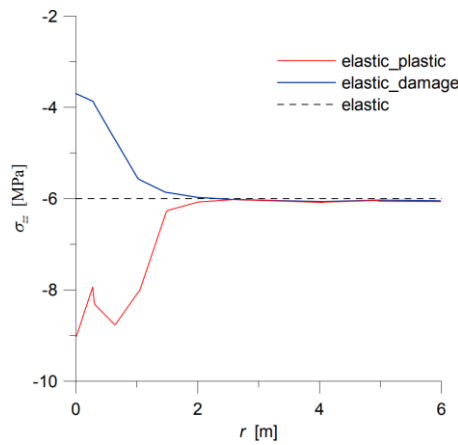


**Figure 2.11** : values of the axial stress  $\sigma_{zz}$ , for  $p_0 = 0$ , along a radial direction of Figure 2.9b and Figure 2.10b. Outside the failure zone, the elastic solution  $\sigma_{zz} = 2\nu\sigma_{xx(0)}$  is found.

As a completion of the current section, the code *POROFIS* has been tested for a mesh sensitivity analysis of perfect yielding conditions. The elastic-plastic case according to Figure 2.9, with the same boundary conditions and parameters reported in Table 2. 2, is considered for this analysis. The mesh reported in Figure 2.8a is chosen as the intermediary one and is compared with other two meshes, one less and one more refined. The same circular section tunnel with a 4 m diameter in a square domain where the side measures 44 m constitutes the problem geometry. Each mesh accounts for a progressive reduction of the average elements size of three times the previous one, in an area  $\approx 6r$  around the circular opening (Figure 2.12). Figure 2.13 reports the contour plot for plastic deformations at the end of the tunnels unloading, where the result at the centre of the figure corresponds to Figure 2.9a. At a first view, it is possible to notice approximately the same circular extension of the failure (plastic) zone, but a more detailed analysis is provided for a radial direction in Figure 2.14. Here, it can be seen that the mesh previously adopted constitutes an acceptable numerical choice since the extension of the plastic radius and values assumed by are almost the same for the refined mesh. On the other side, a less refined mesh (on the left) would not be a reliable option. This exercise is intended to provide an indication of a suitable mesh size

to be adopted for the next simulation. Table 2.3 reports the exact extension of each plastic radius for the meshes in Figure 2.12 (from left to right, Mesh 1, 2 and 3), with an estimation of the relative error due to the finite elements approximation, evaluate as:

$$\frac{|r_p(\text{Mesh1}) - r_p(\text{Mesh3})|}{r_p(\text{Mesh2})} \% \quad (2.30)$$

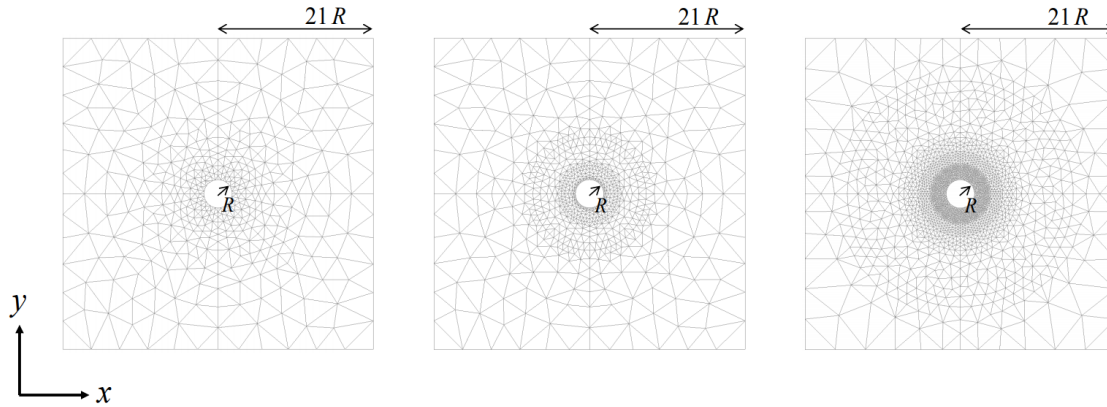


**Figure 2.12** : three meshes adopted to perform the mesh sensitivity analyses in elastic-perfect-plastic conditions.

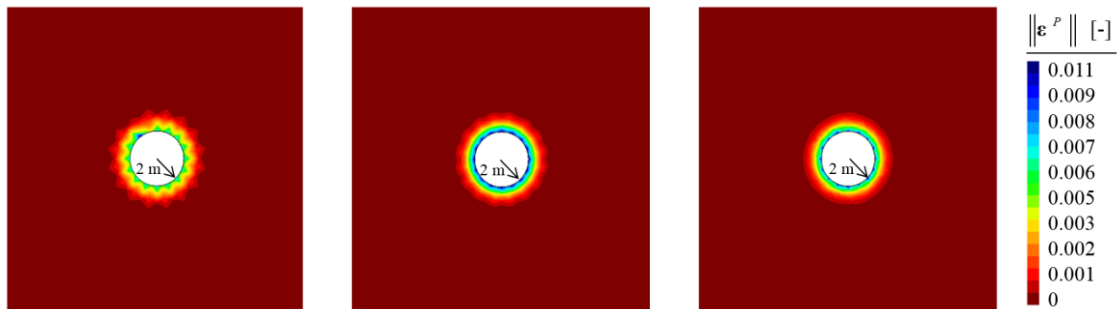


**Figure 2.13** : extension of the plastic deformations for the three meshes reported in Figure 2.12.

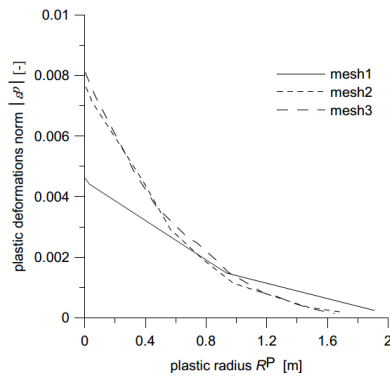


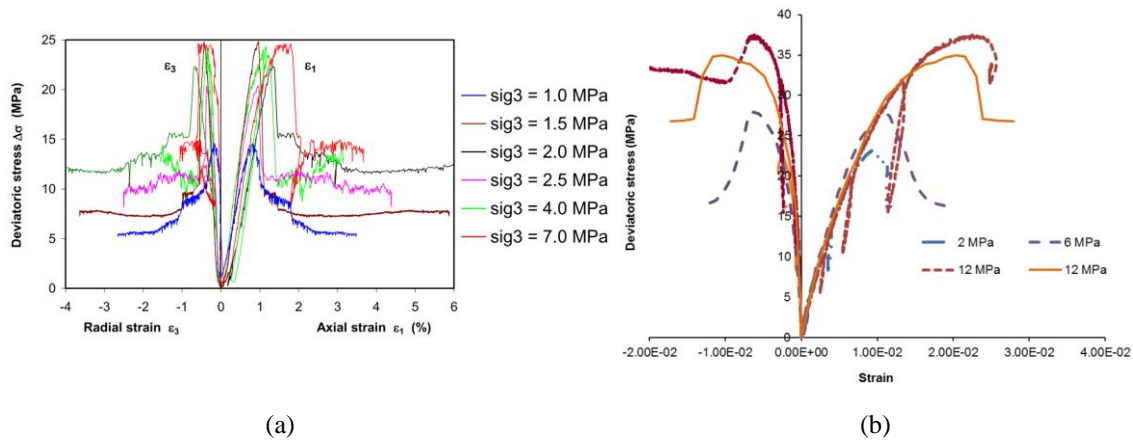
**Figure 2.14** : plastic radius evolution for the three meshes reported in Figure 2.12.

**Table 2.3** : extension of plastic radius for each of the results reported in Figure 2.13. From left to right, Mesh 1, 2 and 3.

	Mesh1	Mesh 2	Mesh 3	Avg. error (%)
Average $r_p$ [m]	1.95	1.69	1.66	17.1%

## 2.2 Main differences between plasticity and damage in softening

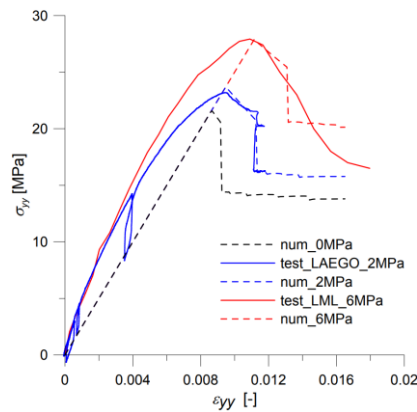
This section will discuss numerical results considering the COx claystone brittleness, at yielding. In Section 1.1, in the general presentation of the material, the decrease of shear resistance under uniaxial or triaxial conditions has been cited to be its typical post-peak behaviour, for low confinements. This has been experimentally observed and reported by several authors and research groups (e.g. [9], [14], [46], [57] and [117]). In the previous section, a first difference between elastic-plasticity and elastic-damage has already been introduced and showed the change of the axial stress  $\sigma_{zz}$  according to the dissipation mechanism chosen for numerical simulations in perfect yielding conditions. Nonetheless, the shape and extension of the failure zone, either in plasticity or damage, maintained the same geometric characteristics (Figure 2.9a and Figure 2.10a). Here, softening characteristics of the material are accounted in the models presented, with the assumption of the parameter  $\eta_r < 1$  (Eq. 2.5b, Table 2.1). Two examples of experimental results, previously cited, are shown (Figure 2.15). The failure response of the claystone, for confinements ( $p_c$ ) limited up to  $p_c \sim 6$  MPa, presents the typical compressive strength,  $\sigma_0(p_c)$ , included in an interval between 20 and 30 MPa (21 MPa for the uniaxial compressive strength,  $\sigma_0$ ; e.g. [8]). This uniaxial or triaxial compressive strength, corresponding to the elastic limit, decreases during yielding down to an eventual residual value and can be simulated referring to the model in Figure 2.4. On the other hand, it is important to state that the considered plastic and damage models (in particular, Eq. 2.14a-b and 2.20a-b) cannot reproduce a yielding behaviour characterized by a hardening stage, occurring after the elastic limit and, eventually, followed by the softening. In fact, if data show a reduction of the resistance for zero or low confinements, similarly, an initial hardening response at yielding,  $f = \dot{f} = 0$ , has been observed in the laboratory experiences for higher confinements. The mechanical response of the COx, when  $p_c$  reaches a value of 10 or 12 MPa, presents a first increase of the resistance up to a strength peak which, in this case, will not coincide with the elastic limit ( $f \leq 0$ ). Figure 2.15, cited before, presents two typical examples of this *softening to hardening* transition of the claystone mechanical response for an increasing confinement applied during a the shear stage of a triaxial compressive test (TXC). Focusing on Figure 2.15a, a linear behaviour before the resistance peak is observed for  $p_c$  not overcoming 7 MPa. This can be compared to the reversible elastic phase, followed by a significant resistance decrease down to a residual value.



**Figure 2.15:** triaxial stress-strain data, reported in [117] (a) and [9] (b). In (b), to be noted the hardening yielding before the softening phase shown for a confinement of 12 MPa.

This  $\sigma : \epsilon$  behaviour corresponds to the model plotted in Figure 2.4. A similar response is confirmed in Figure 2.15b, unless the  $p_c$  does not overcome 6 MPa. Then, at 12 MPa, the eventual softening is anticipated by a hardening phase where failure already occurs in the material. Based on some selected triaxial compression data [9], a validation of the failure and softening post-failure behaviour, calculated with *POROFIS*, is provided in Figure 2.16, both for the elastic-plastic and elastic-damage softening models. Consequences of the model’s choice on the post-peak behaviour will be further discussed in this section. They present significant implications on the numerical modelling of the failure zone shape, developed around a circular opening, in plane strains.

In the following, an application of the two softening models is presented for the failure zone evolution due to a circular excavation, on the cross section plane  $x ; y$ , in plane strains. Table 2.4 reports the set of 6 parameters obtained from the triaxial compression specimens calibration in Figure 2.16 and assigned to the elastic-plastic and elastic-damage materials for these simulations (to be noted,  $\eta_r < 1$ ). The excavation is simulated through a homogeneous isotropic unload according to Figure 2.7. Same geometry, initial/boundary conditions and mesh reported in Figure 2.8 have been assumed for both numerical models.



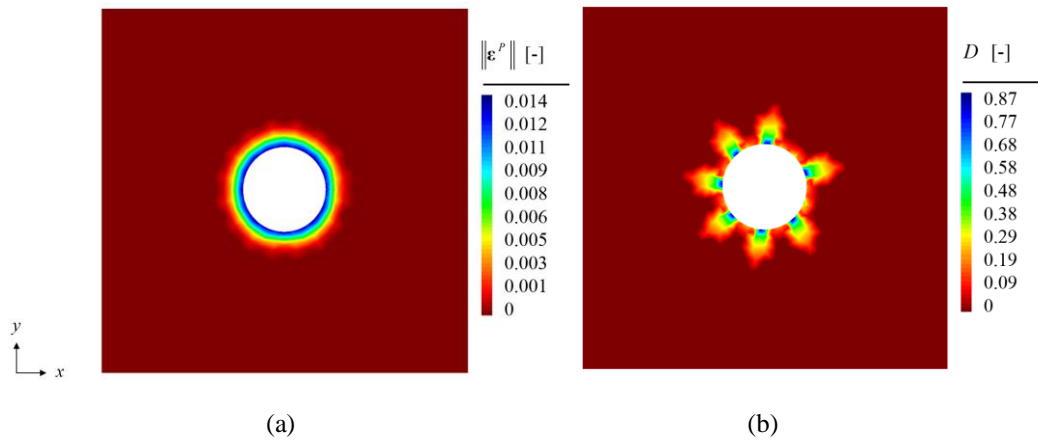
**Figure 2.16:** *POROFIS* validation of the elastic-softening models based on triaxial test data from [10].

Figure 2.17a shows the plastic deformations norm  $\|\epsilon^p\|$ , for  $p_0 = 0$ , with the softening elastic-plastic material. Figure 2.17b shows, for the same final step, the distribution of damage,  $D$ , for the softening elastic-damage material. The results reported in Figure 2.17 constitute an important difference among the softening elastic-plastic and elastic-damage approaches, for a circular excavation in isotropic conditions (i.e. homogeneous stress and material). In Figure 2.17a, a circular failure zone appears if the material dissipates in plasticity and a unique plastic radius,  $r_p$ , can be assigned to this area, qualitatively similar to the numerical results obtained for perfect yielding conditions in Figure 2.9a. On the contrary, in Figure 2.17b, a softening behaviour to describe the material yielding affects the regularity of the failure zone, if damage dissipation is assumed. The numerical model reproduces a pattern of localisations around the gallery, instead of the circular damage expansion obtained in Figure 2.10, under perfect yielding conditions.

It is remembered that, at the current state of the work, the aim is to focus more on the implications of a damage-based modelling applied to the problem of a (circular) excavation in a softening, pre-compressed and dissipative medium. In Chapter 3 and Chapter 4, particularly, presented works will be addressed more and more to propose an elastic-damage softening model for the failure zones encountered at the Andra Underground Research Laboratory (URL), taking into account some specific material characteristics. Discussions will move from the general and theoretical background proposed in the sections of this chapter to the specific research applications. Thus, results presented in this section are not specifically intended to be realistic of in-situ observations.

**Table 2.4** : parameters obtained by elastic-plastic and elastic-damage softening calibration (Figure 2.16).

$E$ [MPa]	$\nu$ [-]	$\sin\alpha$ [-]	$K$ [MPa]	$\beta$ [-]	$\eta_r$ [-]
2500	0.2	0.3	15.0	0.7	0.7



**Figure 2.17:** plastic deformations (a) and damage variable  $D$  (b) for an isotropic gallery excavation with elastic-plastic and elastic-damage materials, respectively. Parameters reported in Table 2.4.

On the contrary, they are meant to better provide an interpretation of differences between a plastic and a damage failure system, characterized by a progressive decrease of the material resistance. In this context, it can be questioned if whatever change of the conditions imposed for the results in Figure 2.17 can modify substantially the results themselves. These conditions may be any numerical input set before the processing of the FE model, i.e. the material parameters, the boundary conditions (BCs) and the initial conditions (ICs). In particular, other two simulations, respectively in elastic-plasticity and elastic-damage, are performed, decreasing significantly the parameter  $K$  of the material: physically, this corresponds to a less cohesive material. Every other condition is not modified (e.g. BCs, ICs, geometry, and mesh) and every other parameter value remains correspondent to those reported in Table 2.4. Only the value of  $K$  is decreased from 15 to 6 MPa. The extension of the plastic deformations and the pattern assumed by the damage variable are shown, respectively, in Figure 2.18a and b. If, in general, it is possible to imagine that a wider failure zone is obtained in presence of a weaker material, the elastic-plastic result confirms this statement. The size of the plastic radius around the circular opening is at least twice the  $r_p$  length reported in Figure 2.17a. In an elastic-damage softening medium, the length of damage localizations, or *lobes*, has significantly increased with respect to Figure 2.17b. On the contrary, their quantity is almost one half of the precedent. A number of 7 lobes can be clearly seen in the previous case, with the likely initiation of other two localizations on the right side of the circular cavity. In Figure 2.18b, numerical results show that, for a less cohesive material under the same external conditions, the elastic-damage softening model reproduces a higher dissipation which develops in a lower number of localizations. When the internal pressure vanishes, 4 damage lobes can be observed. Nonetheless, small zones of damage exist in the proximity of the circular perimeter, approximately on the same position of localizations shown in Figure 2.17b. These correspond to zones of damage initiation when the failure at the tunnel wall has been attained. Then, during the unloading process, only some of these *failure initiation* zones continue to develop up to the formation of the elongated lobes in Figure 2.18b.

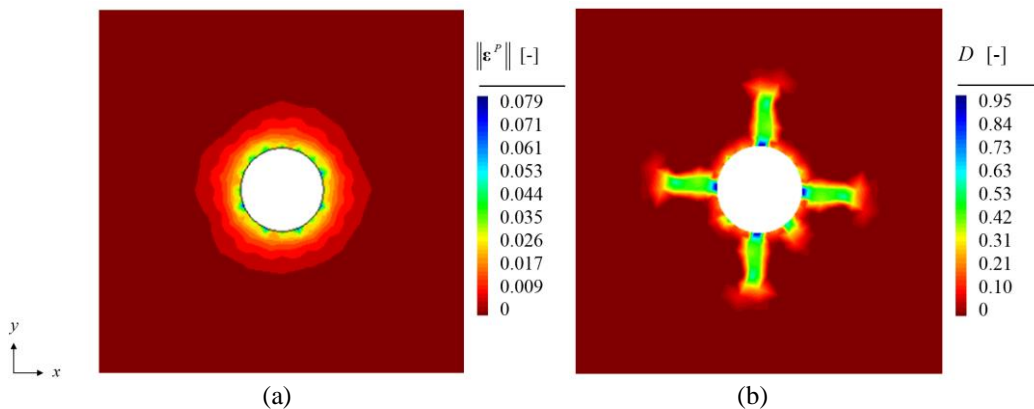


**Figure 2.18:** plastic deformations (a) and damage variable  $D$  (b) for the same numerical models reported in Figure 2.17. The only exception is the value of  $K = 6$  MPa.

This recalls a significant topic of geomaterials failure. The concepts of *instability* and *bifurcation* already mentioned in Chapter 1, Section 1.2, in the context of *localizations* and *breakouts analyses* around boreholes, constitute some reference keywords. These subjects cover an extremely wide source of references, from early fundamental works to recent developments (e.g. [65], [83]). As already stated; an exhaustive review would go beyond the scopes of this work. Nonetheless, it is worth introducing here some related concepts and ideas. This is intended to explain the choice of a damage-based mechanical approach.

In geomechanics, the concept of *instability* refers to the Lyapunov's theoretical works upon the stability of the solids' motion [53] and the evolution over time of a defined perturbation in a given mechanical system. A mechanical system is *stable* if a small disturbance of its initial conditions corresponds to a finite, time-limited, response. A mechanical system is *unstable* if, given the same small perturbation of its initial conditions, the effect generated evolves with a virtually infinite response. Physically, a little disturbance of the initial conditions, in a *stable* system, will not increase with time. *Bifurcation* refers to the loss of uniqueness of the solutions of a given boundary problem: in particular, for mechanical boundary problems, the bifurcation point identifies a state of the system where the stress-strain response may follow more than one (*unique*) evolution. A very solid presentation of these notions can be found in the works of Chambon et al. [23] and Sulem [98]. Of course, these notions may refer to a mechanical system with defined boundary and initial conditions: a circular opening in a pre-compressed medium constitutes a typical example, where instabilities and bifurcations can be induced by inhomogeneous stress and strain states. To discern between the two terms, with a perspective on this work, Figure 2.18 can provide a useful indication: in particular, the plastic radius evolution during the unloading of the internal pressure  $p_0$  in Figure 2.18a, is traced in Figure 2.19. A discontinuous development of  $r_p$  is shown: for certain unloading intervals ( $\dot{p}_0 < 0$ ), the system does not evolve ( $\dot{r}_p = 0$ ), while, for some instants, ( $\dot{p}_0 \rightarrow 0$ ) the system evolves instantaneously ( $\dot{r}_p > 0$ ).

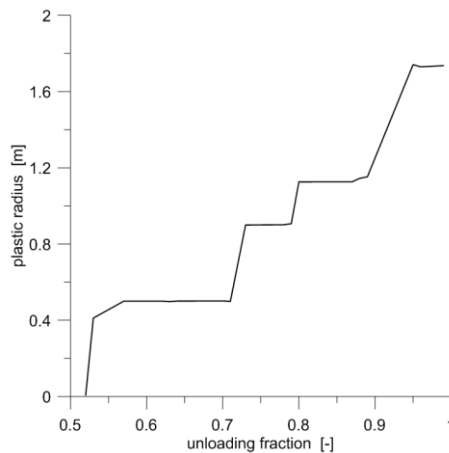


**Figure 2.19:** evolution of the plastic radius  $r_p$  during the unloading (normalized) of the opening in Figure 2.18a. Values are traced for a normalized unloading  $> 0.5$  since, for lower values, failure did not occur.

It is important to specify that the diagram of  $r_p$  evolution is traced following the development of the plastic deformations  $\|\epsilon^p\|$  as nodal average on the FEM model: otherwise, if the local variable at the Gauss point was considered, numerical discontinuities would be obtained, induced by the domain discretisation. Each instant of rapid development of the plastic radius can be identified with an *instability*, in a *global sense*: whatever the radial direction considered, the same evolution is observed. For a boundary mechanical problem, this corresponds to the absence of bifurcation in the solution. Hence, it is possible to observe the existence of instabilities without bifurcations. On the contrary, if the analysis of the same boundary problem moves from plastic to the damage configuration, the observation of differences between Figure 2.17b and Figure 2.18b is sufficient to clarify the notion of bifurcation. For a certain threshold of material resistance, is it possible to notice already that the energy dissipation does not cover a full circular area around the opening. It develops with some *lobes*, assuming *localized* characteristics within the domain of the boundary problem. If the resistance threshold of the material is decreased (or, similarly, a further unloading can be applied at the perimeter), the zone of dissipation assumes a different localized pattern. These numerical results show an example of the existence of instabilities, in a *local sense*: at the scale of the boundary problem, bifurcations of the solutions occur. Similar results can also be obtained when the system is limited to a specimen, a representative material volume in a homogeneous state of stress and strain [98]: it is worth citing the occurrence of *shear bands* as a well-known type of instability as bifurcation in geomaterials. The works of Rice (e.g. [83]) provide an exhaustive background for *shear bands* mathematical formalism, clarifying the term *loss of ellipticity*, often encountered in literature, related to the non-uniqueness (bifurcation) of the solution. Particularly for uniaxial or triaxial compression conditions, the loss of uniqueness might result in the development of shear bands among the possible types of solutions, at the bifurcation point. These boundary conditions cover a strong interest in the current work because, as already mentioned, they correspond to the mechanical solicitations induced by tunnelling. In laboratory, at a specimen scale, shear bands occur as localized areas of energy dissipation and reduction of material resistance in softening state. Outside the area included in the shear band, an elastic unloading is observed. The post-peak behaviour varies in function of the softening degree of the material and strong discontinuities correspond to very thin bands ([66], [99]). The peak of resistance individuates the bifurcation point: in Figure 2.20, the post-peak behaviour shows the solution non-uniqueness, in softening, and the implications on the shear band thickness, from a qualitative point of view. Concerning the numerical applications discussed in this section, two examples of post-bifurcation are introduced for the same specimen under uniaxial compression. In Figure 2.21a, the same stress-strain uniaxial response is reported for an elastic-plastic and an elastic-damage specimen, according to the series of model validation already reported in Figure 2.16 (where both uniaxial and some triaxial conditions are treated).

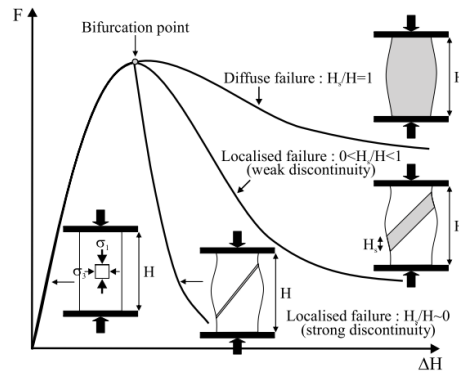


**Figure 2.20:** Post-peak behaviour and related to the shear band thickness for a specimen under uniaxial compression evolution ([66], [99]).

In Figure 2.21b, we observe the post-peak, or post-bifurcation, response, of the specimen in case of plasticity (on the left) and damage (on the right). These responses correspond, at a lower scale, to the numerical results, respectively, of Figure 2.18a and b (or Figure 2.17a and b). In the specimen dissipation zone,  $f = \dot{f} = 0$ , the same stress-strain response is observed, but the dissipation assumes different geometric configurations with respect to plasticity and damage. With reference to Figure 2.20, if a diffused failure is observed for the first, a localized failure – in form of a shear band – is observed for the second. In presence of small anisotropies in the geometry and loads, damage-based approaches can contribute to the reproduction of possible dissymmetry in the failure zones, as numerically shown also at the gallery scale in isotropic conditions (e.g. Figure 2.17 and Figure 2.18). Symmetry breakage can be shown because of the instability of the failure evolution mainly due to brittle damage ([77], [78]). This is the same concept of instability present in buckling phenomenon of beams and shells. One peculiarity of this type of instability is to break the symmetry of the initial shape.

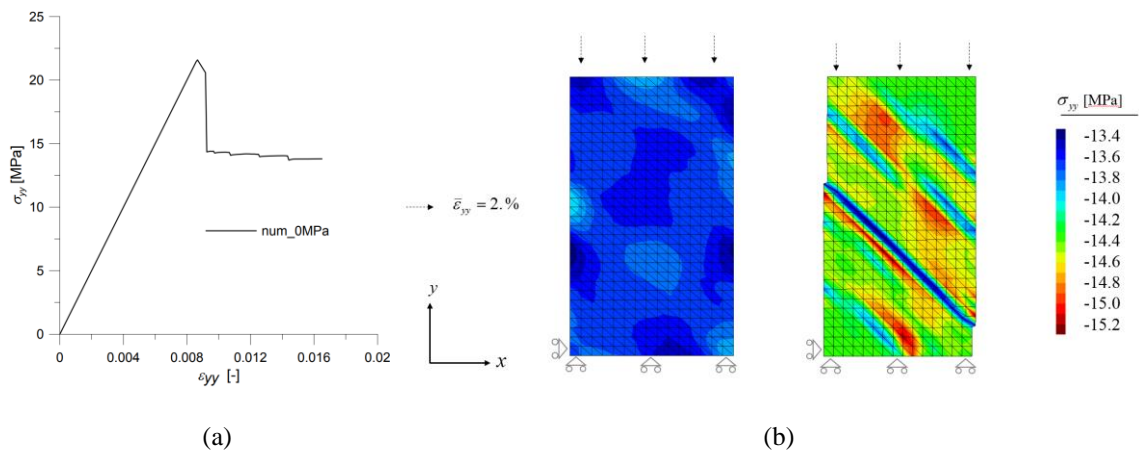


**Figure 2.21:** uniaxial response of specimen compression simulated in *POROFIS*. The same stress-strain diagram is obtained for elastic-plastic and elastic-damage model (a). In (b), the plastic diffused dissipation (on the left) and the localized damage dissipation (on the right) are reported.

For cylindrical structures submitted to radial forces, the instability can result in a loss of the axial symmetry, even if the initial problem is based on the symmetries of geometry, loading and material properties ([18], [104]). For instance when a cylindrical tube buckles under an external pressure exceeding some critical value, the deformed shape presents different buckling modes which have no more the circular symmetry [95]. Of course, this symmetry breakage occurring here for elastic buckling can occur also for cylindrical structures in dissipative materials, with the origin of different *failure branches* (Figure 2.22).

In a framework of perfect-brittle stress-strain behaviour, the possible instability encouraged by a damage-based approach can be explained in a physical way. For sake of simplicity, it can be assumed that, in an isotropic rock formation, where a circular gallery is excavated, the failure obeys to the Mohr-Coulomb criterion. The initial stress of the rock formation is isotropic,  $\sigma_{\infty,(0)}$ , corresponding to the stress boundary condition. Another simplification is introduced: the perfect brittle behaviour implies zero material strength after a material zone has reached failure, either in plastic or in damage conditions. Figure 2.23 reports the uniaxial compressive behaviour described: referring to the diagram in Figure 2.4, the limit case of  $\beta = 0 \rightarrow \varepsilon_0 \equiv \varepsilon_r$  and  $\eta_r = 0 \rightarrow \sigma_r = 0$  is considered. For a gallery cross section, the excavation can be, as usual, modelled with a uniform unloading of the internal pressure at the perimeter (Figure 2.7). If the final configuration coincides with a null internal pressure,  $p_0 = 0$ , the elastic solution in cylindrical stress components at the perimeter ( $r = r_a$ ), for a certain unloading fraction  $\Delta$ , writes:

$$\sigma_{rr} = (1 - \Delta)\sigma_{\infty,(0)} \quad (2.31)$$

$$\sigma_{\theta\theta} = 2\Delta\sigma_{\infty,(0)} + (1 - \Delta)\sigma_{\infty,(0)} \quad (2.32)$$

The failure occurs when the deviator  $q = \sigma_{\theta\theta} - \sigma_{rr}$  reaches the critical value of the rock compression strength, for a certain value of  $\Delta$ . It writes:

$$q = (\sigma_{\theta\theta} - \sigma_{rr}) = 2\Delta\sigma_{\infty,(0)} \quad (2.33)$$

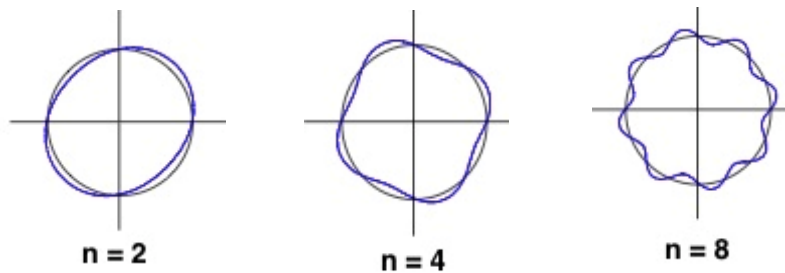


**Figure 2.22:** possible bifurcated configuration of failure zone in  $n$  branches, around a cylindrical structure, on a cross-section plane.

Of course, this limit can be simultaneously attained around the perimeter of the circle corresponding to a trivial solution: an annular failure zone will develop. Nonetheless, due to possible bifurcations, the shape of the deformed section at the elastic limit may develop, for instance, in an ellipse, elongated on the horizontal, according to Figure 2.24. At this point, it becomes necessary to recall the constitutive relations for stress and strains in elastic-plasticity and elastic-damage, respectively Eq. 2.6 and 2.17. In plasticity, according to Eq. 2.6, even in presence of strong plastic deformations, the elliptical shape in Figure 2.24 corresponds to the plastic failure zone. In any case, the material stiffness tensor,  $\mathbf{C}$ , remains unchanged (e.g. the Young modulus  $E$  does not decrease). On the contrary, if a damage-based approach is considered, with the material response illustrated in Figure 2.23 the damage variable correspondent to the failure zone assumes the value  $D = 1$ . This implies a completely damaged stiffness tensor  $\mathbf{C}$  according to Eq. 2.17, i.e.  $\mathbf{C} = 0$ . Physically, this situation corresponds to a material which is not capable to develop any further stress and the damaged failure zone can be replaced with a new gallery section, having the same elliptical shape, where the minor semi-axis is equal to the initial radius  $r_a$ , and a major semi-axis  $r_a' > r_a$ .

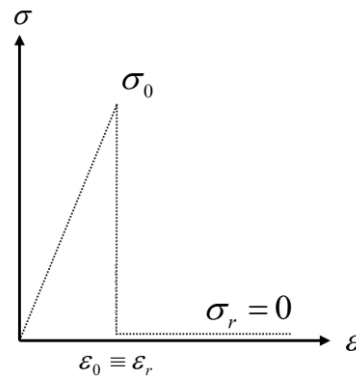


**Figure 2.23:** elastic-perfect brittle behaviour as a particular case for of the uniaxial compressive behaviour in Figure 2.4 ( $\beta = 0$ ).

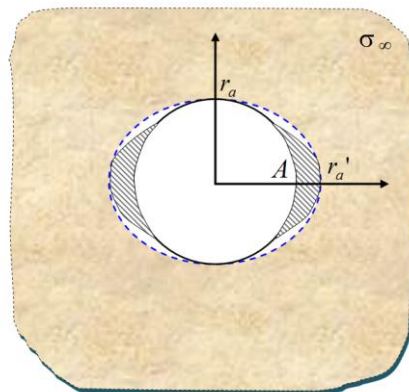


**Figure 2.24:** elliptical-shaped gallery deformation at the elastic limit, derived from an initial circular gallery perimeter. Modified from [77].

In this case, the elastic solution at the point A around the deformed section in Figure 2.24, where  $f \leq 0$ , writes:

$$\sigma_{rr} = (1 - \Delta) \frac{r_a'}{r_a} \sigma_{\infty,(0)} \quad (2.34)$$

$$\sigma_{\theta\theta} = 2\Delta \frac{r_a'}{r_a} \sigma_{\infty,(0)} + (1 - \Delta) \frac{r_a'}{r_a} \sigma_{\infty,(0)} \quad (2.35)$$

According to Eq. 2.33, the deviator is equal to:

$$q = (\sigma_{\theta\theta} - \sigma_{rr}) = 2\Delta \frac{r_a'}{r_a} \sigma_{\infty,(0)} \quad (2.36)$$

For symmetry to the point A, the same solution is valid at the left side of the gallery, on the horizontal. In this case, Eq. 2.36 shows that the stress deviator at this point increases because  $r_a' > r_a$ , and so the failure will continue to progress at this point leading to greater dissymmetry ratio  $r_a'/r_a$  for the elliptical section. Therefore, the elliptical-shape of the evolution of the section, which is a possible solution, reveals to be unstable. This shows the existence of a potential instability phenomenon affecting the circular shape of the gallery in a brittle material due to damage, correspondent to the physical phenomenon of *boreholes breakouts* (e.g. [28], [38]). Thus, with respect to elastic-plastic conditions, a damage-based dissipation induces *structural* anisotropies, which play a fundamental role in a different redistribution of the stress field in the elastic zone, subjected to incipient failure. In this simplified analysis, the ratio  $r_a'/r_a$  would increase to infinity. In reality, geomaterials are not perfectly brittle and, after failure, maintain a residual strength, possibly increasing with the lateral confinement. In addition, a real deformation process in deep rock formations includes plasticity, creep or other irreversible phenomena than pure damage, and this limits the extension of the failure zone and the dissymmetry ration  $r_a'/r_a$ .

A numerical example of the stronger anisotropy induced by localized damage compared to a more diffused plastic zone is given for a weak initial 2d anisotropic stress state. The same geometry and mesh in Figure 2.8 are employed, with the boundary conditions reported in Table 2.5 and shown in Figure 2.25. Material parameters are those of Table 2.4. Because of the anisotropy of the stress state in the plane  $x; y$ , the numerical unloading procedure in Figure 2.7 is implemented according to Eq. 2.24a and follows the scheme in Appendix A, Figure A.3. For a complete unloading ( $p_0 = 0$ ), the elastic-plastic failure zone develops, as it could be expected, along the direction corresponding to the lower initial stress component, in this case  $\sigma_{yy,(0)}$ , as illustrated in Figure 2.26. To analyse this, a cylindrical coordinates system to define each local stress-strain response at the gallery perimeter, shown in the schemes for analytical solutions in Section 1.2, can be considered. The global Cartesian coordinates system defines, as usual,  $\sigma_{(0)}$ .

**Table 2.5** : initial stress state components for the geometry reported in Figure 2.25.

$\sigma_{xx,(0)}$ [MPa]	$\sigma_{yy,(0)}$ [MPa]	$\sigma_{zz,(0)}$ [MPa]
-14.0	-12.0	$\nu(\sigma_{xx,(0)} + \sigma_{yy,(0)})$

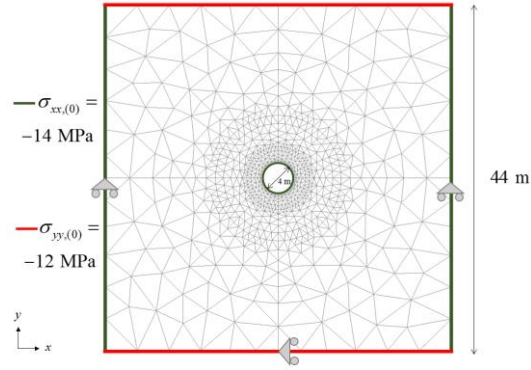


**Figure 2.25:** initial and boundary conditions on the same geometry of Figure 2.8, with an anisotropic 2d in the gallery cross section.

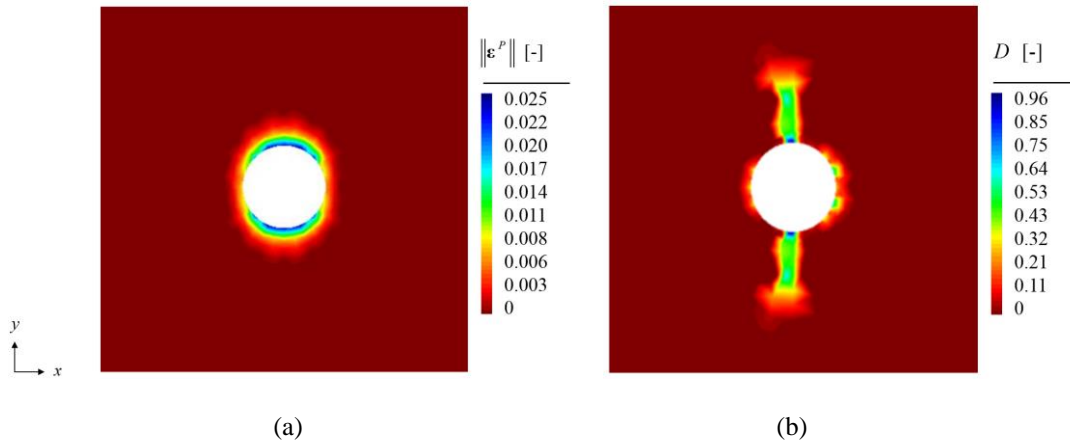


**Figure 2.26:** plastic deformations in (a) and damage variable  $D$  in (b) for a complete unloading of the circular gallery.

According to the elastic limit conditions discussed in Section 1.2, the initiation of failure must occur where the local deviator stress  $q$  reports the maximal value around the gallery perimeter  $r = r_a$ . The failure is attained along the direction  $y$  of the principal coordinates system, for the local cylindrical coordinates  $\theta = \frac{\pi}{2}$  and  $\frac{3}{2}\pi$ .

It is worth showing other two series of simulations providing interesting connections with the theoretical framework described above, based on numerical results. To conclude this section, a brief discussion concerning the correct values' interval for Young modulus, in the context of short-term, purely mechanical analyses, is included. For numerical simulations, a new, circular mesh is adopted to avoid numerical effects induced by the corners of the previous squared-shape domain: new reference geometry and mesh are reported in Figure 2.27: boundary conditions of

the plane strain analyses to define initial stresses and to simulate the excavation are reported in Figure 2.27a and b. The central contoured rectangle identifies the zoomed area including the contour plots. In this excavation, a perfect-brittle behaviour as described by Figure 2.23 is reproduced, with a parameter choice compatible with calibration (Table 2.4) and computational needs: numerically, setting  $\beta = \eta_r = 0$  would imply a non-convergence of the simulation. Parameters are reported in Table 2.6 ( $\beta = 10^{-2}$  to simulate the ideal stress-strain diagram in Figure 2.23). The mesh employed maintains, around the circular gallery, the same finite elements size of the one in Figure 2.8. Failure zones are reported in Figure 2.28.

**Table 2.6** : parameters to reproduce a perfect-brittle yielding response for failure zone in Figure 2.28.

$E$ [MPa]	$\nu$ [-]	$\sin\alpha$ [-]	$K$ [MPa]	$\beta$ [-]	$\eta_r$ [-]
2500	0.2	0.3	15.0	0.01	0.7

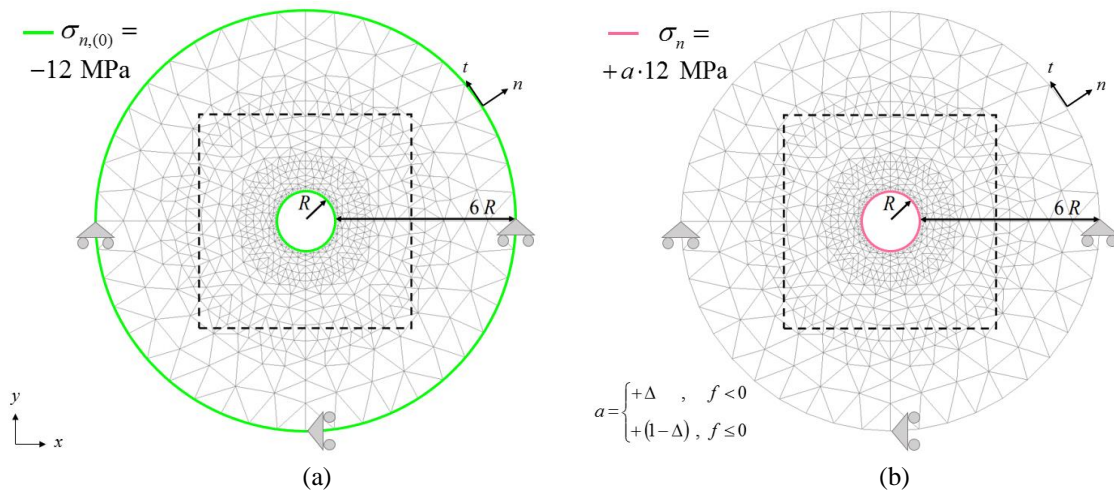


**Figure 2.27:** circular geometry adopted for numerical simulations further presented. In (a), imposition of the geostatic stress state. In (b), excavation procedure according to Figure 2.7.

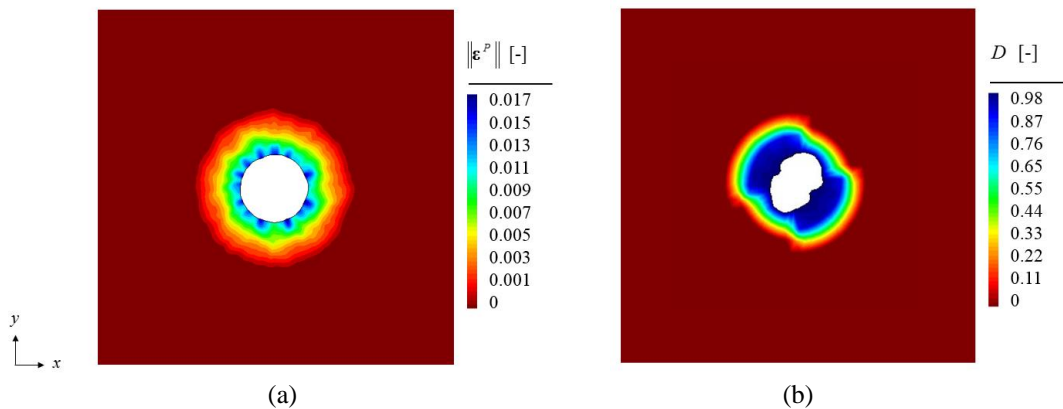


**Figure 2.28:** plastic deformations in (a) and damage in (b) for a complete unloading of the circular gallery according to BCs and geometry in Figure 2.27 and parameters in Table 2.6. Contour plots are shown in the deformed mesh configurations.

In Figure 2.28, the deformed configurations, for a complete excavation ( $p_0 = 0$ ), are reported: plastic zone in Figure 2.28a and damage zone in Figure 2.28b. Compared to the annular plastic zone, the correspondence between the displacements and failure development, with damage, can be remarked. Figure 2.28b shows also a relation with the phenomenological model of an elliptic failure zone in very brittle conditions as Figure 2.24 illustrates. Nonetheless, the direction of the localization is arbitrary: initial stress state and material properties are isotropic inside the cross-section analysed. In FEM analyses, dependencies on the mesh pattern must also be considered. A second numerical analysis is presented, showing an example of softening damage contribution for particular failure shapes. They constitutes, for instance, a well-known type of failure in the petroleum engineering research domain (*wellbores sand production*, e.g. [28]). A detailed discussion with experimental evidences and numerical examples can be found in the works of Van den Hoek et al. ([106] and [107]) on artificial sandstone. The aim of the simulation presented is not a quantitative prediction of an artificial sandstone post-peak behaviour: it provides only an idea of the correlation between the phenomena studied in this work and another application in tunnelling-induced failure in geomaterials, under the assumptions of damage-based mechanics. The same initial and boundary stress-displacements conditions shown in Figure 2.27 are maintained. Some material parameters have been changed, considering:

- An increase of the material stiffness (i.e. Young modulus  $E$ );
- A decrease of the material cohesion  $C$ .

These modifications characterize, qualitatively, the elastic and failure behaviour of a sandstone, showing higher stiffness than a claystone and reduced cohesion. Moreover, a lower cohesion (related to parameter  $K$ ; Eq. 2.4b) reduces material strength and allows a wider development of the damaged failure zone. Material parameters are reported in Table 2.7. Different shapes of the failure zone simulated by changing the parameters and/or the boundary conditions are supported by experimental evidences [77]. The failure zone calculated in Figure 2.29 reports a localized damage pattern with 8 elongated lobes. It shows clear similarities with the experiment and simulation in Figure 2.30. This last one reports the failure zone around an artificial sandstone cavity, discussed in Van den Hoek et al. ([106] and [107]), as previously cited. According to the authors, the failure prediction in Figure 2.30b has been modelled with friction hardening and cohesive softening Mohr-Coulomb criterion.

**Table 2.7** : parameters employed for the failure zone calculus in Figure 2.29.

$E$ [MPa]	$\nu$ [-]	$\sin\alpha$ [-]	$K$ [MPa]	$\beta$ [-]	$\eta_r$ [-]
6000	0.2	0.3	6.0	0.7	0.7

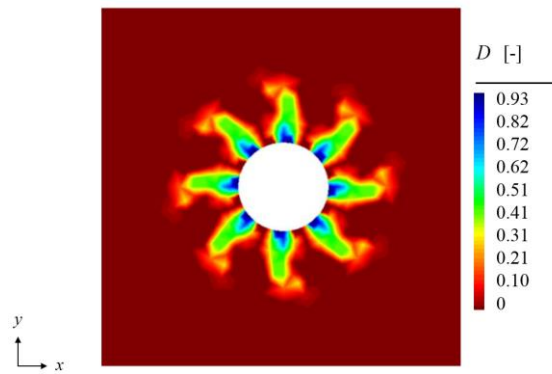


**Figure 2.29:** 8 lobes – shaped failure zone after complete unloading.

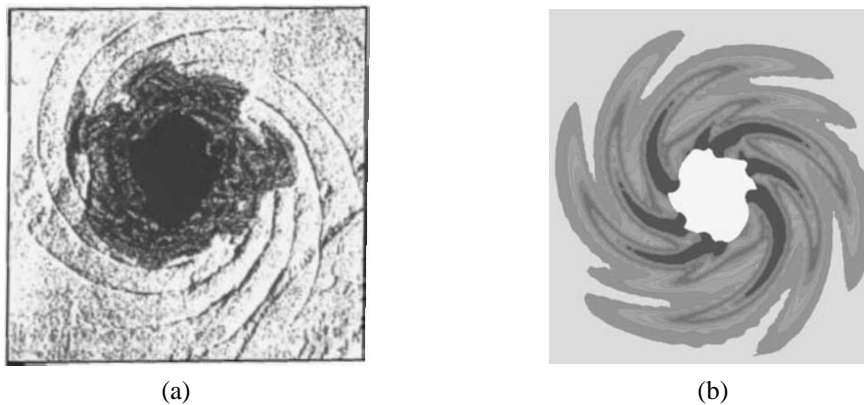


**Figure 2.30:** spiral shear bands in artificial sandstone. Experiments (a) and simulation (b) on artificial sandstone ([106] and [107]).

This type of response is evident in cavity inflation experiments for material such as Berea and Castlegate sandstones. It is consistent with the theoretical application of Coulomb failure to a cylindrically loaded borehole (e.g. [28]). As for sandstones, this shear type failure mode may be expected also in dilatant soft rocks as the Callovo-Oxfordian claystone formation.

Young modulus' value in Table 2.7 will be adopted, as average  $E$ , in numerical analyses presented in the forthcoming chapters, as indicative for the short-term, undrained behaviour of Callovo-Oxfordian claystone. Data from in-situ borehole tests confirms a mean  $E = 6000$  MPa, for natural samples with high saturation ( $>95\%$ ) and located in the geological unit of COx claystone correspondent to the main level of the Andra URL [10]. In fact, performing purely mechanical, undrained analyses (no hydraulic couplings are present in any simulation), it was questioned if the estimated Young modulus from calibration in Figure 2.16 ( $E = 2500$  MPa) was truly representative for this type of behaviour. A review on some hydro-mechanical tests' results on COx claystone (e.g. [14], [43], [46], [57], [114] and [119]) revealed a misunderstanding concerning the correct strain rate imposed, for instance, in TXc drained tests to distinguish these conditions. This could have led to possible errors when providing indications on drained/undrained stiffness parameters. In the following, a brief discussion debating this aspect is reported, considering the simple hydro-mechanical problem in Figure 2.31: a Terzaghi's mono-

dimensional consolidation along  $y$ . The problem considers a fully saturated, porous medium, in oedometric mechanical conditions. The final governing equation corresponds, under assumptions widely reported in literature (e.g. [32]), to the diffusion equation:

$$A \cdot \frac{\partial^2(\Delta p_w)}{\partial y^2} - \frac{\partial(\Delta p_w)}{\partial t} = 0 \quad , \quad A = k_w \frac{E_{oed}}{\gamma_w} = c_v \quad (2.37a-b)$$

$\Delta p_w$  is the pore over-pressure immediately generated in the specimen after a vertical stress increment. The coefficient  $A$  corresponds to the consolidation coefficient,  $c_v$ , and depends on the material's hydraulic conductivity  $k_w$ , oedometric modulus  $E_{oed}$  and water specific gravity  $\gamma_w$  (Eq. 2.37b).  $k_w = 4.5 \cdot 10^{-13}$  m/s is calculated based on the indications of material's permeability,  $K_w$ , reported in Belmokhtar et al. [12], where the authors show the remarkable decreasing of consolidation's time for COx, if lateral drainage is allowed, in triaxial compression (TXc). Concerning the oedometric modulus,  $E_{oed} = 2500$  MPa can be assumed, according to Mohajerani et al. [59], where the same conditions for a top-drained specimen in TXc test are described (lateral compression at  $p_c = 12$  MPa). A value  $c_v \approx 1.1 \cdot 10^{-9}$  m<sup>2</sup>/s is obtained for the consolidation coefficient (Eq. 2.37b). With  $H = 78$  mm (standard TXc specimen, e.g. [12]), a complete dissipation of  $\Delta p_w$  occurs between 50 and 60 days, according to the following equation:

$$t = \frac{T \cdot H^2}{c_v} \quad (2.38)$$

Eq. 2.38 adopts the Terzaghi normalized time factor  $T$ , for a consolidation ratio between 0.9 and 1. Allowing drainage also on the lateral specimen's surface would increase significantly the process speed, with almost 3 days of consolidation corresponding to an equivalent drainage length  $H \approx 20$  mm [12]. In conclusion, only an imposed strain rate not exceeding  $\sim 7 \cdot 10^{-8}$  s<sup>-1</sup> would guarantee real drained condition in TXc tests, with Young modulus' estimations consistent with the original value  $E = 2500$  MPa (Figure 2.16).

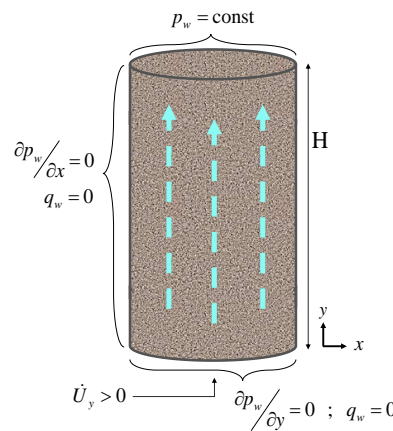


**Figure 2.31:** scheme of hydraulic boundary conditions for a specimen in a 1d consolidation problem;  $p_w$  = pore water pressure,  $q_w$  = pore water flux per unit area,  $\dot{U}_y$  = imposed rate of vertical displacements.

### 2.3 An anisotropic upgrade of the *elastic-damage* softening model

In this section, only the stress-strain elastic-damage constitutive law is considered and a first modification, referring to Eq. 2.17-2.21, is presented. In this part of the work, galleries excavated along the major horizontal stress  $\sigma_H$  are considered. In particular, GCS drift is studied and in-situ observations will be used to validate the model. It is excavated along the orientation N155°E and it disposes of a various dataset from geological, geotechnical and geophysical monitoring (e.g. [8], [9], and [60]). In its cross section, stresses in the principal (Cartesian) system coincides with the vertical and horizontal components, meaning  $\sigma_{xx} = \sigma_h$  and  $\sigma_{yy} = \sigma_v$ . As already reported in Chapter 1, Section 1.1, for the description of Andra's URL site, the following components describe the undisturbed stress state:  $\sigma_h \approx 12.4$  MPa,  $\sigma_v \approx 12.7$  MPa and  $\sigma_H \approx 16.2$  MPa ([7], [113]). This stress components generally constitutes the boundary conditions for the calculations further discussed. It is remembered that these values correspond to average estimations from in-situ measurements: small fluctuations can be considered, for numerical purposes. For the drift studied, the stress component  $\sigma_H$  corresponds to the *axial stress*, according to the reference system adopted for numerical calculations, meaning  $\sigma_H = \sigma_{zz}$ . The predictive elastic-damage model upgrades discussed in this section, in Chapter 3 and Chapter 4 answer to the first research axis main question: the simulation of an excavation-induced area, in short term, around the drifts at Andra URL, according to a 2-dimensional approximation on the drifts' cross section. It is important to recall, in fact, that tunnelling constitutes a typical 3-dimensional geotechnical problem. 2d approaches, as well as failure conceptual models, must be considered with caution according to their level of approximation. The elastic-damage model modification accounts for a damage expansion which can be called *cross-anisotropic*. In the next Figure 2.32, the conceptual model of failure expansion in two-dimension is illustrated, for tunnels excavated along the main horizontal stress  $\sigma_H$ . In particular, it refers to the case study of GCS drift. It provides details for different aspects of the failure zone description, such as the expansion, in metrics, on the cross section (a) and the different types of fractures generated (b). This figures are shown in several publications and thesis works related to the Andra's context of investigation (e.g. [9], [42], [57] and [66]).

According to the principle of a predictive model of the area where, mathematically,  $f = \dot{f} = 0$  in the drifts transverse section,  $D$  is made evolve inside the plane containing this section itself. According to the adopted references, this plane is identified by the global Cartesian coordinates  $x$  and  $y$  and it is perpendicular to the direction of axis  $z$ .

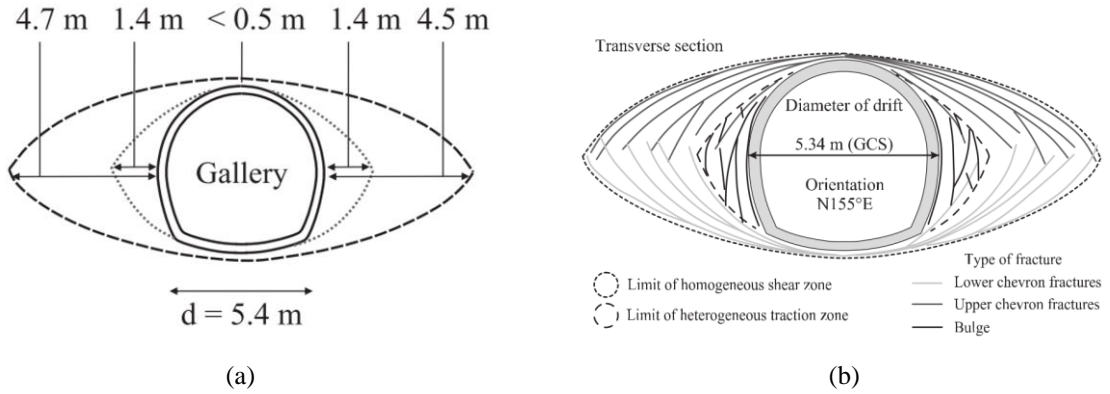


**Figure 2.32:** in (a) conceptual model and geometrical characteristic of the 2d excavation-induced zone referring to the observation for GCS drift. In (b), indication of the type of fractures included in the EDZ and EdZ on the same 2d numerical model.

Figure 2.33 reports a scheme the model upgrade proposition. The damage variable  $D$  may assume positive values, i.e.  $D \in [0 ; 1]$ , only within the plane of the cross section,  $\Gamma$ . Damage reduces the material stiffness along these same directions. It is remembered that, for the moment, the Young modulus is the same for every direction, corresponding to isotropic elasticity. With this model formulation, the *axial* stress variable  $\sigma_{zz}$ , still included in the failure criterion (Eq. 2.18), is not directly influenced by damage. The entity of the *axial* (or out-of-plane, as referred sometimes in literature) stress component,  $\sigma_{zz}$ , appears to be fundamental in stabilizing (or not) the expansion of the damage failure (e.g. [81]). This aspect is later clarified and confirmed by numerical simulations in the next chapter. In general, it is underlined that a three-dimensional stress state influences the results of the damaged zone simulated on a two-dimensional geometry. Thus, the upgrade of the basic elastic-damage model is also intended to limit the contribution of the out-of-plane direction  $z$  to the development of the damage variable within the gallery cross-section. In 2d plane strains conditions, meaning  $\varepsilon_{zz} = 0$ , Eq. 2.39 in the following corresponds to the stress-strain constitutive law for the basic elastic-damage model. Contrarily to Eq. 2.17, it is written in terms of the compliance matrix  $\mathbf{C}^{-1}$ :

$$\begin{bmatrix} \varepsilon_{xx} \\ \varepsilon_{yy} \\ \varepsilon_{zz} \\ 2\varepsilon_{xy} \end{bmatrix} = \mathbf{C}^{-1}(D) : \begin{bmatrix} \sigma_{xx} \\ \sigma_{yy} \\ \sigma_{zz} \\ \sigma_{xy} \end{bmatrix}, \quad \mathbf{C}^{-1} = \frac{1}{(1-D)} \begin{bmatrix} \frac{1}{E} & \frac{-\nu}{E} & \frac{-\nu}{E} & 0 \\ \frac{-\nu}{E} & \frac{1}{E} & \frac{-\nu}{E} & 0 \\ \frac{-\nu}{E} & \frac{-\nu}{E} & \frac{1}{E} & 0 \\ 0 & 0 & 0 & \frac{2(1+\nu)}{E} \end{bmatrix} \quad (2.39)$$

The explicit expression of  $\mathbf{C}^{-1}$  remarks that the coefficient  $(1-D)^{-1}$  is applied to the entire matrix. To develop the *cross-anisotropic* elastic-damage model, the mathematical formulation of the final stiffness matrix  $\mathbf{C}$  starts indeed from the correct definition of its compliance matrix  $\mathbf{C}^{-1}$  considering that the axial (or out-of-plane) direction  $z$  is not affected by damage.

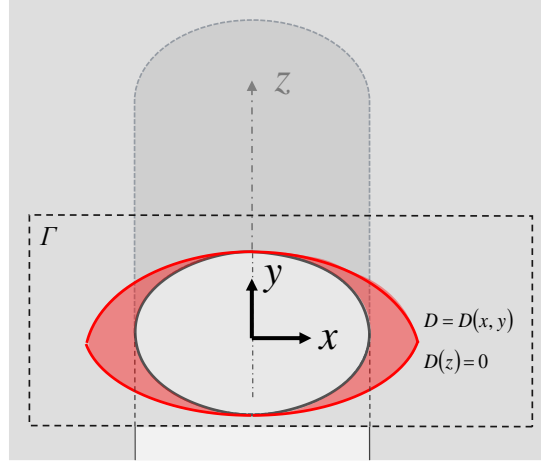


**Figure 2.33:** scheme of the implemented anisotropic damage expansion in the reference coordinates.

Each terms  $C_{ij}$  has been later implemented in *POROFIS*. In Eq. 2.40, the stress-strain constitutive law defined with the modified compliance matrix  $\tilde{\mathbf{C}}$  for the model upgrade is reported:

$$\begin{bmatrix} \varepsilon_{xx} \\ \varepsilon_{yy} \\ \varepsilon_{zz} \\ 2\varepsilon_{xy} \end{bmatrix} = \tilde{\mathbf{C}}^{-1} : \begin{bmatrix} \sigma_{xx} \\ \sigma_{yy} \\ \sigma_{zz} \\ \sigma_{xy} \end{bmatrix}, \quad \tilde{\mathbf{C}}^{-1} = \begin{bmatrix} 1 & -\nu & -\nu & 0 \\ E(1-D) & E(1-D) & E & 0 \\ -\nu & 1 & -\nu & 0 \\ E(1-D) & E(1-D) & E & 0 \\ -\nu & -\nu & 1 & 0 \\ E & E & E & 0 \\ 0 & 0 & 0 & \frac{2(1+\nu)}{E(1-D)} \end{bmatrix} \quad (2.40)$$

It can be noticed that the coefficient  $(1-D)^{-1}$  multiplies separately the compliance tensor components  $\tilde{\mathbf{C}}_{ij}^{-1}$  satisfying the condition:

$$(i = 1; 2; 4) \wedge (j = 1; 2; 4) \quad (2.41)$$

The compliance component  $\tilde{\mathbf{C}}_{44}^{-1}$  corresponds to the shear compliance  $\tilde{\mu}_{xy}^{-1}$  in the cross section plane  $\Gamma$  (Figure 2.33) and it is, as well, affected by damage. The condition in Eq. 2.41 shows that only the compliance components depending on direction  $z$  are not multiplied by  $(1-D)^{-1}$ . The new compact stress-strain constitutive law, in terms of the stiffness matrix  $\mathbf{C}$ , can be written for the new *cross-anisotropic* elastic-damage model, according to Eq. 2.42:

$$\boldsymbol{\sigma} = \tilde{\mathbf{C}}(D) : \boldsymbol{\varepsilon} \quad (2.42)$$

The developed model will be identified by the notation  $2d\_ED$  when recalling it in the sequel, meaning that it describes, for the elastic-damage basic model ( $ED$ ), a bi-dimensional (2d) damage expansion, according to the principal reference directions  $x$  and  $y$ . The explicit expression of the modified stiffness matrix for the  $2d\_ED$  model is reported in the following and writes:

$$\tilde{\mathbf{C}} = \frac{E(1-D)}{1-\nu-2\nu^2(1-D)} \begin{bmatrix} \frac{1-\nu^2(1-D)}{1+\nu} & \frac{\nu[1+\nu(1-D)]}{1+\nu} & \nu & 0 \\ \frac{\nu[1+\nu(1-D)]}{1+\nu} & \frac{1-\nu^2(1-D)}{1+\nu} & \nu & 0 \\ \nu & \nu & \frac{1-\nu}{1-D} & 0 \\ 0 & 0 & 0 & \frac{1-\nu-2\nu^2(1-D)}{2(1+\nu)} \end{bmatrix} \quad (2.43)$$

Once the mathematical formulation established, as introduced, each component  $\tilde{C}_{ij}$  of the modified stiffness matrix  $\tilde{\mathbf{C}}(D)$  in Eq. 2.43 has been implemented in a FORTRAN subroutine, based on the initial elastic-damage model. In particular, referring to the material subroutine structure in Appendix A, Figure A.1, the part correspondent to the variables definition identifying the stiffness matrix components has been modified. According the structure of the code *POROFIS*, described in Section 2.1, the subroutine has been coded as a new, user-defined constitutive law in the open-access file *Utilizer.f90* (Figure 2.2).

As previously stated, the next objective consists in providing a first realistic predictive model of the excavation-induced damage in proximity of a gallery excavation, respecting the direction of development. It is important to remember that the rock/claystone surrounding the proximities of the cavity interface are subjected to a (quasi) uniaxial stress state. The deviator assumes, here, values very close to the uniaxial compressive strength  $\sigma_0$  and the low confinement induces very brittle post-peak behaviours. In particular, ideal conditions for the phenomena of rock spalling and breakouts around the wall, are satisfied. Thus, at least for Callovo-Oxfordian claystone, these conditions appears extremely suitable for an instantaneous mechanical damage response. The first results on the case study drift GCS are shown in the next chapter, with the employment of the *2d\_ED* model described here. To conclude this section and chapter, a mesh sensitivity analyses for softening conditions in *POROFIS* is presented in the following. The *2d\_ED* model is compared to the response of the other basic model used in this chapter, in elastic-plasticity. The same numerical discretization adopted at the end of Section 2.1, reported in Figure 2.12 (from left to right, Mesh 1, 2 and 3) are employed here. The same parameters are maintained, but a quite strong softening is assumed by changing the residual to initial strength resistance ratio,  $\eta_r$ , implying important accumulation of plastic deformations and/or damage bifurcations. In fact, it must be underlined that every constitutive law adopted corresponds to a local definition of the mechanical stresses, strains and internal variables. Numerically, the response at each Gauss point of the FE domain is consequence of the constitutive law defined at the same Gauss point only. Hence, in principle, if bifurcation phenomena occur, they may be numerically subjected to the biases of mesh discretisation level ([63], [65]). As done in the first section, this analysis is performed only to provide an indication of an affordable mesh size to be adopted in the following.

At the same time, limitations of local mechanical models in softening conditions are shown in quantitative terms. To simulate a circular opening, the same boundary conditions reported in Figure 2.8 are adopted, with FE discretization illustrated in Figure 2.12, applying the same mesh size reduction. Table 2.8 reports the parametrization for both the elastic-plastic and the  $2d\_ED$  models. Results of the plastic deformations extension for the complete unloading are reported in Figure 2.34, while damage evolution is reported in Figure 2.35. As done for the perfect-yielding behaviour, the radial expansion of failure is quantitatively analysed. It can be noticed that an estimation of the plastic radius for each result in Figure 2.34 can be easily provided. Concerning the damage development, bifurcation occur for the fines mesh (Figure 2.35, on the right). In any case, for the  $2d\_ED$  model, an approximation of each failure zone with an annular area around the circular opening can be traced. In particular, the result shown in the central contour plot of Figure 2.35 easily allows an approximation to a circular area. In terms of elements' minimum size around the gallery, it corresponds to the same mesh in Figure 2.8. This is the one adopted for results presented in Sections 2.1 and 0.

**Table 2.8** : parameters for the softening mesh size sensitivity analyses.

$E$ [MPa]	$\nu$ [-]	$\sin\alpha$ [-]	$K$ [MPa]	$\beta$ [-]	$\eta_r$ [-]
6000	0.25	0.25	15.0	1.0	0.4

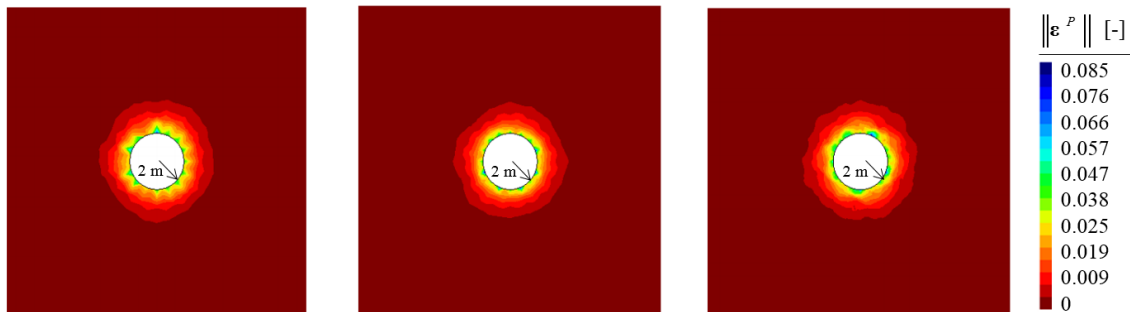


**Figure 2.34**: mesh size sensitivity analyses in softening plasticity. Boundary condition are reported in in Figure 2.8, FE discretization in Figure 2.12 and parameters in Table 2.8.

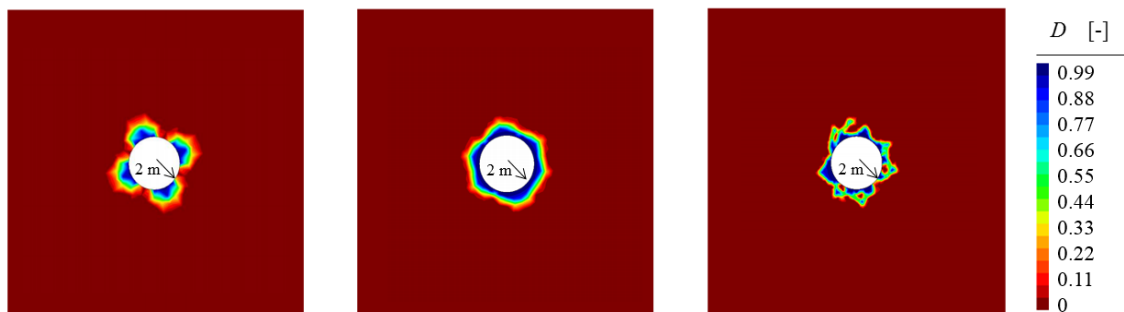


**Figure 2.35**: mesh size sensitivity analyses in softening damage with the  $2d\_ED$  model. Boundary condition are reported in in Figure 2.8, FE discretization in Figure 2.12 parameters in Table 2.8.

Even after the change from a squared to a circular external perimeter of the FE domain (Figure 2.27) the same mesh size in the area surrounding the gallery, interested by failure, is maintained. Thus, this mesh size can be considered suitable to avoid extreme and unlikely bifurcation phenomena as, for instance, shown in the right contour plot of Figure 2.35. In Figure 2.36, respectively (a) and (b) plastic and damage (approximate) radius extensions are reported for each of the previous results discussed. In particular, to approximate the second one, for each contour plot in Figure 2.35 the same 6 radial directions are considered to compute locally the radial extension of the failure zone, corresponding to the existence of values of  $D \in (0 ; 1]$ . Each plastic and estimated damage radius extensions are reported in Table 2.9 with an the average error due to the mesh discretization levels, as already done in perfect yielding conditions, according to Eq. 2.30.

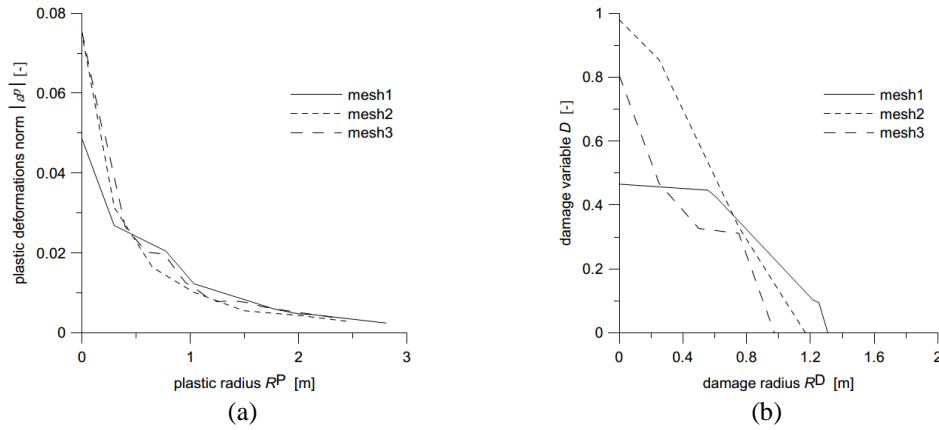


**Figure 2.36:** extension of the failure radius in softening plasticity (a) and softening  $2d_{ED}$  model (b). The second one corresponds to an average smoothed on the same distinct radial directions for each mesh.

**Table 2.9:** extension of plastic radius for each of the results reported in Figure 2.34 and Figure 2.35. Average errors of numerical discretization, calculated according to Eq. 2.30.

	Mesh1	Mesh 2	Mesh 3	Average error (%)
Average $r_P$ [m]				
(softening plasticity)	2.81	2.48	2.33	19.3%
Average $r_P$ [m]				
(softening damage)	1.31	1.17	0.97	28.6%

## Conclusion

The main features of *POROFIS*, the FEM processor employed for the major analyses presented in this manuscript, have been described and some validation examples of simulations have been presented. Two fundamental softening mechanical constitutive laws have been presented, corresponding to distinct hypotheses of plasticity and damage dissipation. After a first modelling approach in perfect yielding conditions, the softening and fragile response of the material simulating a circular opening is analysed showing the main contributions/differences offered by a dissipative approach based on damage, if compared to a more traditional approach in plasticity. The analyses presented have already been included in some conference proceedings listed in this manuscript's references ([77], [78]).

It is important to remember to the reader that, in this work, a damage-based approach is intended as a complement / integration of a wide framework of models based on elastic-plasticity, possibly with creep effects already proposed for the problem of the failure zone generation and evolution for drifts at Andra URL.

At last, the anisotropic elastic-damage softening ( $2d_{ED}$ ) model, its mathematical formulation and its physical motivations have been presented. In particular, it seemed significant to introduce a modification on the elastic-damage tensor neglecting the influences of damage evolution along the direction perpendicular to a drift cross section. This constitutes, in fact, the selected area where the study of the failure evolution is performed. Numerical results presented in Chapter 3 will be based on the  $2d_{ED}$  model formulation. As a completion of this chapter's last section, mesh-size sensitivity analyses, accounting for softening conditions, have been presented.

## **Chapter 3**

# **General Damage-Based Modelling on Drifts Section**



In this chapter, numerical analyses aiming the reproduction of the failure system, defined EDZ-EdZ in Chapter 1, are proposed. A brief recall of the 2d conceptual models provided by Andra (e.g. [9], [93]) and based on in-situ observations at the Underground Research Laboratory (URL) in Bure (e.g. [7], [60]) is provided throughout the chapter before the analyses' presentation. An initial approach focuses on the reproduction of the failure zone (EDZ) for one of the two main drifts' directions. The elastic-damage stiffness tensor, employed for the forthcoming analyses, is based on the model formulation defined  $2d_{ED}$  and presented in Chapter 2, Section 2.3.

After an evaluation on the effects of the initial axial stress imposed on the drifts' sections, some upgrades to the  $2d_{ED}$  model are presented and formalized in mathematical terms, taking into account the anisotropic characteristics of the Callovo-Oxfordian formation. Discussions of the results obtained, for one or both the main drifting directions at the Andra URL, are reported to evaluate the upgrades' contribution to the overall modelling exercise for the simulation of failure expansion and displacements' estimation around drifts.

An analyses of the failure conditions accounting a certain material anisotropy, at the same time, for the two drifts' directions (implying, numerically, different boundary value problems), is reported in the last section of this chapter: in fact, a model validation is required for both horizontal directions of excavation at the URL. Discussions reported at the end of the chapter provide a summary to link the contents of this part of research to the forthcoming numerical analyses, for 2d failure in plane strain conditions, presented in Chapter 4. In this chapter, several references to the Appendix B occur, where the mathematical formalisms of the implemented anisotropic model are detailed.

### 3.1 Failure analysis with a 2d *global* damage model

In this section, a first application of  $2d\_ED$  model introduced at the end of Chapter 2 is presented to model the failure shape and extension around drifts along the major horizontal stress  $\sigma_H$  at the Andra URL, with a focus on the EDZ only. This corresponds to the damaged area included in the inner dotted line (heterogeneous shear and extensional fractures) of Figure 3.1 (e.g. [93]). Along the horizontal ( $x$ ), its major extension measures 1.1 – 1.4 m, as already illustrated in Chapter 1 (Table 1.1, Section 1.1). Boundary and initial stress components, according to in-situ estimations, are reported in Table 3.1.

A total of 6 parameters for the  $2d\_ED$  model must be defined. In the next analyses, parameters for linear elasticity  $E$  and  $\nu$  are respectively equal to 6000 MPa and 0.2 (e.g. [10], [37], [43]). The Young modulus is considered as the average undrained value for the considerations on the short-term response in terms of total stresses discussed in Section 2.2. Concerning the unconfined compressive strength  $\sigma_0$  ( $UCS$ ) a range of 17 – 25 MPa is reported in Chapter 1 (Table 1.3, Section 1.1). Sometimes, it is possible to find in literature also a wider range defined around an average  $UCS$  value, giving  $21 \pm 7$  MPa (e.g. [8], [9]). With respect to Table 2.4 in Section 2.2, a prudential value is assumed for the following calculation:  $\sigma_0 = 17$  MPa. Friction angle  $\varphi = 20^\circ$ , according to the average value for the Callovo-Oxfordian (COx) formation (Table 1.3, Chapter 1, Section 1.1; e.g. [8]). The softening (post-failure behaviour) parameters, denoted in  $POROFIS$  by  $\beta$  and  $\eta_r$  and described in Section 2.1 (Figure 2.4 and Eq. 2.5a-b), are assumed both equivalent to 0.7 according to the calibration in Figure 2.16, in the same chapter (Section 2.2). Table 3.2 contains a summary of the 6 model parameters.

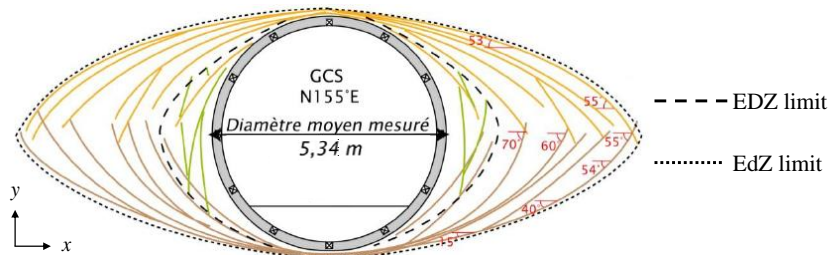


**Figure 3.1** : 2d conceptual model for the system EDZ-EdZ for a drift excavated along stress  $\sigma_H$  at the Andra URL (e.g. [7], [9], [60] and [94]).

**Table 3.1** : boundary and initial stress components for the numerical analyses of EDZ shape and extension (inner heterogeneous failure) reported in Figure 3.1.

$\sigma_{xx,(0)}$ [MPa]	$\sigma_{yy,(0)}$ [MPa]	$\sigma_{zz,(0)}$ [MPa]
-12.0	-13.0	-16.0

**Table 3.2** : numerical values for the parametrization of the  $2d\_ED$  model adopted in the following.

Elastic parameters		Failure parameters		Softening parameters	
$E$ [MPa]	$\nu$ [-]	$\varphi$ [°]	$\sigma_0$ [MPa]	$\beta$ [-]	$\eta_r$ [-]
6000	0.2	20	17.0	0.7	0.7

Figure 3.2a illustrates the numerical model together with the boundary conditions applied, referring to the drift GCS, discussed as a reference case in Section 1.1 and adopted as one of the two case studies throughout the entire thesis work. The internal radius  $r_a = 2.6$  m, indicated as the theoretical radius length designed in the excavation phase and adopted in other works and publications (e.g. [42], [43]). The imposed axial stress  $\sigma_{zz,(0)}$  is indicated by the symbol  $\otimes$  in Figure 3.2a. The linear decreasing of the initial stress state  $\sigma_{(0)}$  (Table 3.1), which boundary conditions applies according to Figure 3.2b, follows the procedure presented for 2d plane strain simulations in Section 2.1 (Figure 2.7). Contour plots in Figure 3.3 and Figure 3.4 show, respectively, the expansion of damage variable  $D$  and the horizontal and vertical displacement field.

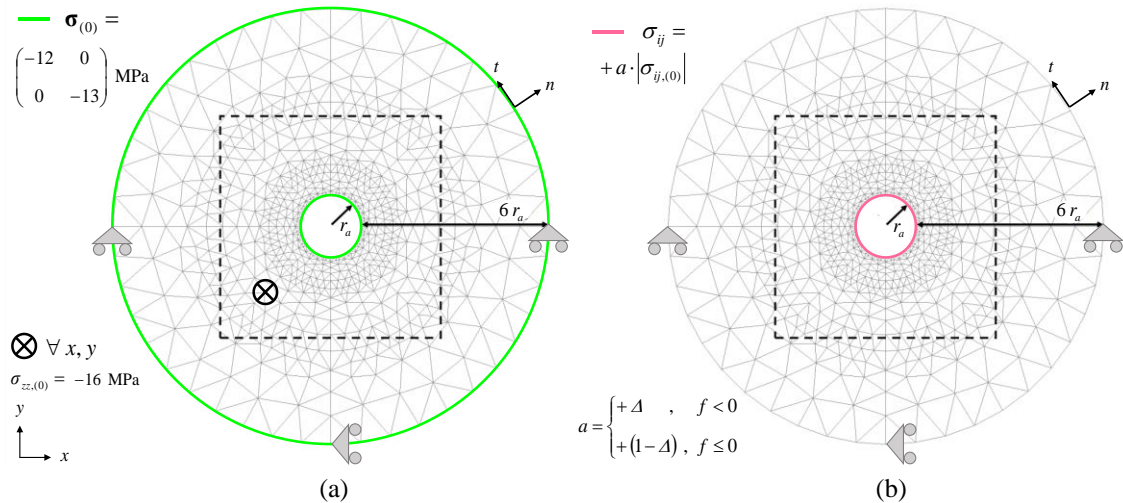


**Figure 3.2** : numerical model, initial conditions (a) and excavation boundary conditions (b) for the numerical analyses presented in the current section.

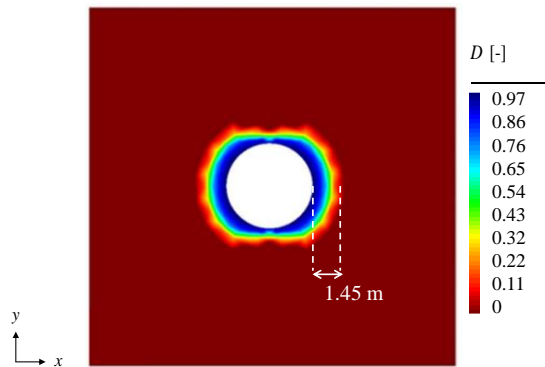


**Figure 3.3** : contour plot for the damage  $D$ , at the end of the excavation, with its the horizontal extension.

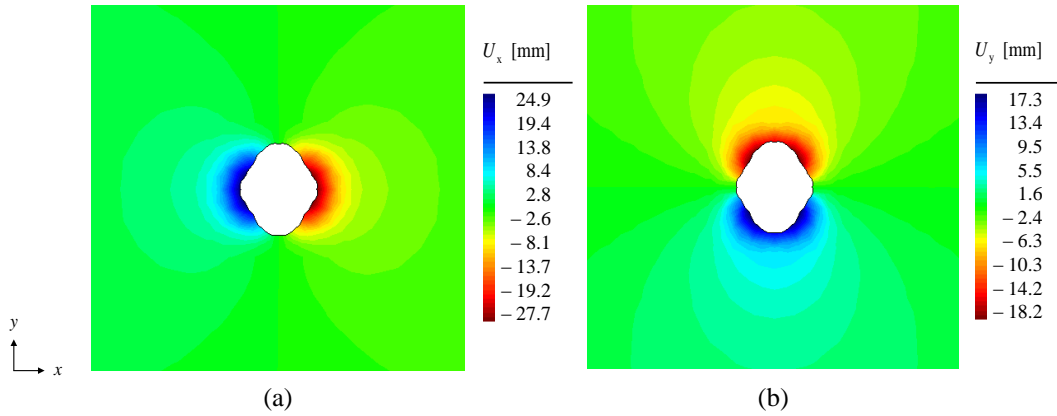


**Figure 3.4** : contour plots for horizontal ( $U_x$ ) displacement (a) and vertical ( $U_y$ ) displacements field (b).

A discussion on the results illustrated in Figure 3.4 show can be provided considering the very initial values for the total displacements measured at the perimeter of GCS drift by extensometers installed around the excavation and reported in Figure 3.5. Here, short-term displacements induced by the excavation process can be extrapolated by total measurements (lasting several hundreds of days) according to excavation chronograms available for drift GCS [60]. An interval of about 1 month corresponds to an advancement of 2 times the drift’s diameter from the studied cross-section, which can be assumed the limit time lap including the short-term response induced by the excavation. Nonetheless, it must be underlined that creep effects in the COx formations may occur immediately after a mechanical perturbation and even “short-term” observations from laboratory or real-scale experiments should be careful handled. Includes a comparison between estimated values intervals for  $U_x$  and  $U_y$  at the drift’s wall together with computed values.

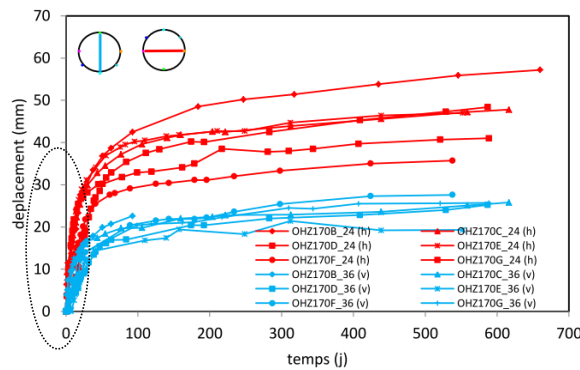


**Figure 3.5** : total horizontal (red line) and vertical displacements (blue line), measured at the GCS drift’s perimeter, with a focus on the initial values likely to correspond to the excavation-induced response. Modified from [93].

**Table 3.3** : comparison between estimated intervals and computed values for short-term  $U_x$  and  $U_y$ .

	$ U_x $ [mm]	$ U_y $ [mm]
in-situ measures (interval)	[20 ; 30]	[10 ; 15]
calculated (max. value)	27.7	18.2

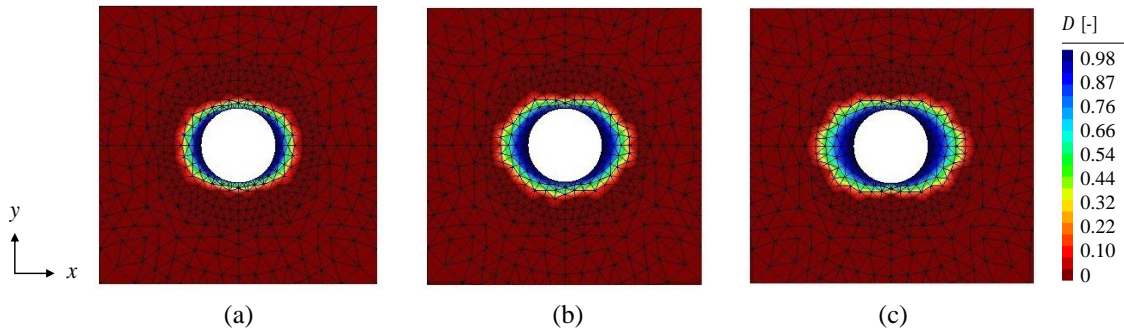


**Figure 3.6** : increasing of  $D$  expansion with the decreasing of  $\sigma_{zz,(0)}$  imposed as axial boundary/initial conditions (a)  $\sigma_{zz,(0)} = -10$  MPa; (b)  $\sigma_{zz,(0)} = -8$  MPa; (c)  $\sigma_{zz,(0)} = -5$  MPa.  $\sigma_{xx,(0)}$  and  $\sigma_{yy,(0)}$  as in Table 3.1.

Comparison provided in Table 3.3 show a good agreement of the model's calculations, which are included within the intervals obtained from in-situ monitoring.

An analyses on the effects of the imposed value of the initial axial stress,  $\sigma_{zz,(0)}$ , concludes this section. Indeed, the choice of considering (or not) the axial stress for this type of boundary value problems, simplified in 2d, is a debated topic in the related scientific literature (e.g. [80], [81]). Here, since the adopted failure criterion bases on a Drucker-Prager model and includes  $\sigma_{zz}$ , it seemed worth mentioning this aspect to underline that it can constitute a crucial boundary/initial condition when dealing with numerical simulation to predict excavation effects due to tunnelling. As it may be logically expected, according to the damage contour plots in Figure 3.6, the damage expansion along the horizontal doubles if the initial value  $\sigma_{zz,(0)}$  is reduced than one half. For the results presented in Figure 3.6, obtained from numerical model and excavation in Figure 3.2b, the same parameters reported in Table 3.2 were maintained for the  $2d\_ED$  model. This analyses concludes the section.

### 3.2 Modelling the anisotropic failure response

In the previous section, the variability of the unconfined compressive strength ( $UCS$ ) has been mentioned. As already reported in the material presentation (Section 1.1), this variability corresponds to the anisotropic characteristic of the COx formation at the microscale. The variation of the material resistance with the inclination to the main load directions concurs to the localization of failure, together with possible anisotropies of the initial stress state on the drift's cross-section, denoted as  $\Gamma$  in the reference scheme in Figure 3.7. Here, with the simplification of a 2d stress state on a plane, a horizontally-stratified material is represented, with the local stresses response at the gallery perimeter, in a polar coordinates system ( $r; \theta$ ). In particular, for a volume element around the gallery perimeter, the orthoradial component  $\sigma_{\theta\theta}$  corresponds to the uniaxial compressive strength ( $UCS$  or  $\sigma_0$ ), if the effect of retaining structures is neglected ( $\sigma_{rr} = 0$ ).

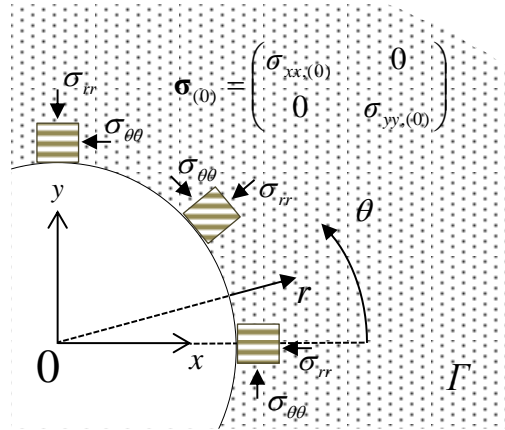


**Figure 3.7** : reference scheme of the excavation problem in a 2d stress state simplification with the global (Cartesian) and local (polar) coordinates systems.

In this section, the variability of  $UCS$  is considered through the implementation of an anisotropic failure formulation based on the Drucker-Prager criterion previously adopted. In particular, a second (II) order *rotation* tensor describing the anisotropic response as function of the inclination angle of the material “structure” to the main loading directions, is presented and formalized. It is to be integrated in the Drucker-Prager failure criterion in the model  $2d\_ED$ . Because of the numerical works remain in a framework of 2d, plane strain analyses, the introduced rotation tensor does not affect the axial component  $\sigma_{zz}$ , which is anyway accounted in the failure criterion according to the Drucker-Prager formulation. The formalisation of the anisotropic criterion includes initially the definition of the normal unitary vector  $\mathbf{n}$  to the material stratification (bedding), and the angle  $\omega$  included between  $\mathbf{n}$  and the horizontal (i.e.  $x$ ).  $\mathbf{n}$  and the II order anisotropic rotation tensor write:

$$\mathbf{n} = (\cos \omega \quad \sin \omega \quad 0)^T \quad ; \quad \mathbf{M} = \delta_{ij} + h(\mathbf{n} \otimes \mathbf{n}) \quad (3.1a-b)$$

$$\mathbf{M} = \begin{bmatrix} 1 + h \cos^2 \omega & h \sin \omega \cos \omega & 0 \\ h \sin \omega \cos \omega & 1 + h \sin^2 \omega & 0 \\ 0 & 0 & 1 \end{bmatrix} \quad (3.2)$$

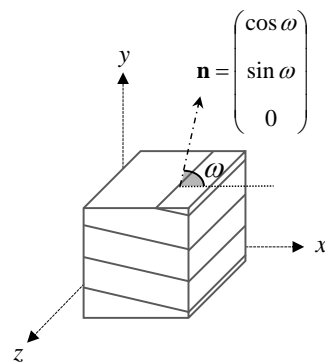


**Figure 3.8** : conceptual model for the implementation of the anisotropic Drucker-Prager failure criterion.

In Eq. 3.1b,  $h$  is defined as anisotropic scaling coefficient and it quantifies the material anisotropy, as shown later. Whatever stress state can be evaluated for failure attainment (i.e.  $f = 0$ ), with anisotropic conditions of material strength, by modifying the original stress tensor  $\boldsymbol{\sigma}$  with  $\mathbf{M}$ :

$$\tilde{\boldsymbol{\sigma}} = \mathbf{M}^T \cdot \boldsymbol{\sigma} \cdot \mathbf{M} \quad (3.3)$$

Eq. 3.3 above (explicated in Appendix B.1) provides a modified or *equivalent* stress tensor,  $\tilde{\boldsymbol{\sigma}}$ , including in its formulation the anisotropic characteristics of the material.

$$\tilde{\boldsymbol{\sigma}} = \begin{bmatrix} \tilde{\sigma}_{xx} & \tilde{\sigma}_{xy} & 0 \\ \tilde{\sigma}_{yx} & \tilde{\sigma}_{yy} & 0 \\ 0 & 0 & \tilde{\sigma}_{zz} \end{bmatrix} \quad (3.4)$$

This stress tensor is finally adopted for whatever failure evaluation by the adoption of its stress variable in the original Drucker-Prager failure criterion:

$$f = \sqrt{3\tilde{J}_2} + \sin \alpha \tilde{I}_1 - g(D)K = 0 \quad (3.5)$$

$$\tilde{I}_1 = tr\{\tilde{\boldsymbol{\sigma}}\} \quad ; \quad \tilde{J}_2 = \frac{1}{2} \tilde{s}_{ij} \tilde{s}_{ji} \quad (3.6a-b)$$

The scheme illustrated in Figure 3.8 has a particular case for the Callovo-Oxfordian stratification at the main level of the URL, where the excavation directions are parallel to the material bedding. Here, the material stratification, or *bedding*, is equivalent to the scheme reported for the volume elements in Figure 3.7 and the axis of transverse anisotropy coincides with the vertical axis  $y$ . With these conditions, because of the in-situ material characteristics, it is possible to write  $\omega = 90^\circ$ . To describe the anisotropic resistance of the material, two parameters are defined for the *UCS*, denoted also  $\sigma_0$ , discerning between the quantity perpendicular to the stratification,  $\sigma_{0,90^\circ}$ , and the one parallel to the stratification (for a loading perpendicular to a  $y$ ), indicated with  $\sigma_{0,0^\circ}$ . Their ratio allows the definition of the anisotropy scaling factor  $h$ :

$$h = \sqrt{\frac{\sigma_{0,0^\circ}}{\sigma_{0,90^\circ}}} - 1 \quad (3.7)$$

The entire derivation of Eq. 3.7 is reported in the Appendix B.1. Here, the expressions for the two *UCS* values are reported:

$$\sigma_{0,0^\circ} = \frac{K}{(1 - \sin \alpha)} \quad (3.8)$$

$$\sigma_{0,90^\circ} = \frac{K}{(1 + h)^2 (1 - \sin \alpha)} \quad (3.9)$$

In Eq. 3.8,  $\sigma_\theta$  for  $\omega = 0^\circ$  (parallel to the bedding) maintains the original formulation of the isotropic criterion. It is underlined that the condition  $\sigma_{0,0^\circ} = \sigma_{0,90^\circ}$ , consequently  $h = 0$ , would also correspond to the original isotropic criterion. Numerical employment of the failure function in Eq. 3.5 requires the identification of the parameters  $\sin\alpha$ ,  $K$ ,  $h$ . According to Eq. 3.8 and 3.9, once a set of reference values for the friction angle  $\varphi$ , for  $\sigma_{0,0^\circ}$  and  $\sigma_{0,90^\circ}$  is fixed, the parameters reported above can be obtained analytically, as follows:

- $\sin\alpha$  is determined from  $\varphi$  (according to Eq. 2.4a in Chapter 2).
- $K$  is determined from  $\sigma_{0,0^\circ}$  and  $\sin\alpha$  according to Eq. 3.8.
- $h$  is determined, for instance, from  $\sigma_{0,0^\circ}$  and  $\sigma_{0,90^\circ}$  according to Eq. 3.7.

The  $2d\_ED$  model accounting for the anisotropic Drucker-Prager failure criterion, as implemented in *POROFIS*, includes 8 parameters.  $\omega$  and  $h$  are the new parameters, with respect to the set of 6 parameters in the initial elastic-damage formulation (Table 2.1, Chapter 2, Section 2.1). Through the invariants  $\tilde{I}_1$  and  $\tilde{J}_2$  (Eq. 3.6a-b), whatever stress state, represented by the tensor  $\tilde{\sigma}$  in Eq. 3.4, can be reproduced. An example providing the mathematical validity of the proposed model is reported, in Figure 3.9, showing numerical simulations of unconfined or confined compression tests, in plane strain. In particular, in Figure 3.9b, the variability of the compressive strength with  $\omega$  is traced for different level of confining stress,  $p_C$ , and compared to an analogue anisotropic model [91] already proposed for COx claystone. Here, the material's resistance varies monotonically with  $\omega$ , showing maximal values for compressions occurring parallel to the bedding and minimum values for compressions perpendicular to the stratification. It is underlined that, in the comparison model, the angle describing the material's orientation to the main loading directions is the complementary to  $\omega$ , i.e. the angle between the normal  $\mathbf{n}$  to the bedding and the vertical ( $y$ ), meaning  $(\pi/2 - \omega)$  in Figure 3.8. Compressive strength, varying with  $\omega$  and  $p_C$ , is denote by  $\sigma_0(p_C)_{,\omega}$ .

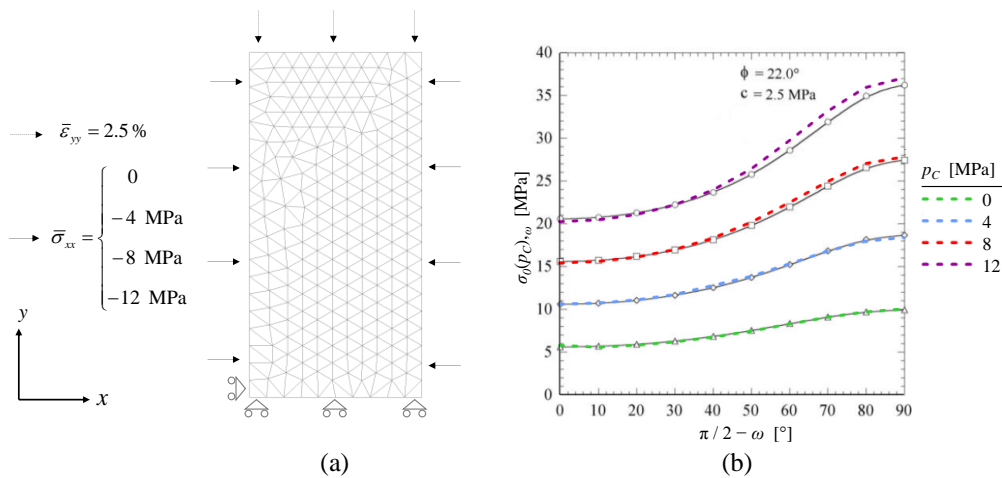


**Figure 3.9** :simulation of confined compression tests with  $\sin\alpha = 0.28$ ,  $K = 5.3$  MPa and  $h = 0.3$ . Original failure parameters:  $\varphi = 22^\circ$  and  $C = 2.5$  MPa.

Numerical analysis presented hereby is intended to reproduce the entire failure system EDZ-EdZ for the drift GCS, already considered in Section 3.1, by means of the  $2d\_ED$  model integrated by the anisotropic Drucker-Prager criterion presented above. To perform its parametrization, a general variability of  $UCS$  between 17 – 25 MPa (Table 1.3, Chapter 1) can be considered, even if a wider range is indicated around an average  $UCS$  value,  $21 \pm 7$  MPa (e.g. [8], [9]). The anisotropic criterion has been employed firstly to consider a monotonic variation of the failure resistance under uniaxial or triaxial conditions, respectively  $\sigma_{0,\omega}$  and  $\sigma_0(p_C)_{,\omega}$ . Few available data on triaxial tests (TXc) at failure, for different orientations, suggested that resistance is, in general, higher when parallel to the material bedding:  $\sigma_0(p_C)_{,0^\circ} > \sigma_0(p_C)_{,90^\circ}$ ,  $\forall p_C$ . This is consistent with the reviewed model adopted for the comparison in Figure 3.9b. Available indications on compressive strength for COx along the directions parallel and perpendicular to the bedding are resumed in Table 3.4. To define a unique set of failure parameters for the  $2d\_ED$  model with the anisotropic Drucker-Prager criterion, a series of numerical simulations, based on the boundary conditions in Figure 3.9a, has been performed according to the following procedure:

- $\varphi = 20^\circ$  was assumed for the friction angle (as average value already reported in Table 1.3, Section 1.1) to fix the parameter  $\sin\alpha$ ;
- an initial set of failure parameters ( $K ; h$ ) was chosen and employed to simulate, numerically, failure in uniaxial ( $p_C = 0$ ) or TXc tests ( $p_C = 12$  MPa);
- for every uniaxial and TXc tests at failure, each simulation returned a criterion error,  $f \neq 0$ , on the computed value;
- according to the failure stress points ( $p_C ; \sigma_0(p_C)_{,\omega}$ ) in Table 3.4, a *Least Squares Method* procedure was executed, minimizing the sum of  $(f)^2$  by means of a numerical solver to estimate a unique set of parameters ( $K ; h$ ).

Adopting the numerical specimen model in Figure 3.9a and the parameters in Table 3.5, diagrams in Figure 3.10 of confined compression at  $p_C = 12$  MPa (TXc test) are obtained, with  $\omega = 0^\circ$  and  $90^\circ$ . These results, showing the vertical stress at failure, i.e.  $\sigma_{yy} = \sigma_0(p_C)_{,\omega}$ , confirm the variability reported in Table 3.4

**Table 3.4** : summary of  $\sigma_{0,\omega}$  and  $\sigma_0(p_C)_{,\omega}$  (e.g. Table 1.3, Chapter 1; [8], [9]; Andra database) employed for calibration of the anisotropic Drucker-Prager criterion.

	$\omega = 0^\circ \parallel$	$\omega = 90^\circ \perp$
$p_C = 0$	[25 ; 28]	[14; 17]
$p_C = 12$ MPa	[41; 46]	[35; 41]

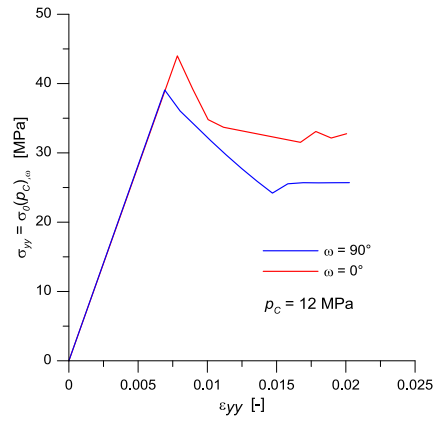


**Figure 3.10** : numerical results simulating a confined compression at  $p_C = 12$  MPa with the anisotropic Druger-Prager criterion, for loading perpendicular (blue line) and parallel (red line) to an horizontally-stratified material.

**Table 3.5** : parametrisation for stress-strain diagrams in Figure 3.10 and for the next numerical failure analysis around GCS drift.

Elasticity		Failure		Softening		Anisotropy	
$E$ [MPa]	$\nu$ [-]	$\varphi$ [°]	$\sigma_{0,0^\circ}$ [MPa]	$\beta$ [-]	$\eta_r$ [-]	$h$ [-]	$\omega$ [°]
6000	0.2	20	25.0	0.7	0.7	0.25	90

Table 3.6 reports the components of the initial stress state  $\sigma_{(0)}$  constituting initial and boundary conditions for the following excavation analysis. With respect to Table 3.1, the components of  $\sigma_{(0)}$  were modified for the following reasons:

- Referring to the scheme in Figure 3.7, a unique value for the components  $\sigma_{xx,(0)}$  and  $\sigma_{yy,(0)}$ , on the cross-section plane  $\Gamma$ , has been chosen. This value of  $-12.5$  MPa corresponds to the average between the correspondent ones in Table 3.1 and is intended to focus more on the anisotropy of the failure criterion as the determining cause for failure localization leading to the shape and extension in Figure 3.1.
- Compared to the in-situ, undisturbed value of  $-16.2$  MPa [113], an *axial effect* of the tunnel front, completely excavated, behind the drift section analysed, was considered. Hence, the value  $\sigma_{zz,(0)} = -8$  MPa was assumed, equal to the half of the correspondent component adopted in Table 3.1.

In order to simulate the entire failure zone in Figure 3.1, a wider numerical model was employed, adopting quadrilateral finite elements with one Gauss point for each element,  $n$ , and linear interpolating shape functions at the nodes,  $N$ . The numerical model with the imposed boundary conditions and excavation procedure (linear unloading at the circular drift's perimeter) are illustrated, respectively, in Figure 3.11a and b.

**Table 3.6:**  $\sigma_{(0)}$  components for the next numerical failure analysis around GCS drift.

$\sigma_{xx,(0)}$ [MPa]	$\sigma_{yy,(0)}$ [MPa]	$\sigma_{zz,(0)}$ [MPa]
-12.5	-12.5	-8.0

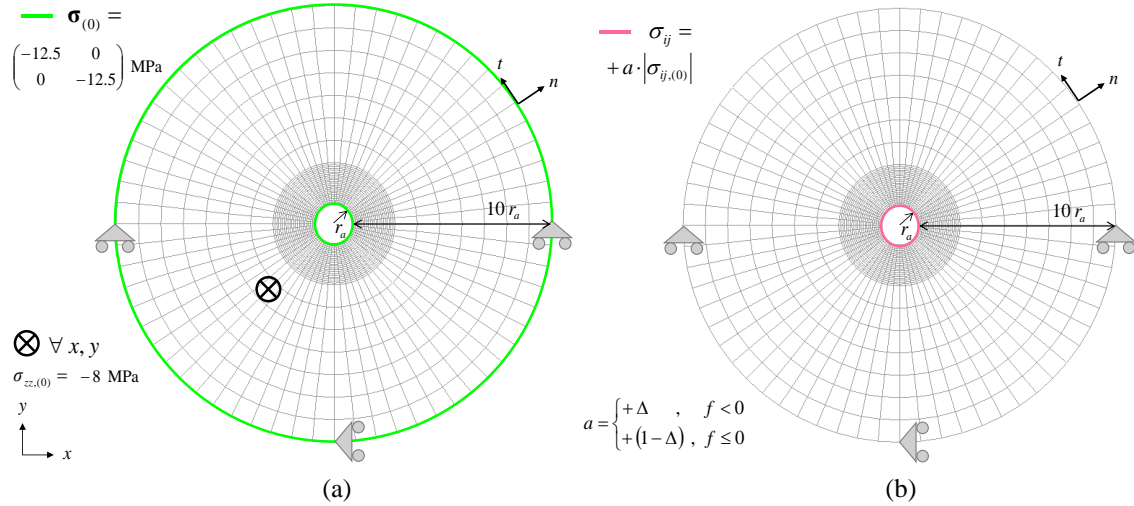


**Figure 3.11 :** initial/boundary conditions (a) and excavation procedure (b);  $r_a = 2.6$  m, corresponding to the theoretical radius designed before the excavation for the GCS drift section.

The calculated failure geometry in Figure 3.12 shows a coherent orientation: in particular, the horizontal extension equal to 3.2 m is in agreement with the 2d model in Figure 3.1 and similar to the average lateral extension of the area including a distinct system of homogeneous shear fractures (EdZ), as discussed in Section 1.1 (Table 1.1). In Figure 3.13, the deformed mesh, showing the results of horizontal and vertical displacements fields ( $U_x$  and  $U_y$ ), indicates that localization of failure (and its elongation) coincides with localizations of horizontal displacements.

After the presentation of numerical results for drift GCS, the same model and the relative parametrization has been tested to verify if in-situ evidences for perpendicular drifts, excavated along the major horizontal component  $\sigma_H$ . The instrumented drift GED, already discussed in the introduction, provides another set of useful failure observations: a contemporary reference to both drifts, in fact, allows a validation of modelling propositions according to a strong change in initial (i.e. undisturbed) conditions of whatever boundary value problem. In Figure 3.14, the 2d conceptual model for the excavation-induced failure around GED drift is reported [9] (an analogue 2d model was presented when describing failure evidences at the URL in Figure 1.9b (Section 1.1). Here, the theoretical radius for excavation corresponds to  $r_a = 2.3$  m. Numerical analyses are based on the same model and unloading procedure in Figure 3.11. Again, Table 3.5 contains the parameters for the  $2d_{ED}$  model with Drucker-Prager anisotropic criterion.

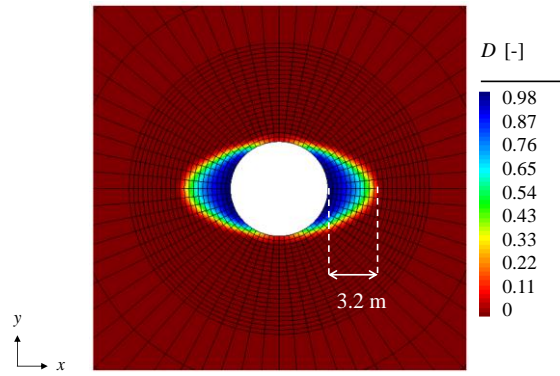


**Figure 3.12** : contour plot for the damage  $D$ , at the end of the excavation.

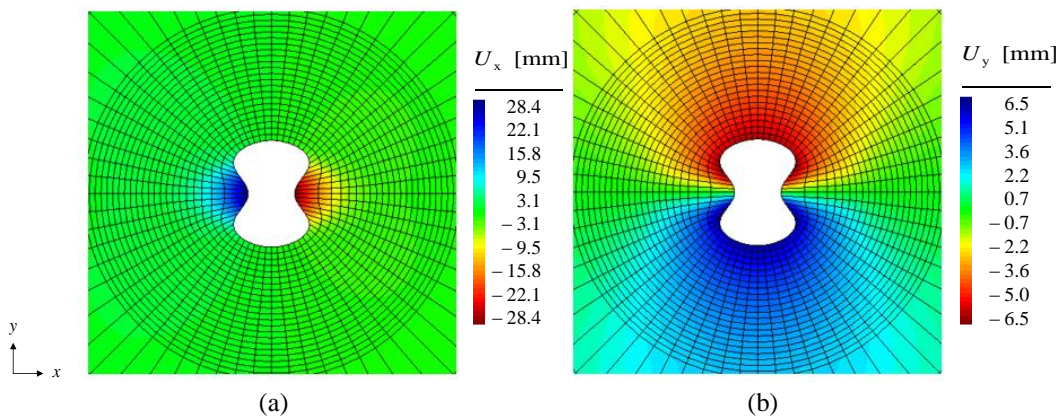


**Figure 3.13** : contour plots for horizontal ( $U_x$ ) displacement (a) and vertical ( $U_y$ ) displacements field (b).

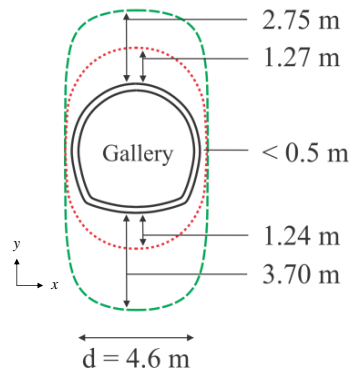


**Figure 3.14** : 2d conceptual model for GED drift [9], with a theoretical radius conceived before the excavation  $r_a = 2.3$  m.

Since the drift is excavated along the minor stress component  $\sigma_h$ , boundary conditions corresponding to the initial stress state  $\sigma_{(0)}$  (indicated in Figure 3.11a) have been modified according to the in-situ components at the Andra URL (Section 1.1) as follows:

- For this type of drift, horizontal and vertical principal stresses acting on the section  $\Gamma$  correspond, respectively, to the components  $\sigma_H$  and  $\sigma_v$  at the Andra URL, estimated equal to

16.2 and 12.7, in compression. In the the numerical model in Figure 3.11a,  $\sigma_{xx,(0)} = -16$  MPa and  $\sigma_{yy,(0)} = -13$  MPa were assumed as initial stresses on  $\Gamma$ .

- The axial stress  $\sigma_{zz}$  corresponds to the component  $\sigma_h = -12.4$  MPa at the main level of the URL. Under the same assumption for drift GCS (Figure 3.12 and Figure 3.13), which considers a reduction of the undisturbed value of the axial component due to the pre-excavation behind the section,  $\sigma_{zz,(0)}$  has been set equal to  $-6$  MPa.

At the end of the excavation, contours of the damage  $D$  for GED drift in Figure 3.15 do not reproduce the vertical orientation in Figure 3.14. Similarly to the numerical result in Figure 3.12, even in this case, failure is attained firstly on the horizontal around the drift perimeter and develops a damaged zone along this direction. To comment displacements' results in Figure 3.16, the same consideration on the short-term response at the drift's perimeter are accounted, as done for GCS drift in the previous section (referring to Figure 3.5). In Figure 3.17, total convergences on the horizontal and vertical directions are reported for GED drift (modified from [91]). It is underlined that horizontal and vertical convergences are defined, respectively, as  $2 \cdot U_x$  and  $2 \cdot U_y$ , being respectively the horizontal and vertical displacements, measured at the wall.

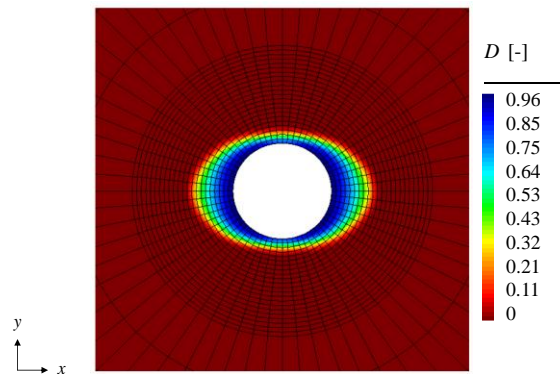


Figure 3.15 : contour plot for the damage  $D$ , at the end of the excavation.

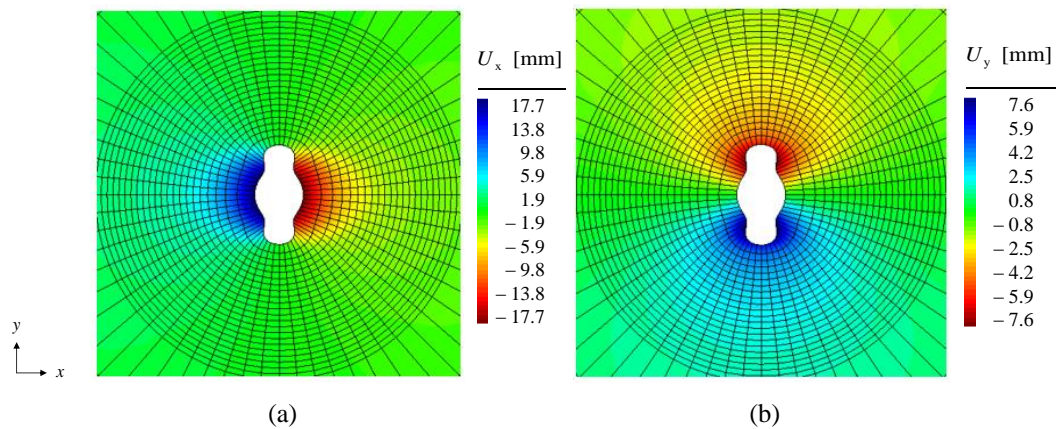
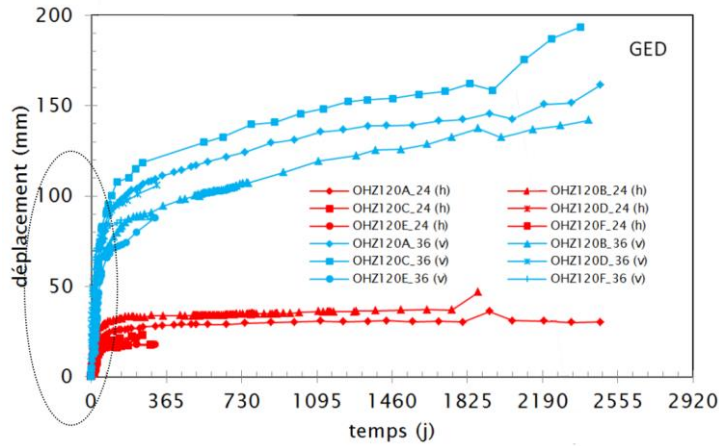


Figure 3.16 : contour plots for horizontal ( $U_x$ ) displacement (a) and vertical ( $U_y$ ) displacements field (b).



**Figure 3.17** : total horizontal (red line) and vertical convergences (blue line), measured at the GED drift's perimeter, with a focus on initial values likely to correspond to the excavation-induced response. Modified after [91].

In the following, Table 3.7 reports a summary of the maximal short-term values for horizontal and vertical displacements components at both drifts' perimeter, measured respectively on the horizontal and vertical direction, i.e.  $\theta = 0^\circ$  and  $90^\circ$  on the plane  $\Gamma$  (e.g. Figure 3.7). In-situ estimations are compared with calculated values above, for both simulations of drifts GCS and GED. Calculated values show a general inconsistency to simulate the displacements occurring at the drifts' perimeter. In particular, an overestimation of about 70% is observed for  $|U_x|$  in GED drift and a very important underestimation is observed, in general, for  $|U_y|$ . Only  $|U_x|$  calculated for GCS tunnel, along the horizontal, respects the variability according to in-situ estimations.

The discrepancy in displacements' calculation has been treated with the implementation of an anisotropic elastic-damage tensor, based on the  $2d_{ED}$  model presented in Section 2.3. This formulation, presented in the next section of the current chapter, is capable to improve displacements' simulation only for GCS drift, which constitutes a strong limitation to the model proposed. Concerning GED drift, the problem of the failure zone orientation must be treated at first. This discussion, regarding the conditions for failure localization and the mathematical modelling for the anisotropic failure criterion, constitutes the final section of this chapter.

**Table 3.7:** calculated maximal values of  $|U_x|$  and  $|U_y|$  around GCS and GED perimeters, on the horizontal and vertical direction, based on results in Figure 3.13 and in Figure 3.16. Comparison with in-situ surveys from extensometers.

	GCS drift		GED drift	
	$ U_x , \theta=0^\circ$ [mm]	$ U_y , \theta=90^\circ$ [mm]	$ U_x , \theta=0^\circ$ [mm]	$ U_y , \theta=90^\circ$ [mm]
in-situ measures	[20 ; 30]	[10 ; 15]	~ 10	~ 40
calculated at drifts' wall	28.4	5.4	17.7	5.2

### 3.3 Transverse-isotropic elasticity

Accounting for anisotropic elasticity in transverse isotropic materials would require, in general, the definition of 5 independent parameters. In Figure 3.18, the scheme of a stratified element volume for the Callovo-Oxfordian formation, oriented as the in-situ conditions and identified by the main Cartesian coordinates' system, is reported. According to this conceptual model, horizontal Young moduli, parallel to the stratification, are equal and both differ from the vertical Young modulus,  $E_y$ : vertical directions corresponds to the anisotropy axis. Data for COx claystone (e.g. [10], [118] and [119]) indicate lower stiffness along the anisotropy axis,  $y$  in Figure 3.18. Formally, according to the scheme, it is possible to write:  $E_x = E_z > E_y$ . The variability of  $E$  due to the implications of micro-structural anisotropy of COx formation was already discussed in Chapter 1, presenting the material (e.g. Section 1.1, Table 1.3). In Figure 3.18, the classical definition of cross-anisotropic elasticity would account also for the parallel and perpendicular Poisson's ratios, and a shear modulus,  $\mu$ , normal to the plane of isotropy. Nonetheless, it is possible to propose a model for anisotropic elasticity considering the particular in-situ stress state at the main level of Andra URL with respect to the coordinates' system in Figure 3.18, i.e. the main loading directions correspond to the axis describing the transverse isotropy in three dimensions.

According to the transverse isotropic properties defined above for the volume element in Figure 3.18, the compliance matrix  $\mathbf{C}^{-1}$  writes:

$$\mathbf{C}^{-1} = \begin{bmatrix} C_{xxxx}^{-1} & C_{xyxy}^{-1} & C_{xxzz}^{-1} & & & \\ C_{xyxy}^{-1} & C_{yyyy}^{-1} & C_{xyxy}^{-1} & & & \\ C_{xxzz}^{-1} & C_{xyxy}^{-1} & C_{xxzz}^{-1} & & & \\ & & & C_{xyxy}^{-1} & 0 & 0 \\ & & & 0 & 2 \cdot (C_{xxxx}^{-1} - C_{xxzz}^{-1}) & 0 \\ & & & 0 & 0 & C_{xyxy}^{-1} \end{bmatrix} \quad (3.10)$$

In case of 2d problem ( $\varepsilon_{xz} = \varepsilon_{yx} = 0$ ):

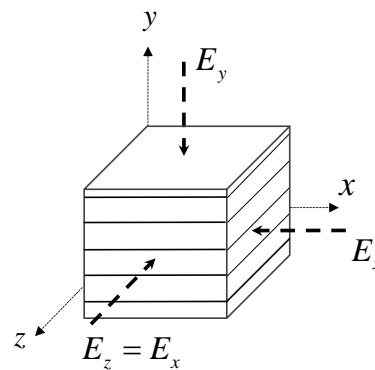


**Figure 3.18**: conceptual model of an horizontally stratified geological formation to formalize and implement the anisotropic elasticity.

$$\mathbf{C}^{-1} = \begin{bmatrix} C_{xxxx}^{-1} & C_{xxyy}^{-1} & C_{xxzz}^{-1} & 0 \\ C_{xxyy}^{-1} & C_{yyyy}^{-1} & C_{xyxy}^{-1} & 0 \\ C_{xxzz}^{-1} & C_{xxyy}^{-1} & C_{xxxx}^{-1} & 0 \\ 0 & 0 & 0 & C_{yyxy}^{-1} \end{bmatrix} \quad (3.11)$$

Eq. 3.10 and 3.11 include the 5 independent parameters of transverse isotropic elasticity, as mentioned before. At this point, the volume element in Figure 3.18 can be considered as a medium where the horizontal stratification corresponds to a series of parallel discontinuities within the matrix, with a thickness  $e_0$  negligible with respect to their distance  $d$ , i.e.  $e_0/d \rightarrow 0$ . The definition of the stiffness tensor  $\mathbf{C}$ , for this type of medium, corresponds to the formulation of an equivalent continuum mechanical elastic tensor, with homogenised stiffness parameters, according to the proposition of Pouya et al. [75] (2013). In Figure 3.18, thanks to the property  $e_0/d \rightarrow 0$ , whatever deformation along the direction  $j$  due to a compression along  $i$ , (i.e. a deformation tensor component  $\varepsilon_{ij}$ ), leads to the same evaluation for the Poisson's ratio. Formally, it is possible to reduce the initial 5 independent variables in Eq. 3.10 and 3.11, writing:

$$C_{xxyy}^{-1} = C_{xxzz}^{-1} \quad (3.12)$$

Even if characterized by a negligible thickness  $e_0$ , parallel discontinuities providing the transverse anisotropy to the medium own a normal and shear stiffness modulus, respectively  $K_m$  and  $K_t$ . After the reduction expressed in Eq. 3.12, the 4 independent parameters to define the elastic anisotropy, according to a simple homogenisation theory, write [75]:

$$C_{xxxx}^{-1} = \frac{1}{E_x} \quad (3.13)$$

$$C_{yyyy}^{-1} = \frac{1}{E_y} = \frac{1}{E_x} + \frac{1}{d \cdot K_{nn}} \quad (3.14)$$

$$C_{xxyy}^{-1} = -\frac{\nu}{E_x} \quad (3.15)$$

$$C_{xyxy}^{-1} = \frac{1}{\mu} + \frac{1}{d \cdot K_{tt}} \quad (3.16)$$

Among these equations, only Eq. 3.14 and 3.16 correspond to *homogenised* stiffness parameters, including both stiffness characteristics of the medium *matrix* and included *discontinuities*. The couple of parameters Young and shear modulus,  $E$  and  $\mu$ , is indicated, respectively,  $E_{HOM}$ ;  $\mu_{HOM}$  and  $E_{MAT}$ ;  $\mu_{MAT}$ , when referred to the homogenised medium or the matrix only. Eq. 3.13-3.16 can be rewritten as follows, also as function of the distance  $d$  between discontinuities:

$$\frac{1}{E_x} = \frac{1}{E_{MAT}} = \frac{1}{E} \quad (3.17)$$

$$\frac{1}{E_y} = \frac{1}{E_{HOM}} = \frac{1}{E} + \frac{1}{dK_{nn}} \quad (3.18)$$

$$-\frac{\nu}{E_x} = -\frac{\nu}{E} \quad (3.19)$$

$$\frac{1}{\mu_{MAT}} + \frac{1}{d \cdot K_{tt}} = \frac{1}{\mu_{HOM}} = \frac{1}{\mu} + \frac{1}{dK_{tt}} \quad (3.20)$$

Introducing the ratio  $\kappa = K_{tt} / K_{mm}$ , the shear modulus  $\mu$  can be expressed as function of  $E$  and  $\nu$  according to the classical elastic formulation,  $K_{mm}$  can be explicitly indicated in Eq. 3.18 and Eq. 3.20 can be rewritten. The following equations summarize the procedure:

$$\text{- From Eq. 3.17 and 3.18:} \quad dK_{nn} = \frac{E_x E_y}{E_x - E_y} \quad (3.21)$$

$$\text{- From Eq. 3.20 and 3.21:} \quad \frac{1}{\mu} + \frac{1}{dK_{tt}} = \frac{2(1+\nu)}{E_x} + \frac{1}{\kappa dK_{nn}} \quad (3.22)$$

$$\text{- From Eq. 3.20, 3.21 and 3.22:} \quad \frac{[2\kappa(1+\nu)-1]E_y + E_x}{\kappa E_x E_y} = \frac{1}{\mu_{HOM}} \quad (3.23)$$

Based on the formulation in Eq. 3.11, the compliance elastic matrix for the anisotropic volume element, oriented according to the conceptual scheme in Figure 3.18, writes:

$$\mathbf{C}^{-1} = \begin{bmatrix} \frac{1}{E_x} & -\frac{\nu}{E_x} & -\frac{\nu}{E_x} & 0 \\ -\frac{\nu}{E_x} & \frac{1}{E_y} & -\frac{\nu}{E_x} & 0 \\ -\frac{\nu}{E_x} & -\frac{\nu}{E_x} & \frac{1}{E_x} & 0 \\ 0 & 0 & 0 & \frac{[2\kappa(1+\nu)-1]E_y + E_x}{\kappa E_x E_y} \end{bmatrix} \quad (3.24)$$

The compliance matrix in Eq. 3.24 defines entirely the anisotropic elasticity to be modelled, with 4 independent parameters, but it does not include the damage internal variable constituting the dissipation mechanism for the failure around drifts. In fact, adopting the series of equations presented in this section, the integration of this specific elastic anisotropy must be included in the original  $2d\_ED$  damage-based mechanical model already presented. Adopting the compliance formulation with isotropic elasticity presented in the previous chapter (Section 2.3, Eq. 2.40), the final matrix relating  $\boldsymbol{\varepsilon}$  to  $\boldsymbol{\sigma}$ , in the  $2d\_ED$  model accounting for elastic anisotropy, writes:

$$\mathbf{C}^{-1} = \begin{bmatrix} \frac{1}{(1-D)E_x} & -\frac{\nu}{(1-D)E_x} & -\frac{\nu}{E_x} & 0 \\ -\frac{\nu}{(1-D)E_x} & \frac{1}{(1-D)E_y} & -\frac{\nu}{E_x} & 0 \\ -\frac{\nu}{E_x} & -\frac{\nu}{E_x} & \frac{1}{E_x} & 0 \\ 0 & 0 & 0 & \frac{[2\kappa(1+\nu)-1]E_y + E_x}{\kappa(1-D)E_x E_y} \end{bmatrix} \quad (3.25)$$

$\tilde{\mathbf{C}}$  indicates a modification to an original elastic-damage tensor considering damage evolution also along the axial direction  $z$ . The inversion of the tensor in Eq. 3.25 provides the final stiffness matrix  $\tilde{\mathbf{C}}$ . As done for the stiffness tensor defining the isotropic  $2d\_ED$  model, each component  $\tilde{C}_{ij}$  has been implemented in a FORTRAN subroutine, structured according to the illustration in Appendix A, Figure A.1. The explicit expression of  $\tilde{\mathbf{C}}$  obtained by numerical inversion of Eq. 3.25 is detailed in Appendix B.4.

This transverse-isotropic formulation for the  $2d\_ED$  elastic-damage tensor was tested on the numerical model of drift GCS drift. The same values of parameters reported in Table 3.5 were adopted, with the exception of those describing the anisotropic elasticity presented before. According to published data for COx (e.g. [37], [118]) and numerical modelling describing elastic anisotropy (e.g. [42], [43]), a ratio of 1.4 was chosen for the parallel to perpendicular values of Young modulus, assuming as average value  $E = 6000$  MPa for isotropic (undrained) elasticity in Section 3.2. Poisson's ratio did not vary than  $\nu = 0.2$  in Table 3.5. Based on this value, an isotropic shear modulus  $\mu = 2500$  MPa is obtained, resulting in a ratio  $\mu/E = 0.4$ . This value was assumed for the ratio  $\kappa$  among shear and normal stiffness of horizontal inclusions (i.e. discontinuities) in the volume element Figure 3.18. Parameters of transverse-isotropic elasticity are reported in Table 3.8. Concerning stress initial conditions, FEM domain discretisation and excavation procedure, this analysis refers to Table 3.6, Figure 3.11a and b.

With respect to the horizontal extension of the failure zone, representing the system EDZ-EdZ in Figure 3.12, contour plot of  $D$ , in Figure 3.19, show a slight reduction, possibly due by the increased stiffness in the horizontal direction.

**Table 3.8:** elastic parameters accounting for transverse isotropy, adopted in the next numerical analysis.

$E_x$ [MPa]	$E_y$ [MPa]	$\kappa = K_{tt} / K_{nn}$
7000	5000	0.4

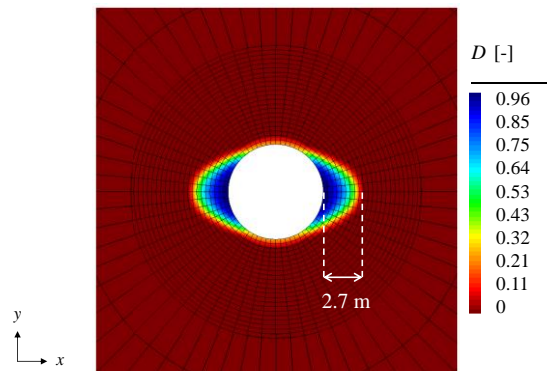


**Figure 3.19 :** contour plot for the damage  $D$ , at the end of the excavation; a shorter failure extension is observed compared to Figure 3.12.

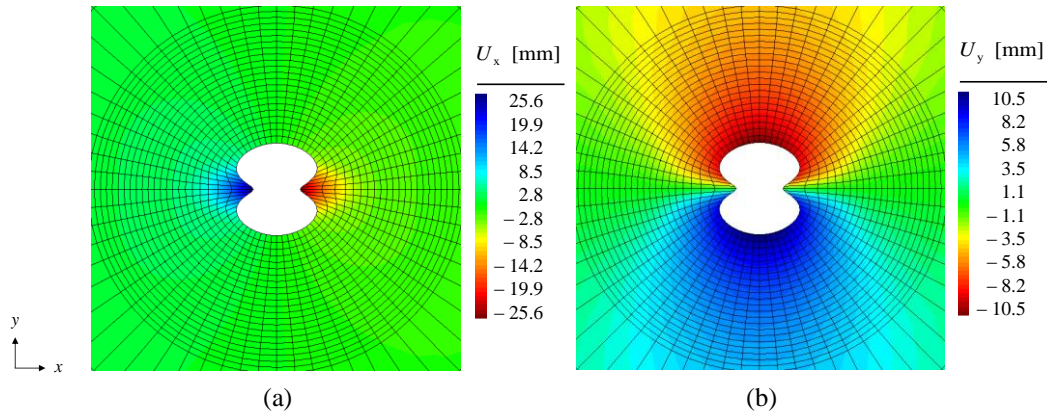


**Figure 3.20** : contour plots for horizontal ( $U_x$ ) displacement (a) and vertical ( $U_y$ ) displacements field (b).

**Table 3.9** : calculated maximal values of  $|U_x|$  and  $|U_y|$  around GCS perimeters, compared with in-situ surveys from extensometers.

	$ U_x , \theta=0^\circ$ [mm]	$ U_y , \theta=90^\circ$ [mm]
in-situ measures	[20 ; 30]	[10 ; 15]
calculated at drifts' wall	25.6	10.5

Concerning displacements results illustrated in Figure 3.20, calculated values are consistent with admissible intervals from extensometers around the perimeter of GCS drift. Maximal values calculated on the horizontal and vertical directions are reported in Table 3.9 and confirm the horizontal to vertical displacement ratio,  $|U_x|/|U_y|$ , indicated as the average value of 2 (e.g. [41], [42]). As mentioned at the end of Section 2.2, anisotropic elasticity implemented in the  $2d\_ED$  model improves displacements' estimations for GCS even if, at the same time, reduces the extension of the calculated failure zone, identified as the system EDZ-EdZ. Nonetheless, it cannot be applied to improve results for GED drift, because, in this case (Figure 3.15 and Figure 3.16), damage localises firstly on the horizontal, in contrast with in-situ evidences. Accounting for anisotropic elasticity would not resolve this problem; on the other hand, a revision of the failure criterion seems to be a more efficient solution to follow. This aspect constitutes the last discussion for failure modelling around drifts in this chapter.

### 3.4 Non-monotonic failure anisotropy in two dimensions

The orientation of failure zone is strongly dependent on the initial damage localisation, i.e. the area around the drift perimeter where failure conditions are firstly attained. From the numerical point of view, in the context of FEM analyses, this area corresponds to the finite element(s) where failure criterion  $f$ , calculated at Gauss points, firstly satisfies the condition  $f = 0$ . Coupled anisotropic conditions derived from in-situ stress and the material constitutive model lead to

different failure localisations around the gallery during the unloading path that simulates the excavation process. Even if the implementation of anisotropic elasticity may solve the problem related to the convergence/displacements calculations for the GCS drift, in this case, the imposed anisotropy for the failure criterion is the main responsible for the damage localisation on the horizontal. With the same failure criterion conditions, a stronger anisotropy of the initial stress state is not capable to induce a vertical-oriented damage zone for the drift GED (Figure 3.15). According to results obtained for both boundary value problems, in the latter case, only a change of the monotonic failure criterion previously defined would induce, possibly, a damage initiation developing along the vertical direction. For the stratified material (which constitutive modelling must be common to both drifts), the conditions for their boundary value problems on the cross section (plane  $\Gamma$ ), together with the expected failure zone (i.e. EDZ-EdZ), are reported in Figure 3.21. Based on this conceptual scheme, in the following it is reported a simple analysis of failure localisation at the perimeter ( $r = r_a$ ) according to numerical values of in-situ stress components (e.g.  $\sigma_v$ ,  $\sigma_h$ , and  $\sigma_H$  at the main level of Andra URL). Considering firstly GCS drift, for a complete excavation without any internal support, a horizontal failure localization implies:

$$\sigma_{\theta\theta}(A) - \sigma_{0,90^\circ} > \sigma_{\theta\theta}(B) - \sigma_{0,0^\circ} \quad (3.26a)$$

$$3\sigma_v - \sigma_h - \sigma_{0,90^\circ} > 3\sigma_h - \sigma_v - \sigma_{0,0^\circ} \quad (3.26b)$$

$$\sigma_v - \sigma_h > \frac{(\sigma_{0,90^\circ} - \sigma_{0,0^\circ})}{4} \quad (3.26c)$$

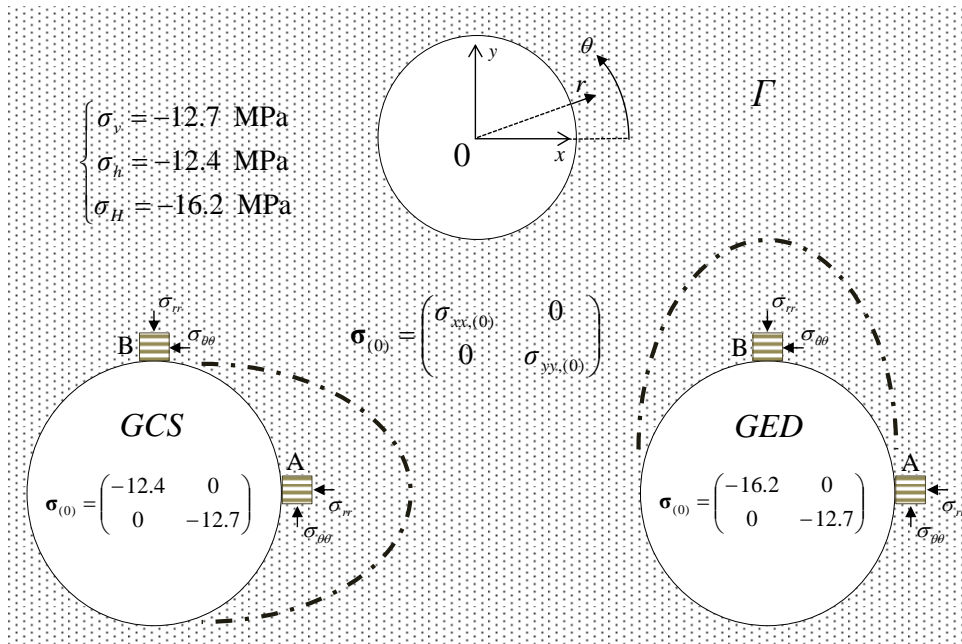


**Figure 3.21** : conceptual 2d scheme for failure localisation of drifts GCS and GED, with the relative stress boundary conditions. The global (Cartesian) and local (polar) coordinates systems are also reported.

According to boundary conditions for stress components  $\sigma_v$ ,  $\sigma_h$  in Figure 3.21, the conditions expressed in Eq. 3.26c is always satisfied: as indicated also in Section 3.2, data on material anisotropy satisfy the condition  $\sigma_{0,0^\circ} > \sigma_{0,90^\circ}$ . An analogue discussion can be made for GED drift:

$$\sigma_{\theta\theta}(\text{A}) - \sigma_{0,90^\circ} < \sigma_{\theta\theta}(\text{B}) - \sigma_{0,0^\circ} \quad (3.27a)$$

$$3\sigma_v - \sigma_H - \sigma_{0,90^\circ} < 3\sigma_H - \sigma_v - \sigma_{0,0^\circ} \quad (3.27b)$$

$$\sigma_H - \sigma_v > \frac{(\sigma_{0,0^\circ} - \sigma_{0,90^\circ})}{4} \quad (3.27c)$$

In these case, the condition expressed in Eq. 3.27c is satisfied only based on the difference between  $\sigma_{0,0^\circ}$  and  $\sigma_{0,90^\circ}$ . Following the approach based on the former analytical scheme, in the forthcoming simulations the failure criterion does not account the axial stress component  $\sigma_{zz}$ , even if it continues to exist as boundary value and stress variable in the numerical problem. It is possible to write a new anisotropic failure criterion based on the 2d conceptual model for a stratified material in Figure 3.22. Here, the unitary vector  $\mathbf{n}$  normal to bedding substitutes the expression in Eq. 3.1a (Section 3.1). Redefining  $\mathbf{n}$ , the anisotropic rotation tensor  $\mathbf{M}$ , previously expressed according to Eq. 3.1b, can be written as reported in the following Eq. 3.28 for a 2d stress tensor.

$$\mathbf{M} = \begin{bmatrix} 1 + h \cos^2 \omega & h \sin \omega \cos \omega \\ h \sin \omega \cos \omega & 1 + h \sin^2 \omega \end{bmatrix} \quad (3.28)$$

Applying Eq. 3.2 to modify the original stress tensor, eventually, it is possible to write, in two dimensions:

$$\begin{aligned} \tilde{\boldsymbol{\sigma}} &= \begin{bmatrix} \tilde{\sigma}_{xx} & \tilde{\sigma}_{xy} \\ \tilde{\sigma}_{xy} & \tilde{\sigma}_{yy} \end{bmatrix} = \\ &= \begin{bmatrix} 1 + h \cos^2 \omega & h \sin \omega \cos \omega \\ h \sin \omega \cos \omega & 1 + h \sin^2 \omega \end{bmatrix} \cdot \begin{bmatrix} \sigma_{xx} & \sigma_{xy} \\ \sigma_{xy} & \sigma_{yy} \end{bmatrix} \cdot \begin{bmatrix} 1 + h \cos^2 \omega & h \sin \omega \cos \omega \\ h \sin \omega \cos \omega & 1 + h \sin^2 \omega \end{bmatrix} \end{aligned} \quad (3.29)$$

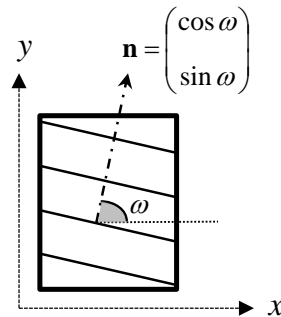


**Figure 3.22** : conceptual model for the implementation of the anisotropic 2d failure criterion in Eq. 3.30.

Adopting the modified stress tensor previously defined, the following *Mohr-Coulomb type* criterion can be defined:

$$f(\tilde{\boldsymbol{\sigma}}, D) = \sqrt{(\tilde{\sigma}_{xx} - \tilde{\sigma}_{yy})^2 + 4\tilde{\sigma}_{xy}^2} + \sin \varphi (\tilde{\sigma}_{xx} + \tilde{\sigma}_{yy}) - g(D)K \quad (3.30)$$

In Eq. 3.30, the friction angle  $\varphi$  and  $K$  appears explicitly as failure parameters, while the anisotropy scaling coefficient  $h$  is implicitly present in the modified stress component  $\tilde{\sigma}_{ij}$ .  $K$ , depending on  $\varphi$ , as well as on the cohesion  $C$ , can be written as function of the *UCS*, in case of unconfined compression along  $y$  and parallel to the material bedding ( $\omega = 0^\circ$ , e.g. Eq. 3.8):

$$K = \sigma_{0,0^\circ} \cdot (1 - \sin \varphi) \quad (3.31)$$

From the mathematical point of view, the failure function  $f$  in Eq. 3.30 was analyzed to verify its employment in the simulation of a non-monotonic criterion, as function of the inclination of material stratification. In particular, it was possible to define analytically the explicit expressions for compressions strengths, in case of uniaxial or confined loadings, respectively  $\sigma_{xx} = 0$ ;  $\sigma_{yy} \neq 0$  and  $|\sigma_{xx}| = p_C$ ;  $\sigma_{yy} \neq 0$ . For the first case, the modified stress tensor  $\tilde{\boldsymbol{\sigma}}$  in Eq. 3.29 writes:

$$\tilde{\boldsymbol{\sigma}} = \begin{bmatrix} h^2 \sin^2 \omega \cos^2 \omega \cdot \sigma_{yy} & h \sin \omega \cos \omega (1 + h \sin^2 \omega) \cdot \sigma_{yy} \\ h \sin \omega \cos \omega (1 + h \sin^2 \omega) \cdot \sigma_{yy} & (1 + h \sin^2 \omega)^2 \sigma_{yy} \end{bmatrix} \quad (3.32)$$

Adopting the matrix in Eq. 3.32 to rewrite the anisotropic  $f$  in Eq. 3.30, the analytical formulation for *UCS*, as function of the stratification angle  $\omega$ , is eventually expressed as follows:

$$\sigma_{0,\omega} = \frac{K}{C_{\text{dev}} - C_{\text{sph}}} \quad (3.33)$$

Eq. 3.33 is also defined through coefficients  $C_{\text{dev}}$  and  $C_{\text{sph}}$ : they are respectively denoted *deviatoric* and *spherical* because related to the deviatoric and hydrostatic part of Eq. 3.30. Their complete expressions are reported in the Appendix B.2. In case of axial loading along  $y$  with a confinement  $p_C$  along  $x$  (according to the scheme in Figure 3.22), the confined material strength as function of  $\omega$ ,  $\sigma_0(p_C, \omega)$ , is analytically found as the positive solution of a second order polynomial function, which complete formulation is again described in the Appendix B.2. Linear and radar graphics of  $\sigma_{0,\omega}$  and  $\sigma_0(p_C, \omega)$  as function of  $\omega$  are reported, respectively, in Figure 3.23a and b. For the confined compressive strength, a value of  $p_C = 12$  MPa was assumed. The functions show a periodicity of the strength values in  $\omega = [0; 180^\circ]$  and, focusing on Figure 3.23b, it is possible to state that the II order tensor  $\mathbf{M}$  in Eq. 3.28 define an *elliptical* anisotropy for  $f$  in Eq. 3.30. These functions' periodicity allows to consider a non-monotonic behaviour at failure, limiting  $\omega$  in the physical interval between 0 and  $90^\circ$ , as evidenced in Figure 3.24 for uniaxial compression already shown in Figure 3.23. Hence,  $\omega$  corresponds to the inclination of minimal resistance.

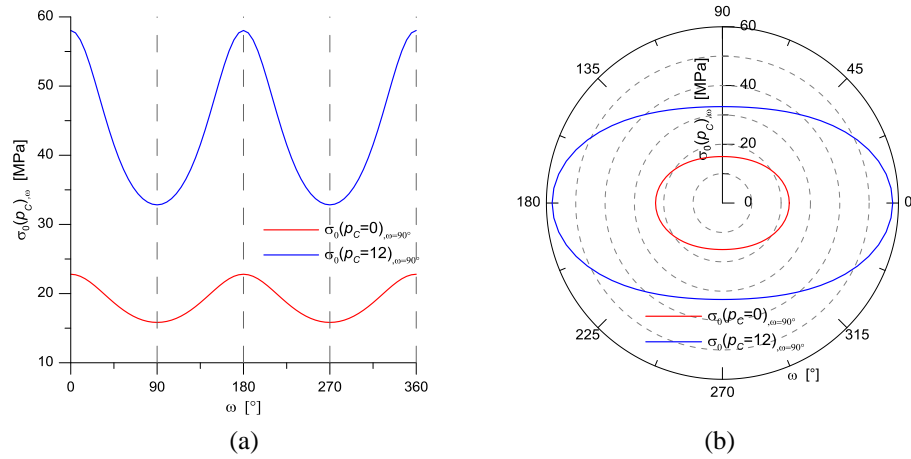


**Figure 3.23 :** plots of  $\sigma_{\theta,\omega}$  (red) and  $\sigma_{\theta}(\rho_C)_{,\omega}$  confined at 12 MPa (blue), for  $\varphi = 20^\circ$ ,  $K = 15$  MPa,  $h = 0.2$ . In (a), linear plot for  $[0; 360^\circ]$  showing the functions' periodicity on  $[0; 180^\circ]$ . In (b), radar plot representation.

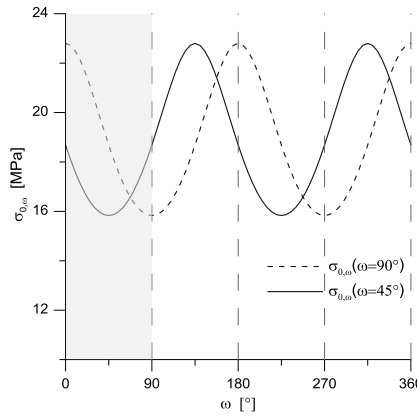


**Figure 3.24 :**  $\sigma_{0,\omega}$  for  $\varphi = 20^\circ$ ,  $K = 15$  MPa,  $h = 0.2$ . Dotted line represents a monotonic variation between  $0^\circ$  and  $90^\circ$ , while the continuous line shows a resistance with its minimum for a loading inclined at  $45^\circ$ .

New available data for failure of COx specimens, sampled with different orientations and derived from TXc tests confined at 12 MPa [91], showed indeed that a different interpolating function for the criterion may better reproduce the material anisotropic response, with a minimum between 0 and  $90^\circ$ . Table 3.10 reports the over mentioned data in terms of deviator  $q$  at failure.

**Table 3.10 :** data for  $\sigma_{\theta}(\rho_C)_{,\omega}$  with  $\rho_C = 12$  MPa [91], on specimens sampled with different inclinations and approximately the same initial water content.

$\omega$ [°]	$q$ at $\rho_C = 12$ MPa [MPa]
0	45.9
0	40.9
12	38.4
45	27.0
50	41.0
75	39.6
77	35.3

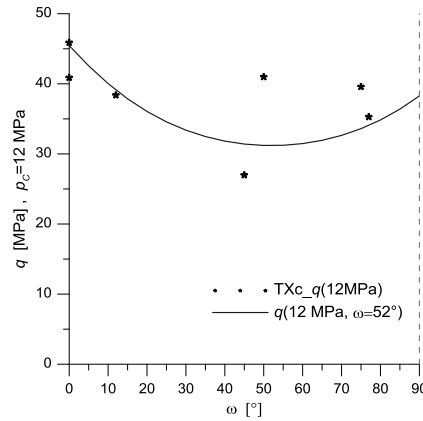


**Figure 3.25** : non-monotonic calibration strength in specimen confined at 12 MPa [91];  $q$  reported as function of  $\omega$ . Data interpretation with minimum of  $\sigma_0(p_c)$  at  $\omega = 52^\circ$ .

An interpretation of data in Table 3.10 for a non-monotonic variation of the material failure are reported in Figure 3.25, where the minimum of the shear strength is set at  $\omega = 52^\circ$ . At the same time,  $\sigma_{0,0^\circ} > \sigma_{0,90^\circ}$ . This failure criterion configuration has been tested on the geometry in Figure 3.11, for both drifts GCS and GED, respectively with  $r_a = 2.6$  and 2.3 m. Parametrization of the  $2d\_ED$  model corresponds to the same values reported both in Table 3.2 and Table 3.5, regarding the parts *Elasticity* ( $E$  and  $\nu$ ) and *Softening* ( $\beta$  and  $\eta_r$ ). It is remembered that, in these analyses, the model accounts for isotropic elasticity. According to the model calibration based on deviator  $q$ , at failure, in Figure 3.25, Table 3.11 contains the criterion parameters and correspondent *UCS* values in case of: compression parallel to the bedding ( $\omega = 0^\circ$ ), along the direction of minimal resistance ( $\omega = 52^\circ$ ) and perpendicular to the bedding ( $\omega = 90^\circ$ ). Boundary and initial conditions, applied on the domain in Figure 3.11, are described as follows:

- Stress components acting on the drifts' cross section were imposed according to the conditions reported for the plane  $\Gamma$ , in Figure 3.21.
- Axial stress,  $\sigma_{zz}$ , is neglected in the calculation of failure openings during drifts' unloading at the internal perimeter (e.g. Eq. 3.28 and 3.30). For this reason, in these numerical analyses, no hypothesis were made on the initial value  $\sigma_{zz,(0)}$ . It assumes automatic value calculated by *POROFIS* and derived for the plane strain condition:

$$\varepsilon_{zz} = 0 \rightarrow \sigma_{zz,(0)} = \nu(\sigma_{xx,(0)} + \sigma_{yy,(0)}) \quad (3.34)$$

To summarize, the imposed stress components are listed in Table 3.12. Numerical excavation procedure is the same applied before, based on Figure 3.11b, already described in Section 2.1. Results for both GCS and GED drifts are illustrated in the following: shape and extension of the internal variable  $D$  is reported, respectively, in Figure 3.26 and Figure 3.28, while the contour plots for horizontal and vertical displacement fields are reported in Figure 3.27 and Figure 3.29.

**Table 3.11** : model parameters for the anisotropic failure criterion in Eq. 3.30, calibrated in Figure 3.25.

$\omega$ [°]	$h$ [-]	$\sigma_{0,0^\circ}$ [MPa]	$\sigma_{0,\omega^\circ}$ [MPa]	$\sigma_{0,90^\circ}$ [MPa]
52	0.25	21.0	16.0	18.4

**Table 3.12** : numerical values for components  $\sigma_{xx,(0)}$ ,  $\sigma_{yy,(0)}$  as reported in Figure 3.21. Values for  $\sigma_{zz,(0)}$  are calculated according to Eq. 3.31, with  $\nu = 0.2$  (e.g. Table 3.2).

$\sigma_{xx,(0)}$ [MPa]	$\sigma_{yy,(0)}$ [MPa]	$\sigma_{zz,(0)}$ [MPa]
-12.4	-12.7	-5.02
-16.2	-12.7	-5.78

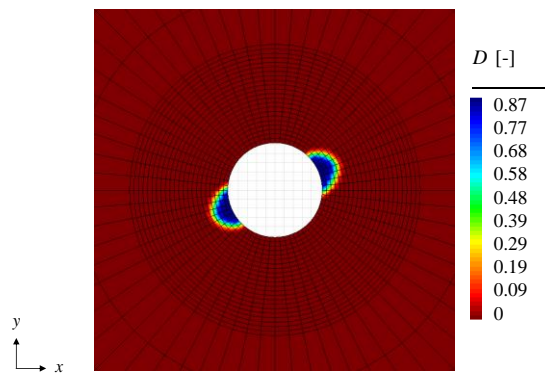


**Figure 3.26** : contour plot for the damage  $D$ , GCS drift.

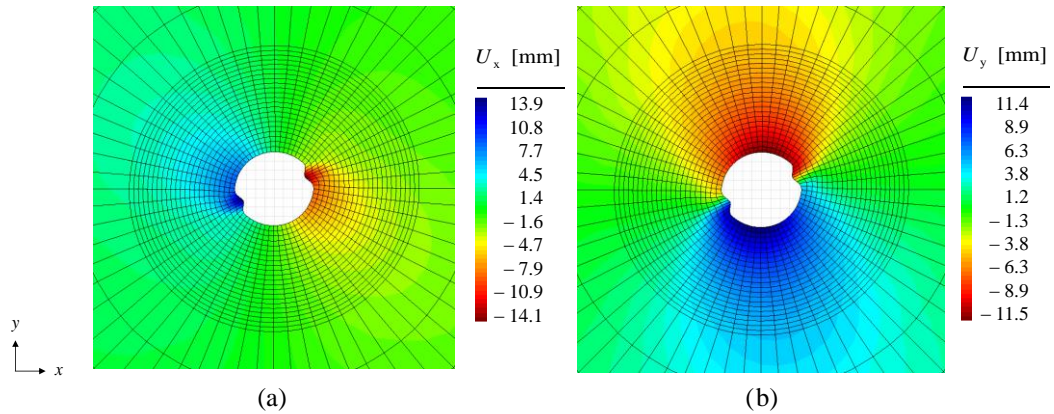


**Figure 3.27** : contour plots for horizontal ( $U_x$ ) displacement (a) and vertical ( $U_y$ ) displacements field (b), GCS drift.

An inclined failure localization, with respect to the horizontal, is shown in Figure 3.26. Nonetheless, even if damage is firstly attained and localises around a polar coordinate  $0 < \theta < 90^\circ$  (e.g. Figure 3.21), it should be expected to develop towards the horizontal (or the vertical), according to initial boundary conditions, i.e.  $\sigma_{(0)}$ , during the unloading process, reproducing the in-situ observation at the URL. Moreover, considering the symmetry of the problem geometry

and the horizontal stratification of the material in every point of the domain, failure does not develop symmetrically. With a direct reference to Figure 3.26, since material anisotropy must be overall homogeneous, the inclined damage lobes shown should have, for symmetry, a specular development with respect to axis  $x$ . For the calculated displacements, the horizontal component  $U_x$  (Figure 3.27a) results underestimated, with respect to measurements at the drift's perimeter (e.g. Table 3.7). Results reported in Figure 3.28 and Figure 3.29 for drift GED confirm, in general, the same modelling defects previously described. An absence of complete symmetry for the damage development around the excavation is revealed in Figure 3.28 and displacements' underestimation occurs in correspondence of failure localisation.

At the current state of numerical analyses, improvements of 2d modelling for *continuous* failure (e.g. Chapter 1, Section 1.1) were required, to overcome the following problems:

- The absence of symmetry around the circular opening when failure conditions are (locally) attained.
- The direction (orientation) of damage expansion, evolving towards the horizontal or vertical direction as function of the initial and boundary stress, improving, possibly, the estimation of displacements in correspondence of failure.

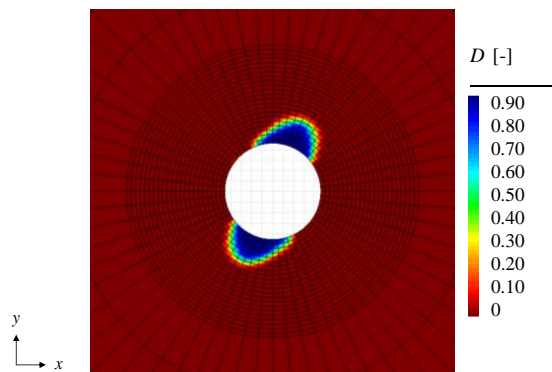


Figure 3.28 : contour plot for the damage  $D$ , GED drift.

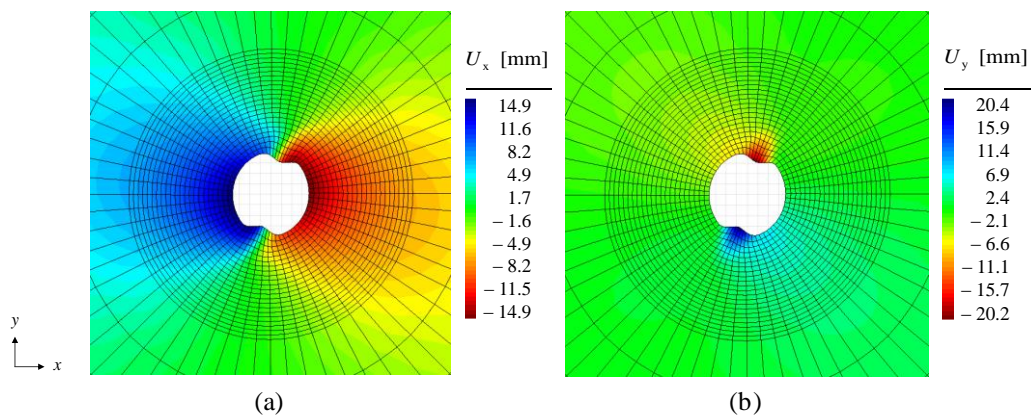


Figure 3.29 : contour plots for horizontal ( $U_x$ ) displacement (a) and vertical ( $U_y$ ) displacements field (b), GED drift.

## Conclusion

With respect to the framework provided in Chapter 2, to justify the interest of a damage-based modelling approach, this chapter was dedicated to the 2d modelling of failure localizations and damage evolution for drifts at the Andra URL. Two drifts excavated along the horizontal principal stress direction were considered, to test the proposed modelling exercises with different boundary and initial conditions. The formation of the failure zone generated by the excavation, for one of the main horizontal directions, was discussed, with a model providing a consistent estimation of displacements at the wall. The effect of the imposed axial stress in numerical simulation has been also considered.

A first proposition to account the anisotropic response at failure, exhibited by the Callovo-Oxfordian formation at the laboratory scale, was formulated. Considering the horizontal stratification of the material, a monotonic variation of the compressive strength was proposed and its effects on damage and displacements calculations shown. Meanwhile, anisotropic elasticity, based on the homogenised model in Section 3.3, was introduced, showing its capacity to improve the calculation of perimeter's displacements for a drift along  $\sigma_H$  at the URL. Nonetheless, the failure attainment and orientation for a drift along  $\sigma_h$  still remained an unsolved issue.

In the last section, a revision of failure localisation conditions was discussed, adopting a simplified approach which neglects the contribution of  $\sigma_{zz}$  in the criterion's function. At the same time, laboratory data from compression tests showed the possibility to consider a non-monotonic variation of material's resistance. These data were used to calibrate a failure model accounting for this non-monotonic variation. Final numerical tests were performed based on in-situ stresses of both drifts' direction. They show the impossibility, for the current modelling, to reproduce correctly the observations, in particular concerning symmetry and orientation of failure.

In the overall manuscript's structure, this chapter was intended to provide indications on possible modelling difficulties considering anisotropic characteristics of the material. Modelling exercises presented here provide useful indications and constitute the transition to the final damage-based constitutive framework presented in Chapter 4 for the first axis of this research.



## **Chapter 4**

# **Shear Damage-Based Modelling on Drifts Section**



The final numerical analyses for the 2d plane strain damage evolution around drifts at the Andra URL are discussed hereby. Chapter 4 concludes, in fact, the first axis of research, constituting the major part of this thesis' works. In the first section, the proposition for a new elastic-damage stress-strain law, based on some principles already considered for the formalization of the *2d\_ED* model, is presented. In particular, damage evolution along the axial coordinate  $z$  is still neglected. The new elastic-damage law is further tested and considerations on the influence of a fragile or ductile softening post-peak behaviour are provided.

The second section is dedicated to a series of excavation analyses for the experimental drift considered (Trivellato et al., 2018 [102]), where the proposed elastic-damage stiffness matrix is employed in presence of a very fragile softening material with monotonic anisotropic failure, according to the II order modelling formalized in Chapter 3, Section 3.2.

To overcome the antisymmetric failure localizations, discussed through numerical examples at the end of the previous chapter, the third section describes the synthesis of a second *anisotropic rotation tensor* providing a failure criterion capable to resolve the problem encountered. A calibration, based on more recent triaxial compression data, is further operated to set the failure parameters adopted in the last analyses. Afterwards, Section 4.4 described a proposition of numerical treatment of the increasing ductile behaviour of Callovo-Oxfordian claystone, in its post-peak phase under confined compression.

The conclusive Section 4.5 reports and describes numerical results of the analyses performed, where a reduced geometry, including one fourth of the circular symmetric domain represented before. A mesh refinement is applied to the discretization of the numerical model, corresponding to the area, surrounding the drifts' perimeter, potentially subjected to damage-based failure.

### 4.1 Shear-damage elastic model for 2d plane strain problem

In this section, the final numerical analyses covering the failure expansion around galleries at the Andra URL during their excavation are introduced. Here, it is worth reporting the 2d conceptual models of failure constituting the analyses' targets, in Figure 4.1. In particular, this section presents the last type of elastic-damage constitutive law applied in 2d plane strain numerical simulations. The new model includes the  $2d\_ED$  presented in Chapter 2, as it neglects every damage of the axial stiffness (along  $z$ ). At the same time, it reproduces a damage-based degradation affecting only the shear component of the material's stiffness in the plane ( $x ; y$ ), often denoted  $\Gamma$ , i.e. the gallery cross section. From the physical point of view, the basic idea is a reduction of the cohesive properties of the damaged material: it becomes progressively granular, when  $D$  increases, and maintains, at the same time, its frictional properties. The correspondent strain response requires the material bulk modulus,  $K$ , would not be affected by damage. Only the shear modulus  $\mu$ , in  $\Gamma$ , is degraded by the internal variable  $D$  [34].

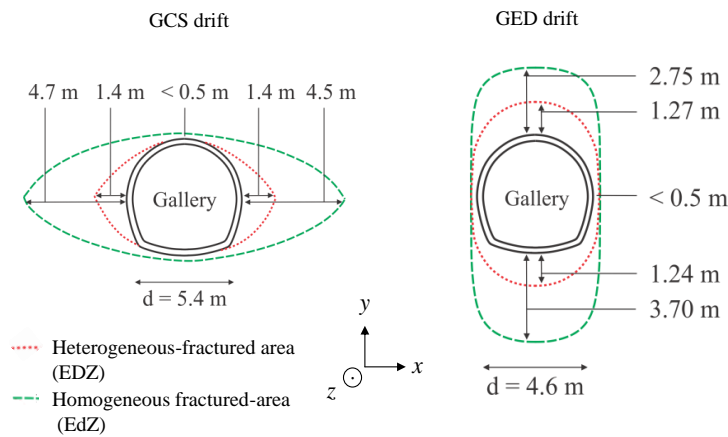


**Figure 4.1 :** bi-dimensional schemes of the extension of EDZ-EdZ around the studied drifts, along  $\sigma_H$  and  $\sigma_h$ , at the Andra URL (modified after [9]).

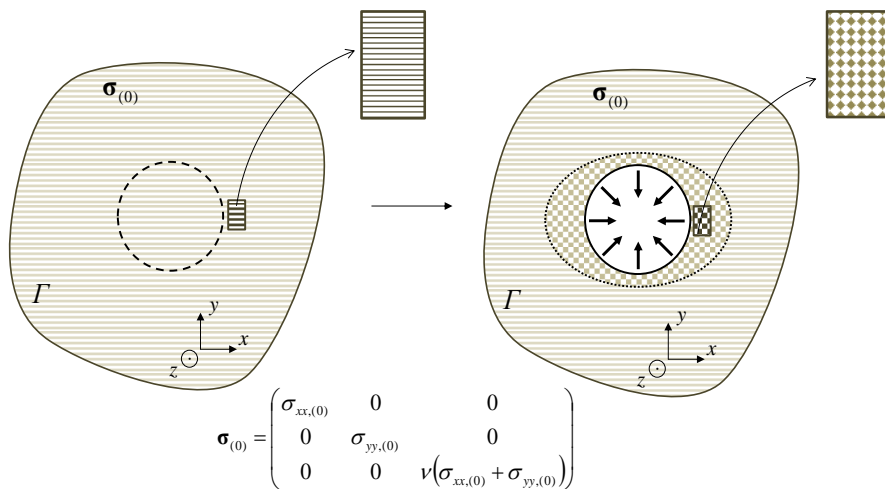


**Figure 4.2 :** conceptual model of the damage mechanism occurring in the material at failure.

According to the scheme reported in Figure 4.2, this model can be described by the equations reported hereby. Firstly, a division of the stress-strain constitutive law, discerning the volumetric from the deviatoric part, is considered:

$$\sigma_{ij} = 3K \cdot \frac{1}{3} \delta_{ij} \cdot tr\{\boldsymbol{\varepsilon}\} + 2\mu \cdot \left( \varepsilon_{ij} - \frac{1}{3} \delta_{ij} \cdot tr\{\boldsymbol{\varepsilon}\} \right) \quad (4.1)$$

In Eq. 4.1, the *hydrostatic* or volumetric part of the stress tensor  $\boldsymbol{\sigma}$  corresponds to:

$$\frac{1}{3} \delta_{ij} \cdot I_1 = 3K \cdot \frac{1}{3} \delta_{ij} \cdot tr\{\boldsymbol{\varepsilon}\} \quad (4.2)$$

While the second term constitutes its deviatoric part:

$$s_{ij} = 2\mu \cdot \left( \boldsymbol{\varepsilon} - \frac{1}{3} \delta_{ij} \cdot tr\{\boldsymbol{\varepsilon}\} \right) = 2\mu \cdot e_{ij} \quad (4.3)$$

In Eq. 4.2 and 4.3,  $K$  is the bulk modulus and  $\mu$  the shear modulus. In this type of modelling, the damage coefficient  $(1-D)$  affects only the stiffness coefficient relating the deviatoric strain and stress tensors, respectively  $\mathbf{e}$  and  $\mathbf{s}$  (i.e.  $e_{ij}$  and  $s_{ij}$  in their indicial forms). Meanwhile, the formalism of the elastic-damage stiffness matrix, to be implemented in the correspondent FORTRAN subroutine in *POROFIS* (e.g. Appendix A, Figure A.1), is based on the following a compliance law conceived for a 2d, plane strain problem, i.e.  $\varepsilon_{zz} = 0$ :

$$\boldsymbol{\varepsilon} = \begin{bmatrix} \varepsilon_{xx} \\ \varepsilon_{yy} \\ 0 \\ 2\varepsilon_{xy} \end{bmatrix} = \tilde{\mathbf{C}}^{-1} : \begin{bmatrix} \sigma_{xx} \\ \sigma_{yy} \\ \sigma_{zz} \\ \sigma_{xy} \end{bmatrix} \quad (4.4)$$

The final *elastic-shear-damage* law, as implemented in *POROFIS*, corresponds to Eq. 4.5a:

$$\tilde{\mathbf{C}} = \mathbf{A} \cdot \begin{bmatrix} 1 + (1-D)(1-2\nu) & 1 - (1-D)(1-2\nu) & 2\nu & 0 \\ 1 - (1-D)(1-2\nu) & 1 + (1-D)(1-2\nu) & 2\nu & 0 \\ 2\nu & 2\nu & 2(1-\nu) & 0 \\ 0 & 0 & 0 & (1-D)(1-2\nu) \end{bmatrix} \quad (4.5a)$$

In the previous equation, the coefficient  $\mathbf{A}$  writes:

$$\mathbf{A} = \frac{E}{2(1+\nu)(1-2\nu)} \quad (4.5b)$$

Eq. 4.5a respects symmetry conditions  $\tilde{C}_{ij} = \tilde{C}_{ji}$ . Every component  $i = z$  or  $j = z$ , or both, is not affected by the damage coefficient  $(1-D)$ . This model, defined elastic *shear-damage* model, will be denoted *2d\_ESD*. The entire formulation describing the *2d\_ESD* constitutive model is an internal *POROFIS* code, developed and implemented in its most recent version [34].

After the elastic-damage model's introduction, this section is dedicated to some preliminary numerical simulations with boundary conditions corresponding to the stress conditions for GCS ( $r_a = 2.6$  m) and GED drifts ( $r_a = 2.3$  m) on their cross-section, according to the values in Table 4.1. The geometry reported in Figure 3.11, Section 3.2 was employed and the same numerical procedure for the excavation was performed. It is worth reporting hereby the linear softening plus residual stress-strain curve initially shown in Section 2.1. Even with the  $2d\_ESD$  model, it remains the reference curve describing the material response in uniaxial compression. Again, the softening post-peak response is described by the parameters  $\beta$  and  $\eta_r$  (Figure 4.3). It is important to underline that the analyses presented in this chapter's section do not aim to reproduce the evidences at the Andra URL (e.g. Figure 4.1) and the parametrization of softening behaviour is not entirely representative for the Callovo-Oxfordian formation (COx). Parameters' choice wants to show the influence of a drastic difference of the *stress-softening ratio*,  $\eta_r$ , in the employment of the  $2d\_ESD$  model. Parameters describing the linear isotropic elasticity,  $E$  and  $\nu$ , were chosen equal to 4500 MPa and 0.2, respectively (e.g. [8], [43]). The uniaxial compressive strength (UCS)  $\sigma_0$  and the softening strain coefficient  $\beta$ , in Figure 4.3, are equal to 17 MPa (admissible value according to Table 1.3 in Section 1.1) and 0.5. Two series of numerical analyses were performed, imposing the boundary and initial conditions as indicated in Table 4.1. In the first series,  $\eta_r = 0.9$ , corresponding to a weakly brittle material. In the second, under the hypothesis of strong fragility,  $\eta_r = 0.2$ . In the following pages, the results' presentation concludes this first section. Comparisons of the damaged failure zone, between boundary conditions corresponding to drifts GCS and GED, are reported in Figure 4.4 and Figure 4.7. Contour plots in Figure 4.5, Figure 4.6 and Figure 4.8, Figure 4.9 reports, respectively, the horizontal and vertical displacements fields for  $\eta_r = 0.9$  and  $\eta_r = 0.2$ .

**Table 4.1:**  $\sigma_{(0)}$  components for the next numerical excavation analysis around GCS and GED drifts.

<i>drift</i>	$\sigma_{xx,(0)}$ [MPa]	$\sigma_{yy,(0)}$ [MPa]	$\sigma_{zz,(0)}$ [MPa]
GCS	-12.4	-12.7	$\nu \cdot (\sigma_{xx,(0)} + \sigma_{yy,(0)})$
GED	-16.2		

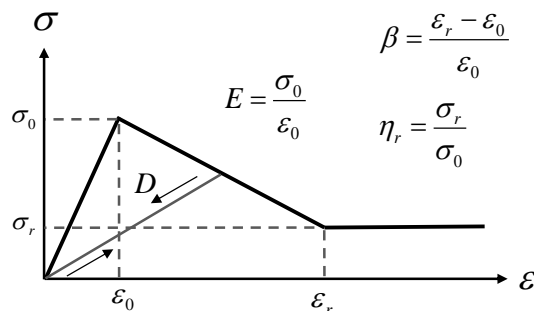


**Figure 4.3 :** model stress-strain curve under monotonic uniaxial loading and damage unloading-reloading

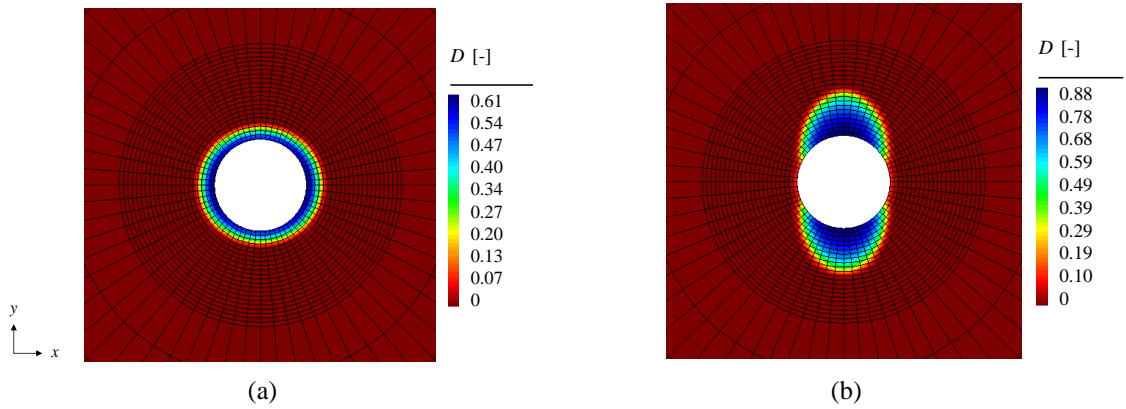


**Figure 4.4** : damage extensions according to boundary and initial conditions in Table 4.1 of GCS in (a) and GED drifts in (b), after complete excavation.  $\eta_r = 0.9$ .

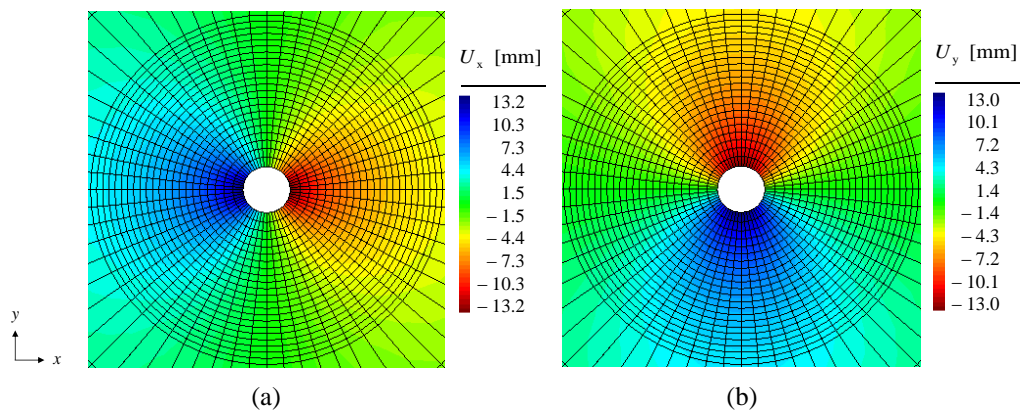


**Figure 4.5** : horizontal (a) and vertical (b) displacements fields according to boundary and initial conditions in Table 4.1 of GCS drift (Figure 4.4a).  $\eta_r = 0.9$ .

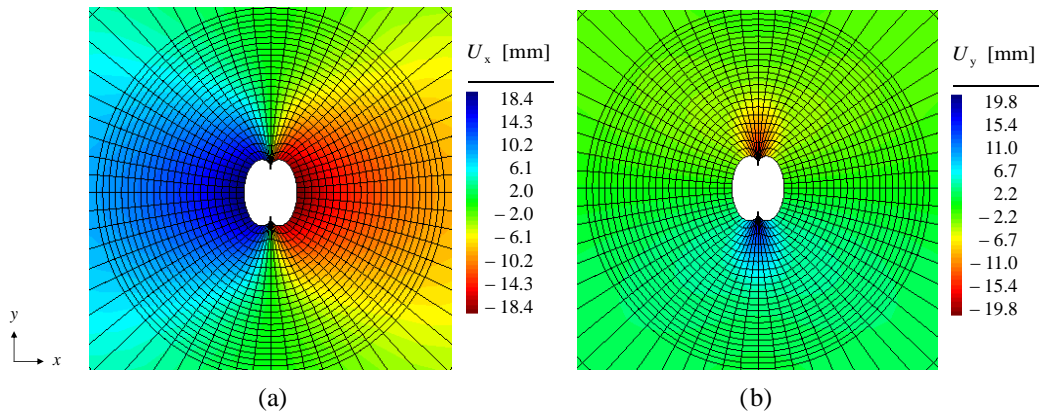


**Figure 4.6** : horizontal (a) and vertical (b) displacements fields according to boundary and initial conditions in Table 4.1 of GED drift (Figure 4.4b).  $\eta_r = 0.9$ .

With  $\eta_r = 0.9$  (almost perfect-yielding material), it is possible to notice that damage distributes concentrically around the circular opening, if the quasi-isotropic initial stress condition for GCS are applied. Similarly, no stress localisations appears around the drift (Figure 4.5a-b). On the contrary, the initial stress anisotropy existing in the GED drift's cross-section, governs the anisotropic damage repartition on the vertical direction, confirmed by displacement's localisation.

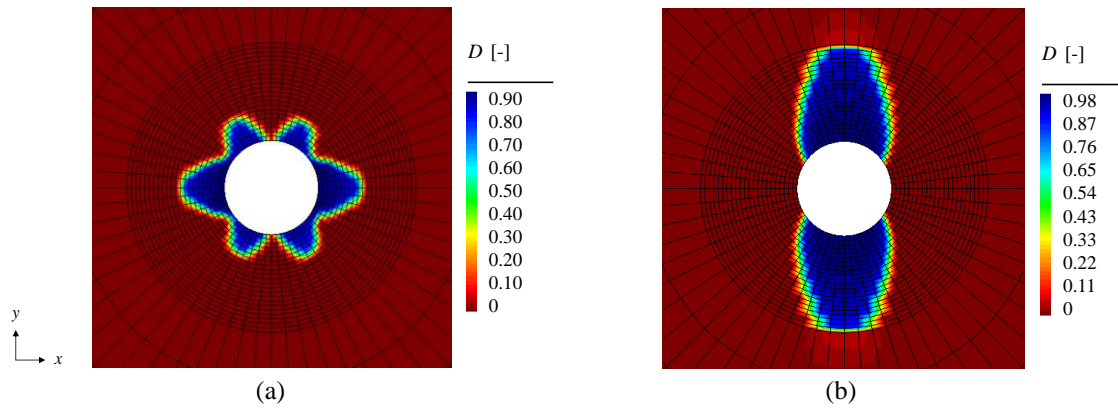


**Figure 4.7** : damage extensions according to boundary and initial conditions in Table 4.1 for GCS in (a) and GED drifts in (b), after complete excavation.  $\eta_r = 0.2$ .

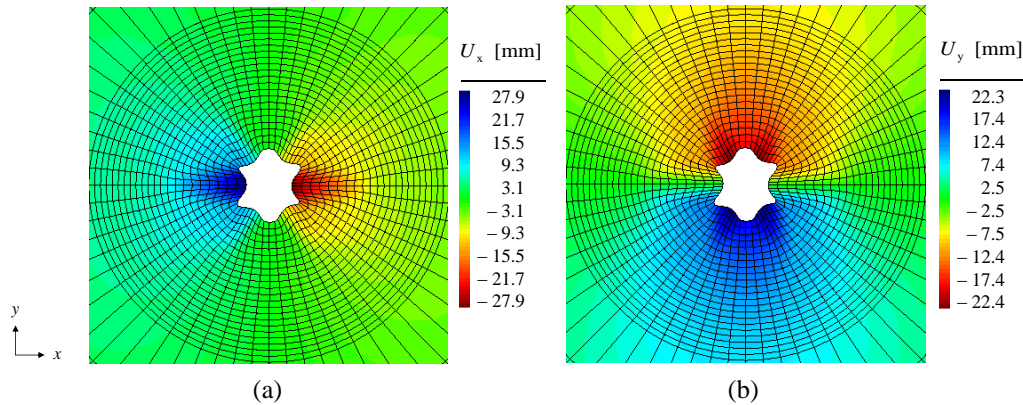


**Figure 4.8** : horizontal (a) and vertical (b) displacements fields according to boundary and initial conditions in Table 4.1 of GCS drift (Figure 4.7a).  $\eta_r = 0.2$ .

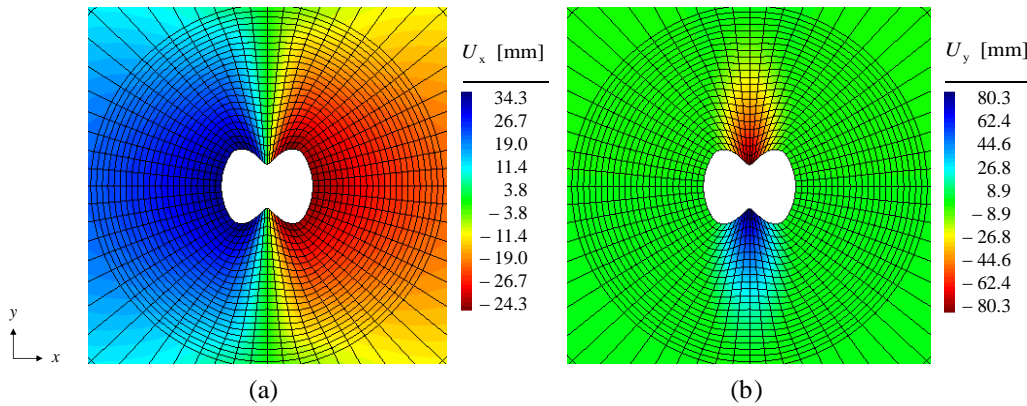


**Figure 4.9** : horizontal (a) and vertical (b) displacements fields according to boundary and initial conditions in Table 4.1 of GED drift (Figure 4.7b).  $\eta_r = 0.2$ .

Applying  $\eta_r = 0.2$  (very brittle material), a very different results is obtained with a quasi-isotropic  $\sigma_{(0)}$  in Figure 4.7a. Apart from 2 damage lobes around the opening's floor and ceiling, failure shape assumes a clear horizontal direction, since  $\sigma_{xx,(0)} < \sigma_{yy,(0)}$ . In Figure 4.7b, the vertical expansion of  $D$  is enhanced up to reaching the finer mesh limit conceived in the geometry design to delimit the potential failure zone. The corresponding  $U_x$  and  $U_y$  contour plots confirm the direction of damage, on either the horizontal or the vertical, with important localisations.

Numerical exercises presented in this section underline the significant contribution of  $\eta_r$  in the failure evolution. Experimentally, as introduced in Chapter 1 (*The Callovo-Oxfordian claystone formation*, 1.1.2), a homogeneous value of the stress-softening ratio throughout the entire domain would not be realistic of the material's response, under the mechanical conditions induced by a gallery excavation. Section 4.4 is introducing this subject, considering a variable  $\eta_r$  in the analyses' domain. In the next section, significant results including the anisotropy of the failure criterion with the *2d\_ESD* constitutive law are discussed.

## 4.2 Preliminary results with monotonic failure anisotropy

The modelling of the material's response at failure is accounted with the criterion introduced in Section 3.2 and then simplified in Section 3.4, to neglect the contribution of the axial component  $\sigma_{zz}$  (e.g. Eq. 3.28-3.30 and Figure 3.22). In the following, the basic equations formalizing the criterion are recalled:

$$\mathbf{n} = (\cos \omega \quad \sin \omega)^T \quad ; \quad \mathbf{M} = \delta_{ij} + h(\mathbf{n} \otimes \mathbf{n}) \quad (4.6a-b)$$

$\mathbf{n}$  is the normal unit vector to the material stratification, inclined with  $\omega$  to the horizontal. The II order anisotropic rotation tensor  $\mathbf{M}$  allows for the definition of a modified 2d stress tensor  $\tilde{\boldsymbol{\sigma}}$ , to simulate the variation of the local material resistance according to  $\omega$  and the anisotropy scaling factor  $h$  (e.g. Eq. 3.7 in Section 3.2).

$$\mathbf{M}^T \cdot \tilde{\boldsymbol{\sigma}} \cdot \mathbf{M} \quad (4.7)$$

$$f(\tilde{\boldsymbol{\sigma}}, D) = \sqrt{(\tilde{\sigma}_{xx} - \tilde{\sigma}_{yy})^2 + 4\tilde{\sigma}_{xy}^2} + \sin \varphi (\tilde{\sigma}_{xx} + \tilde{\sigma}_{yy}) - g(D)K \quad (4.8)$$

Adopting the *2d\_ESD* model, with the anisotropic failure criterion in Eq. 4.8, a first series of analyses is performed to investigate if this model can reproduce both failure zones in Figure 4.1, depending on the respective boundary conditions, reported in Table 4.1 [102]. Parametrization for these analyses does not differ, in general, from the one imposed for results in Section 4.1, particularly those in Figure 4.7, Figure 4.8 and Figure 4.9. Linear elasticity and softening parameters are reported in Table 4.2.

**Table 4.2:** values of linear elastic and softening parameters adopted for the *2d\_ESD* model applied to the following simulation, referring to Figure 4.3.

<i>Elastic parameters</i>		<i>Softening parameters</i>	
$E$ [MPa]	$\nu$ [-]	$\beta$ [-]	$\eta_r$ [-]
4500	0.2	0.5	0.2

Focusing on the softening stress ratio,  $\eta_r$ , the previous section showed the importance of its choice as a numerical parameter influencing the results of the modelling proposed. The value adopted ( $\eta_r = 0.2$ ) is justified by the material stress-strain behaviour in uniaxial loading: Figure 4.10 shows a very brittle post-peak response in softening conditions, without confinement stress ( $p_c = 0$ ). These stress-strains diagrams [8] were already presented in Chapter 1, in the general introduction of COx formation's mechanical properties (Section 1.1, Figure 1.18). In the analyses hereby, anisotropic failure's parameters are based on the same constant friction angle,  $\varphi = 20^\circ$ . Figure 4.11 reports a monotonic interpretation of data in Table 3.10, (Section 3.4). It illustrates the deviator values,  $q$ , at failure, as a function of the bedding inclination  $\omega$ . Hence, calibration reported in Figure 4.11 is assumed for the anisotropic failure criterion (Eq. 4.6-4.8) adopted in the following analyses. Numerical model of the geometry with the initial and boundary conditions to simulate the in-situ stress state ( $\sigma_{(0)}$  defined by values in Table 4.1) and the excavation procedure are illustrated in Figure 4.12. Since this modelling exercise is based on a strong softening behaviour ( $\eta_r = 0.2$ , e.g. Figure 4.3), results obtained from the geometry in Figure 4.12 are compared with an analogue analysis performed to the finer mesh employed in Section 4.1 and illustrated in Figure 3.11, Section 3.2.

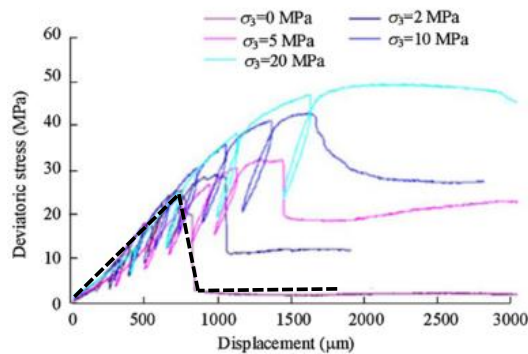


**Figure 4.10** : uni- and triaxial compression tests (TXc) on COx specimens, focusing on the fragile response in uniaxial compressions. Modified after [8].

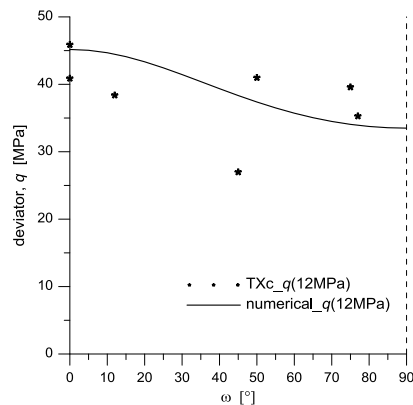


**Figure 4.11** : monotonic interpretation of data in Table 3.10 (Section 3.4), according to the failure criterion in Eq. 4.8.

This is intended to perform a mesh-size sensitivity analyses, with the finer mesh's elements 3 times smaller, in surface, than those in Figure 4.12, in the area potentially failing around the circular opening [102].

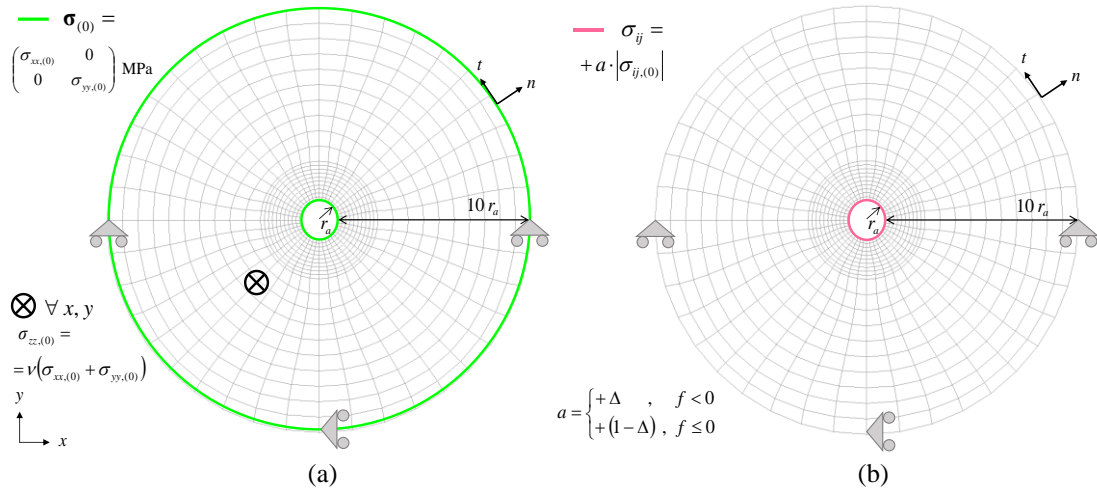


**Figure 4.12 :** Figure 3.2 : numerical model, initial conditions (a) and excavation boundary conditions (b) for the numerical analyses presented.

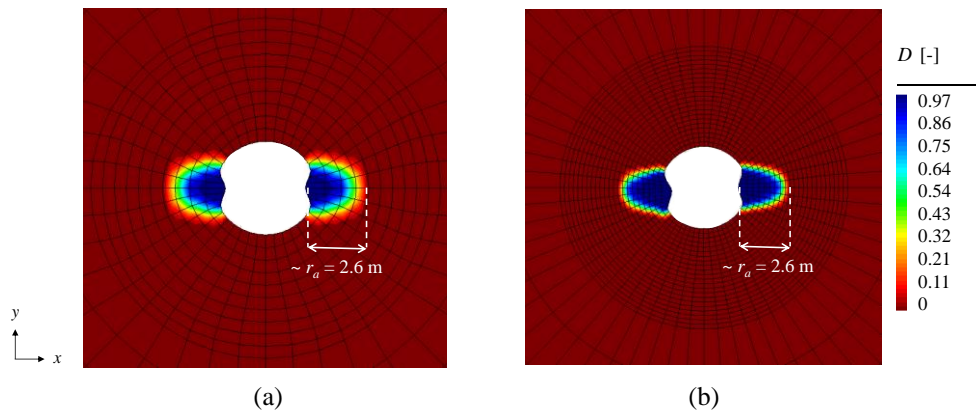


**Figure 4.13 :** damage extensions according to boundary and initial conditions in Table 4.1 of GCS drift. Coarse mesh reported in Figure 4.12 in (a) and fine mesh reported in Figure 3.11, Section 3.2.

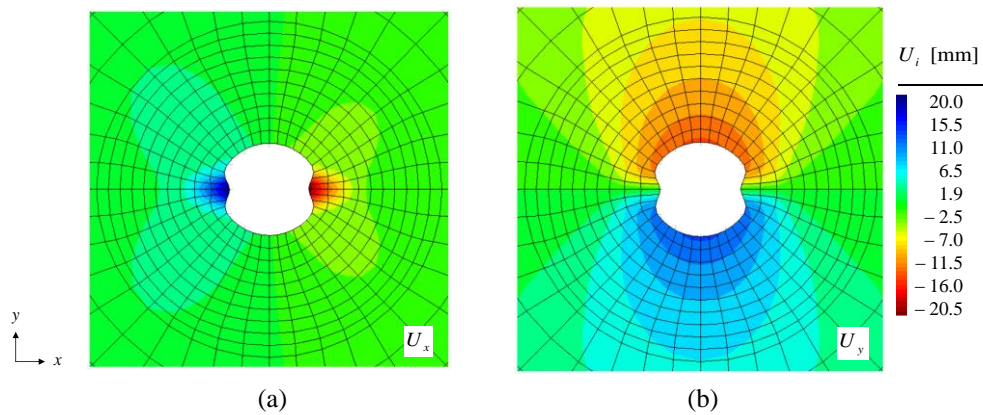


**Figure 4.14 :** horizontal (a) and vertical (b) displacements fields according to boundary and initial conditions in Table 4.1 of GCS drift, with the coarse mesh reported in Figure 4.12.

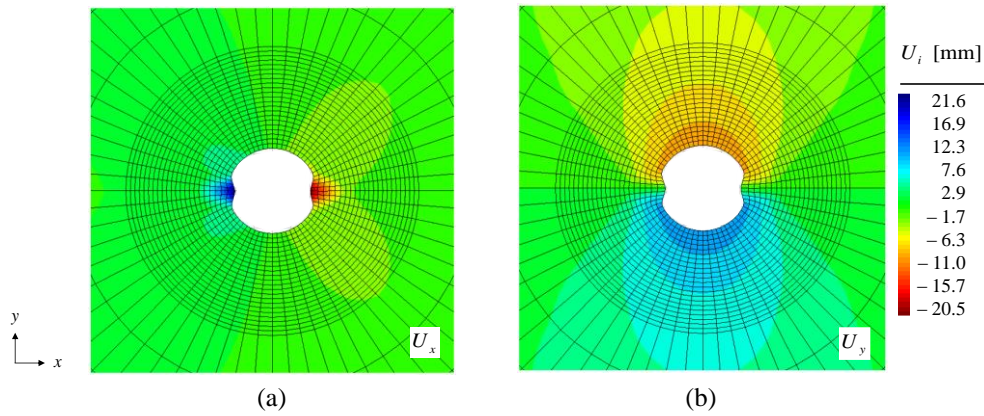


**Figure 4.15** : horizontal (a) and vertical (b) displacements fields according to boundary and initial conditions in Table 4.1 of GCS drift, with the fine mesh reported in Figure 3.11, Section 3.2.

These results confirm a correct localisation of the damage variable,  $D$ , even if the length does not reach the extension of 4.5 m as indicated in Figure 4.1 for GCS drift. The model is able to reproduce a failure zone comprehended between the EDZ and EdZ, which does not show a significant dependence by the mesh size. Displacements at the perimeter are consistent with the observations reported, for GCS drift, in Figure 3.5 and Table 3.3 (Section 3.1).

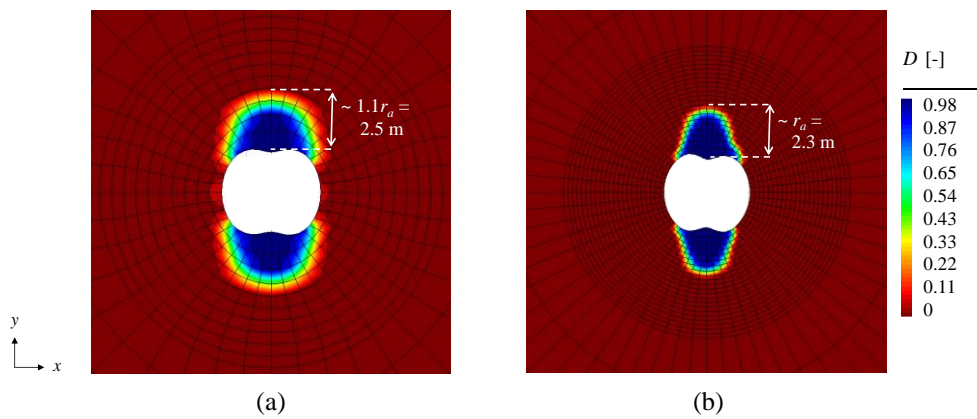


**Figure 4.16** : damage extensions according to boundary and initial conditions in Table 4.1 of GED drift. Coarser mesh reported in Figure 4.12 in (a) and finer mesh reported in Figure 3.11, Section 3.2.

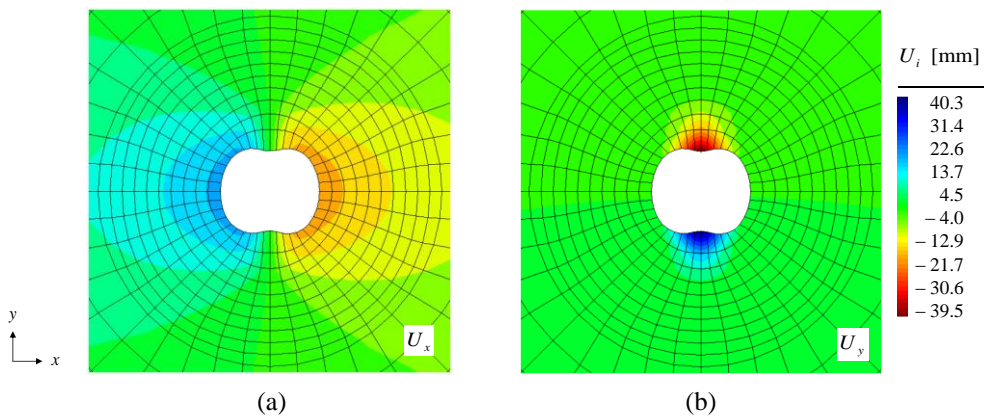


**Figure 4.17** : horizontal (a) and vertical (b) displacements fields according to boundary and initial conditions in Table 4.1 of GED drift, with the coarse mesh reported in Figure 4.12.

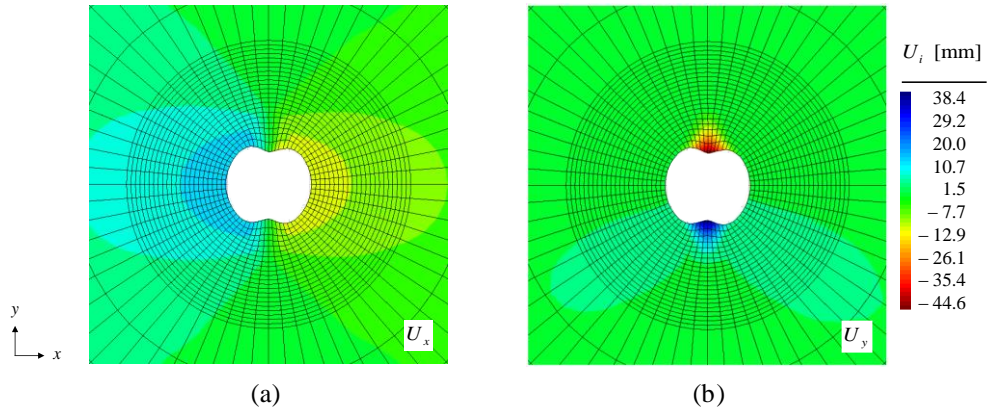


**Figure 4.18** : horizontal (a) and vertical (b) displacements fields according to boundary and initial conditions in Table 4.1 of GED drift, with the fine mesh reported in Figure 3.11, Section 3.2.

For the analyses of GED drift, the failure zone calculated in Figure 4.16, with the coarse mesh (a) is almost able to attain the upper vertical extension reported in Figure 4.1. Nonetheless, the GED conceptual model for failure zone shows a different extension on the vertical, between the development at the ceiling and at the base of the tunnel; in particular, the latter is extended up to 1 m more. This difference cannot be overcome by the modelling proposed, which reproduces, on the other hand, a vertical failure zone symmetrical with respect to the axis  $x$ . Again, no significant differences are noticed concerning the mesh-size dependency for  $D$ . Horizontal and vertical displacements are in accordance with measured values, referring to Figure 3.17 and Table 3.7 for GED drift (Section 3.2). For every gallery, relative errors of displacement components ( $U_i$ ) due to the mesh-size dependence are resumed in Table 4.3 and Table 4.4, respectively for GCS and GED. This error is evaluated according to Eq. 4.9, with  $U_i$  calculated at the perimeters; in Eq. 4.9, “FM” refers to the finer mesh, while “CM” to the coarser (Figure 4.12). Table 4.3 and Table 4.4 reports also, for every mesh, the horizontal to vertical displacements’ ratio  $|U_x|/|U_y|$ . In particular, for GCS and GED drift, the finer mesh is able to provide a consistent estimation, according to the values reviewed in literature, respectively:  $\sim 2$  and  $\sim 0.25$  (e.g. [42], [60] and [66]).

$$\frac{|U_i(\text{FM}) - U_i(\text{CM})|}{|U_i(\text{CM})|} \% \quad (4.9)$$

**Table 4.3** : GCS drift, mesh-size sensitivity on displacements at the perimeter.

		$ U_x $ max. [mm]	$ U_y $ max. [mm]	$ U_x / U_y $ [-]
Coarse mesh	(Figure 4.12)	20.0	12.5	1.64
Fine mesh	(Figure 3.11, Section 3.2)	21.6	10.9	1.98
Max. error (%)	(absolute value)	8 %	12.8 %	20.7 %

**Table 4.4** : GED drift, mesh-size sensitivity on displacements at the perimeter.

		$ U_x $ max. [mm]	$ U_y $ max. [mm]	$ U_x  /  U_y $ [-]
Coarse mesh	(Figure 4.12)	18.2	40.3	0.45
Fine mesh	(Figure 3.11, Section 3.2)	15.2	44.6	0.34
Max. error (%)	(absolute value)	16.5 %	10.6 %	24.4 %

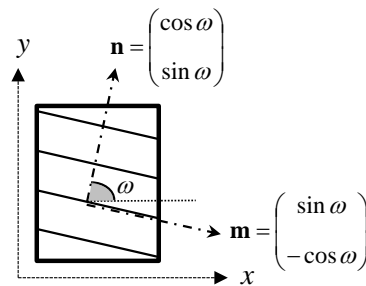
These analyses have shown, generally, a symmetric repartition of damage around the circular openings. Even if the final results are correct, it must be underlined that this symmetry is due by the particular interpretation of anisotropic failure data in Figure 4.11. It provides, in numerical analyses, the correct failure localizations for every drift considered. Nonetheless, if a non-monotonic interpretation (i.e. failure parameters' calibration) of these data occurred, symmetric damage localization would not be reproduced around the entire drift perimeter,  $\theta \in [0; 2\pi]$ , as discussed in details at the end of Section 3.4. This problem was overcome developing the anisotropic failure model described in the following section.

### 4.3 Fourth-order modelling of non-monotonic failure anisotropy

In this section, a second proposition for the implementation of an anisotropic failure criterion is detailed. This criterion is also neglecting the axial stress  $\sigma_z$ , according to Eq. 4.8. To solve the problem of the dissymmetry in the failure localization for  $\theta \in [0; 2\pi]$  around the circular perimeter of a gallery, the fourth (IV) order rotation tensor  $\mathbf{H}$  is formalized in Eq. 4.11, as function of the unit vectors  $\mathbf{m}$  and  $\mathbf{n}$  in Eq. 4.10, respectively parallel and perpendicular to the material's stratification, as reported in Figure 4.19 :

$$\mathbf{n} = (\cos \omega \quad \sin \omega)^T \quad ; \quad \mathbf{m} = (\sin \omega \quad -\cos \omega)^T \quad (4.10a-b)$$

$$\begin{aligned} \mathbf{H} = & h_n (\mathbf{n} \otimes \mathbf{n}^T) \otimes (\mathbf{n} \otimes \mathbf{n}^T) + (\mathbf{m} \otimes \mathbf{m}^T) \otimes (\mathbf{m} \otimes \mathbf{m}^T) + \\ & + \frac{h_s}{2} [(\mathbf{m} \otimes \mathbf{n}^T + \mathbf{n} \otimes \mathbf{m}^T) \otimes (\mathbf{m} \otimes \mathbf{n}^T + \mathbf{n} \otimes \mathbf{m}^T)] \end{aligned} \quad (4.11)$$

**Figure 4.19** : conceptual model for the implementation of the new anisotropic 2d failure criterion.

$h_n$  and  $h_s$  are defined, respectively, the *normal* and *shear* anisotropic scaling factors. It is possible to demonstrate that, if  $h_n = h_s = 1$ ,  $\mathbf{H}$  is a IV order identity matrix, i.e.  $\delta_{ijkl}$ . As done in Section 3.2 for the II order tensor  $\mathbf{M}$ , in this case, the *anisotropic rotation* tensor  $\mathbf{H}$  serves to provide an equivalent stress tensor for a variable failure threshold. This is function of the inclination between the material's stratification and the main loading direction,  $\omega$  (Figure 4.19).

$$\tilde{\boldsymbol{\sigma}} = \mathbf{H} \cdot \boldsymbol{\sigma} \quad (4. 12)$$

In indicial notation, it writes:

$$\tilde{\sigma}_{ij} = H_{ijkl} \cdot \sigma_{hk} \quad (4. 13)$$

Since Eq. 4.10-4.13 apply to a stress tensor in two dimensions (the axial stress component  $\sigma_{zz}$  is always neglected in the failure evaluation), the explicit formulation of Eq. 4.13 considers the indexes  $i$  and  $j$  corresponding to  $x$  or  $y$  only:

$$\tilde{\boldsymbol{\sigma}} = \begin{bmatrix} \tilde{\sigma}_{xx} \\ \tilde{\sigma}_{yy} \\ \tilde{\sigma}_{xy} \end{bmatrix} = \begin{bmatrix} H_{xxxx} & H_{xxyy} & H_{xyxx} \\ H_{yyxx} & H_{yyyy} & H_{yyxy} \\ H_{xyxx} & H_{xyyy} & H_{xyxy} \end{bmatrix} \cdot \begin{bmatrix} \sigma_{xx} \\ \sigma_{yy} \\ \sigma_{xy} \end{bmatrix} \quad (4. 14)$$

$\mathbf{H}$  can be directly written as a 3x3 matrix, since  $\tilde{\sigma}_{xy} = \tilde{\sigma}_{yx}$  and  $\sigma_{xy} = \sigma_{yx}$ , and it is defined symmetric, as the II order tensor  $\mathbf{M}$  presented in the previous chapter. The entire formulation of  $\mathbf{H}$ , particularly the definition of its components  $H_{ij}$ , is detailed in the Appendix B.3. As introduced, the anisotropic rotation tensor  $\mathbf{H}$  replaces the tensor  $\mathbf{M}$ , by employing the components of the modified or *equivalent* stress tensor  $\tilde{\boldsymbol{\sigma}}$  in Eq. 4.14 for the evaluation of anisotropic failure (Eq. 4.8). This model is capable to resolve the dissymmetry previously encountered in the failure localisations and shown at the end of Chapter 3 in Figure 3.26 and Figure 3.28. In fact, if failure around the gallery cross-section (plane  $\Gamma$ ) firstly localizes at a certain coordinate  $\theta \in [0 ; \pi/2]$ , the same physical condition must be respected symmetrically both to the axes  $x$  and  $y$ , according to the scheme illustrated in Figure 4.20. According to this scheme, it can be deduced that numerical analyses may be performed also on a reduced geometry correspondent to one fourth of the whole cylindrical-symmetric domain, reduced to a circumference in 2d. Damaged zones reported in Figure 4.21 have the only scope to show, on the entire circular domain, the symmetric localizations of failure around the opening. Nonetheless, initial and boundary conditions corresponding the two main drifting directions, following  $\sigma_H$  and  $\sigma_h$  (e.g. Table 4.1), the Andra URL were imposed, respectively in Figure 4.21a and Figure 4.21b.

As done with the previous modelling of material's strength anisotropy, the failure criterion in Eq. 4.8 can be written for uniaxial or laterally-confined stress states, respectively  $\sigma_{xx} = 0 ; \sigma_{yy} \neq 0$  and  $|\sigma_{xx}| = p_C ; \sigma_{yy} \neq 0$ . For the first case, the uniaxial compressive strength (*UCS*) as a function of  $\omega$ ,

$\sigma_{\theta,\omega}$ , can be analytically defined, in analogy with the formulation presented in Section 3.4, Eq. 3.33. In case of monotonic compression, the modified stress tensor (e.g. Eq. 4.14) writes:

$$\tilde{\boldsymbol{\sigma}} = \begin{bmatrix} H_{xxyy} & H_{xyyy} \\ H_{xyyy} & H_{yyyy} \end{bmatrix} \cdot \boldsymbol{\sigma}_{yy} \quad (4.15)$$

The stress state described in Eq. 4.15 is detailed in Appendix B.3, related to the mathematical formalism of this anisotropic failure criterion. With this stress condition, failure is expressed as follows:

$$f(\tilde{\boldsymbol{\sigma}}, D) = \sqrt{(H_{xxyy} - H_{yyyy})^2 + 4H_{xyyy}^2} |\sigma_{yy}| + \sin \varphi (H_{xxyy} + H_{yyyy}) \sigma_{yy} - K = 0 \quad (4.16)$$

It is remembered that, when failure is firstly attained,  $D = 0 \rightarrow g(D) = 1$ . Since  $|\sigma_{yy}| = -\sigma_{yy}$  and  $-\sigma_{yy} = \sigma_{\theta,\omega}$ , the UCS writes:

$$\sigma_{\theta,\omega} = \frac{K}{\sqrt{(H_{xxyy} - H_{yyyy})^2 + 4H_{xyyy}^2} - \sin \varphi (H_{xxyy} + H_{yyyy})} \quad (4.17)$$

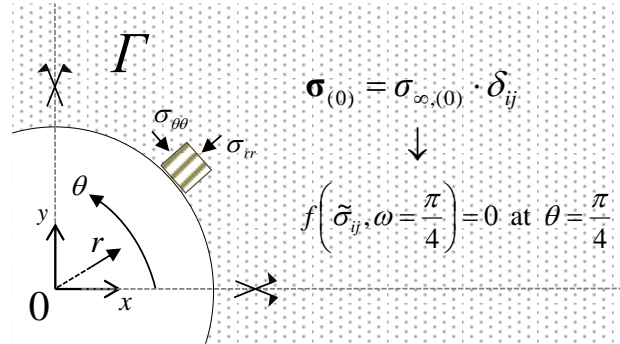


**Figure 4.20** : scheme of failure localization at a coordinate  $0 < \theta < \pi/2$  (in this case,  $\pi/4$ ), symmetric to both axis  $x$  and  $y$  on the cross-section plane  $\Gamma$ .

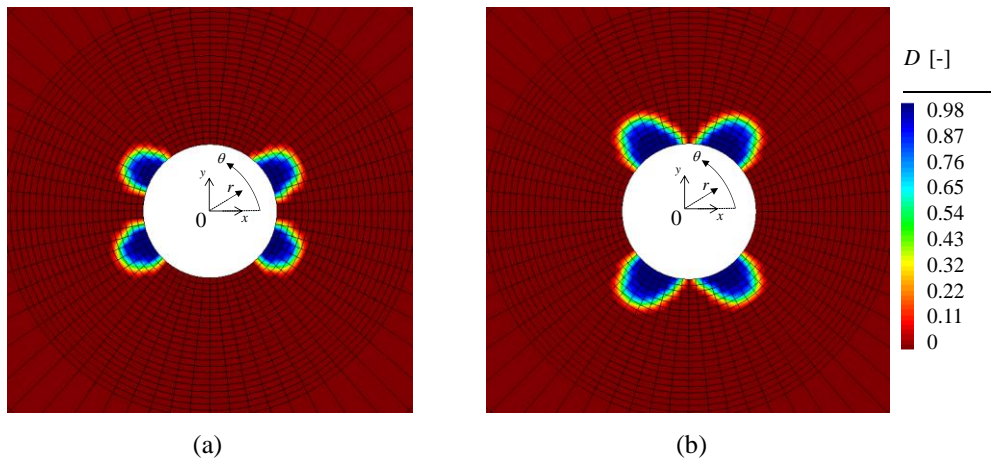


**Figure 4.21** : numerical simulations validating the symmetric failure attainment calculated with the 2d anisotropic criterion modified by  $\mathbf{H}$ . Boundary stress conditions are equivalent to GCS drift in (a) and GED in (b) (e.g. Table 4.1).

In Figure 4.22, a comparison between the UCS as a function of  $\omega$  is provided, between the modelling with the II order tensor  $\mathbf{M}$  and this one. Values of  $\sigma_{0,\omega}$  with  $\mathbf{M}$  are equivalent to those presented at the end of Chapter 3 (Figure 3.23), assuming failure parameters  $\varphi$  and  $K$  respectively equal to  $20^\circ$  and 15 MPa. Values of  $\sigma_{0,\omega}$  with  $\mathbf{H}$  are traced to obtained the same UCS values for monotonic compressions parallel and perpendicular to the bedding, i.e.  $\omega = 0^\circ$  and  $90^\circ$ . In the case of the tensor  $\mathbf{H}$ , it is important to underline that the scaling factors  $h_n$  and  $h_s$  correspond only to calibration parameters: they modify the model's shape according to a certain dataset of strength values at failure, measured in specimens differently inclined to the load direction. None of these two parameters is related with the anisotropic scaling factor  $h$ , comparing in the definition of the tensor  $\mathbf{M}$  and quantifying the anisotropy between  $\omega = 0^\circ$  and  $90^\circ$ . The function of  $\sigma_{0,\omega}$  modelled with the tensor  $\mathbf{H}$  shows, again, a periodicity of its values in  $\omega = [0; 180^\circ]$ .

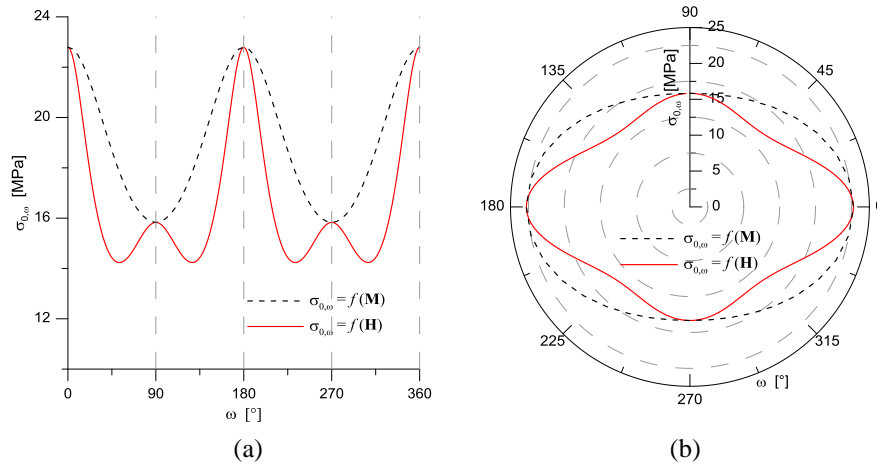


**Figure 4.22** :  $\sigma_{0,\omega}$  modelled with  $\mathbf{H}$  (red line) and  $\mathbf{M}$  (dotted line).  $\varphi = 20^\circ$ ,  $K = 15$  MPa.  $h_n = h_s = 1.44$  with  $\mathbf{H}$ .  $h = 0.2$  with  $\mathbf{M}$ . Linear representation in (a), radar representation in (b).

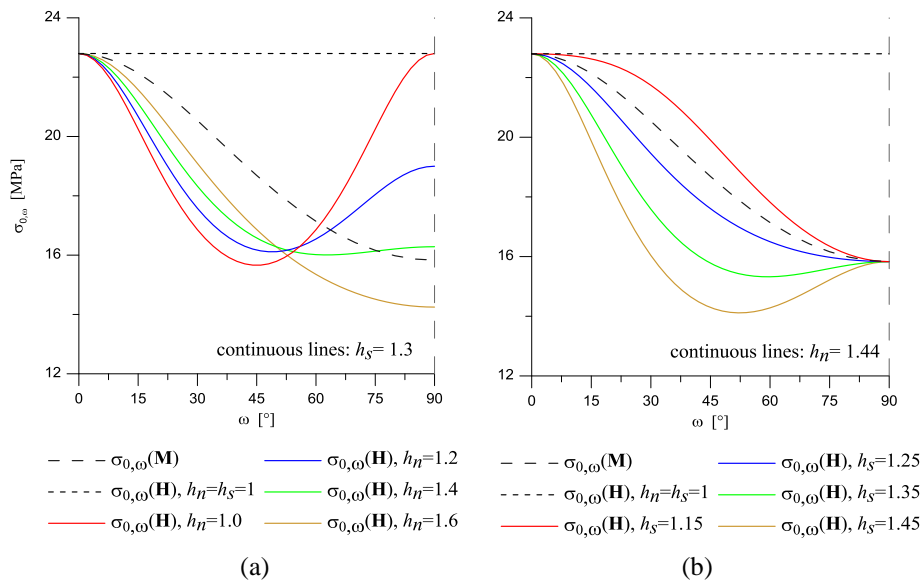


**Figure 4.23** :  $\sigma_{0,\omega}$  variation according to, separately,  $h_n$  (a) and  $h_s$  (b).  $\varphi = 20^\circ$ ,  $K = 15$  MPa. Comparison with the case of constant UCS ( $h_n = h_s = 1$ ) and UCS modelled with the II order tensor  $\mathbf{M}$  ( $h = 0.2$ ).

Figure 4.23 focuses on the interval  $[0; 90^\circ]$ , providing some examples of the possible values' range for parametrisation of failure localization (e.g. Figure 4.20). In this interval, the scaling factor  $h_n$  fixes the function's extremity at  $\omega = 90^\circ$  (Figure 4.23a), determining, for a constant value of the scaling factor  $h_s$ , a monotonic or non-monotonic trend. Similarly, this can be also defined by the variation of  $h_s$ , with the extremes at  $\omega = 0$  and  $90^\circ$  fixed by a constant value of  $h_n$  (e.g. Figure 4.23b). It is possible to notice that for  $h_n = h_s = 1$ , a constant  $\sigma_{0,\omega}$  (*UCS*) is found:

$$\sigma_{0,0^\circ} = \sigma_0 = \frac{K}{1 - \sin \varphi} \quad (4.18)$$

Eq. 4.18 is the *UCS* parallel to the stratification, coinciding with the simple case of constant material strength,  $\forall \omega$ , if  $h_n = h_s = 1$ . Radar plot in Figure 4.22b provides an intuitive example to understand that the weakest material's strength is localised around  $\omega = \pi/4 + n\pi/2$  ( $n=1, 2, 3\dots$ ). In case of isotropic stress state on the cross-section  $\Gamma$ , this condition provokes failure localisation in the correspondent orthoradial coordinate,  $\theta$ , according to the scheme in Figure 4.20. The analytic explicit formulation of material's strength exists also in case of confined compression. With these boundary conditions, the stress tensor writes:

$$\boldsymbol{\sigma} = \begin{bmatrix} \sigma_{xx} = p_C & 0 \\ 0 & \sigma_{yy} \end{bmatrix} \quad (4.19)$$

Stress components of the modified tensor  $\tilde{\boldsymbol{\sigma}}$ , based on Eq. 4.14, assume the following forms:

$$\tilde{\sigma}_{xx} = H_{xxxx} p_C + H_{xxyy} \sigma_{yy} \quad (4.20a)$$

$$\tilde{\sigma}_{yy} = H_{yyxx} p_C + H_{yyyy} \sigma_{yy} \quad (4.20b)$$

$$\tilde{\sigma}_{xy} = H_{xyxx} p_C + H_{xyyy} \sigma_{yy} \quad (4.20c)$$

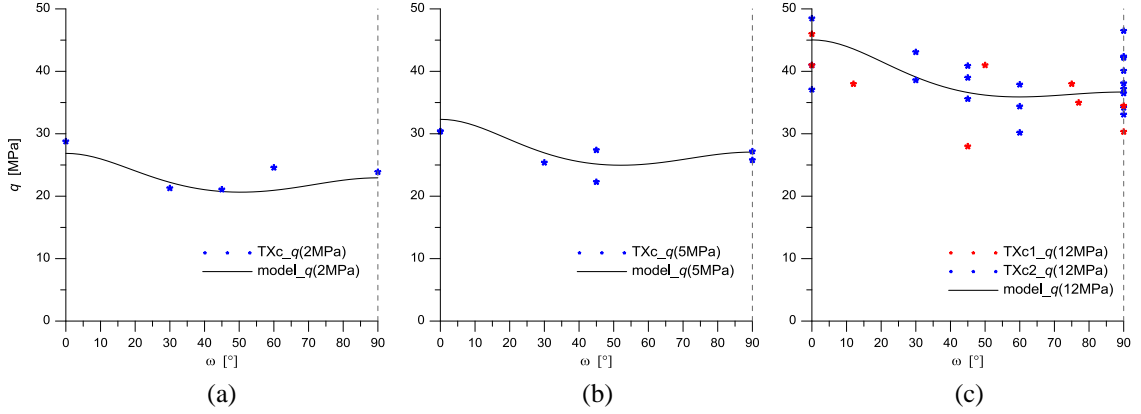
The failure criterion (i.e. Eq. 4.8) writes:

$$f(\tilde{\boldsymbol{\sigma}}, D) = \sqrt{\left[ (H_{xxxx} - H_{yyxx}) p_C + (H_{xxyy} - H_{yyyy}) \sigma_{yy} \right]^2 + 4(H_{xyxx} p_C + H_{xyyy} \sigma_{yy})^2} + \sin \varphi \left[ (H_{xxxx} + H_{yyxx}) p_C + (H_{xxyy} + H_{yyyy}) \sigma_{yy} \right] - K = 0 \quad (4.21)$$

Based on Eq. 4.21, imposing  $|\sigma_{yy}| = \sigma_\theta(p_C, \omega)$ , the analytical expression of the latter can be found as function of  $h_n$  and  $h_s$ ,  $p_C$  and  $\omega$ . The explicit function of  $\sigma_\theta(p_C, \omega)$  is detailed in Appendix B.3. The formulation of this anisotropic failure modelling was established in parallel with the availability of a new, consistent dataset of deviator values for Callovo-Oxfordian specimens at failure (Andra internal database). Sampled with different inclinations with respect to the stratification (i.e.  $\omega$ ), they were sheared under different values of confinement, in TXc tests, in particular  $p_C = 2, 5$  and  $12$  MPa.

**Table 4.5:** calibration of the Mohr-Coulomb type anisotropic criterion (i.e. Eq. 4.8) defined with  $\tilde{\sigma}(\mathbf{H})$ .

$\varphi$ [°]	$K$ [MPa]	$h_n$ [-]	$h_s$ [-]
20	17	1.15	1.25


**Figure 4.24 :** calibration of the Mohr-Coulomb type anisotropic criterion (i.e. Eq. 4.8) defined with  $\tilde{\sigma}(\mathbf{H})$ .

Through the expression of  $\sigma_0(p_C)_{,\omega}$ , for these values of confinement, it was possible to define a unique set of failure parameters, assuming  $\varphi = 20^\circ$ . The adaptation of the deviator's function shape,  $q(\omega) = \sigma_0(p_C)_{,\omega} - p_C$ , was compared varying  $K$ ,  $h_n$  and  $h_s$ . Figure 4.24 illustrates the calibrations of  $q(\omega)$ , for every confinement level, according to the available data. The final failure parameters are reported in Table 4.5 and are adopted for the definition of anisotropic failure criterion implemented in the *2d\_ESD* model routine employed for the final numerical analyses for damage expansions around GCS and GED drifts (results in Section 4.5).

#### 4.4 Modelling the softening brittle-ductile transition

This section concerns the numerical treatment, within the analyses domain, of the change in the softening post-peak behaviour experimentally shown by the COx formation, when a higher lateral confinement occurs in the material. The stress-strains curves in Figure 4.10 [8] provide a clear example of a different response after failure, observed at the laboratory scale, experiencing an increasing ductility of the softening up to an almost perfect yielding when confinement  $p_C$  is equal to 20 MPa. Other data showing the progressive ductile response of COx claystone with the lateral confinement are illustrated in Figure 4.25 and Figure 4.26, from reviewed reports and publications on laboratory testing ([14], [46]). In general, these data confirm a *brittle to ductile transition* of the claystone softening behaviour under a more confined loading. For the problem of a circular excavation, referring to the elastic solution (e.g. Section 1.2) it is possible to assume that the increasing radial stress  $\sigma_{rr}$  may correspond, for 2d analyses, to the increasing confinement.

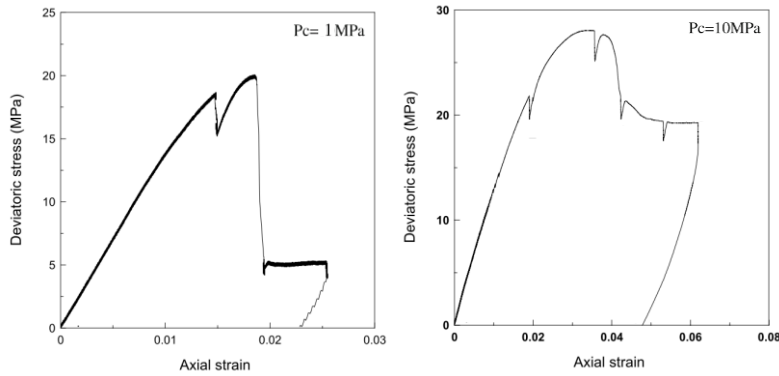


**Figure 4.25** : deviator stress vs. axial strain for TXc tests confined at 1 MPa (left) and 10 MPa (right). Modified from [14].

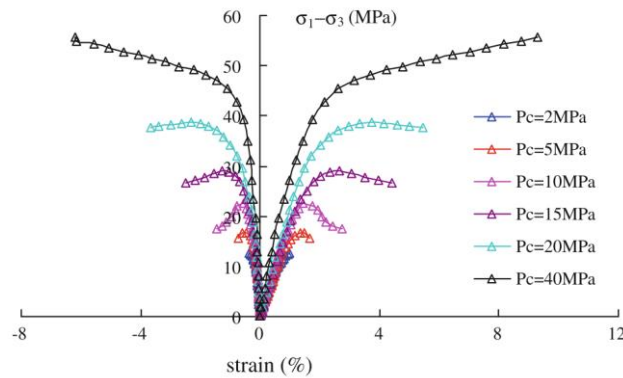


**Figure 4.26** : stress-strain curves in TXc tests with different confining stresses [46].

If Figure 4.3 represents the unconfined stress-strain curve, at the material point scale, the same confined specimen, with an increasing  $p_c$ , reproduces the behaviour reported in Figure 4.27a. As the confined (or triaxial) compressive strength  $\sigma_0(p_c)$  increases, the residual strength  $\sigma_r$  also arises. Even this is a necessary condition to describe the confinement effect, it is not sufficient: referring to the experimental results previously illustrated, in numerical analyses, it should be accounted also that the ratio between  $\sigma_r$  and a correspondent  $\sigma_0(p_c)$  must increase, when  $p_c$  increases. In other terms, extending the definition of the softening stress ratio  $\eta_r$  (e.g. Figure 4.3) also to the ratio between the residual and peak compressive strength, with  $p_c > 0$ ,  $\eta_r$  increases with  $p_c$  and does not remain constant. Without any modification to the structure of the  $2d\_ESD$  model, it appeared necessary the definition of different zones, concentrically distributed around a circular opening, where the level of residual strength would increase for a certain upper threshold of confinement, identified by the radial stress component  $\sigma_{rr}$ . With the model in Figure 4.3, the numerical technique immediately available to reproduce the *brittle-ductile* transition was the increase of the softening parameters  $\beta$  and  $\eta_r$  in every annular zone around the drift, as reported in Figure 4.27b. In this work, these zones are called *transition zones*, denoted *TZ* in the following. From the numerical point of view, this method, applied to the final analyses presented in Section 4.5, includes the definition of one softening  $2d\_ESD$  material for every *TZ*, with the same elastic and failure parameters, and different values for  $\beta$  and  $\eta_r$ .

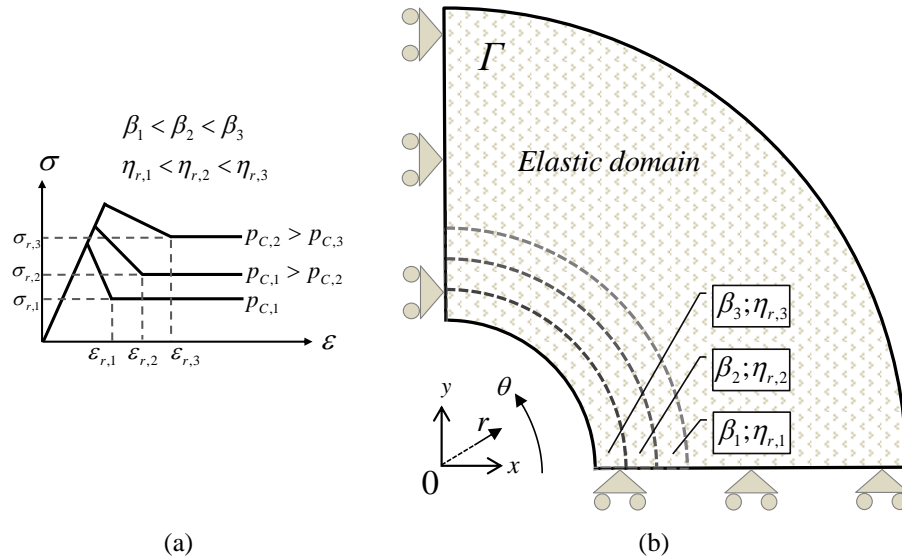


**Figure 4.27** : conceptual model for the subdivision of concentrically brittle-ductile transition zones in the area potentially subjected to damage.

Once the “numerical-geometrical” technique accounting for the brittle-ductile transition was established, a method to assign numerical values to the softening parameters for each *TZ* was needed. For simplicity, a revision of triaxial compression (TXc) data on COx claystone was performed (e.g. [10], [57] and [117]) in order to calculate, for every stress-strain path, the softening parameters  $\beta$  and  $\eta_r$  and establish a unique function with the confining pressure  $p_c$ , for each parameter. It is important to notice that this is an approximation, in relation to the condition previously stated, i.e.  $\eta_r$  increases with  $p_c$  when defined as  $\sigma_r/\sigma_0(p_c)$ , because softening parameters of the *2d\_ESD* model correspond, by definition, to the uniaxial compressive behaviour. It would be necessary a stress-strain constitutive model capable to account, eventually, for a *softening-hardening* post-peak transition, according to the confinement on the material point or, similarly, the first invariant  $I_1$ . Nonetheless, according to the method in Figure 4.27, the reviewed data of TXc test were processed, identifying, in every curve of the shearing phase, the peak and residual strength. Axial deformations corresponding to these stress values were also recorded and, for every stress-strain curve, a couple of softening parameters  $\beta$  and  $\eta_r$  was obtained and correlated to the confinement  $p_c$ . Figure 4.28a and b reports; respectively, the calculated values of  $\beta$  and  $\eta_r$ , versus  $p_c$ , for every TXc tests considered in the review, including the sources previously mentioned. The legend in Figure 4.28 includes the publications where the TXc stress-strain series to calculate  $\beta$  and  $\eta_r$  were recorded. Each plot reports also a curve interpolating the values of  $\beta$  and  $\eta_r$  in order to provide a function with the confinement, to be employed later in their assignment on the numerical model’s geometry (e.g. Figure 4.27b). Figure 4.28a calculated values for  $\beta$  show a relatively elevated dispersion. Since this parameter depends on strains, this variability may be due to the different displacement rate while shearing, even if the 70% of available data confirms an increasing tendency of  $\beta$  with the testing confinement.

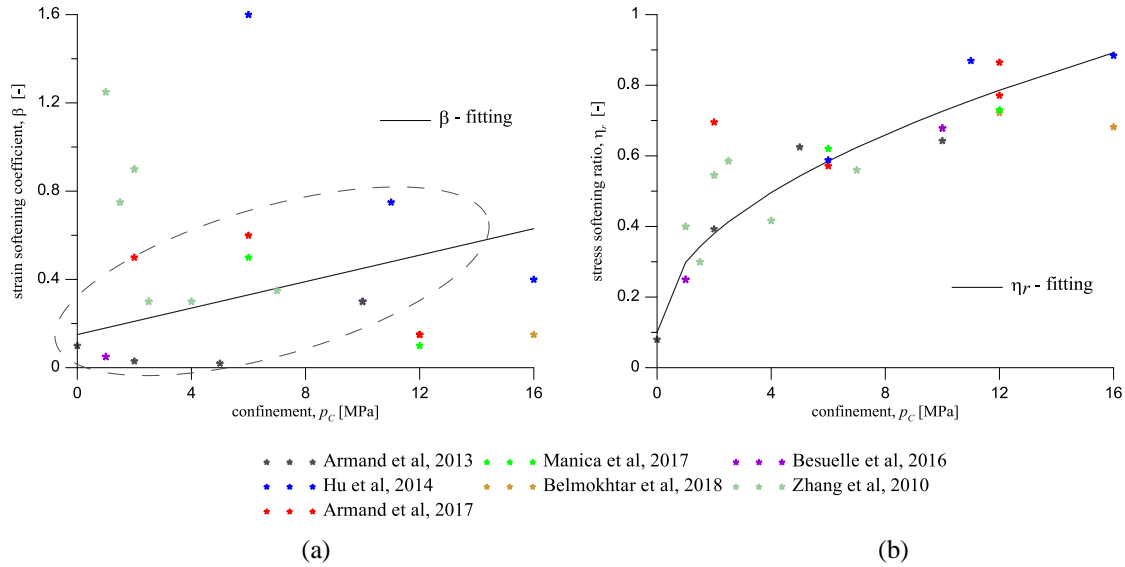


**Figure 4.28** : values of softening parameters  $\beta$  and  $\eta_r$  (respectively, in (a) and (b)) calculated from TXc data recorded in various bibliographic references (i.e. [8], [10], [12], [14], [46], [57] and [117]).

For data confirming an increasing trend of  $\beta$  with  $p_C$ , a linear correlation was established and the relative fitting curve is reported in Figure 4.28a. On the other hand, data on peak and residual strength in TXc tests, used to calculate  $\eta_r$ , show a clearer relation with the confining stress. Eventually, it was possible to propose the following equations for the interpolating curves of Figure 4.28, assuming  $p_C = \sigma_{rr}$  for their employment in numerical analyses of circular drifts' excavation:

$$\beta(\sigma_{rr}) = 0.15 + 0.03 \cdot \sigma_{rr} \quad (4.22)$$

$$\eta_r(\sigma_{rr}) = 0.1 + 0.2 \cdot \sigma_{rr}^{0.5} \quad (4.23)$$

$\sigma_{rr}$  in Eq. 4.22 and 4.23, assimilated to the TXc confinement  $p_C$  in Figure 4.28, is approximated with its elastic solution under the hypothesis of a completely excavated gallery, i.e.  $p_0 = 0$ . In anisotropic conditions of initial stress acting on the main directions (vertical and horizontal) on the gallery's cross-section  $\Gamma$ , the radial stress component writes, for  $p_0 = 0$  (e.g. [48]):

$$\sigma_{rr}(r, \theta) = \sigma_{xx,(0)} \cos^2 \theta + \sigma_{yy,(0)} \sin^2 \theta - \frac{\sigma_{xx,(0)} + \sigma_{yy,(0)}}{2} \frac{r_a^2}{r^2} + \frac{\sigma_{yy,(0)} - \sigma_{xx,(0)}}{2} \left( 4 - \frac{3r_a^2}{r^2} \right) \frac{r_a^2}{r^2} \cos 2\theta \quad (4.24)$$

Following the scheme in Figure 4.29, for each circular TZ around the drift's perimeter, the representative stress  $\sigma_{rr}$  corresponds to the elastic solution, according to Eq. 4.24, at the internal radial coordinate of the same TZ. This approach can be justified assuming that, since failure propagates from the previous (inner) zone, elastic conditions ( $f \leq 0$ ) are firstly encountered at the internal radial coordinate of the following (outer) TZ. In the further numerical modelling of drifts at the Andra URL, the extension of this partitioned circular area, from the perimeter  $r = r_a$ , was set to  $(r - r_a) = 6$  m, considered as the potentially damaged area according to Figure 4.1.

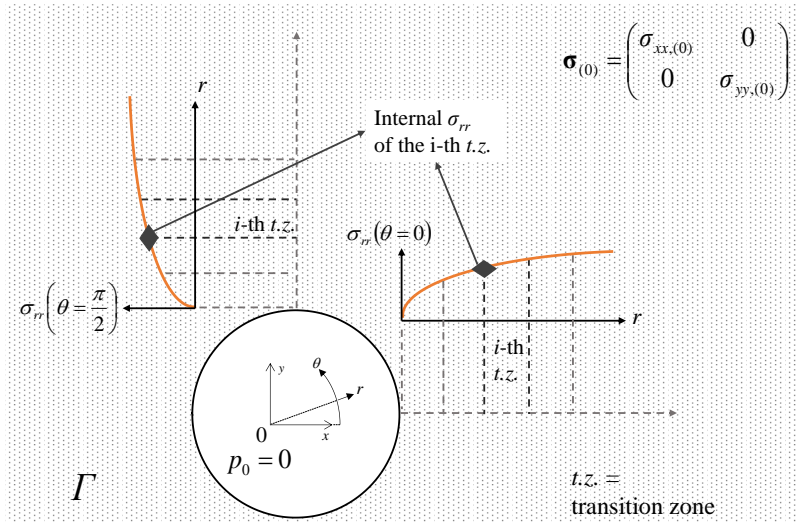


**Figure 4.29** : scheme of the approach to select  $\sigma_{rr}$  representing every *transition zone* for the variation of softening parameters in the post-peak simulation of COx claystone behaviour.

In this area, 3 or 6 transition zones were identified, with a respective thickness of 2 and 1 m. Two series of numerical simulations were performed, according to the boundary conditions representing either GCS or GED drift, to test the existence of possible differences between the first and the second choice. Adopting the relations in Eq. 4.22 and 4.23, the diagrams in Figure 4.30 and Figure 4.31 were plotted, respectively for the elastic solution of  $\sigma_{rr}$  in GCS and GED, and employed to set the couple of parameters  $\beta$  and  $\eta_r$ , representative for every *TZ*. Considering Figure 4.30a and Figure 4.31a, the relation  $\beta(\sigma_{rr})$  is traced, and the values of  $\beta$  are reported on the left vertical axis. Similarly, Figure 4.30b and Figure 4.31b report the relation  $\eta_r(\sigma_{rr})$ . In the same graphics, the elastic solutions for  $\sigma_{rr}(\theta = 0)$  and  $\sigma_{rr}(\theta = \pi/2)$  are traced as a function of the radial coordinate  $(r - r_a)$ , represented on the right vertical axis. The stress values appear on the horizontal axis. As described in Figure 4.29, the reference coordinate to define  $\sigma_{rr}$  for a certain transition zone is the internal one, for *TZ*. To provide an example, for the first *TZ* encountered ahead of the drift perimeter, the inner side corresponds to the perimeter itself, i.e.  $(r - r_a) = 0$ . Similarly, for the case of 3 concentrically *TZs*, the inner side for the external one corresponds to  $(r - r_a) = 2$  m, ahead of the drift's perimeter. In every diagram, once the radial coordinate  $(r - r_a)$  is selected, for a certain transition zone, two  $\sigma_{rr}$  solutions are found, at  $\theta = 0$  and  $\theta = \pi/2$ . Based on a prudential choice, the lowest value of radial stress is considered to choose the correspondent softening parameters  $\beta$  and  $\eta_r$ , i.e.:

$$\sigma_{rr} = \min \left\{ \sigma_{rr}(\theta = 0) ; \sigma_{rr} \left( \theta = \frac{\pi}{2} \right) \right\} \quad (4.25)$$

Every diagram, according to  $\sigma_{rr}$  in Eq. 4.25, provides the value  $\beta$  and  $\eta_r$  for a certain *TZ*. The symbol \* identifies  $\beta$  and  $\eta_r$  at the intersection between the parameter's function and the representative  $\sigma_{rr}$  stress for every *TZ* (delimited by the horizontal dotted lines).

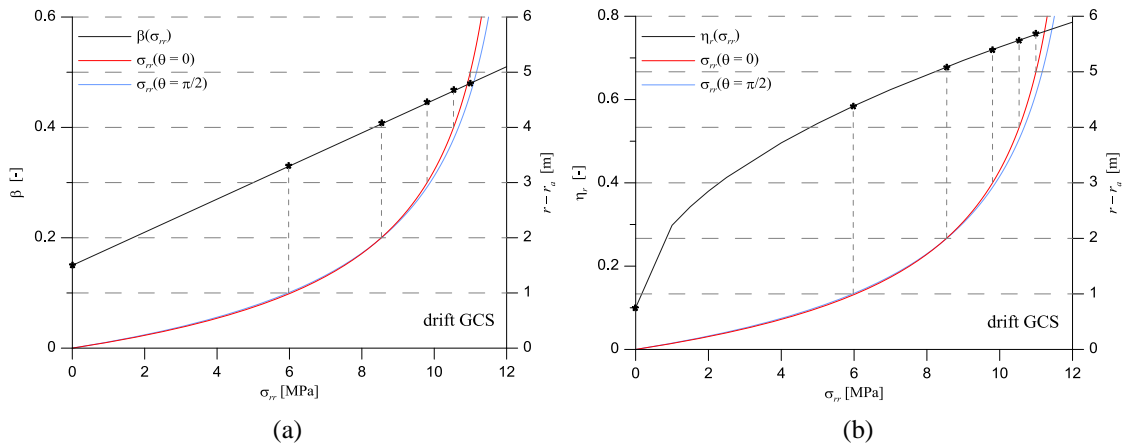


**Figure 4.30** : diagrams for the definition of  $\beta$  (a) and  $\eta_r$  (b) in the transition zones defined in the geometry of numerical modelling for GCS drift.

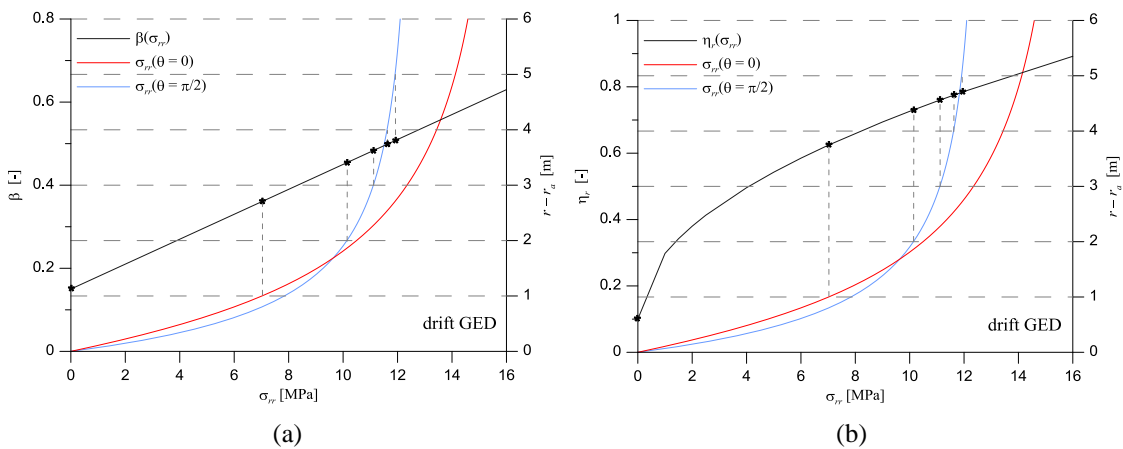


**Figure 4.31** : diagrams for the definition of  $\beta$  (a) and  $\eta_r$  (b) in the transition zones defined in the geometry of numerical modelling for GED drift.

This section concludes the discussion of mathematical and numerical aspects of the modelling for the final 2d plane strain excavation analyses, focusing, successively, on the stress-strain elastic-damage constitutive law (i.e.  $2d\_ESD$  stiffness tensor), the evaluation of anisotropic failure and the variable softening post-peak behaviour.

### 4.5 Final results for plane strain damage around the URL drifts

In the following, numerical results of the FEM analyses performed with the  $2d\_ESD$  anisotropic model are presented and discussed. Together with the description of the different parts forming the whole modelling adopted hereby, the correspondent parametrization was presented. Here, it must be mentioned only the choice of the isotropic elasticity parameters,  $E$  and  $\nu$ , respectively equal to 6000 MPa 0.25. With respect to the previous  $E = 4500$  MPa imposed this chapter's works, 6000 MPa results more representative for the short-term (undrained) response of the highly

saturated material in-situ, as discussed in Section 2.2. (e.g. [10]). The Poisson's ratio corresponds to an average from values reported in published hydro-mechanical analyses accounting for COx anisotropy ([42] and [58]) and corresponds to its interval of variation (e.g. [8], [9]). Parameters for anisotropic failure are included in Table 4.5, for the anisotropic failure criterion described in Section 4.3, and softening parameters accounting for the brittle-ductile transition are identified in the diagrams of Figure 4.30 and Figure 4.31 in Section 4.4. Eventually, the  $2d\_ESD$ , considering the introduced anisotropies and the *brittle-ductile* transition, includes 9 parameters for each *transition zone (TZ)*, around the excavation.  $E$  and  $\nu$  for the  $2d\_ESD$  stress-strain elastic-damage matrix,  $\varphi$  and  $K$  for the failure criterion, the stratification's angle ( $\omega = 90^\circ$ , horizontal bedding) and the coefficients  $h_n$  and  $h_s$ , and couple of softening parameters ( $\beta; \eta_r$ ). Numerical models of geometry and boundary conditions defining the in-situ stress state and reproducing the excavation phase are illustrated in Figure 4.32, with  $r_a = 2.6$  m for the drift GCS and 2.3 m for GED. The initial values of the principal stress components on the cross section  $T$  are reported in Table 4.1. Figure 4.32a reports the equation of the automatic calculus of the initial  $\sigma_{zz,(0)}$  value due to the condition  $\varepsilon_{zz} = 0$ . Results of every numerical analysis present the expansion of the damaged zones and, on the correspondent contour plot, both the extensions of the EDZ and EdZ failure areas are indicated, based on the dotted lines in the 2d scheme in Figure 4.1, depending on the drift considered. Afterwards, for the same analysis, the field of displacements norm,  $\|U\|$ , is shown. It is obtained from the horizontal and vertical components according to Eq. 4.26. Eventually, the distribution plot of the principal stress component  $\sigma_{ij}$ , correspondent to the direction of damage expansion (horizontal or vertical) is illustrated.

$$\|U\| = \sqrt{U_x^2 + U_y^2} \quad (4.26)$$

Numerical results previously introduced are distinguished for the type of drift, GCS or GED, and the quantity of *brittle-ductile* transition zones defined in the geometry numerical model: for every drift, a subdivision of 3 or 6 TZ was simulated. In the first case, every zone, concentrically defined around the circular opening, has a thickness of 2 m. In the second case, each zone is 1 m thick. Includes the following results' illustrations, detailing the subdivision of TZ and the correspondent drift.

**Table 4.6:** contour plots of the analyses' results, according to the boundary conditions and imposed division of transition zones.

		<i>transition zones</i>	
		3	6
<i>drift</i>	GCS	Figure 4.33, Figure 4.34	Figure 4.35, Figure 4.36
	GED	Figure 4.37, Figure 4.38	Figure 4.39, Figure 4.40

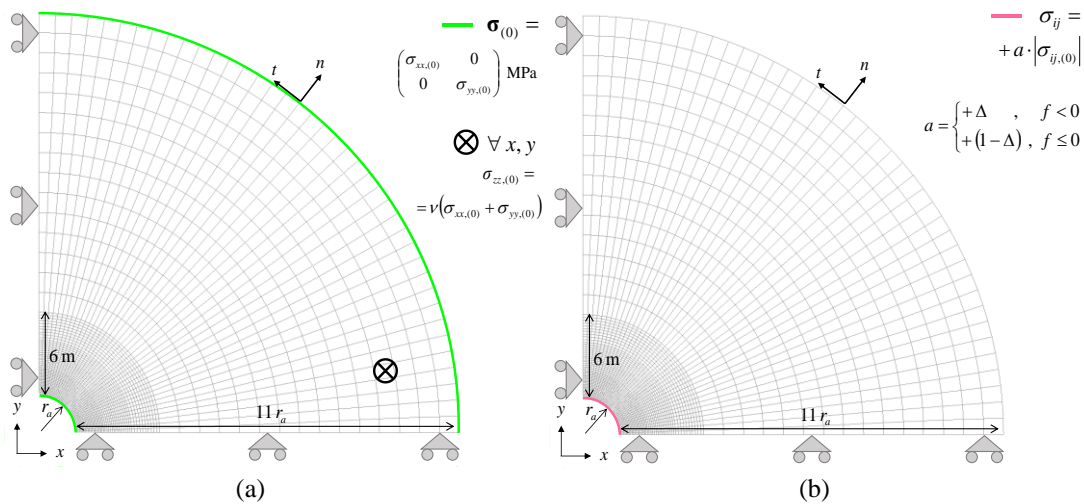


**Figure 4.32** : numerical model, initial conditions (a) and excavation boundary conditions (b) for the last 2d plane strain numerical analyses.

In Figure 4.23, the area surrounding the drift’s perimeter with a finer mesh, 6 m thick, corresponds to the potentially damaged area divided in *brittle-ductile* transition zones. The external area, included up to the external boundary ( $r = 12 \cdot r_a$ ) was assigned with a purely elastic material ( $E = 6000$  MPa and  $\nu = 0.25$ ). Results’ reported in Table 4.6 are now illustrated, listed for every case.

- GCS drift, 3 brittle-ductile transition zones: Figure 4.33 shows the contours for the internal variable  $D$ , which extends around the central coordinate between the EDZ and EdZ, very localized on the horizontal. Figure 4.34a shows the correspondent norm of principal displacements components (Eq. 4.26), with a significant concentration at the perimeter for  $\theta = 0$ . The maximal calculated value,  $\sim 55$  mm at  $x \equiv r = r_a$ , largely overestimates the short-term displacements induced by excavation (e.g. Figure 3.5 and Table 3.3, Section 3.1). The area highly damaged, in the short-term, by the excavation, may be also identified as the zone where stress component is highly reduced, for the case of horizontal damage, the correspondent component is shown. Figure 4.34b shows the distribution of the horizontal stress  $\sigma_{xx}$ .

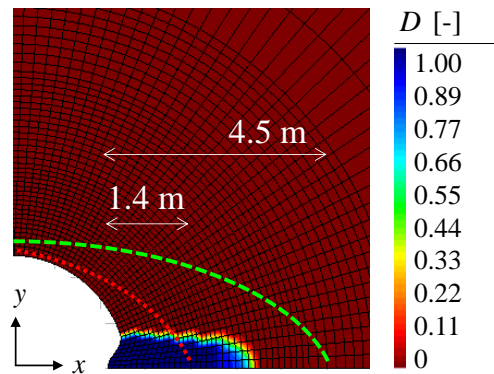


**Figure 4.33**: distribution of the damage variable  $D$  for a complete unloading of the GCS drift with 3 *brittle-ductile* transition zones.

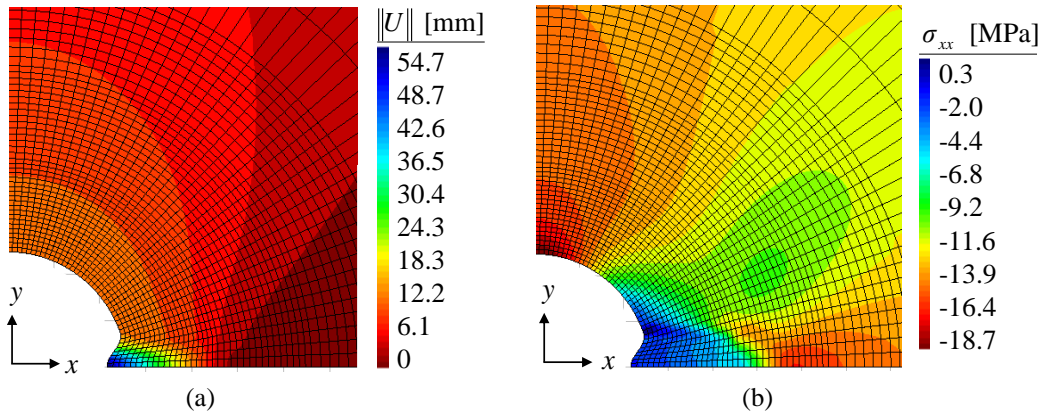


**Figure 4.34:** distribution of displacements' norm (a) and horizontal stress (b) for a complete unloading of the GCS drift with 3 *brittle-ductile* transition zones.

- GCS drift, 6 brittle-ductile transition zones: Figure 4.35 shows the contours of  $D$ , extending beyond the EDZ limit, but still far from the internal EdZ. In this case, it is possible to notice an area, included between the damaged zone and the perimeter, where elastic conditions are still maintained. Physically, it can be considered rigid block potentially subjected to a translation inside the galleries. Its existence recalls in-situ observations showing locally a less damaged area, at the galleries perimeter, surrounded by a diffusely fractured medium, in the EDZ [60]. In Figure 4.35, damage is attained at  $\theta > 0$  (because of the non-monotonic failure calibration in Figure 4.24) and reaches, before the end of excavation, the horizontal. Figure 4.36a shows the correspondent norm of principal displacements' norm components. The localization in correspondence of the perimeter deformation confirms the failure initiation at  $\theta > 0$  and the reported value is very consistent with short-term measures. In particular, for the drift GCS, an interesting work of analysis of the short-term displacements were performed and discussed in some publications (e.g. [8] and [41]), to discern the “immediate” mechanical response, due to the excavation, from displacements associated to creep phenomena, naturally occurring in the COx formation, even at the short-term.

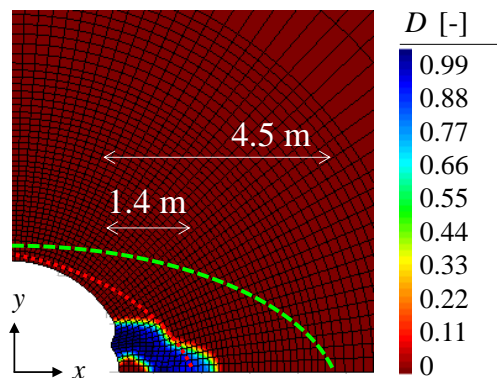


**Figure 4.35:** distribution of the damage variable  $D$  for a complete unloading of the GCS drift with 6 *brittle-ductile* transition zones.

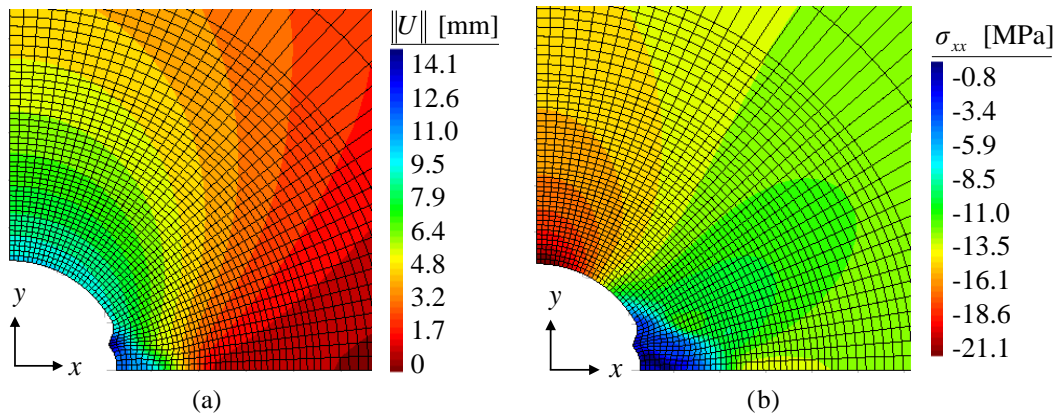


**Figure 4.36:** distribution of displacements' norm (a) and horizontal stress (b) for a complete unloading of the GCS drift with 6 *brittle-ductile* transition zones.

To quantify the mentioned effects, it is reported that, at a distance of about  $4r_a$  from the cross-section analyzed, the “immediate” mechanical response of the material does not occur in any further change. Particularly for GCS drift, at an instrumented section with *mine-by* surveys (Section 1.1) an  $U_x \approx 4$  mm was measured, at  $r = r_a$ , just before the drift's front transition. Adding this value to the material's displacements recorded afterwards, processed to separate the “immediate” response from the creep, a  $U_x \approx 15$  mm was estimated [8], consistent with the value of 14.1 mm calculated at the perimeter. Concerning the contour of  $\sigma_{xx}$  in Figure 4.36b, an almost null radial stress is calculated in the damaged area.

- GED drift, 3 brittle-ductile transition zones: here, the vertical extension of  $D$  appears more important with respect to numerical analyses for GCS and it almost reaches the internal EdZ extension (Figure 4.37). Nonetheless, crossing the external EDZ, it tends to develop with a horizontal *lobe*, likely due to the calibration performed on the failure criterion's anisotropy. In the following, Figure 4.38a and b illustrates respectively  $\|U\|$  and  $\sigma_{yy}$ , which vanishes for quite an extended area up to the external EDZ. At  $\theta = \pi/2$ , a concentration of vertical displacements, comparable to in-situ surveys (e.g. Section 3.2, Figure 3.17), is calculated.

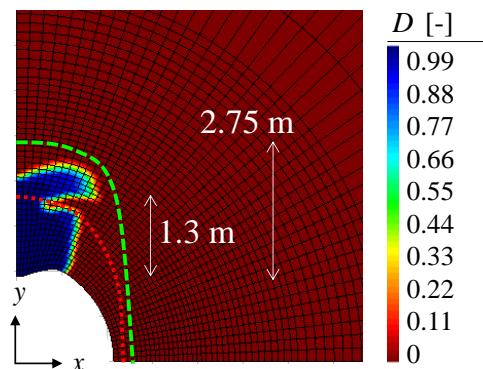


**Figure 4.37:** distribution of the damage variable  $D$  for a complete unloading of the GED drift with 3 *brittle-ductile* transition zones.

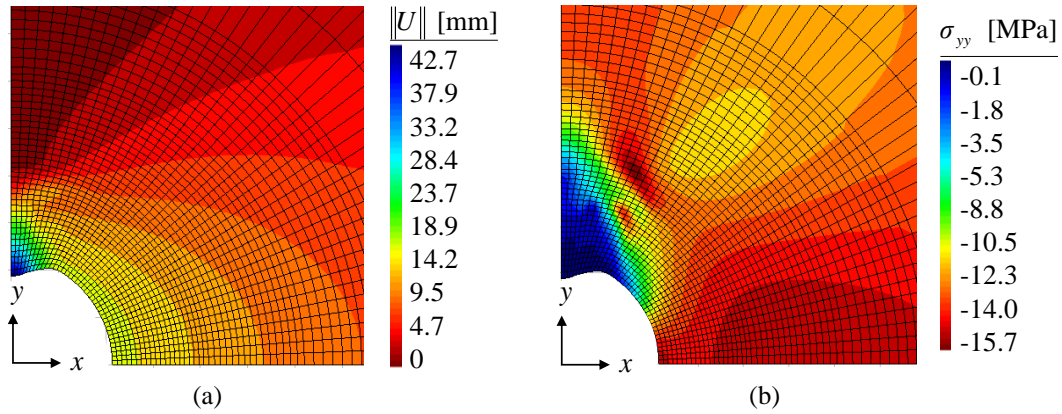


**Figure 4.38:** distribution of displacements' norm (a) and vertical stress (b) for a complete unloading of the GED drift with 3 *brittle-ductile* transition zones.

Nonetheless, for this drift, a reduced quantity of data does not permit a discussion similar to the previous one for GCS, in terms of separation between “immediate” material response and creep effects.

- GED drift, 6 brittle-ductile transition zones: Figure 4.39 illustrates the contour plot for  $D$  and Figure 4.40a and b those for  $\|U\|$  and  $\sigma_{yy}$  respectively. With a finer subdivision of the entire *brittle-ductile* zone, subjected to failure, the numerical result of damage may be qualitatively compared to Figure 4.35. In this case, the stronger anisotropy of the initial  $\sigma_{(0)}$  provokes failure localization at  $\theta < \pi/2$ . Then, the internal variable evolves towards the vertical and joins the symmetric damage lobe, in a unique failure zone crossing the upper limit of the EDZ. Eventually, an area of about 1 m remains in elastic conditions and translates rigidly towards the drift's perimeter. Further the EDZ limit, in the area upper delimited by the EdZ, damage produces another horizontal localizations, smaller the one in Figure 4.37 but likely governed by the same phenomena of stresses' redistribution around the area where  $0 < D < 1$  and  $f = 0$ . Concerning vertical displacements localized at the failure initiation, the calculation ( $\sim 23$  mm) results in an underestimations of the measures by extensometers ( $\sim 40$  mm).

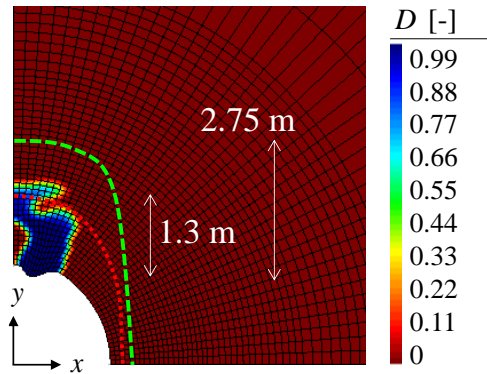


**Figure 4.39:** distribution of the damage variable  $D$  for a complete unloading of the GED drift with 6 *brittle-ductile* transition zones.

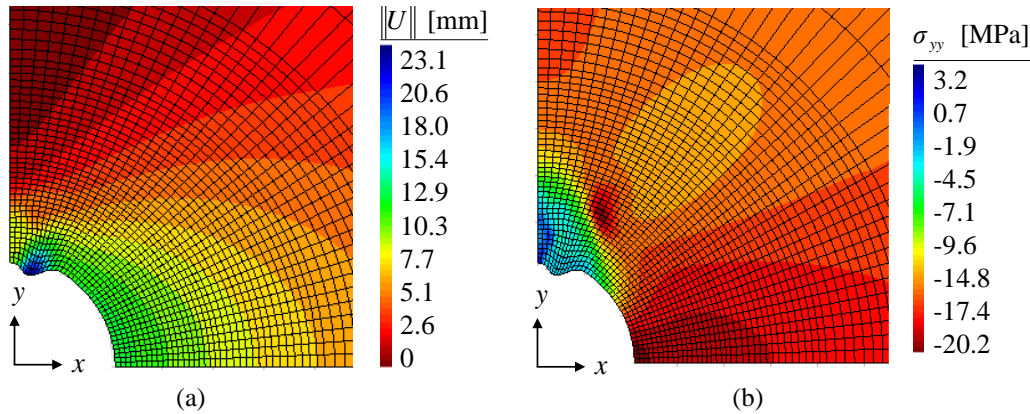


**Figure 4.40:** distribution of displacements' norm (a) and vertical stress (b) for a complete unloading of the GED drift with 6 *brittle-ductile* transition zones.

Before moving to the conclusion of this chapter, in the following, two last numerical analyses are presented, respectively for GCS and GED drift, identical to those previously reported, for the case of 6 transition zones distributed around the circular opening. Hereby, the only difference corresponds to value chosen for the parameter  $\beta$  (deformation softening coefficient) in the  $2d\_ESD$  model. In particular, as mentioned already in the relative Section 4.4, it can be stated that the trend adopted to relate  $\beta$  to  $\sigma_{rr}$  would not be as precise as the one for  $\eta_r$ , due to the higher dispersion of the values obtained by the reviewed data (e.g. Figure 4.28a and b). The linear fitting curve proposed in Eq. 4.22 is based on the 70% of the considered data, to provide a relation that indicates an increasing  $\beta$  with  $\sigma_{rr}$ , consistent with the analogue relation of  $\eta_r$  in Eq. 4.23 and the conceptual model in Figure 4.27. Here, the case of a constant  $\beta = 0.4$  for every *transition zone* is analysed. This value correspond to the mathematical average of the values obtained from the TXc tests reviewed and reported in the plot in Figure 4.28b and, this time, this average includes every data from TXc. The radial variation of the stress softening ratio,  $\eta_r$ , is exactly equal to the former analyses (Table 4.6). Results illustrated from Figure 4.41 to Figure 4.44 are listed in the following:

- GCS drift, 6 *brittle-ductile* transition zones,  $\beta = 0.4$ :

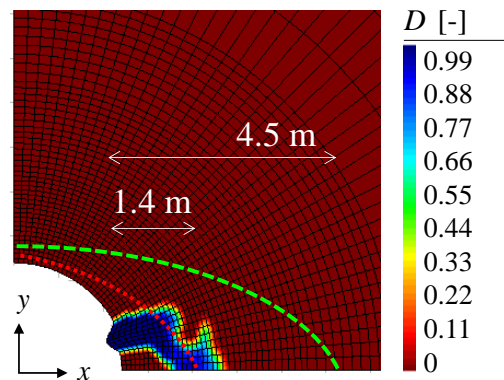


**Figure 4.41:** distribution of the damage variable  $D$  for a complete unloading of the GCS drift with 6 *brittle-ductile* transition zones and  $\beta = 0.4$ , everywhere assigned.

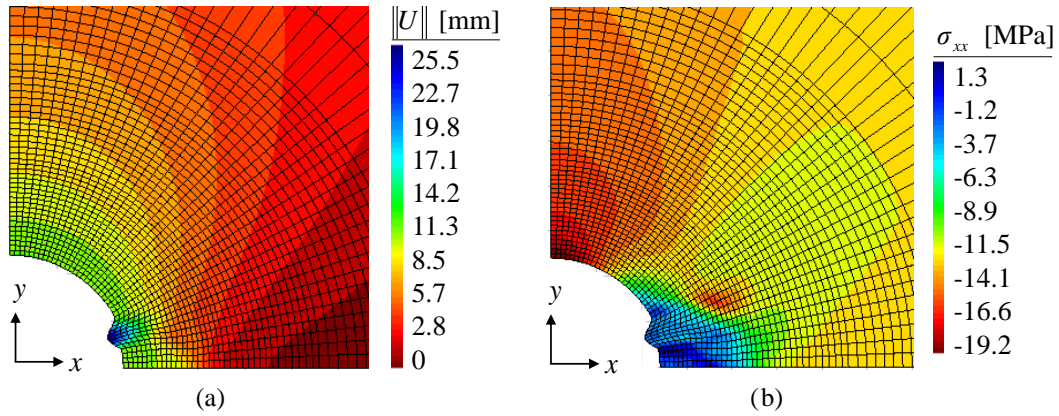


**Figure 4.42:** distribution of displacements' norm (a) and horizontal stress (b) for a complete unloading of the GCS drift with 6 brittle-ductile transition zones and  $\beta = 0.4$  everywhere assigned.

- GED drift, 6 brittle-ductile transition zones,  $\beta = 0.4$ :

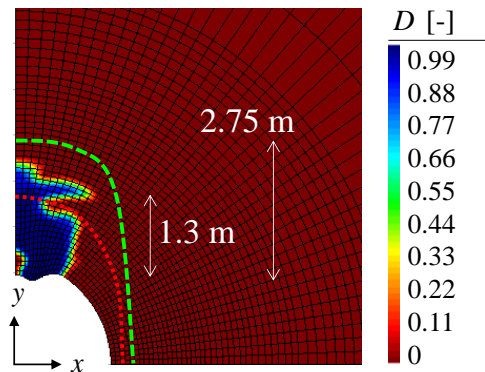


**Figure 4.43:** distribution of the damage variable  $D$  for a complete unloading of the GED drift with 6 brittle-ductile transition zones and  $\beta = 0.4$ , everywhere assigned.

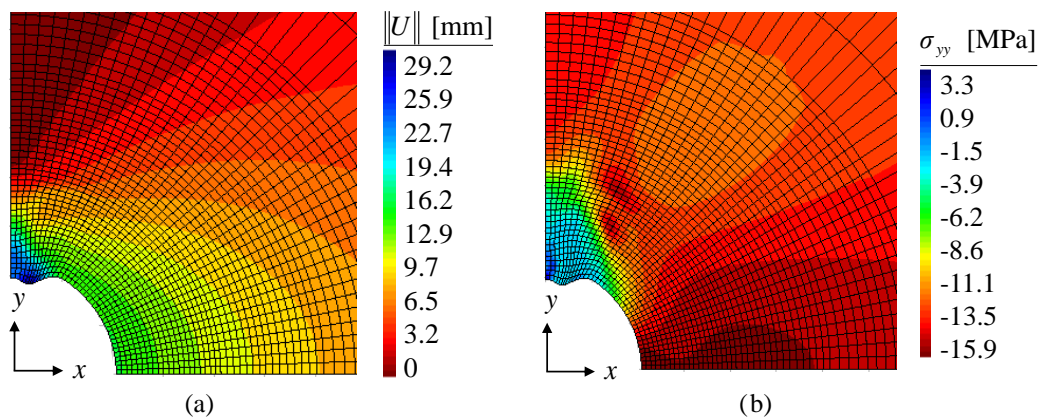


**Figure 4.44:** distribution of displacements' norm (a) and vertical stress (b) for a complete unloading of the GED drift with 6 brittle-ductile transition zones and  $\beta = 0.4$ , everywhere assigned.

In analogy with every case of 6 transition zones and  $\beta$  variable, the elastic limit is attained neither along the horizontal direction ( $x$ ) nor along the vertical ( $y$ ). Because of the failure criterion's calibration (Figure 4.24), damage variable  $D$  initiates along an inclined direction between the horizontal and vertical:  $\theta > 0$  for GCS and  $\theta < \pi/2$  for GED. Particularly evident in Figure 4.41, a

sub-horizontal damage *lobe* or *band*, is produced at  $r = r_a$ , for  $\theta > 0$ , and develops beyond the external EDZ. Then, it evolves towards the horizontal and joins, for symmetry, an equivalent damage zone located at  $\theta < 0$ . Analogue considerations can be done for the excavation analysis of GED and, eventually, in both cases, an elastic zone at  $r = r_a$ ,  $\theta = 0$  (GCS) or  $r = r_a$ ,  $\theta = \pi/2$  (GED) is calculated. Concerning the shape and extension of the failure zone, results in Figure 4.41 and Figure 4.43 can be compared to the corresponding ones, respectively, in Figure 4.35 and Figure 4.39. More precisely, if  $\beta = 0.4$  constant in the entire domain, the final contour plots of damage  $D$  attain an extension, on the horizontal or vertical according to the boundary conditions, relatively higher than assuming  $\beta = \beta(\sigma_r)$ . In any case, compared to GCS, the shape and extension of  $D$  in GED covers better the area included in the EDZ-EdZ system, illustrated in the 2d conceptual model in Figure 4.1. In the following, Table 4.7 summarizes the computed displacements at every drift's perimeter. It seemed more appropriate to define them as *sub-horizontal* and *sub-vertical*, instead of horizontal and vertical, because of the cases where the most important localizations do not occur exactly at  $\theta = 0$  or  $\theta = \pi/2$ . In the same Table, estimated values from extensometers or mine-by tests at the Andra URL are reported. In particular, the interval of admissible values for GCS *sub-horizontal* displacements is reduced, for instance, with respect Table 3.7 in Section 3.2 for the availability of data and analysis from mine-by tests, with the separation of *excavation-induced* from creep effects. Logically, a finer discretization of *transition zones* would allow finer calculations, to avoid overestimations as in Figure 4.34a (GCS). Nonetheless, Figure 4.38a shows a better estimation of  $U_y(\theta \approx 90^\circ)$  with 3 transition zones (GED). The integration of a damage law  $g(D)$  accounting for a post-peak transition from softening to hardening seems the logical consequent upgrade to the model, not to the monotonic unconfined compression (i.e. Figure 4.3) as the only experimental observation to simulate the stress-strain material's behaviour.

**Table 4.7:** summary of sub-horizontal and sub-vertical displacements calculated around GCS and GED drifts' perimeter ( $r = r_a$ ), specifying the number of transition zones *TZs*, with the short-term estimations at the Andra URL ([8], [41], [42], [91] and [93]).

		$ U_x , \theta \approx 0$ [mm]		$ U_y , \theta \approx 90^\circ$ [mm]	
		<i>calculation</i>	measures	<i>calculation</i>	measures
GCS, 3 <i>TZs</i>	Figure 4.34a	54.7		11.6	
GCS, 6 <i>TZs</i>	Figure 4.36a	14.1	[15 ; 20]	8.7	~ 10
	Figure 4.42a	25.5		10.8	
GED, 3 <i>TZs</i>	Figure 4.38a	14.6		42.7	
GED, 6 <i>TZs</i>	Figure 4.40a	11.4	~ 10	23.1	~ 40
	Figure 4.44a	14.5		29.2	

## Conclusion

With this chapter, finite element analyses on 2d plane strain models for damage-based *diffused* failure around drifts at the Andra URL are concluded. The final mathematical and numerical upgrades are presented to improve the modelling propositions in Chapter 3, based on the framework introduced in Chapter 2. The elastic-damage constitutive law, formalized through the  $2d\_ED$  model at the end of the second chapter and adopted in the third, was substituted with the  $2d\_ESD$  model, available in the most recent version of *POROFIS*.

With respect to the failure criterion in Chapter 3, a formulation based on a IV order *anisotropic rotation tensor* was presented here to overcome the dissymmetry of damage attainment around the excavations' perimeter, initially encountered in numerical analyses. In parallel, an arbitrary quantity of concentrically distributed areas was defined within the analysis' domain before simulations: this "geometrical-numerical" procedure is proposed to consider the progressive ductility in the material's softening behaviour, shown by Callovo-Oxfordian specimens under confined compression.

The chapter is concluded with the discussion and presentation of the excavations' numerical analyses for the considered drifts at the Andra URL, according to the respective boundary conditions (quasi-isotropic or anisotropic initial stress state in the drift's cross-section). Short-term shape and extension of calculated damaged areas develop according to the conceptual models from in-situ surveys ([9], [60], [91] and [93]), covering mostly the part denoted as EDZ, even if they are not capable to cover the entire EDZ-EdZ failure system. A finer discretization for the *brittle-ductile* transition of the material provides a damage distribution more diffused around the perimeter, instead of localizing along one of the main directions (e.g. the horizontal, for GCS). At the end of the excavation, the formation of an *elastic block* is calculated, in the proximity of the perimeters, on either the horizontal or the vertical, moving as a rigid body within the surrounding damaged formation.

Concerning displacements' analyses, they are generally consistent with in-situ measurements, even if under- or over-estimations are obtained. With the  $2d\_ESD$  constitutive law, a re-implementation of anisotropic elasticity may improve the displacements prediction. For this type of deep galleries, coupling an instantaneous and fragile phenomenon as damage with viscoplasticity effects may constitute an interesting perspective to this work. This type of consideration constitutes the object of a more detailed discussion in the thesis' conclusions and perspectives.



## **Chapter 5**

# **Discrete Modelling of *Chevron* Fractures**



The last chapter presenting Finite Element analyses concerns the modelling of fractures patterns around drifts at Andra Underground Research Laboratory (URL). The problem is approximated in 2d axisymmetric conditions for the simulations' purposes; moreover, this part of analyses introduces also, for geometry discretization, linear *joint* elements (e.g. [39]) in order to reproduce discontinuities in a FEM-based numerical model. Unloading effects around drifts and localizations of shear strains in the geological formation of Callovo-Oxfordian claystone lead to the formation of discontinuous structures, induced by the excavation, often named *Chevron* or *herringbone* fractures, constituting the subject of this chapter.

As described in Chapter 1, the forthcoming numerical analyses constitutes a second axis of research within the thesis' works. It must be underlined that it is not studied as deeply as the first axis of research, discussed through Chapter 2, 3 and 4. This topic is more intended as complementary for the investigation of the short-term failure initiation and evolution for drifting at the Andra URL and constitutes a transition from a continuous to a discontinuous mechanical approach. In particular, while the calculated fractures' length is discussed from a quantitative point of view, in relation with in-situ measurements, the possibility of a periodical appearance of fractures along the drift's perimeter is limited to a qualitative discussion, related to the numerical methodology to simulate a gallery excavation.

### 5.1 Problem definition with constitutive and numerical modelling

This section opens describing the mechanical problem to simulate real scale observations of fractures' occurrences at the Andra URL, detailed in Chapter 1, Section 1.1. Concluding that section, the division of the thesis in two axis of research was discussed. The first, main part, dealing with plane strain analyses of the excavation around drifts' cross-section, assumed failure as "diffused" in a calculated damaged zone (where failure criterion  $f=0$ ). This second part, driven by 2d axisymmetric simulations, constitutes a complementary approach to the description of a damage-based, short-term failure around galleries at the Andra URL, according to Figure 5. 1 - with the specific case of GCS drift in Figure 5. 1b. Analyses presented hereby consider failure as a *discontinuous system* of excavation-induced fractures: numerical simulations treat the occurrence of *distinct fractures*, often called *Chevron* or *herringbone* fractures (e.g. [9], [55] and [60]), described in Section 1.1. Failure localizations, considered in the previous chapters as a *continuous system*, collapse in fractures, creating displacements' discontinuities, which thickness becomes negligible compared to the initial localization. Existing publications (e.g. Lisjak et al., 2014 [54]) discuss analogue approaches from *continuum* to *discontinuum* mechanics, related to the drifting action in claystones and shales.

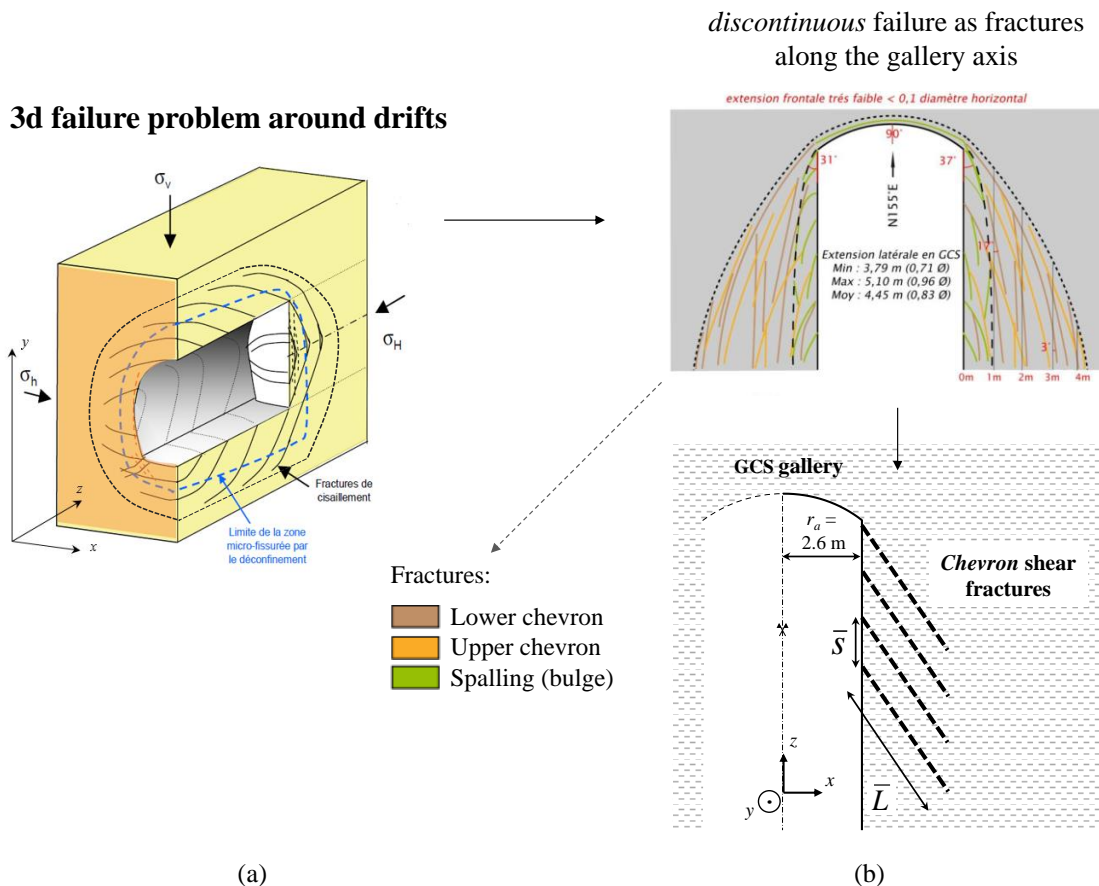


**Figure 5. 1:** conceptual model of the 3d geomechanical problem in (a) and proposed simplification of 2d axisymmetric modelling of discontinuities in (b). Original figures modified from [60] and [93].

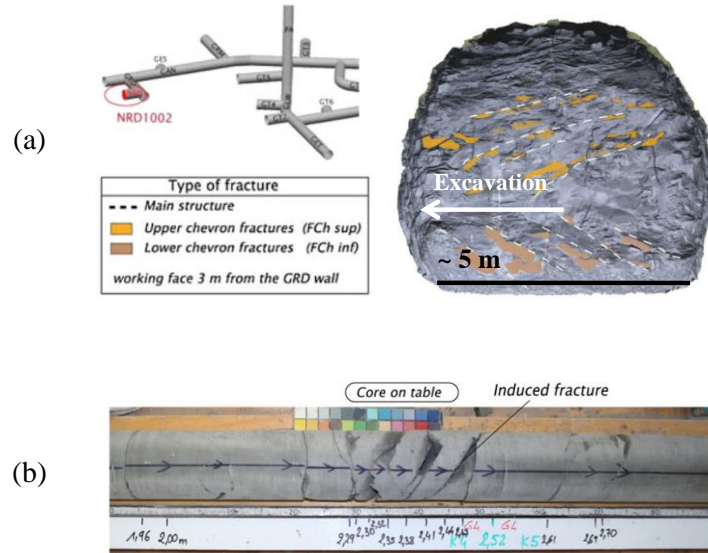


**Figure 5. 2:** 3d scan structural survey for the interpretation of shear *Chevrons*' structure, in (a), and excavation-induced fractures in drill core, in (b). Modified from [9].

Focusing on the specific case of Andra URL, several drifts show systematic fracturing in the area defined as EDZ-EdZ in Chapter 1. Section 1.1 describes with more details these cracking occurrences, which interpretation and conceptual models are illustrated from Figure 1.6 to Figure 1.9. Figure 5. 2a reports a 3d scan interpretation in a pilot drift to reconstruct the pattern of excavation-induced fractures (*Upper* and *Lower Chevron* fractures) in a perpendicular gallery at the Andra URL, while Figure 5. 2b shows a drill core where shear fractures were observed at a radial coordinate  $r \sim 2.4$  m from the sidewall [9]. The numerical treatment of the 2d axisymmetric problem in Figure 5. 1b is executed with both the FEM code *POROFIS* [72] and *DISROC* (<http://www.fracsima.com/>), introduced in Chapter 2, Section 2.1. These FEM codes allow the processing of Finite Elements models with the inclusion of linear *joint elements* (e.g. [39]) in the mesh. They adopt the modulus *DISCRAC* (<http://www.fracsima.com/>) to include joint elements, creating *Joints-Enriched* Finite Element numerical models (*JFEM*). Discontinuities in the displacement field may exist with the relative stress values verifying the constitutive laws at the integration points (e.g. Gauss points) of the linear joints. Figure 5. 3 reports a schematisation of the geomechanical problem at the different analysis' scales: from the left, the same conceptual model for 2d axisymmetric simulations shown in Figure 5. 1b is reported, describing shear Chevron fractures (*FCh*) as a system of parallel discontinuities, with a certain inclination to the drift sidewall. This illustration refers to the specific case of GCS drift, adopted throughout the entire chapter as case study gallery. It is preferred when performing 2d axisymmetric analyses, because, according to the Cartesian system  $(x, y, z)$  and the stress state  $\sigma_{(0)}$  in Table 5. 1, it is possible to write:

$$\sigma_h \approx \sigma_v \rightarrow \sigma_{xx,(0)} \approx \sigma_{yy,(0)} \quad (5. 1)$$

**Table 5.1** : description of  $\boldsymbol{\sigma}_{(0)}$  for GCS drift (e.g. [9], [60], [113]).

$\sigma_h = \sigma_{xx,(0)}$ [MPa]	$\sigma_v = \sigma_{yy,(0)}$ [MPa]	$\sigma_H = \sigma_{zz,(0)}$ [MPa]
-12.4	-12.7	-16.2

For numerical analyses presented in this chapter, boundary conditions assume  $\sigma_{xx,(0)} = \sigma_{yy,(0)}$ . In general, an average value of  $\sigma_{xx,(0)} = \sigma_{yy,(0)} = -12.5$  MPa is imposed in numerical analyses, while  $\sigma_{zz,(0)} = -16.2$  MPa. In Figure 5.3, the problem simplification focuses on two variables describing the system of parallel *FCh*: their (finite) length of propagation,  $\bar{L}$ , and mutual spacing  $\bar{s}$ , i.e. the distance separating two consecutive fractures. In particular, these variables constitute the targets of the forthcoming numerical analyses: for sake of simplicity,  $\bar{L}$  can be assumed as the horizontal average extension of the failure system EDZ-EdZ around GCS drift (e.g. Table 1.1, Chapter 1). In general, it can be approximated to an average value  $\sim 1.6 \cdot r_a$ , where  $r_a = 2.6$  m is the design GCS radius. Nonetheless, according to the 2d schematization in Figure 5.3, the single *FCh*, included in the area corresponding to the system EDZ-EdZ, presents a certain inclination  $\alpha$  with respect to the drift's perimeter, estimated from in-situ measurements within an interval  $\alpha \in [30^\circ; 40^\circ]$  (e.g. [60]). Thus, with respect to the EDZ-EdZ horizontal extension  $\sim 1.6 \cdot r_a$ , the effective extension  $\bar{L}$  of the single fracture, taking into account  $\tan(\alpha)$ , would include an interval included between 5 and 7 m. Concerning the variable  $\bar{s}$ , this is typically assessed from resin-injection tests on radial core-drillings [9]. From Figure 1.7 in Section 1.1, an average density of 5-6 fractures per meter at the side of GCS drift is esteemed, but a great variation along the radial direction may occur. Concerning this variable, the principal objective in the performed analyses is to control if a certain fracturing periodicity can be obtained. Referring to the sequence of *FCh* assimilated with joint elements (Figure 5.3), fracturing periodicity means the simulation of one activated sequence of joints (i.e. open fracture) every finite quantity  $n$ . While  $\bar{L}$  can be studied even with a single-fracture model (presented in Section 5.2), for spacing  $\bar{s}$ , a multi-fractures approach is needed (i.e. JFEM models with multiple sequences of parallel joints, presented in Section 5.3).

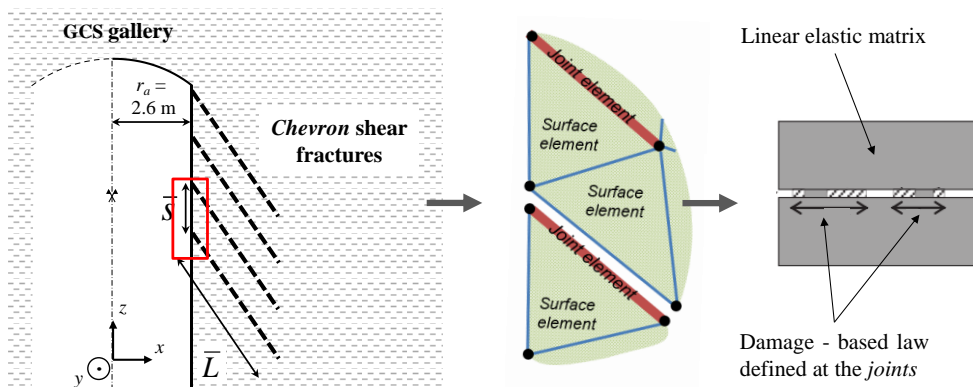


**Figure 5.3**: multi-scale scheme for 2d axisymmetric simulations. From the left: simplified geometry at the drift scale, numerical implementation of potential fractures with joint elements and definition of the discontinuities' constitutive law (modified from [76]).

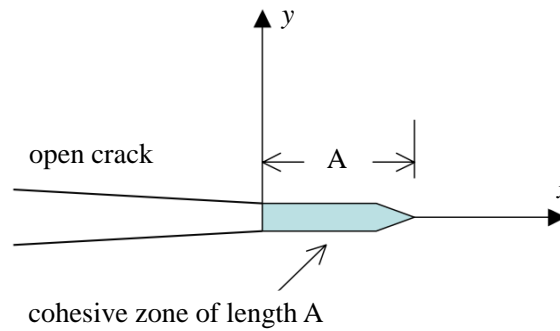


**Figure 5. 4:** schematization of a cohesive zone model for crack evolution. Modified from [47].

The ultimate level of the modelling approach in Figure 5. 3 concerns the definition of the constitutive law for joints. From the mechanical point of view, potential fractures are modelled according to the *cohesive fracture* approach. In a cohesive zone model, a narrow band of vanishing thickness, the *cohesive zone*, is assumed ahead of a crack tip to represent the fracture process zone, as reported in Figure 5. 4 [47]. The upper and lower surfaces of this band are defined *cohesive surfaces* and are yieldable following a constitutive law that relates the stress state  $\sigma$  with the relative displacements  $\mathbf{u}$  among the surfaces themselves. In a bi-dimensional modelling, both  $\sigma$  and  $\mathbf{u}$  have two components, normal and tangential. Crack growth occurs when the separation at the tail of the cohesive zone (physical crack tip) reaches a critical value according to a defined failure criterion, for one or more failure mechanisms. The advantage of a cohesive zone modelling is the absence of stress singularities at the crack tip, present in classical fracture mechanics (e.g. LEFM, Linear Elastic Fracture Mechanics) [47]. As done in the previous chapters for FEM numerical models of *continuous failure*, a damage dissipation constitutes the unique yielding mechanism governing the constitutive law evolution that relates  $\sigma$  and  $\mathbf{u}$ . Damage mechanics describes the phenomena of progressive degradation of strength and stiffness in the rock, eventually leading to fractures. In the constitutive model adopted, material damage as yielding process is integrated in the *cohesive fracture* framework proposed by Pouya and Bemani [76]. Damage internal variable  $D$  corresponds to the measure of the degradation occurring in every potential discontinuity, numerically assumed as a joint element. After first yielding ( $D = 0$ ), this may be damaged up to a complete failure of the *cohesive zone*, corresponding to the fracture activation ( $D = 1$ ), with the occurrence of a discontinuity in the surrounding displacements' field, according to the scheme in Figure 5. 5.

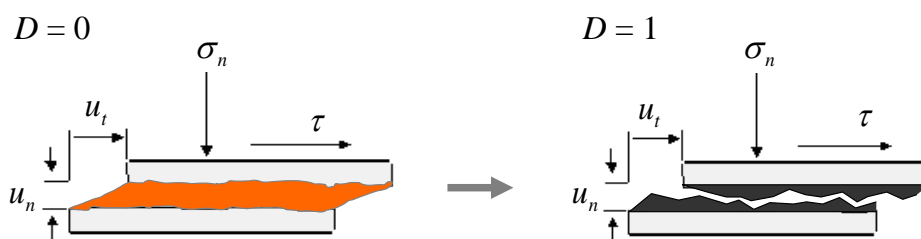


**Figure 5. 5:** damage degradation of the single joint cohesive zone (<http://mecharock.net/>).

Figure 5. 5 illustrates, in the initial and fully damaged configurations of the interface, tangential and normal components of  $\boldsymbol{\sigma}$  and  $\mathbf{u}$ , respectively,  $[\tau \ \sigma_n]^T$  and  $[u_t \ u_n]^T$ . According to the modelling framework (e.g. [34], [76]), the damage-based constitutive law relating kinematic with static variables, writes:

$$\boldsymbol{\sigma} = \begin{bmatrix} \tau \\ \sigma_n \end{bmatrix} = (1 - D)\mathbf{K} \cdot \mathbf{u} + s \cdot \mathbf{k}_\theta \cdot \mathbf{u} \quad ; \quad \mathbf{u} = \begin{bmatrix} u_t \\ u_n \end{bmatrix} \quad (5. 2a-b)$$

$s$  is defined as a binary contact parameter, i.e.  $s = 0$  in absence of contact between the fracture's surfaces and  $s = 1$  if contact occurs. From the physical point of view,  $s = 1$  corresponds to compressive behaviour, e.g. fracture closing,  $u_n \leq 0$ : the damage cohesive model respects the condition of non-penetration of the surfaces, meaning  $u_n > -e_0$ , where  $e_0$  is the joint aperture. The tensor  $\mathbf{K}$  identifies the stiffness of intact material, degraded by the internal variable  $D$  at yielding:

$$\mathbf{K} = \begin{bmatrix} K_{tt} & 0 \\ 0 & K_{nn} \end{bmatrix} \quad (5. 3)$$

In Eq. 5.2a, a residual stiffness  $\mathbf{k}_\theta$  of the discontinuity's cohesive surfaces is accounted even with  $D = 1$ , when contact occurs between the surfaces, i.e.  $s = 1$ :

$$\mathbf{k}_\theta = \begin{bmatrix} k_{0t} & 0 \\ 0 & \frac{k_{0n}}{\left(1 + \frac{u_n}{e_0}\right)^2} \end{bmatrix} \quad (5. 4)$$

The term  $a_{ij} = a_{22}$  in Eq. 5.4 corresponds to a residual constitutive parameter in presence of normal loading, already described by the hyperbolic-shaped model proposed by Bandis et al. [11]. Concerning the formalisms of the criterion describing failure of the cohesive zone, the model implies a hyperbolic yield surface, which shape assures a smooth transition from the pure normal or shear mode failure to mixed modes, according to the model in Figure 5. 6a, for  $D = 0$  [76]. This type of yield surface follows a series of analogue criteria, as the formulation proposed in Carol et al. [21], where two limit situations may be distinguished for crack initiation:

- cracking under pure tension with zero shear stresses, i.e. mode *I*, when the yield surface is reached along the horizontal axis in Figure 5. 6a;
- cracking under shear and very high compression, when the surface is reached in its asymptotic region, where the hyperbola approaches a Coulomb criterion (i.e. asymptotic mode *II*).

As mentioned, at yield fractures may also develop in a mixed mode included between the former threshold modes. Cohesive fracture's failure criterion, in the proposition of Pouya and Bemani [76] is expressed as function of tangential and normal stresses,  $\tau$  and  $\sigma_n$ , and damage,  $D$ , writing:

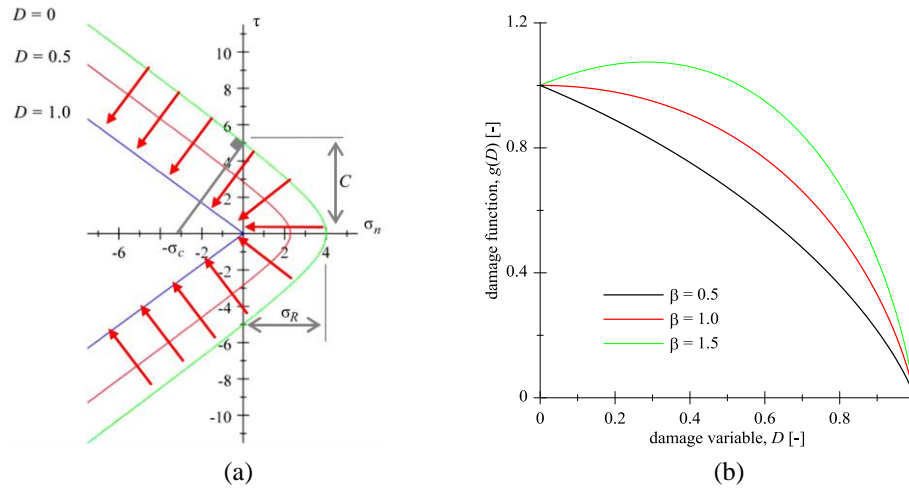


**Figure 5. 6:** cohesive fracture's yield surface, in (a), modified from [76]. Damage law  $g(D)$ , for different values of the yielding parameter  $\beta$ .

$$F(\boldsymbol{\sigma}, D) = \tau^2 - \sigma_n^2 \tan^2 \varphi + 2g(D)\sigma_n\sigma_c - g^2(D)C^2 \quad (5. 5)$$

In Eq. 5.5,  $\varphi$  represents the friction angle, still acting as unique failure parameter in residual condition, i.e. damaged joint with  $D = 1$ .  $C$  and  $\sigma_R$  are, respectively, the cohesion and the tensile resistance of the intact joint ( $D = 0$ ); in particular,  $C$  represents its shear strength under zero normal stress. The yield surface in Figure 5. 6a implies also the condition  $C > \sigma_R \cdot \tan \varphi$ .  $\sigma_c$  is an auxiliary constant parameter, related the strength parameters previously mentioned, writing:

$$\sigma_c = \frac{C^2 + \sigma_R^2 \tan^2 \varphi}{2\sigma_R} \quad (5. 6)$$

As illustrated in Figure 5. 6a, the parameter  $\sigma_c$  may be geometrically interpreted in relation to the shape of the yield surface: if the perpendicular to the yield surface is traced at a pure shear stress state ( $\sigma_n = 0$ ,  $\tau = C$ ), this line intersects the  $\sigma_n$  axis at the point  $\sigma_n = -\sigma_c$ . Eq. 5.5 includes the damage yielding law,  $g(D)$ , function of the internal damage variable, defined within  $[1; 0]$ . Its behaviour varies according to a parameter,  $\beta$  that describes the hardening/softening yielding process after cracking initiation. Figure 5. 6a reports, for a certain choice of failure parameters (e.g.  $C = 5$  MPa and  $\sigma_R = 4$  MPa), the evolution of the yield surface  $f$  when damage increases. In particular, if  $D = 1$ ,  $f$  turns into a Mohr-Coulomb failure criterion (purely frictional joint). This is confirmed mathematically in Eq. 5.5, due to the definition of the extreme values of  $g(D)$ :

$$g(D=0)=1 \quad \wedge \quad g(D=1)=0 \quad (5. 7)$$

The following and final part of Section 5.1 describes the definition of the  $g(D)$  (Figure 5. 6b), playing a crucial role in the evolution of fractures numerically simulated and presented in the next sections. From a physical point of view, cracking and damage may initiate before the maximum stress is attained on the stress-displacement curve, when the potential discontinuity is solicited.

Even if damage always produces a decrease of the elastic stiffness, an immediate decrease of the stress is not necessarily implied. On the contrary, an initial hardening phase may occur in the material. Again, in less recent models, the ultimate damage state is usually attained for a finite strain; nonetheless, experimental data show that, for shear deformation under high compressive stresses, the shear stiffness maintains a finite residual value even after great displacements [76]. The cohesive model adopted overcomes this limitation defining the damage variable evolution by an exponential function of the relative displacement. It is supposed that, under a normal tensile stress on the cohesive fracture,  $D$  remains equal to zero up to a displacement value  $u_{n(0)}$ , representing the elastic limit, and then  $D$  increases with  $u_n > u_{n(0)}$ :

$$D = 1 - \exp\left[-\frac{(u_n - u_{n(0)})}{\beta \cdot u_{n(0)}}\right] \quad (5.8)$$

This evolution is governed by the parameter  $\beta$ , which increases as the cohesive zone ductility. Progressive modifications to the internal variable  $D$  depend on the consistency law  $f = \dot{f} = 0$  during damage process:

$$\dot{f} = \frac{\partial f}{\partial \boldsymbol{\sigma}} \dot{\boldsymbol{\sigma}} + \frac{\partial f}{\partial D} \dot{D} = 0 \quad \rightarrow \quad \dot{D} = -\frac{\partial f}{\partial \boldsymbol{\sigma}} \cdot \left(\frac{\partial f}{\partial D}\right)^{-1} \cdot \dot{\boldsymbol{\sigma}} \quad (5.9a-b)$$

The analytical determination of  $g(D)$  is possible considering a simple case of monotonic loading, when, at yielding,  $f = \dot{f} = 0$ . Under a pure increasing tensile stress  $\sigma_n$ , with  $\tau = 0$ , the cohesive zone starts to dissipate at a normal stress  $\sigma_n = \sigma_R$ , the tensile strength. According to this yielding condition, the criterion in Eq. 5.5 writes:

$$F(\boldsymbol{\sigma} = \sigma_n, D) = -\sigma_n^2 \sigma_R \tan^2 \varphi + g(D) \sigma_n C^2 + g(D) \sigma_n \sigma_R^2 \tan^2 \varphi - g^2(D) \sigma_R C^2 \quad (5.10a)$$

$$= [\sigma_n - g(D) \sigma_R] \cdot [g(D) C^2 - \sigma_n \sigma_R \tan^2 \varphi] = 0 \quad (5.10b)$$

Eq. 5.10b vanishes when the elastic limit is reached for the first time, meaning  $f = 0$  with  $D = 0$ . According to  $g(D)$  thresholds in Eq. 5.7 and the yield surface's shape, from Eq. 5.10b, one writes:

$$\sigma_n = \sigma_R, \quad g(D) = 1, \quad C^2 > \sigma_R^2 \tan^2 \varphi = 0 \quad \rightarrow \quad \sigma_n = g(D) \sigma_R \quad (5.11)$$

The last condition in Eq. 5.11, replaced in Eq. 5.10b when the monotonic loading increases, implies:

$$[\sigma_n - g(D) \sigma_R] \cdot [g(D) C^2 - \sigma_n \sigma_R \tan^2 \varphi] = g(D) \cdot (C^2 - \sigma_R^2 \tan^2 \varphi) \quad (5.12)$$

Since  $C > \sigma_R \cdot \tan \varphi$  for the yield surface's geometry, Eq. 5.12 must respect the condition  $f = 0$  only if  $[\sigma_n - g(D) \sigma_R]$  remains equal to zero (e.g. Eq. 5.11) during the entire loading process and not only at the elastic limit.

During this monotonic process, the normal relative displacement can be explicitly written from Eq. 5.8:

$$u_n = u_{n(0)} [1 - \beta \cdot \ln(1 - D)] \quad (5.13)$$

$u_{n(0)}$  is defined as the elastic limit displacement, equal to  $\sigma_R / K_{nn}$ . At the same time, the following stress-displacement relation describes the monotonic loading, according to the constitutive law in Eq. 5.2a:

$$\sigma_n = (1 - D) K_{nn} u_n \quad (5.14)$$

Referring to Eq. 5.13 and 5.14, the final condition in Eq. 5.11 corresponds to:

$$\sigma_n = (1 - D) K_{nn} \cdot \frac{\sigma_R}{K_{nn}} [1 - \beta \cdot \ln(1 - D)] = g(D) \sigma_R \quad (5.15)$$

Eventually, Eq. 5.15 provides the analytical formulation of the damage function:

$$g(D) = (1 - D) [1 - \beta \cdot \ln(1 - D)] \quad (5.16)$$

$g(D)$  in Eq. 5.16 is traced in Figure 5. 6b, for different values of  $\beta$ . In particular, for  $\beta > 1$ , a hardening phase, characterized by an increasing stress, exists. It includes an expansion of the yield surface, before the second phase characterized by softening, which is always present. This damage law, integrated in the failure criterion (Eq. 5.5), allows the actualization of the damage variable  $D$  for whatever loading process of the cohesive zone, between the limit conditions in mode *I* and *asymptotic* mode *II*, after the elastic limit, according to the consistency in Eq. 5.9.

## 5.2 Single-fracture numerical analyses

This section presents the analyses for a *single fracture* evolution induced during a drift excavation, with evaluations of the length of propagation,  $\bar{L}$ . Figure 5. 7 reports boundary and initial conditions for numerical simulations: in (a), the in-situ stress state is defined for a 2d axisymmetric problem according to stresses Table 5. 2 and, in (b), the excavation procedure is shown. In analogy with the unloading the 2d plane strain problems on the drifts' cross-sections, in Figure 5. 7b, a fraction  $\Delta$  of the total unloading is firstly applied to attain a stress state close to the elastic limit. Then, the complementary part  $(1-\Delta)$  corresponds to the second boundary condition to simulate the rest of the excavation when failure occurs ( $f = 0$  on joint elements).

**Table 5. 2 :**  $\sigma_{(0)}$  as initial/boundary conditions for 2d axisymmetric simulations.

$\sigma_{xx,(0)}$ [MPa]	$\sigma_{zz,(0)}$ [MPa]	$\sigma_{yy,(0)}$ [MPa]
-12.5	-16.2	$\sigma_{yy,(0)} = \sigma_{xx,(0)}$

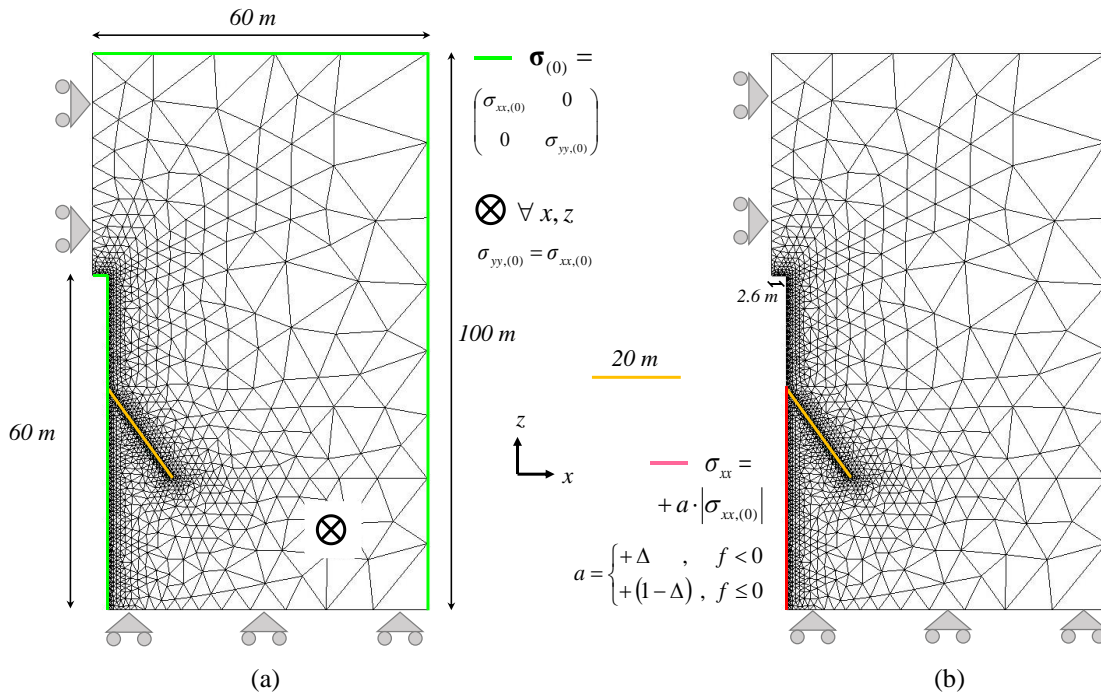


**Figure 5. 7:** boundary/initial conditions (a) and excavation procedure (b) for 2d axisymmetric simulations in single fracture numerical analyses.

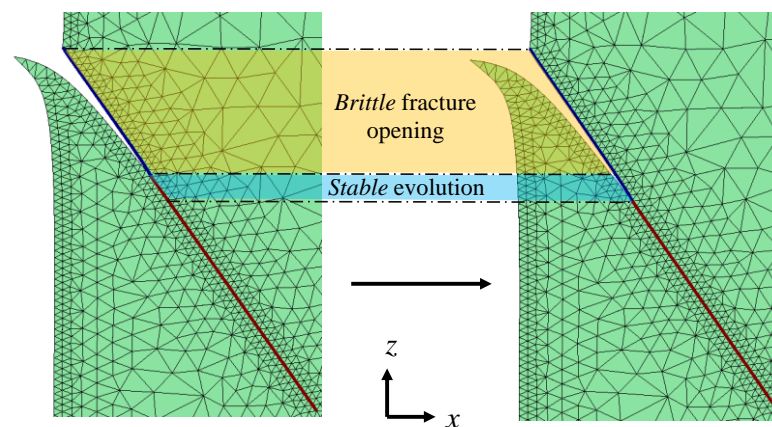
A simple parametrisation corresponding to a linear elastic material with  $E = 5000$  MPa and  $\nu = 0.25$  (e.g. [42] and Table 1.3, Section 1.1) is assigned on surface (triangular) elements in Figure 5. 7, for the intact Callovo-Oxfordian (COx) claystone. Concerning the *cohesive fracture* model for joints, numerical parametrisation of a discontinuity may not be as simple as for surface elements, due to more complex procedures in laboratory testing for measurements on fractures. Relatively to the analyses in this section, in presence of a singular discontinuity, the initial stiffness was imposed to define a sequence of joint elements with no mechanical influence on the geostatic stress state (e.g. Table 5. 2), meaning the intact stiffness tensor  $\mathbf{K} \gg K$  (elastic bulk modulus) and  $E$ . In particular,  $\mathbf{K} = 3 \cdot 10^6$  MPa/m ( $K_m = K_n$ ), assuming a bulk modulus  $K \approx 3300$  MPa from  $E$  and  $\nu$  defined on the surface elements. Concerning the initial joint thickness  $e_0$ , this parameter can be only supposed based on the radial core-drilling evidences, with the hypothesis that the sampling operations had not excessively damaged the medium surrounding the original *FCh* fracture generated during the excavation. If evidences in Figure 5. 2b are considered (drill-core reported on a centimetre scale, e.g. [9]), the final aperture of the fracture is around an order of 1 mm: the initial joint thickness was assumed equal to  $10^{-4}$  m = 0.1 mm. Failure parameters and damage law coefficient  $\beta$  are reported in Table 5. 3. Values of the failure parameters were chosen lower than those reported in Table 1.3, Section 1.1. This initial attempt was intended to obtain a propagation length  $\bar{L}$  verifying if the fracture did not propagate for the entire joints sequence, to confirm the validity of the numerical model.

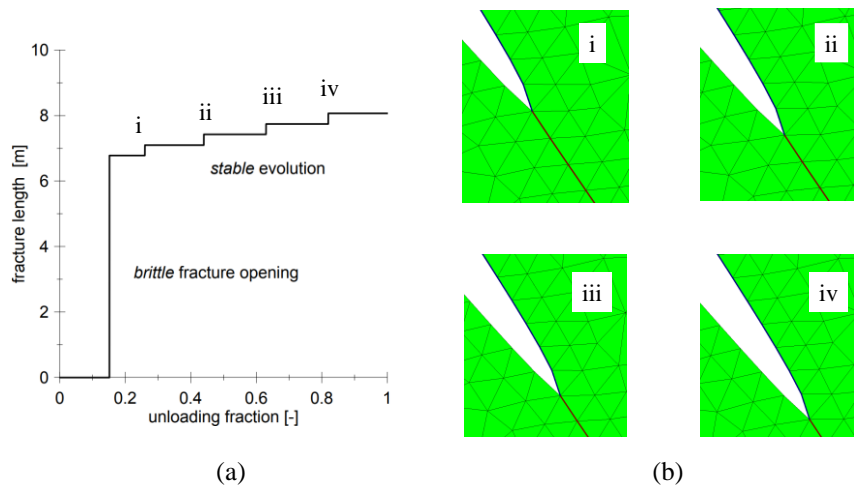
**Table 5. 3** : failure and damage yielding parameters for the first *single fracture* numerical simulation.

$\sigma_R$ [MPa]	$\varphi$ [°]	$C$ [MPa]	$\beta$ [-]
1.0	20	2.0	1.0

For the coefficient  $\beta$ , it must be underlined that no available data on laboratory analyses of cracking in COx claystone exist to determine it. The arbitrary value  $\beta = 1$  was imposed as the upper limit of a pure softening behaviour for the cohesive zone, after the elastic limit (Figure 5. 6b). A similar absence of laboratory data exists also for the residual stiffness parameters  $k_{or}$  and  $k_{on}$ ; it is possible, at the end of the cracking process, an existing contact among the cohesive surfaces, with the possibility of a free relative tangential displacement among them. Thus, numerical parametrisation for the residual joints' stiffness correspond to  $k_{or} = 0$  and  $k_{on} = 3300$  MPa/m =  $K$ , the bulk modulus for the linear elastic surface elements (i.e. the surrounding claystone).

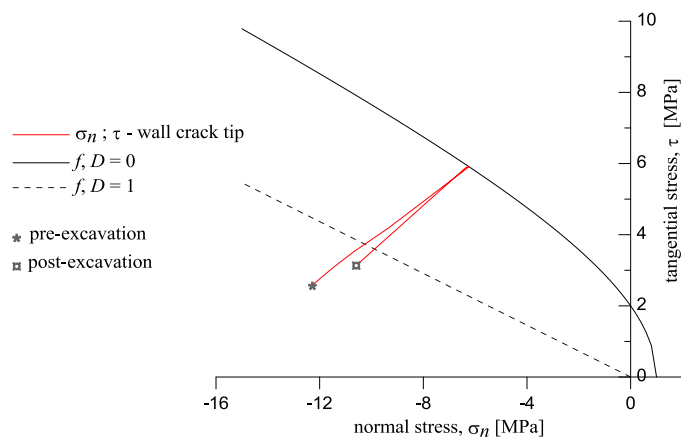
Two different steps of the fracture opening are reported in Figure 5. 8; deformations and displacements are magnified for graphic purposes. Figure 5. 8a illustrates the fracture initiation, for a certain value of the steady-state unloading  $+(1-\Delta)\cdot\sigma_{xx,(0)}$  (e.g. Figure 5. 7b) applied at the drift's sidewall. A *brittle* activation occurs, meaning that several consecutive joint elements reach  $D = 1$  simultaneously. Physically, this corresponds to an instantaneous dissipation of the elastic energy stored within the discontinuity, i.e. the fracture's energy dissipation rate  $G$  attains its critical value  $G_C$  along several joints, at the same computing time step. Then, fracture propagates with a *stable* evolution, with only one joint element opening for a certain unloading increment. Figure 5. 9a reports the complete diagram of fracture's evolution: almost at the 20% of the second unloading  $+(1-\Delta)\cdot\sigma_{xx,(0)}$ , the discontinuity is activated for a joints' sequence covering a length of 6.5 m. Afterwards, four successive *single-joint* openings ( $D: 0 \rightarrow 1$ ) are calculated during the rest of the unloading, which openings are graphically reported in Figure 5. 9b.


**Figure 5. 8**: initial unstable fracture opening (a), followed by a progressive *joint-by-joint* (stable) cracking (b).



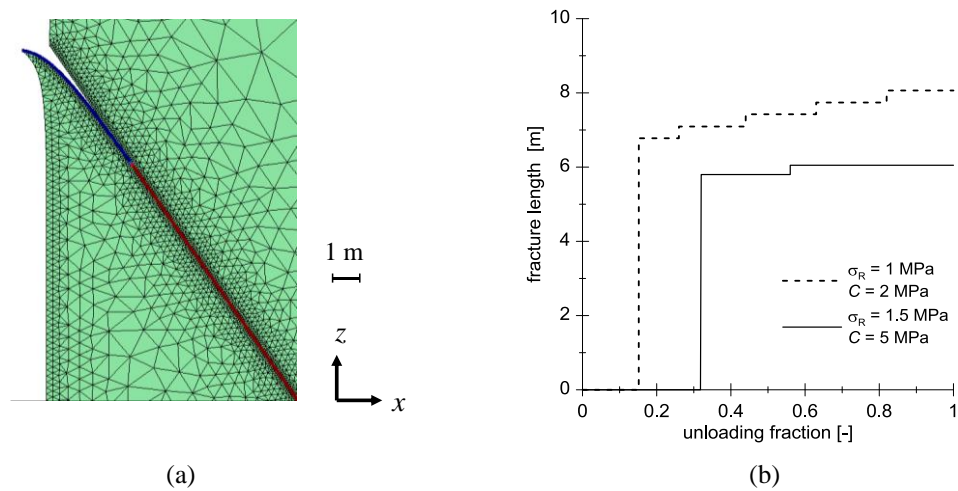
**Figure 5. 9:** diagram of the fracture evolution in (a) and a zoom on every consecutive joint opening in (b), during the final stable propagation.

Figure 5. 9a shows that a constant unloading is required to activate the joint elements correspondent to the fracture's increases (ii), (iii) and (iv), reported in Figure 5. 9b. In fact, far from the perimeter, where in-situ stress conditions are almost restored, the activation of equal cohesive zones (i.e. joint elements with the same length) corresponds to the same release of elastic energy. At the end of the stable evolution, a final  $\bar{L} = 8.13$  m is calculated (Figure 5. 9a). This constitutes an overestimation, relatively to in-situ observations: as mentioned previously, if the fracture inclination  $\alpha$  to the sidewall is accounted, an extension between 5 and 7 m should be attended from numerical simulations. Nonetheless, this extension confirms the validity of the joints' sequence length (20 m, e.g. Figure 5. 7). Figure 5. 10 illustrates the stress path ( $\sigma_n ; \tau$ ) of the joint element at the intersection with the drift's perimeter: starting from the pre-excavation stress state, which values depend on the fracture's inclination to the principal stresses' (Table 5. 2 and Figure 5. 7), the calculated stress path attains the hyperbolic criterion, at  $D = 0$ , with mixed *mode I + II* attainment. Shear mode results the preponderant, as the stress path intersect the yield surface towards the asymptotic Mohr-coulomb yielding, where  $f(D = 0)$  is parallel to  $f(D = 1)$ .



**Figure 5. 10:** stress path for the joint element intersecting the drift's sidewall.

To conclude this section, an increase of failure parameters is imposed for a second single-fracture unloading, with  $\sigma_R = 1.5$  MPa and  $C = 5$  MPa (admissible values from Table 1.3, Section 1.1). Similar values were adopted in other publications concerning failure analyses on CO<sub>x</sub> claystone (e.g. [43]). A contour plot of the final fracture opening and the diagram of fracture's evolution with the unloading, compared with the previous analysis, are reported respectively in Figure 5. 11a and Figure 5. 11b. In this case,  $\bar{L} \approx 6$  m, an admissible value for the mentioned interval, concerning *FCh* fractures' length (5 and 7 m). Figure 5. 12a reports the horizontal displacement field ( $U_x$ ), corresponding to the radial direction in the cross-section (i.e.  $r \equiv x$ ). A plot of  $U_x$  calculated along  $z$ , at the sidewall, is traced in Figure 5. 12b: a radial displacement between 20 and 10 mm is obtained on a distance  $z \approx 3$  m. These values are consistent with the short-term horizontal displacements for drift GCS, mentioned presenting the results for excavation analyses on the cross-section (e.g. Figure 3.5 and Table 3.3, Chapter 3 and Table 4.7, Chapter 4).



**Figure 5. 11:** analogue fracture initiation, increasing the *cohesive zone* strength, in (a) and comparison between the cracking length evolutions for the two *single fracture* simulations in (b).

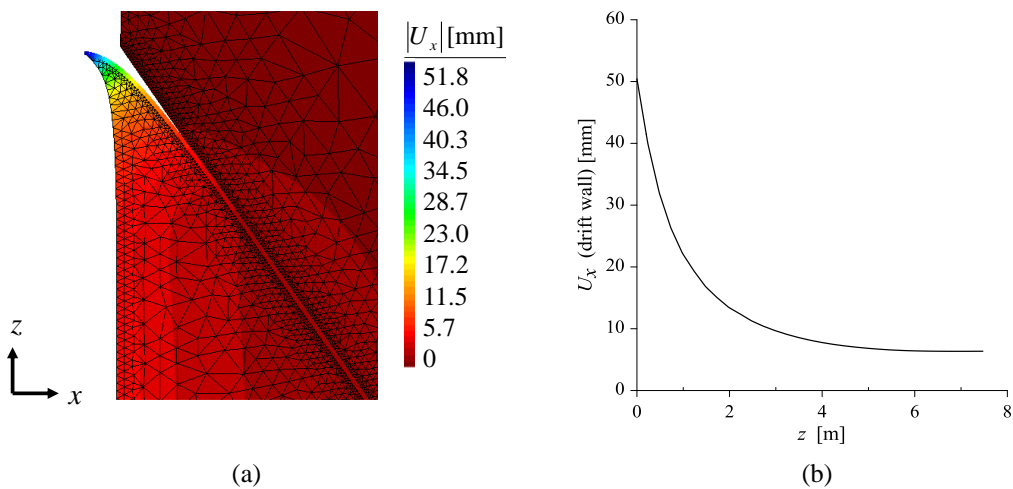


**Figure 5. 12:** horizontal displacement field in (a) and radial displacement of the drift's perimeter along  $z$  in (b), increasing the *cohesive zone* strength.

### 5.3 *Multi-fractures* numerical analyses with drifting simulations

In this last section, *multi-fractures* axisymmetric analyses on *JFEM* numerical models are presented. Without focusing in particular on the distance of *FCh* shear cracks assessed from geological surveys at the Andra URL, these modelling exercises focus mainly on the possibility to simulate, numerically, the appearance of one fracture every finite number of potential discontinuities (e.g., variable  $\bar{s}$ , Figure 5. 3) while the excavation moves forward. Moreover, the simulation of the drifting action offers an opportunity to study different methods of numerical implementations in the FEM codes employed, modifying the boundary conditions correspondent to the undisturbed stress state in the material. Results discussed in the following paragraphs present and describe, every time, the numerical technique performing the drifting action.

#### 5.3.1 *Excavation method 1*

At first, the simulation of the drift's excavation implied the elimination, from the initial mesh, of finite elements representing the material to be excavated. Figure 5. 13a reports the numerical model with the initial stress components  $\sigma_{ij,(0)}$  according to Table 5. 2, while, in Figure 5. 13b, an example of the successive excavation steps on new geometries, eliminating the elements inside the excavation, is reported. In the numerical model, a distance between every discontinuity, i.e. sequence of joint elements, is equal to 0.2 m, along an excavation length  $H_a = 6$  m. With a system of parallel discontinuities, the initial stiffness of cohesive joints (e.g. Eq. 5.3), distributed in a *matrix* modelled as a linear elastic material, can be imposed according to the homogenization of parameters  $E$  (Young modulus) and  $\mu$  (shear modulus):

$$\frac{1}{E} = \frac{1}{E_{HOM}} = \frac{1}{E_{MAT}} + \frac{1}{d \cdot \mathbf{K}_{nn}} \quad (5. 17)$$

$$\frac{1}{\mu} = \frac{1}{\mu_{HOM}} = \frac{1}{\mu_{MAT}} + \frac{1}{d \cdot \mathbf{K}_{tt}} \quad (5. 18)$$

To simplify, the elastic parameters assigned to the matrix (*MAT*) may be imposed equal to the homogenized values (*HOM*), while  $\mathbf{K}_{nn}$  and  $\mathbf{K}_{tt}$  may be increased about 2 or 3 orders of magnitude (e.g.  $\mathbf{K} \approx 10^6$  or  $10^7$  MPa/m), in analogy with the initial stiffness for joint elements in the *single fracture* analyses. With a distance  $d$  between potential discontinuities on an order of magnitude equal to  $[1 ; 10^{-1}]$  m, this parametrization guarantees  $E/E_{HOM} \approx \mu/\mu_{HOM} \rightarrow 1$ . For the simulation presented hereby, the assignment of the other parameters for cohesive joints is based on the previous *single fracture* analyses (e.g. Table 5. 3, Figure 5. 8 and Figure 5. 11). According to Figure 5. 13, this method implies the solution of a FEM steady-state problem, which outputs - in terms of  $\boldsymbol{\sigma}$  and  $\boldsymbol{\varepsilon}$  fields - are applied as initial conditions to the next excavation advancement.

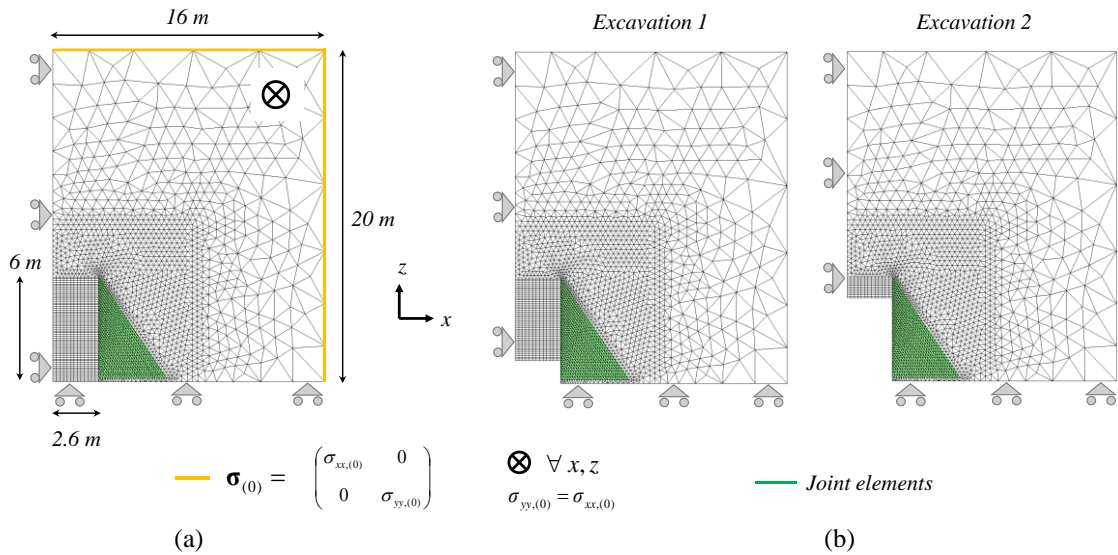


**Figure 5.13:** initial conditions in (a) and modified geometries corresponding to the drift's advancements in (b), for the excavation method 1.

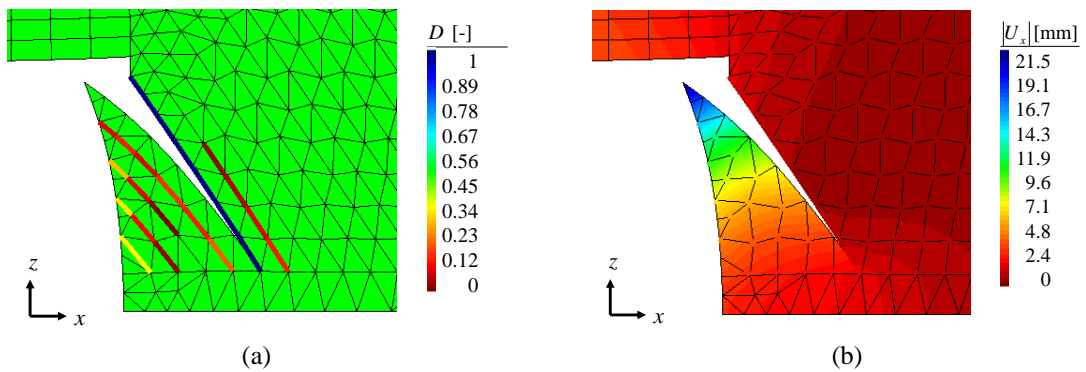


**Figure 5.14:** results of fracture's occurrence after the first excavation step, as reported in Figure 5.13b. In (a), damage calculated at joint elements and, in (b), horizontal displacements' field.

In Figure 5.14, an example of fracture occurrence after the first excavation step (Figure 5.13b) is reported. Immediately, it was realized that the solution of multiple steady-state problems where  $\sigma$  and  $\epsilon$  fields, calculated at the step  $n$ , become initial conditions for the step  $(n+1)$ , may reproduce unrealistic stress concentrations at the corner of the excavation front with the drift sidewall. In Figure 5.14a, the activation of one joint elements' sequence at the area of stress concentration is reported, with partially damaged joints around the calculated fracture. Nonetheless, horizontal displacements, in accordance with in-situ monitoring for drift GCS, are obtained at the sidewall surrounding the fracture (e.g. Figure 5.14b). Eventually, the spacing  $\bar{s}$  calculated by this method can be strongly dependent on the partial excavation length imposed at every new step, i.e. the number of finite elements eliminated along the drift axis  $z$ .

## 5.3.2 Excavation method 2

This second series of *multi-fractures* analyses simulates the drifting action by means of a degradation of stiffness and initial stress state  $\boldsymbol{\sigma}_{(0)}$  in surface elements inside the excavation. They are not eliminated from the original geometry but, defining a specific *excavation function*, they become ineffective for the calculation of the stress-strain response in the FEM problem. For this method, the numerical model with boundary/initial conditions is reported in Figure 5. 15a, while Figure 5. 15b describes the geometry's dimensions. The equations presented in the following, related to the excavation's numerical procedure, were implemented in an iterative cycle in the *POROFIS* module *hydmech.f90* (e.g. Chapter 2, Section 2.1). The *excavation function* for drifting,  $d(z, t)$ , is defined along the longitudinal axis,  $z$ , and in a virtual time,  $t$ , related to the numerical process. In other terms, while the previous analyses were performed in steady state conditions, multi-fractures simulations, from this paragraph, are executed with transient simulations, defined between a time offset  $t_0$  and a final time  $t_f$ . The function  $d(z, t)$  is formulated to degrade the elastic properties of the FE mesh surface elements within the drift, as well as their initial stress tensor,  $\boldsymbol{\sigma}_{(0)}$ . For the material in correspondence of the excavation, the following  $\boldsymbol{\sigma} : \boldsymbol{\varepsilon}$  law was defined:

$$\boldsymbol{\sigma} = \boldsymbol{\sigma}_{(0)} + \tilde{\boldsymbol{\sigma}}_{(0)} + (1 - \tilde{D}) \cdot \mathbf{C} : \boldsymbol{\varepsilon} \quad (5. 19)$$

$\tilde{\boldsymbol{\sigma}}_{(0)}$  and  $\tilde{D}$  can be defined as a *modified* initial stress tensor and a *modified* damage variable, both related to  $d(z, t)$ , formalized as follows:

$$d(z, t) = \frac{1}{2} \left[ 1 - \tanh \left( \frac{z - z_0 - V \cdot t}{L_N} \right) \right] \quad (5. 20)$$

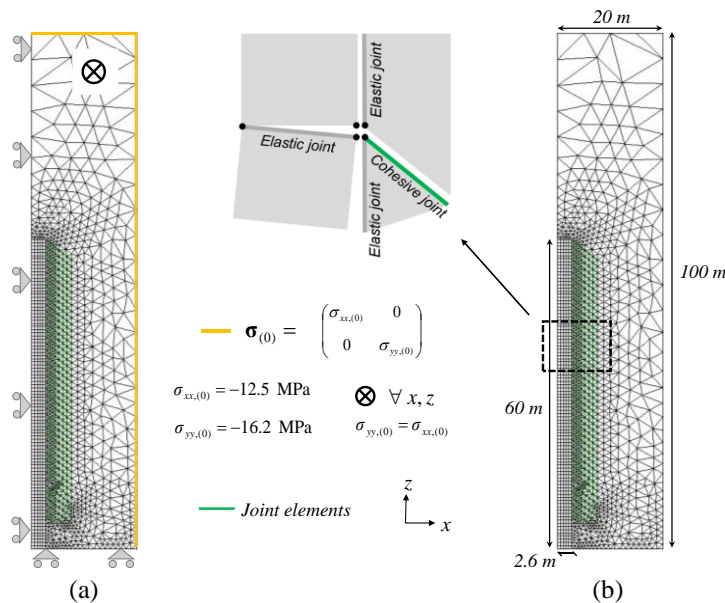


**Figure 5. 15:** numerical model for the excavation method 2, with boundary conditions in (a) and geometry's dimensions in (b).

Eq. 5.20 is set to vary asymptotically in the interval  $[0; 1]$ , from  $t = t_0$  to  $t = t_f$ . The parameters  $z_0$ ,  $V$  and  $L_N$  represent, respectively, the optional excavation offset, the constant velocity of excavation and a coefficient related to the size of finite elements within the drift or at the sidewall. In particular,  $L_N$  calibrates the smoothness of the function  $\tanh$  and, after analytical verifications, it was set  $L_N = 0.1 \cdot l$ , if  $l$  is the main dimension of finite elements. For the numerical purposes, this function corresponds to the transition of an excavation front, at a certain (computing) time  $t$  and for a certain coordinate  $z$  of the excavation axis. Since, in the transient numerical process with a duration  $t = t_f$ , the excavation occurs with a constant velocity  $V$ , the product  $V \cdot t_f$  must correspond to  $z = H_a$ , the total drift length. Every parameter with a dependence on the computing time, in transient numerical applications, has no physical time unit: since the simulation's process is user-defined, these variables may be set on an arbitral time-scale. Concerning the simulation of a drifting process, according to drift GCS excavation's chronogram (e.g. [60]), a reference time scale based on several days may be assumed: for instance, one week. Figure 5. 16a and b represent, respectively, Eq. 5.20 as function of the space ( $z$ ) and time ( $t$ ), assuming an excavation length  $H_a = 60$  m, similar to GCS drift, an excavation front moving at  $V = 2$  (m/week, e.g. [60]),  $t_0 = 0$  and  $t_f = 30$  (weeks). Reconsidering the stress-strain law in Eq. 5.19, the current stress tensor  $\boldsymbol{\sigma}$ , at  $t = t_f$ , vanishes only if  $\tilde{\boldsymbol{\sigma}}_{(0)} = \boldsymbol{\sigma}_{(0)}$  and  $\tilde{D} \rightarrow 1$ . For the first term, *POROFIS* required its time-derivative implementation, in the module *hydmech.f90*, to resolve the incremental form of Eq. 5.19 for every time step  $\Delta t$ . This was performed according to the following mathematical formulation:

$$\int_{t=t_0}^{t=t_f} \dot{\tilde{\boldsymbol{\sigma}}}_{(0)} dt = -\boldsymbol{\sigma}_{(0)}, \quad \forall z \rightarrow \dot{\tilde{\boldsymbol{\sigma}}}_{(0)} = \mathbf{A} \cdot \frac{\partial}{\partial t} d(z, t) \quad (5. 21)$$

By the derivation of Eq. 5.20, it is possible to prove that the following equations are correct:

$$\dot{\tilde{\boldsymbol{\sigma}}}_{(0)} = \frac{\partial \tilde{\boldsymbol{\sigma}}_{(0)}}{\partial t} = -\frac{\tilde{\boldsymbol{\sigma}}_{(0)} V}{2L_N} \cdot \left[ 1 - \tanh^2 \left( \frac{z - z_0 - V \cdot t}{L_N} \right) \right] ; \quad \mathbf{A} = -\frac{\tilde{\boldsymbol{\sigma}}_{(0)} V}{2L_N} \quad (5. 22a-b)$$

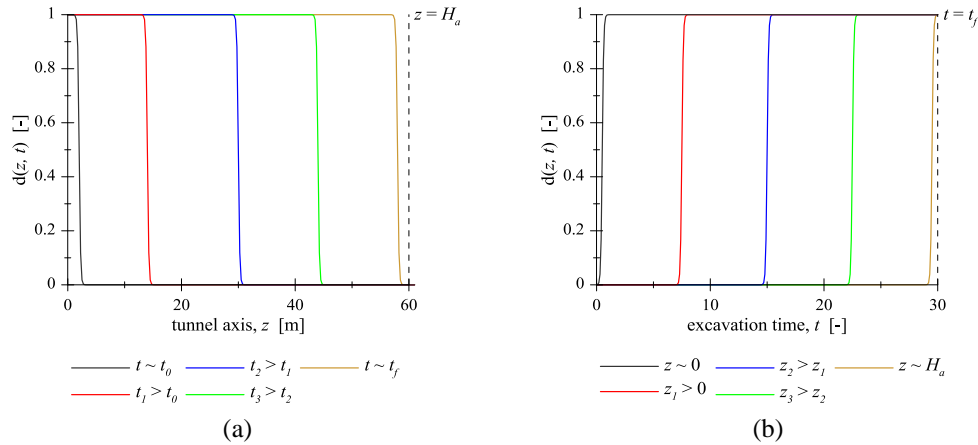


**Figure 5. 16:** excavation function  $d(z, t)$ , as a function of space in (a) and of time in (b).  $V = 2$  m/week and  $H_a = 60$  m (e.g. [60]) and  $t_f = 30$  (weeks, chosen as reference only for the transient numerical process).

To define  $\tilde{D}$ , Eq. 5.20 was modified to avoid numerical instabilities when  $\tilde{D} \rightarrow 1$ , specifically to verify  $\tilde{D}(t = t_f) = (1 - \zeta)$ , with  $\zeta$  set as an infinitesimal tolerance value (e.g.  $\zeta \rightarrow 0$ ):

$$\tilde{D} = \tilde{D}(z, t) = \frac{(1 - \zeta)}{2} \left[ 1 - \tanh\left(\frac{z - z_0 - V \cdot t}{L_N}\right) \right] \quad (5.23)$$

According to Eq. 5.23,  $\tilde{D}(t = t_0) = 0$  and  $\tilde{D}(t = t_f) = (1 - \zeta)$ . Figure 5. 17 reports a result of the implementation of the numerical technique previously described, on the geometry in Figure 5. 15: in particular, it shows the contour plot, for  $d(z, t)$  and  $\tilde{D}(z, t)$ , of a drifting at  $t = 0.5 \cdot t_f$ , when half of the total drift length  $H_a$  has been already excavated. Results of fractures' occurrences, from geometry in Figure 5. 15, are shown in Figure 5. 18, based on the parametrization for joint elements and excavation function reported, respectively, in Table 5. 4 and Table 5. 5. Initial and residual stiffness for joints (tensors  $\mathbf{K}$  and  $\mathbf{k}_0$ ) are set similarly to the numerical analyses presented in the previous paragraph (e.g. Figure 5. 14).

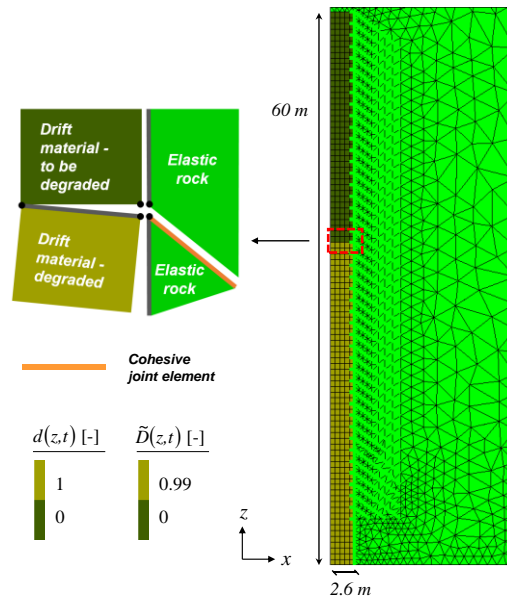


**Figure 5. 17:** contour plot illustrating the binary values assumed by  $d(z, t)$  during a drifting numerical process, with the modified damage variable for elements inside the excavation.

**Table 5. 4 :** failure parameters for joint elements, based on previously simulations and values in Chapter 1 (Table 1.3).

$e_0$ [mm]	$\sigma_R$ [MPa]	$\varphi$ [°]	$C$ [MPa]	$\beta$ [-]
0.1	1.5	20	4.0	1.0

**Table 5. 5 :** parameters for the numerical excavation procedure.

$t_0$ [-]	$t_f$ [-]	$V$ [-]	$z_0$ [m]	$L_N$ [m]
0	30	2.0	0	$6.25 \cdot 10^{-2}$

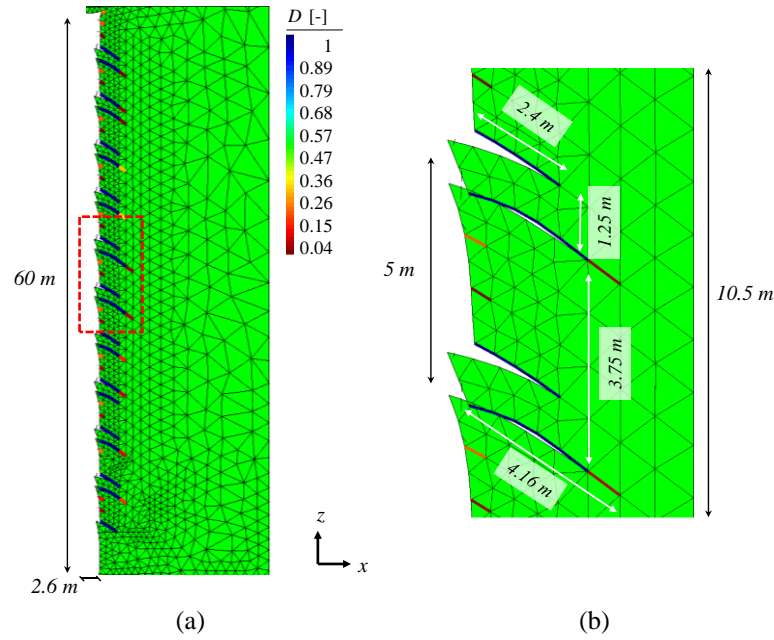


**Figure 5. 18:** contour plot of damage on joint elements, adopting the excavation method 2, showing fractures' occurrences and spacing. Total geometry displayed in (a) and detail on fractures' opening in (b).

Results in Figure 5. 18 show a periodicity of fractures' opening characterized, at every occurrence, by two consecutive joints' activations. In general, one of these overcomes a length of 4 m (e.g. Figure 5. 18b) and approximates the average horizontal extension of the failure system EDZ-EdZ for GCS drift at the Andra URL.

### 5.3.3 Excavation method 3

Numerical implementation of the drifting action is hereby presented according to another technique, based on the excavation function  $d(z, t)$  in Eq. 5.20. This approach does not require the presence of surface elements within the area of the material to be excavated: practically, it allows the adoption of a geometrical model representing the final configuration of the excavation, a mesh with no finite elements in the drift area, as illustrated in Figure 5. 19a, where the imposed boundary conditions are described (e.g. [100], [101]). In this numerical modelling, Eq. 5.20 is adopted to implement a procedure implying a progressive degradation on the boundary conditions set at the tunnel sidewall, according to the scheme in Figure 5. 19b. In fact, at  $t = t_0$ , a normal stress equal to the correspondent geostatic component,  $\sigma_{xx(0)}$ , acts on the gallery interface,  $\forall z$ , to reproduce the pre-drifting conditions. Numerical modification of  $\sigma_{xx(0)}$ , during the advancing of the excavation front, is integrated in the code similarly to the degradation of initial stress state  $\boldsymbol{\sigma}_{(0)}$ , in Eq. 5.21 and 5.22, for material elements within the drift's area (e.g. Figure 5. 17). The following relation was introduced as a transient boundary condition at the gallery wall, for the excavation:

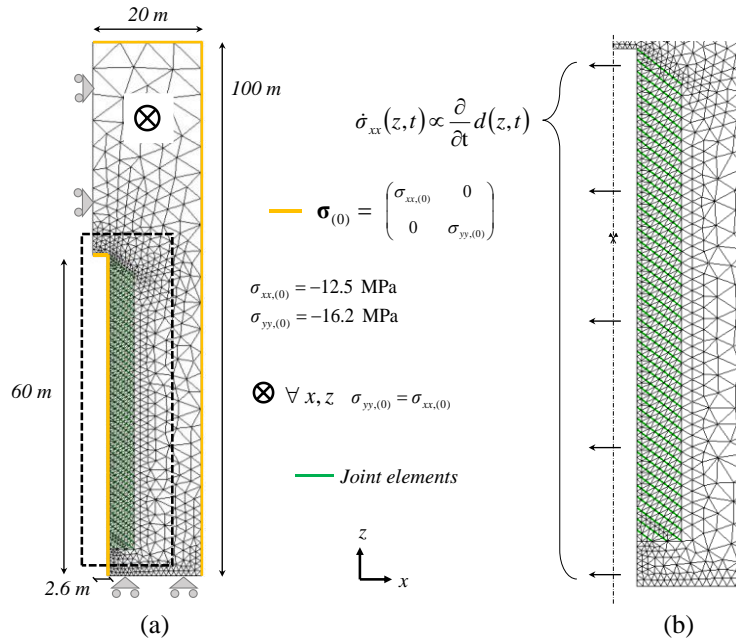


**Figure 5. 19:** numerical model for the excavation method 3. In (a), geometry's dimensions and boundary conditions and, in (b), a schematization of the numerical procedure applied for the excavation.

$$\sigma_{xx}(z,t) = -\sigma_{xx,(0)} \cdot d(z,t) \quad (5.24)$$

According to Eq. 5.20 and Eq. 5.24,  $\sigma_{xx}(z, t = t_0) = 0$  and  $\sigma_{xx}(z, t = t_0) = -\sigma_{xx,(0)}$ , for every  $z$  at the sidewall. In transient conditions, the implementation of the time-derivative,  $\dot{\sigma}_{xx}$  was required:

$$\int_{t=t_0}^{t=t_f} \dot{\sigma}_{xx} dt = -\sigma_{xx,(0)} , \forall z \rightarrow \dot{\sigma}_{xx} = \frac{\partial}{\partial t} [-\sigma_{xx,(0)} \cdot d(z,t)] \quad (5.25)$$

From Eq. 5.25, the variable boundary condition at the sidewall writes:

$$\dot{\sigma}_{xx}(z,t) = \frac{\sigma_{xx,(0)} V}{2L_N} \cdot \left[ 1 - \tanh^2 \left( \frac{z - z_0 - V \cdot t}{L_N} \right) \right] \quad (5.26)$$

Figure 5. 20 shows the results based on numerical model with boundary conditions in Figure 5. 19a-b, respectively for the initial stress state and the excavation procedure [101]. Parameters for potential discontinuities as joint elements and for excavation function are equal to those applied for numerical analyses illustrated in Figure 5. 18 (i.e. Table 5. 4 and Table 5. 5). The obtained length of fractures is around 4 m, consistent with the horizontal extension of GCS drift's failure system, and a bi-periodical fractures' occurrence is calculated. At the sidewall, along the longitudinal axis  $z$ , the average horizontal displacement  $U_x$ , between the values and the cracking initiation and the areas still in elastic conditions, is calculated around 17 and 18 mm, approximating correctly the measurements of short-term sidewall's displacements for the instrumented drift.

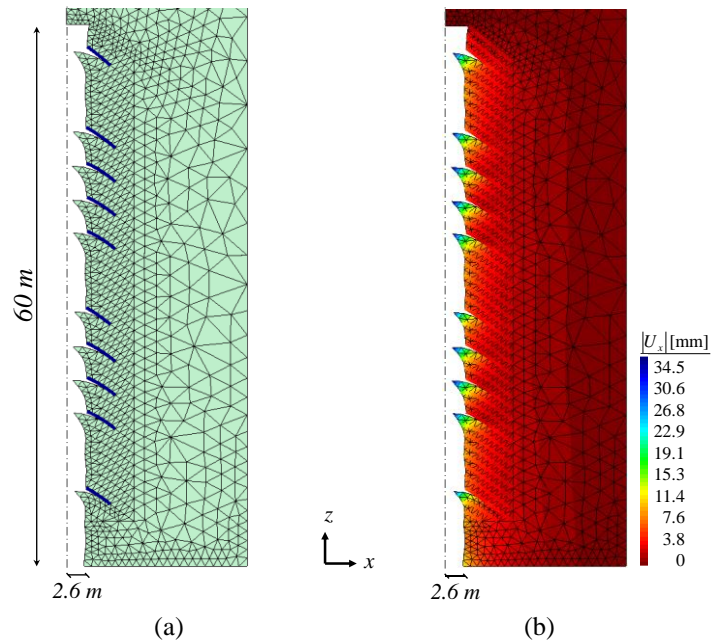


**Figure 5. 20:** contour plots for opened fractures, in (a), and horizontal displacements, in (b), calculated with the excavation method 3.

With respect to results in Figure 5. 18, a smaller fraction of activated (damaged) discontinuities was calculated, corresponding to 20% of the imposed joints' sequences. The spacing  $\bar{s}$  varies between the values of 2.5 and 8 m, along the entire length  $H_a = 60$  m. Differently from Figure 5. 18, a bimodal fracture's spacing is calculated with this excavation method showing that, concerning the adopted processors for FEM problems, the numerical technique of implementing a transient excavation may influence the results.

## Conclusion

These modelling exercises have formed the second research axis of numerical works presented in this manuscript. Within the cohesive fracture's framework proposed by Pouya and Bemani [76], a softening, damage-based constitutive model was employed for linear discontinuities to reproduce the occurrence of *Chevron* fractures (*FCh*) at the Andra URL, according to their length in the EDZ-EdZ failure system, for the instrumented drift GCS. In axisymmetric, joint elements were introduced by the module *DISCRAC* (<http://www.fracsima.com/>), obtaining a series of *joints-enriched* finite element models (JFEM), to study either the initiation and propagation of a single fracture or the periodicity of cracking occurrence with an advancing excavation front.

*Single-fracture* analyses showed, more in detail, the cohesive fracture's evolution, under a monotonic, steady-state unloading at the drift sidewall. According to a typical fragile, damage behaviour, a significant part of the total propagation length occurs in the initiation phase, when the cohesive yield surface, at the initial joint element, satisfies failure conditions. A mixed mode *I+II* of fracture's activation was calculated. Then, under the residual unloading of the steady-state process, a stable fracture propagation is observed, with the activation of one joint element (i.e. damage  $D = 1$ ) at regular unloading intervals (e.g. [100], [101]). Eventually, a set of failure parameters, consistent with data for Callovo-Oxfordian claystone (COx), allowed the calculation of a 6 m length, in accordance with the extension of *FCh* fractures surrounding GCS drift, considering their inclination to the longitudinal drift axis  $z$ .

In the last part, a qualitative analysis of the periodicity of cracking occurrences was performed with *multi-fractures* models, under transient unloading conditions, to simulate an excavation front [101]. This choice offered also the study and comparison of some proposed techniques for the drifting implementation: a different periodicity of fractures was calculated, in equal numerical models, by changing the implementation method. If the modelling proposed seems to simulate correctly the length of fractures with multiple discontinuities, further researches are still required to provide quantitative considerations concerning spacing/periodicity. Considering data on the tenacity (i.e. the critical *stress intensity factor* at the fracture tip) of COx formation, a better assessment of the cohesive zone's parameters can be provided, to obtain calculations for fractures' periodicity with more reliable, physically-based results. Eventually, mesh size or structure geometry dependencies should be considered.

# **General Conclusions and Perspectives**



## Plane section modelling of the failure zone

This section is dedicated to the general summaries and outlines concerning the *continuous* failure analyses around deep excavations, at the Andra Underground Research Laboratory (URL) in Bure (Figure 1.3, Chapter 1). This part treated the mechanical problem with a bi-dimensional, plane strain approach and constitutes the preponderant subject of this dissertation, forming the first axis of the research proposed. Related numerical analyses were presented and discussed from Chapter 2 to Chapter 4. In Chapter 1, in-situ references for the studies were illustrated, discerning two categories of drifts at the Andra URL, due to different boundary stress conditions in their cross-sections. The instrumented drifts GCS and GED offered two evidences of excavation-induced failure zones, with unequal shapes and extensions, both mechanically driven by the effects of a double anisotropy. In fact, on their cross-sections, different stress states act in the same geological formation, the Callovo-Oxfordian claystone (COx), characterized by intrinsic anisotropic properties. Failure's shape and extension for GCS drift results in a horizontally-oriented zone. On the contrary, excavation-induced failure around GED drift, with a stronger anisotropic stress state, exhibits a vertical extension (Figure 1.9, Chapter 1). The proposed modelling describes this zone as the area where material's failure criterion is attained, neglecting the effect of retaining structures after the excavation. With a null internal pressure at the drifts' perimeter, numerical FEM analyses were addressed to the description of a short-term, mechanically-driven failure, characterized by a constant or variable brittle response of the material. At yielding, its dissipation is purely based on damage mechanics, modelled by a damage variable  $D$ , increasing from 0 to 1 and degrading the initial elastic stiffness. Indeed, laboratory observations at the volume element scale suggest, for reduced levels of lateral confinement, a fragile response of COx claystone at failure (Figure 1.18, Chapter 1). While plastic dissipation may correspond to more ductile, time-independent response of this material after the elastic limit, it is possible to consider damage as the dominant failure mechanism occurring in uniaxial conditions, or under very low confinements. If the same discussion is reported from the laboratory scale to the structure scale, for underground excavations, even the 2d elastic solution shows a vanishing lateral confinement, on the surrounding material, towards the drift's perimeter. On the other hand, lateral confinement (i.e. the radial stress) increases with the distance from the gallery (e.g. Figure 1.23, Chapter 1). In this context, it is possible to state that the analyses presented propose a valid modelling, if certain fundamental aspects are verified:

- The object of investigation is a short-term failure, almost instantaneous, or in any case limited to a time scale based on some days/few weeks after the excavation. Otherwise, in particular when dealing with COx claystone, any proposition of geotechnical modelling should account for time-dependent effects due to creep or hydraulic diffusion.

- The area of study should be relatively limited to the structure's proximity, where low-confined conditions are favourable to a fragile dissipation, modelled by a sharp softening. In the previous chapters, this area was denoted as the *continuous* failure system EDZ-EdZ, even if it is necessary to precise that EDZ only is more subjected to the mentioned type of failure.

Accounting for this reduction of strength at yielding (i.e. softening), some implications for a mechanical modelling based on damage were provided in Chapter 2, with numerical analyses of circular excavations, comparing damage softening with plastic softening. A homogeneous unloading, in isotropic stress' and material's conditions, showed significant differences between plasticity and damage, even from a qualitative point of view. In particular, adopting simple numerical FEM models, softening plasticity exhibits, in isotropic conditions, a homogeneous response represented by a symmetric, overall circular failure zone. Softening damage, on the contrary, seems to amplify the effect of possible failure localizations around the circular opening (Figure 2.17 and Figure 2.18, Chapter 2). In general, if failure can localize for whatever reason (simply numerical or induced even by weak anisotropies), softening damage leads to a different redistribution of stresses around the failure zone and seems to provoke, locally, phenomena characterized by a partial/temporary instability, causing a progressive *failure-induced* anisotropy. A simple, analytical stress redistribution for a purely fragile behaviour after the elastic limit (Figure 2.23 and Figure 2.24, Chapter 2), showed the unstable nature of such a phenomenon, when a total damaged material ( $D = 1$ ) replaces, instantaneously, the material in intact conditions ( $D = 0$ ). The main body of Chapter 2 was intended to define important theoretical considerations before introducing the damage numerical modelling addressed to the specific problem of failure around the Andra URL drifts. Here, intrinsic anisotropies of COx formation must be accounted for the synthesis of a valid model describing the mechanical behaviour.

An initial upgrade was introduced, leading to the elastic-damage model named  $2d_{ED}$ , neglecting the influence of damage evolution along the *axial* direction  $z$ , perpendicular to the drifts' cross section (Section 2.3, Chapter 2). The main task of the analyses, a planar failure expansion limited to the cross-section, in two dimensions, justifies this mathematical implementation. After a test of the proposed model, showing a good estimation of the EDZ geometries and the convergences for GCS drift (Figure 3.3 and Figure 3.4, Chapter 3), a first proposition of anisotropic failure criterion was formulated, reproducing a monotonic variation of the compressive strength (Section 3.2, Chapter 3). In parallel, a modification of the  $2d_{ED}$  model's elastic-damage stiffness tensor was inserted, accounting for the transverse-isotropy of the elastic behaviour of COx formation, horizontally layered at the Andra URL site (Section 3.3, Chapter 3). These upgrades improved displacements' calculations of GCS stress conditions, together with consistent estimations of the horizontal EDZ-EdZ failure, mainly driven by the anisotropy of the failure criterion (Figure 3.12

and Figure 3.20, Chapter 3). On the contrary, the failure zone obtained for GED drift was not in good agreement with observations: this gap was estimated to be partially due by the anisotropic expression introduced in the constitutive model (Figure 3.21, Chapter 3). Afterwards, a physically-based upgrade of the  $2d_{ED}$  model was proposed, to consider a *shear damage* modifying only the deviatoric component of the elastic-damage stiffness tensor, written for a plane strain problem. This mathematical proposition, named  $2d_{ESD}$  model, represents a damage yielding where a cohesive material, subjected to mechanical degradation, assumes eventually purely frictional characteristics (Figure 4.2, Chapter 4). Adopting this implementation and a compressive strength varying monotonically, a correct calculation of the failure zone plus an overall consistent estimation of sidewall's displacement is obtained for every stress condition, i.e. GCS and GED drift (Figure 4.13 to Figure 4.18, Chapter 4).

Considering the anisotropic failure response, a wider dataset of experimental evidences on COx formation revealed a non-monotonic variation of material's resistance, in unconfined or confined conditions. Thus, together with the upgrades to the initial elastic-damage stiffness tensor, the model had to be improved by this failure behaviour: a second formulation of an anisotropic criterion was proposed to reproduce easily triaxial evidences on COx specimens, tested under different orientations (Figure 4.21 to Figure 4.23, Chapter 4). A last improvement, in terms of FEM numerical model, consisted in the assumption of concentrically distributed areas, around the circular drifts, to simulate the increasing material's ductility at yielding, moving radially from the perimeter (Figure 4.27, Chapter 4). This phenomenon, named *brittle-ductile transition*, led to the proposition of the diagrams in Figure 4.28, overall useful for numerical simulations, relating the level of confinement (e.g. the radial stress calculated in elasticity) with the parameters describing the fragility/ductility of the stress-strain curve in the  $2d_{ESD}$  model. The final results for GCS and GED drifts are presented and described in Section 4.5, on FEM models characterized by a finer mesh and representing a quarter of the entire circular geometry. Overall, short-term shape and extension of calculated failure areas is consistent with the reference conceptual models and displacements at the sidewall are capable to estimate the in-situ measurements, even if some under- or overestimations are obtained according to differences introduced in the numerical implementation of the procedure previously described (Table 4.7, Chapter 4).

Theoretical analyses and numerical modelling, previously summarized, arise some indications for the excavations' behaviour, referring to the study cases of Andra URL, together with possible perspectives for future researches. First of all, in the context of a purely mechanical modelling based on a total stress' response, the choice of elastic parameters must be handled with attention: according to the simulations presented, likely undrained conditions correspond to a Young modulus overcoming  $4000 \div 4500$  MPa for COx claystone. These indicative values are provided

not only considering the analyses discussed in this work, but also according to some recent publications related to laboratory applications (Section 2.2, Chapter 2). Afterwards, according to the last numerical results (Table 4.7, Chapter 4), a re-implementation of an anisotropic elasticity may improve the displacements' calculus with the  $2d\_ESD$  constitutive law. In particular, the increase of the horizontal stiffness, parallel to the stratification, seems suitable and physically consistent with the material microstructure. This definition of elasticity can be also integrated by short-term poro-mechanical effects, like an anisotropic pore-pressure redistribution by a total stress change, due to the excavation. Concerning the material at failure, a valid and realistic formulation for the criterion must consider a non-monotonic variation of material's resistance around the excavation, for unconfined or confined stress states.

This work, consisting in a physical/numerical modelling entirely based on short-term, damage mechanics, may be intended as a proposal to integrate this behaviour, peculiar for certain stress conditions at failure, with a wider framework of models based on elastic-plasticity, already proposed in the context of drifts' analyses at the Andra URL. In particular, a further development of a coupled plastic-damage model can be provided if plasticity is assumed to be the dominant dissipation mechanism at some distance from the sidewall, where greater confining stresses modify the post-failure response turns from brittle to ductile. At the same time, an extended modelling proposal, starting from a fragile damage dissipation, should include the time-dependent and long-term aspects of CO<sub>x</sub> behaviour, already known from laboratory evidences as well as already considered in some precedent works. This could lead to a predictive model describing an instantaneous fragile behaviour around galleries, mainly governed by damage, with a plastic softening-hardening transition, eventually accounting for viscous effects.

## Discrete modelling of fractures occurrence

The system of excavation-induced failure around drifts in COx claystone includes diffused damage/plastic effects occurring in the geological formation. At the same time, a clear pattern of localisations, coalescing in tensile and shear fractures, is observed. Numerical simulations in Chapter 5 were mainly intended to provide a complementary vision of the problem of excavation-induced fractures around deep drifts, with an adequate mechanical and numerical approach.

Focusing on the *Chevron* of herringbone shear fractures (*FCh*), failure studies can be also driven with a *discontinuous* or *discrete* mechanical model. Another axis of research was started to investigate these failure aspects, thanks to the numerical tools employed, capable to perform Finite Element analyses with the insertion of potential discontinuities, assimilated with joint elements (Figure 2.3, Chapter 2). Numerically, they allow for the separation of surface mesh elements, to reproduce, from the physical point of view, the occurrence of mechanical discontinuities in the solicited medium. This study, based again on a bi-dimensional approach, assumed the hypothesis of axial symmetry, considering one of the two principal drifting directions at the Andra URL, where the in-situ stress state is estimated quasi-isotropic in the drift's section (e.g. GCS drift). With this assumption, the study was focused on the simulation of fractures' occurrence along the gallery's axis. Geometric models consisted in a representation of the case-study drift on its elongation, instead of its cross-section (Figure 5. 1 and Figure 5. 3, Chapter 5).

In accordance with the mechanical modelling adopted for short-term failure, the dissipation mechanism chosen to analyse fractures' evolution is based on damage, represented by the same internal variable,  $D$ , described in the previous section. Deformability of discontinuities and their failure limit were evaluated according to a *cohesive fracture* constitutive law and criterion, based on the model proposed by Pouya and Bemani (2015) [76]. After the attainment of the yield surface, the model implies the degradation of the cohesive zone's stiffness with a decrease of its strength up to purely frictional conditions, reproducing a softening behaviour. At first, the initiation and propagation of a single fracture was tested and analysed (Section 5.2, Chapter 5), moving afterwards to a qualitative study of the periodicity of fractures' appearance, considering the transition of an excavation front at the drift's sidewall (Section 5.3, Chapter 5).

The first series of numerical analyses focused on a quantification of the propagation length, together with the mechanisms of initiation and evolution. The total stress path calculated at the origin of the discontinuity, in the undamaged configuration, showed a mixed mode *I+II* of fracture's activation (Figure 5. 10, Chapter 5). Instantaneously, a very fragile behaviour was calculated, with a significant fracture propagation for an infinitesimal unloading rate, named *unstable initiation*. Then, a *stable evolution* was calculated, at finite unloading intervals,

corresponding to similar quantities of elastic energy's release at every failure attainment, extremely reduced compared to the amount of energy dissipated during the *unstable initiation* (Figure 5. 9, Chapter 5). The final length of propagation, for a complete unloading at the drift's sidewall, resulted consistent with in-situ measurements and conceptual models provided by Andra (Figure 5. 11, Chapter 5).

The study of fractures' periodicity, i.e. the activation of one undamaged discontinuity every finite quantity  $n$ , was then performed on *multi-fractures* numerical models, including several sequences of joint elements. For these analyses, the implementation of a transient process to simulate the passage of an excavation front was proposed. It consisted in modifying progressively the initial stress state conditions at the drift's sidewall (Figure 5. 16, Chapter 5). Once the basic expression for this transient boundary condition was mathematically formulated, it was applied according to different numerical procedures, described in Section 5.3. These simulations calculated a fractures' length analogue with the horizontal extension of the failure system EDZ-EdZ, for the case-study considered, and a certain periodicity was obtained (Figure 5. 18 and Figure 5. 20, Chapter 5). Nonetheless, by varying the numerical procedure to implement the excavation front, the calculated values of fractures' periodicity changed. In a general context of numerical simulations, these results show that possible differences in the implementation techniques of a same physical/real process, can lead to discrepancies in the final calculations. The implementation method to model the excavation action remains an open issue.

Concerning these simulations, the next researches should privilege, at first, a quantitative study for fractures' periodicity. Further developments may account for other propositions to implement the excavation, as well as sensitivity analyses on parameters describing the drifting action and mesh-size dependencies. At the end of the last modelling presented, a numerical technique implying the degradation of the current stress state, at a computing time  $t$ , seemed more precise than the degradation of the initial stress state, which remains constant during the entire process. At the same time, a study based on data for fractures' tenacity can be scheduled, relatively to the COx claystone, providing less uncertainties on cohesive joints' parametrisation.

As concluded for brittle-damage modelling on drifts' plane sections, future upgrades for constitutive laws of potential fractures should include plastic dissipative mechanisms as well as time-dependent aspects, to provide a complete mechanical modelling, before the consideration of further multi-physical coupled phenomena.

## References

- [1] Ababou R., Cañamón Valera I., Poutrel A., “Macro-permeability distribution and anisotropy in a 3D fissured and fractured clay rock: ‘Excavation Damaged Zone’ around a cylindrical drift in Callovo-Oxfordian Argilite (Bure)”, *Physics and Chemistry of the Earth*, 36, 1932–1948, 2006. doi:10.1016/j.pce.2011.07.032
- [2] Alejano, L. R., Bobet, A., “Drucker–Prager Criterion”, *Rock Mechanics and Rock Engineering*, 45(6), 995-999, 2012.
- [3] Alonso, E., Alejano, L. R., Varas, F., Fdez-Mañin, G., Carranza-Torres, C., “Ground response curves for rock masses exhibiting strain-softening behaviour”, *International Journal for Numerical and Analytical Methods in Geomechanics*, 27(13), 1153-1185, 2003.
- [4] Andra, “Stockage réversible profond - Options de conception du stockage en formation géologique profonde”, Dossier C.NSY.ASTE.08.0429.A, 2009.
- [5] Andra, “Everything you ever wanted to know about radioactive waste management”, Brochure Septembre 2013, Edition Andra – Programmes de recherché, ref. 337JVA, 2013.
- [6] Andra, “Bilan des recherches conduites par l’Andra de 2010 à 2012”, Brochure Octobre 2013, Edition Andra – Programmes de recherche. ref. 537, 2013.
- [7] Armand G., “Excavation Damaged Zone (EDZ), Caractérisation initiale, évolution et impact sur les deformations”, Andra technical report *D.RP.ALS.09.0029*, 2012.
- [8] Armand G., Noiret A., Zghondi J., Seyedi D., “Short- and long-term behaviours of drifts in the Callovo-Oxfordian claystone at the Meuse/Haute-Marne Underground Research Laboratory”, *Journal of Rock Mechanics and Geotechnical Engineering*, 5(3), 221-230, 2013.
- [9] Armand, G., Leveau F., Nussbaum C., De La Vaissiere, R., Noiret, A., Jaeggi D., Landrein P., Righini, C. “Geometry and Properties of the Excavation-Induced Fractures at the Meuse/Haute-Marne URL Drifts”, *Rock Mechanics and Rock Engineering*; 47(1), 21-41, 2014.
- [10] Armand G., Conil N., Talandier J., Seyedi D. M., “Fundamental aspects of the hydromechanical behaviour of Callovo-Oxfordian claystone: From experimental studies to model calibration and validation”, *Computers and Geotechnics* 87, 277-286, 2017.
- [11] Bandis S. C., Lumsden A. C., Barton N. R.: Fundamentals of Rock Joint Deformation. *International Journal of Rock Mechanics and Mining Sciences & Geomechanics Abstracts*, 20(6), 249-268 (1983).

- [12] Belmokhtar M., Delage P., Ghabezloo S., Conil N., “Drained Triaxial Tests in Low-Permeability Shales: Application to the Callovo-Oxfordian Claystone”, *Rock Mechanics and Rock Engineering*, 51(7), 1979–1993, 2018.
- [13] Bernier F., Li X.-L., Bastiaens W. “Twenty-five years’ geotechnical observation and testing in the Tertiary Boom Clay formation”, *Géotechnique* 57(2), 229–237, 2007.
- [14] Bésuelle P., Viggiani G., Lenoir N., Desrues J., Bornert M., “X-ray Micro CT for Studying Strain Localization in Clay Rocks under Triaxial Compression”. In *Advances in X-ray Tomography for Geomaterials*, J. Desrues, G. Viggiani & P. Besuelle eds. 2006, ISTE Ltd.
- [15] Bobet A., “Elastic solution for deep tunnels. Application to excavation damage zone and rockbolt support”, *Rock Mechanics and Rock Engineering*, 42(2), 147-174, 2009.
- [16] Bobet A., “Characteristic Curves for Deep Circular Tunnels in Poroplastic Rock”, *Rock Mechanics and Rock Engineering*, 43(2), 185-200, 2010.
- [17] Bonnet-Eymard T., Thiriat F., Piedevache M., Prouvot J., Richard-Panot L., Armand G., Lavignerie R., Martin F., “Soutènement souple pour le creusement de galeries dans les argilites du CMHM”, *Congres AFTES*, Lyon, 17–19 Octobre 2011.
- [18] Boot J.C., “Elastic buckling of cylindrical pipe linings with small imperfections subject to external pressure”, *Tunnelling and Underground Space Technology*, 12, 3-15, 1997.
- [19] Brommundt J., Kaempfer T.U., Enssle C.P., Mayer G., Wendling J., “Full-scale 3D modelling of a nuclear waste repository in the Callovo-Oxfordian clay. Part 1: thermo-hydraulic two-phase transport of water and hydrogen” *Geological Society (London)*, Special Publications 400, 443-467, 2014.
- [20] Brown E. T., Bray, J. W., Ladanyi, B., Hoek, E., “Ground Response Curves for Rock Tunnels”, *Journal of Geotechnical Engineering*, 109(1), 15-39, 1983.
- [21] Carol I., Prat P. C., Lopez C. M.: Normal / shear cracking model: application to discrete crack analysis. *Journal of Engineering Mechanics*, 123(8), 765-773 (1997).
- [22] Carranza-Torres C., Fairhurst C., “The elasto-plastic response of underground excavations in rock masses that satisfy the Hoek-Brown failure criterion”, *International Journal of Rock Mechanics and Mining Sciences*, 36, 777-809, 1999.
- [23] Chambon R., Caillerie D., Viggiani G. “Loss of uniqueness and bifurcation vs instability: some remarks”, *Revue Française de Génie Civil*, 8(5-6), 517-553, 2004.
- [24] Chandler M. R., Meredith P. G., Brantut N., Crawford B. R., “Fracture toughness anisotropy in shale”, *Journal of Geophysical Resources and Solid Earth*, 121, 1706–1729, 2016. doi:10.1002/2015JB012756.

- [25] Chen R., Tonon F., “Closed-form solutions for a circular tunnel in elastic-brittle-plastic ground with the original and generalized Hoek-Brown failure criteria”, *Rock Mechanics and Rock Engineering*, 44(2), 169-178, 2011.
- [26] Chiarelli A.S. “Étude expérimentale et modélisation du comportement mécanique de l’argilite de l’est”, PhD thesis, Université Lille I, 2000.
- [27] Coussy, O.: Poromechanics. Laboratoire Centrale des Ponts et Chaussées, Institut Navier, Marne-la-Vallée, France. 1st edn. John Wiley & Sons Ltd, England (2004).
- [28] Crook T., Willson S., Yu J.G., Owen R., “Computational modelling of the localized deformation associated with borehole breakout in quasi-brittle materials”, *Journal of Petroleum Science and Engineering*, 38(3-4), 177-186, 2003.
- [29] Cruchaudet M., Noiret A., Talandier J., Gatmiri B., Armand G., “OHZ en GED: EDZ initiale et evolution”, Andra technical report *D.RP.AMFS.11.0016*, 2010.
- [30] Cuvilliez S., Djouadi I., Raude S., Fernandes R., “An elastoviscoplastic constitutive model for geomaterials: Application to hydromechanical modelling of claystone response to drift excavation”, *Computers and Geotechnics*, 87, 321-340, 2017.
- [31] Delay J., Lebon P., Rebours H., “Meuse/Haute-Marne centre: next steps towards a deep disposal facility”, *Journal of Rock Mechanics and Geotechnical Engineering*, 2(1), 52-70, 2010. Doi: 10.3724/SP.J.1235.2010.00052.
- [32] Detournay E., Cheng A.H.-D., “Fundamentals of Poroelasticity”, in: *Comprehensive Rock Engineering: Principles, Practice and Projects*, Vol. II, Analysis and Design Method, ed. C. Fairhurst, Pergamon Press, pp. 113-171 (1993).
- [33] Diederichs M. S., “Rock Fracture and Collapse under Low Confinement Conditions”, *Rock Mechanics and Rock Engineering*, 36(5), 339-381, 2003.
- [34] DISROC Materials’ Catalogue, FRACSIMA (<http://www.fracsima.com/>), 2018.
- [35] Emsley S., Olsson O., Stenberg L., Alheid H-J., Falls S.: ZEDEX - A study of damage and disturbance from tunnel excavation by blasting and tunnel boring. Swedish Nuclear Fuel and Waste Management Co., Stockholm, Sweden (1997).
- [36] François B., Labiouse V., Dizier A., Marinelli F., Charlier R., Collin F., “Hollow Cylinder Tests on Boom Clay: Modelling of Strain Localization in the Anisotropic Excavation Damaged Zone”, *Rock Mechanics and Rock Engineering*, 47(1), 71-86, 2014.
- [37] Gens A., “On the hydromechanical behaviour of argillaceous hard soils-weak rocks”, *Proceedings of the 15th European Conference on Soil Mechanics and Geotechnical Engineering – Geotechnics of Hard Soils – Weak Rocks (Part 4)*. In A. Anagnostopoulos et al. (Eds.) IOS Press, 2013. doi:10.3233/978-1-61499-199-1-71.

- [38] Germanovich L.N., Dyskin A.V., “Fracture mechanisms and instability of openings in compression”, *International Journal of Rock Mechanics and Mining Sciences*, 37, 263-284, 2000.
- [39] Goodman R. E.: *Methods of Geological Engineering in Discontinuous Rocks*. 1st edn. West Publishing Company, USA (1976).
- [40] Guan Z., Jiang, Y., Tanabasi, Y., “Ground reaction analyses in conventional tunnelling excavation”, *Tunnelling and Underground Space Technology*, 22(2), 230-237, 2007.
- [41] Guayacán-Carrillo L.M., Sulem J., Seyedi D., Ghabezloo S., Noiret A., Armand G. “Analysis of Long-Term Anisotropic Convergence in Drifts Excavated in Callovo-Oxfordian Claystone”, *Rock Mechanics and Rock Engineering*, 49(1), 97-114, 2016.
- [42] Guayacán-Carrillo L. M., “Analysis of long-term closure in drifts excavated in Callovo-Oxfordian claystone: roles of anisotropy and hydromechanical couplings”, PhD thesis, Ecole Nationale des Ponts et Chaussées, 2016.
- [43] Guayacán-Carrillo L.M., Ghabezloo S., Sulem J., Seyedi D.M., Armand G., “Effect of anisotropy and hydro-mechanical couplings on pore pressure evolution during tunnel excavation in low-permeability ground”, *International Journal of Rock Mechanics & Mining Sciences*, 97, 1–14, 2017.
- [44] Guillon T., Giot R., Giraud A., Armand G., “Response of Callovo-Oxfordian claystone during drying tests: unsaturated hydromechanical behavior”, *Acta Geotechnica*, 7(4), 313-332, 2012.
- [45] Hoek E., Martin C.D., “Fracture initiation and propagation in intact rock – A review”, *Journal of Rock Mechanics and Geotechnical Engineering*, 6(4), 287-300, 2014.
- [46] Hu, D. W., Zhang, F., Shao, J. F., “Experimental study of poromechanical behaviour of saturated claystone under triaxial compression”, *Acta Geotechnica*, 9(2), 207-214, 2014.
- [47] Jin Z-H., Sun C.T., “A comparison of cohesive zone modeling and classical fracture mechanics based on near tip stress field”, *International Journal of Solids and Structures*, 43, 1047-1060 (2006).
- [48] Kolymbas D.: *Tunelling and Tunnel Mechanics – A Rational Approach to Tunneling*. Universität Innsbruck - Institut für Geotechnik und Tunnelbau Technikerstr. Springer-Verlag Berlin, Germany (2005).
- [49] Labiouse V., Sauthier C., You S., “Hollow Cylinder Simulation Experiments of Galleries in Boom Clay Formation”, *Rock Mechanics and Rock Engineering*, 47(1), 43-55, 2014.
- [50] Labiouse V., Vietor T., “Laboratory and In Situ Simulation Tests of the Excavation Damaged Zone around Galleries in Opalinus Clay”, *Rock Mechanics and Rock Engineering*, 47(1), 57-70, 2014.

- [51] Labuz J. F., Zang A., “Mohr–Coulomb Failure Criterion”, *Rock Mechanics and Rock Engineering*, 45, 975–979, 2012. DOI 10.1007/s00603-012-0281-7.
- [52] Lee Y. K., Pietruszczak S., “A new numerical procedure for elasto-plastic analysis of a circular opening excavated in a strain-softening rock mass”, *Tunnelling and Underground Space Technology*, 23(5), 588-599, 2007.
- [53] Lyapunov A.M., “The general problem of stability of motion”, 1892, English translation, Taylor & Francis.
- [54] Lisjak A., Grasselli G., Vietor T., “Continuum–discontinuum analysis of failure mechanisms around unsupported circular excavations in anisotropic clay shales”, *International Journal of Rock Mechanics & Mining Sciences*, 65, 96-115, 2014. <http://dx.doi.org/10.1016/j.ijrmms.2013.10.006>.
- [55] Lisjak A., Figi D., Grasselli G., “Fracture development around deep underground excavations: Insights from FDEM modelling”, *Journal of Rock Mechanics and Geotechnical Engineering* 6, 493-505, 2014.
- [56] Lisjak A., Garitte B., Grasselli G., Müller H.R., Vietor T., “The excavation of a circular tunnel in a bedded argillaceous rock (Opalinus Clay): Short-term rock mass response and FDEM numerical analysis”, *Tunnelling and Underground Space Technology*, 45, 227–248, 2015. <http://dx.doi.org/10.1016/j.tust.2014.09.014>.
- [57] Mánica M., Gens A., Vaunat J., Ruiz D. F. “A time-dependent anisotropic model for argillaceous rocks. Application to an underground excavation in Callovo-Oxfordian claystone”, *Computers and Geotechnics*, 87, 341-350, 2017.
- [58] Menaceur H., Delage P., Tang A. M., Conil N. “The thermo-mechanical behaviour of the Callovo-Oxfordian claystone”, *International Journal of Rock Mechanics and Mining Sciences*, 78, 290-303, 2015.
- [59] Mohajerani M., Delage P., Monfared M., Tang A.M., Sulem J., Gatmiri B., “Oedometric compression and swelling behaviour of the Callovo-Oxfordian argillite”, *International Journal of Rock Mechanics and Mining Sciences*, 48, 606-615, 2011.
- [60] Noiret A., “Etude de la fracturation induite par le creusement et de l'EDZ pour une galerie de conception souple orientée suivant la contrainte horizontale majeure”, Andra technical report *D.RP.AMFS.12.0016*, 2012.
- [61] Nguyen V-L., “Modélisation numérique du comportement hydromécanique des milieux poreux fracturés: analyse des conditions de propagation des fractures”, PhD thesis, Ecole Nationale des Ponts et Chaussées, 2015.
- [62] Papamichos E., “Analysis of borehole failure modes and pore pressure effects”, *Computers and Geotechnics*, 37, 141-152, 2010.

- [63] Papanastasiou P., Vardoulakis I., “Bifurcation Analysis of Deep Boreholes: II. Scale Effect”, *International Journal for Numerical and Analytical Methods in Geomechanics*, 13, 183-198, 1989.
- [64] Papanastasiou P., Vardoulakis I. “Numerical treatment of progressive localization in relation to borehole stability”, *International Journal for Numerical and Analytical Methods in Geomechanics*, 16, 389-424, 1992.
- [65] Papanastasiou P., Zervos A., “Wellbore Stability Analysis: From Linear Elasticity to Postbifurcation Modeling”, *International Journal of Geomechanics*, 4(1), 2-12, 2004.
- [66] Pardoën B., “Hydro-mechanical analysis of the fracturing induced by the excavation of nuclear waste repository galleries using shear banding”, PhD thesis, Université de Liege, 2015.
- [67] Pardoën B., Levasseur S., Collin F., “Using Local Second Gradient Model and Shear Strain Localisation to Model the Excavation Damaged Zone in Unsaturated Claystone”, *Rock Mechanics and Rock Engineering*, 48(2), 691-714, 2015.
- [68] Pardoën B., Seyedi D.M., Collin F., “Shear banding modelling in cross-anisotropic rocks”, *International Journal of Solids and Structures*, 72, 63–87, 2015.
- [69] Pardoën B., Collin F., “Modelling the influence of strain localisation and viscosity on the behaviour of underground drifts drilled in claystone”, *Computers and Geotechnics*, 87, 351-367, 2017.
- [70] Park K. H., Tontavanich B., Lee J. G., “A simple procedure for ground response curve of circular tunnel in elastic-strain softening rock masses”, *Tunnelling and Underground Space Technology*, 23(2), 151-159, 2008.
- [71] Perras M. A., Diederichs M. S., “Predicting excavation damage zone depths in brittle rocks”, *Journal of Rock Mechanics and Geotechnical Engineering*, 8, 60-74, 2016.
- [72] Pouya A., “A finite element method for modelling coupled flow and deformation in porous fractured media”, *International Journal for Numerical and Analytical Methods in Geomechanics*, 39(16), 1836–1852, 2015.
- [73] Pouya A., Bourgeois E., Haxaire A., “Elaboration des modèles mécaniques et hydromécaniques homogénéisés de l’EDZ au champ proche d’un ouvrage de stockage (Fiche M-PS2, A1-4-1)”, Andra internal report *C.RP.0LCP.10.0003*, 2010.
- [74] Pouya A., Bendjeddou, Z., “Elaboration des modèles mécaniques et hydromécaniques homogénéisés de l’EDZ au champ proche d’un ouvrage de stockage (Fiche M-PS2, A1-4-2)”, Andra internal report *C.RP.0LCP.10.0005*, 2010.
- [75] Pouya A., Bendjeddou, Z., Poutrel, A., “Determination of an equivalent continuum mechanical model for the fractured EDZ around underground galleries by homogenization”, *Geosystem Engineering*, 16(1), 47–53, 2013.

- [76] Pouya A., Bémani P., “A damage-plasticity model for cohesive fractures”, *International Journal of Rock Mechanics and Mining Sciences*, 73, 194-202, 2015.
- [77] Pouya A., Trivellato E., Seyedi D., Vu M-N., “Apport des modeles d’endommagement sur la geometrie de la zone de rupture autour des ouvrages profonds dans des roches quasi-fragiles”. *Actes des 8èmes Journées Nationales de Géotechnique et de Géologie de l’Ingénieur, Journées Nationales de Géotechnique et de Géologie de l’Ingénieur*, 6-8 July 2016, Nancy, France.
- [78] Pouya A., Trivellato E., Seyedi D, Vu M-N., “Effect of softening damage and plasticity on the shape and extension of failure zone around deep galleries in quasi-brittle rocks”. *Engineering Mechanics Institute Conference (EMI 2017)*, June 4-7, 2017, San Diego, CA.
- [79] Ramamurthy T, Venkatappa RG, Singh J., “Engineering behaviour of phyllites”, *Engineering Geology*, 33, 209–25, 1993.
- [80] Reed, M. B., “Stresses and displacements around a cylindrical cavity in soft rock”, *IMA Journal of Applied Mathematics*, 36(3), 223-245, 1986.
- [81] Reed, M. B., “The Influence of Out-Of-Plane Stress on a Plane Strain Problem in Rock Mechanics”, TR/03/87, Department of Mathematics and Statistics, Brunel University Uxbridge, UK (1987).
- [82] Reinecker J., Tingay M., Müller B., “Borehole breakout analysis from four-arm Caliper logs”. *World Stress Map Project*, 2003.
- [83] Rice J.R., “The Localization of Plastic Deformation”. In: *Theoretical and Applied Mechanics, Proceedings of the 14th International Congress on Theoretical and Applied Mechanics*, W.T. Koiter (Eds.), 1, 207-220, North-Holland Publishing Co., Delft (Netherlands), 1976.
- [84] Robinet J.C., “Minéralogie, porosité et diffusion dans l'argilite du Callovo-Oxfordien de Bure (Meuse/Haute-Marne,France) de l'échelle centimétrique à micrométrique”, PhD thesis, Université de Poitiers, 2008.
- [85] Sadd M.H.: *Elasticity: Theory, Applications, and Numerics*, 2nd edn. Elsevier (2005).
- [86] Sahara D.P., Schoenball M., Gerolymatou E., Kohl T., “Analysis of borehole breakout development using continuum damage mechanics”, *International Journal of Rock Mechanics and Mining Sciences*, 97, 134-143, 2007.
- [87] Sammartino S., Bouchet A., Prêt D., Parneix J.C., Tevissen E., “Spatial distribution of porosity and minerals in clay rocks from the Callovo–Oxfordian formation (Meuse/Haute- Marne, Eastern France)—implications on ionics species diffusion and rock sorption capability”, *Applied Clay Science*, 23(1–4), 157–166, 2003.

- [88] Santarelli F. J., Dahen D., Baroudi H., Sliman K. B., “Mechanisms of borehole instability in heavily fractured rock media”, *International Journal of Rock Mechanics and Mining Sciences & Geomechanics Abstracts*, 29(5), 457-467, 1992.
- [89] Saroglou H., Tsiambaos G., “A modified Hoek-Brown failure criterion for anisotropic intact rock”, *International Journal of Rock Mechanics and Mining Sciences*, 45(2), 223-234, 2008.
- [90] Sharan S. K., “Elastic-brittle-plastic analysis of circular openings in Hoek-Brown media” *International Journal of Rock Mechanics and Mining Sciences*, 40(6), 817–824, 2003.
- [91] Seyedi, D.M., Armand, G., “Compte-rendu: Réunion plénière du Groupement de Laboratoires (GL) Comportement Mécanique des OUVrages et des composants des stockages (MOUV)”, Andra technical report *DRD/MFS/16-0115*, 2016.
- [92] Seyedi D.M., Vu M.N., Armand G., Noiret A. “Numerical modeling of damage patterns around drifts in the Meuse/Haute-Marne URL”. *The 13th International ISRM Congress 2015*, Montréal, Québec, Canada 10-13 May, 2015.
- [93] Seyedi D. M., Armand G., Noiret A. “ “Transverse Action” – A model benchmark exercise for numerical analysis of the Callovo-Oxfordian claystone hydromechanical response to excavation operations”, *Computers and Geotechnics*, 87, 287-305, 2017.
- [94] Seyedi D. M., Gens A., “Numerical analysis of the hydromechanical response of Callovo-Oxfordian claystone to deep excavations”, *Computers and Geotechnics* 87, 275-276, 2017.
- [95] Silvestre, N., "Generalized beam theory to analyze the buckling behavior of circular cylindrical shells and tubes", *Thin-Walled Structures*, 45(2), 185-198, 2007.
- [96] Sofianos A. I., “Tunnelling Mohr-Coulomb strength parameters for rock masses satisfying the generalized Hoek-Brown failure criterion” *International Journal of Rock Mechanics and Mining Sciences*, 40(3), 435–440, 2003.
- [97] Souley M., Armand G., Kazmierczak J.-B., “Hydro-elasto-viscoplastic modeling of a drift at the Meuse/Haute-Marne underground research laboratory (URL)”, *Computers and Geotechnics*, 87, 306-320, 2017.
- [98] Sulem J., “Bifurcation theory and localization phenomena”, *European Journal of Environmental and Civil Engineering* (Ed. Lavoisier) 14(8-9), 989-1009, 2010.
- [99] Thakur V., “Strain localization in sensitive soft clays”, PhD thesis, Norwegian University of Science and Technology, 2007.
- [100] Trivellato E., Pouya A., Vu M-N., Seyedi D., “Modelling of the gallery excavation-induced fractures in quasi-brittle rocks by a damage-cohesive approach”. In : Hamdi E. (Eds.) *Proceedings of the First International Conference on Advances in Rock Mechanics*. Tunirock 2018, 29-31 March, 2016, Hammamet, Tunisia.

- [101] Trivellato E., Pouya A., Vu M-N., Seyedi D., “Damage-Based Cohesive Modelling for Fractures Initiation and Propagation Around a Deep Tunnel in Quasi-brittle Rocks”. In: Zhang L., Goncalves da Silva B., Zhao C. (eds) *Proceedings of GeoShanghai 2018 International Conference: Rock Mechanics and Rock Engineering*. GSIC 2018. Springer, Singapore.
- [102] Trivellato E., Pouya A., Vu M-N., Seyedi D., “Modélisation en endommagement radoucissant de la zone de rupture autour des ouvrages profonds dans des roches anisotropes quasi-fragiles”, *Actes des 9èmes Journées Nationales de Géotechnique et de Géologie de l'Ingénieur, Journées Nationales de Géotechnique et de Géologie de l'Ingénieur*, 13 - 15 June 2018, Champs-Sur-Marne, France.
- [103] Tsang C.F., Bernier F., Davies C., “Geohydrromechanical processes in the excavation damage zone in crystalline rock, rock salt, and indurated and plastic clays in the context of radioactive waste disposal”, *International Journal of Rock Mechanics and Mining Sciences*, 42(1), 109-125, 2005.
- [104] Ullah H., “Buckling of thin-walled cylindrical shells under axial compression”, *International Journal for Numerical Methods in Engineering*, 79, 1332-1353, 2009.
- [105] Van den Eijnden A.P., Bésuelle P., Collin F., Chambon R., Desrues J., “Modelling the strain localization around an underground gallery with a hydro-mechanical double scale model; effect of anisotropy”, *Computers and Geotechnics*, 87, 384-400, 2017.
- [106] Van den Hoek P.J., Smit D.-J., Kooijman A.P., De Bree P., Kenter C.J., Khodaverdian, M., “Size dependancy of hollow-cylinder stability”, *Eurock 1994*, vol. 94. Balkema, Rotterdam, 1994.
- [107] Van den Hoek, P.J., “Prediction of different types of cavity failure using bifurcation theory”, *The 38th U.S. Symposium on Rock Mechanics (USRMS)*, 7-10 July 2001, Washington, D.C., 2001.
- [108] Varas F., Alonso E., Alejano L. R., Fdez.-Manín G., “Study of bifurcation in the problem of unloading a circular excavation in a strain-softening material”, *Tunnelling and Underground Space Technology*, 20, 311-322, 2005.
- [109] Vardoulakis I., Sulem J., Guenot, A., “Borehole instabilities as bifurcation phenomena”, *International Journal of Rock Mechanics and Mining Sciences & Geomechanics Abstracts*, 25(3), 159-170, 1988.
- [110] Vardoulakis I., Papanastasiou P., “Bifurcation analysis of deep boreholes: I. Surface instabilities”, *International Journal for Numerical and Analytical Methods in Geomechanics*, 12, 379-399, 1988.
- [111] Vo T-D., “Modélisation numérique et analytique de la fissuration de séchage des sols argileux”, PhD thesis, Ecole Nationale des Ponts et Chaussées, 2017.

- [112] Vu T.M., Sulem J., Subrin D., Monin N., “Semi-analytical solution for stresses and displacements in a tunnel excavated in transversely isotropic formation with non-linear behavior”, *Rock Mechanics and Rock Engineering*, 46(2), 213-229, 2013.
- [113] Wileveau Y., Cornet F.H., Desroches J., Blumling P., “Complete *in situ* stress determination in an argillite sedimentary formation”, *Physics and Chemistry of the Earth*, 32(8-14), 866–878, 2007.
- [114] Wileveau Y., Bernier F., “Similarities in the hydromechanical response of Callovo-Oxfordian clay and Boom Clay during gallery excavation”, *Physics and Chemistry of the Earth*, 33, 343–349, 2008.
- [115] Wu B., Tan C.P., Aoki T., “Specially designed techniques for conducting consolidated undrained triaxial tests on low permeability shales” , *International Journal of Rock Mechanics and Mining Sciences*, 34, 336.e1–336.e14, 1997.
- [116] Yao C., Shao J.F., Jiang Q.H., Zhou, C.B., “Numerical study of excavation induced fractures using an extended rigid block spring method”, *Computers and Geotechnics*, 87, 368-383, 2017.
- [117] Zhang C.L., Czaikowski O., Rothfuchs T. “Thermo-Hydro-Mechanical Behaviour of the Callovo-Oxfordian Clay Rock”, Gesellschaft für Anlagen- und Reaktorsicherheit (GRS) mbH, Technical report GRS - 266 ISBN 978-3-939355-42-7, 2010.
- [118] Zhang, C.L., Armand, G., Conil, N., “Investigation on the Anisotropic Mechanical Behaviour of the Callovo-Oxfordian Clay Rock”, ANDRA/GRS cooperation programme, final report, 2015.
- [119] Zhang C.L., Dittrich J., Müller J., Rothfuchs T. Experimental Study of the Hydromechanical Behaviour of the Callovo-Oxfordian Argillites - Part of the MODEX-REP Project. Gesellschaft für Anlagen- und Reaktorsicherheit (GRS) mbH, 2012. Technical report GRS-187 ISBN 3-931995-55-0.
- [120] Zhang, C., Rothfuchs T., “Experimental study of the hydro-mechanical behaviour of the Callovo-Oxfordian argillite”, *Applied Clay Science*, 26, 325-336, 2004.
- [121] <https://www.andra.fr/download/andra-international-en/document/editions/268va.pdf> (*Synthesis argile: evaluation of the feasibility of a geological repository in argillaceous formation*, 2005).
- [122] <https://www.irsn.fr>

# Appendices

## A – Details on the *FEM* codes

In Figure A.1, following: as mentioned in Chapter 2, Section 2.1, the structure model of a typical subroutine for a constitutive law implementation in *POROFIS* is reported. In particular, the three main parts that constitute respectively the failure criterion definition, the update of the damage or plastic law with their internal variables and the linear elastic relation  $\sigma : \varepsilon$  are highlighted.

In Figure A.2, next page: the computing procedure executed by *POROFIS* for a local Newton-Raphson integration of the constitutive law when failure (or non-linearities) occurs. It is shown then, globally, the verification of the consistency law  $f = \dot{f} = 0$  according to an imposed tolerance,  $\zeta$ . If the consistency law verification is rejected, a new Newton-Raphson iteration will be executed for each Gauss point. The same *local-global-local* iterative scheme applies for displacements convergence for each calculation step. It refers to Chapter 2, Section 2.1.

In Figure A.3, next page: illustration of the local reference system as defined in *POROFIS* and *DISROC* is reported, for whatever inclination with respect to the Cartesian reference of axis. For a stress tensor  $\sigma_{(0)}$ , the tangential and normal components,  $\tau$  and  $\sigma_n$ , of the stress state  $T_i$  at the local point  $i$  on the gallery perimeter are written according to Eq. A.1 and A.2.

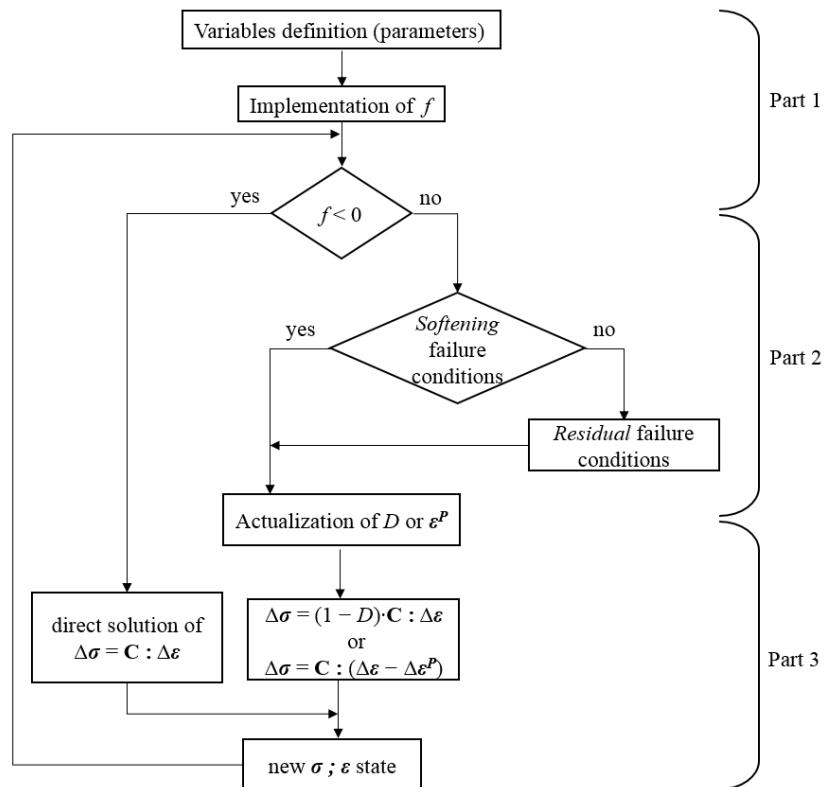


**Figure A.1 :** procedures composing the step-by step resolution of the  $\sigma : \varepsilon$  relation for a classical constitutive law in *Utilizer.f90*.

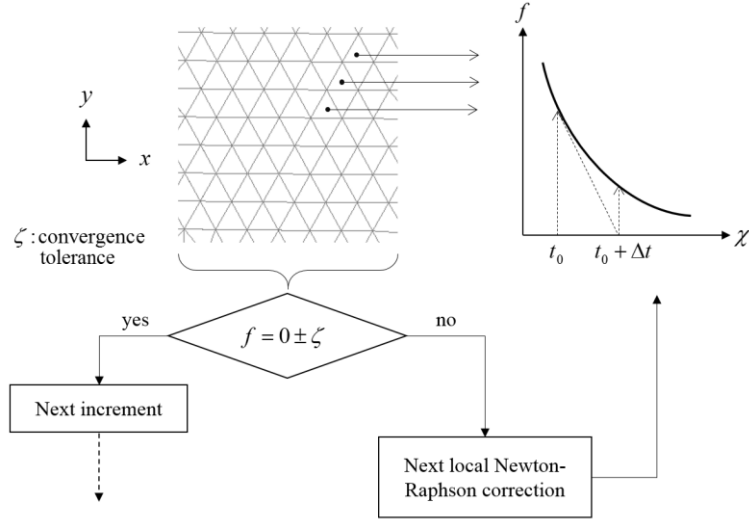


**Figure A.2** : local-global-local iterative procedure for yielding correction with global verification of the consistency law. The failure criterion  $f$  is represented as function of the internal variable(s),  $\chi$ .

$$\boldsymbol{\tau} = \mathbf{t}^T \cdot \mathbf{T}_i = \mathbf{t}^T \cdot \boldsymbol{\sigma}_{(0)} \cdot \mathbf{n} \quad (\text{A. 1})$$

$$\boldsymbol{\sigma}_n = \mathbf{n}^T \cdot \mathbf{T}_i = \mathbf{n}^T \cdot \boldsymbol{\sigma}_{(0)} \cdot \mathbf{n} \quad (\text{A. 2})$$

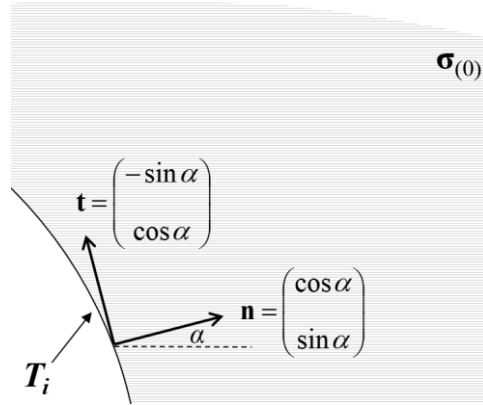


**Figure A.3** : normal and tangential local coordinates system in *POROFIS* and *DISROC*, for the evaluation of the stress state at  $i$ .  $\boldsymbol{\sigma}_{(0)}$  is the (initial) stress tensor defined in the principal coordinates system.

## B – Anisotropies in failure criteria and damage-elasticity

Section B of the Appendix reports the explicit formulations for mathematical modelling of transverse isotropy (failure and elasticity) in the Callovo-Oxfordian claystone, implemented numerically in *POROFIS*.

### B.1 Drucker-Prager failure criterion based on a second (II) order rotation tensor (including the axial stress component $\sigma_{zz}$ )

Here, the criterion's formulation as reported in Chapter 3, Section 3.2, is illustrated, together with the step-by-step procedure to derive the anisotropy scaling factor,  $h$ .

By the unitary normal vector  $\mathbf{n}$ , a second order rotation tensor  $\mathbf{M}$  accounting for material anisotropy is defined and applied to the original stress tensor  $\boldsymbol{\sigma}$ :

$$\mathbf{n} = (\cos \omega \quad \sin \omega \quad 0)^T \quad ; \quad \mathbf{M} = \delta_{ij} + h(\mathbf{n} \otimes \mathbf{n}) \quad (\text{B. 1a-b})$$

$$\tilde{\boldsymbol{\sigma}} = \mathbf{M}^T \cdot \boldsymbol{\sigma} \cdot \mathbf{M} \quad (\text{B. 2})$$

$$\mathbf{M} = \begin{bmatrix} 1 + h \cos^2 \omega & h \sin \omega \cos \omega & 0 \\ h \sin \omega \cos \omega & 1 + h \sin^2 \omega & 0 \\ 0 & 0 & 1 \end{bmatrix} \quad (\text{B. 3})$$

Eq. B.2 is explicitly written:

$$\begin{aligned} \tilde{\boldsymbol{\sigma}} &= \begin{bmatrix} 1 + h \cos^2 \omega & h \sin \omega \cos \omega & 0 \\ h \sin \omega \cos \omega & 1 + h \sin^2 \omega & 0 \\ 0 & 0 & 1 \end{bmatrix} \cdot \begin{bmatrix} \sigma_{xx} & \sigma_{xy} & 0 \\ \sigma_{xy} & \sigma_{yy} & 0 \\ 0 & 0 & \sigma_{zz} \end{bmatrix} \cdot \begin{bmatrix} 1 + h \cos^2 \omega & h \sin \omega \cos \omega & 0 \\ h \sin \omega \cos \omega & 1 + h \sin^2 \omega & 0 \\ 0 & 0 & 1 \end{bmatrix} = \\ &= \begin{bmatrix} \tilde{\sigma}_{xx} & \tilde{\sigma}_{xy} & 0 \\ \tilde{\sigma}_{yx} & \tilde{\sigma}_{yy} & 0 \\ 0 & 0 & \tilde{\sigma}_{zz} \end{bmatrix} \quad (\text{B. 4}) \end{aligned}$$

Adopting the tensor in Eq. B.4, a *modified* Drucker-Prager failure criterion can be defined:

$$f = \sqrt{3\tilde{J}_2} + \sin \alpha \tilde{I}_1 - g(D)K = 0 \quad (\text{B. 5})$$

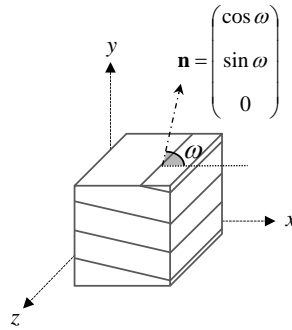


**Figure B.1:** volume element scheme for the anisotropic Drucker-Prager failure criterion.

For uniaxial compression along the vertical axis  $y$  ( $\sigma_{xx} = \sigma_{zz} = \sigma_{xy} = 0$ ):

$$\begin{aligned} \tilde{\boldsymbol{\sigma}} &= \begin{bmatrix} 1+h\cos^2\omega & h\sin\omega\cos\omega & 0 \\ h\sin\omega\cos\omega & 1+h\sin^2\omega & 0 \\ 0 & 0 & 1 \end{bmatrix} \cdot \begin{bmatrix} 0 & 0 & 0 \\ 0 & \sigma_{yy} & 0 \\ 0 & 0 & 0 \end{bmatrix} \cdot \begin{bmatrix} 1+h\cos^2\omega & h\sin\omega\cos\omega & 0 \\ h\sin\omega\cos\omega & 1+h\sin^2\omega & 0 \\ 0 & 0 & 1 \end{bmatrix} = \\ &= \begin{bmatrix} h^2\sin^2\omega\cos^2\omega\cdot\sigma_{yy} & h\sin\omega\cos\omega(1+h\sin^2\omega)\cdot\sigma_{yy} & 0 \\ h\sin\omega\cos\omega(1+h\sin^2\omega)\cdot\sigma_{yy} & (1+h\sin^2\omega)^2\sigma_{yy} & 0 \\ 0 & 0 & 0 \end{bmatrix} \end{aligned} \quad (\text{B. 6})$$

If the uniaxial compression occurs parallel to bedding ( $\omega = 0$  in Figure B.1):

$$\tilde{\boldsymbol{\sigma}} = \begin{bmatrix} 0 & 0 & 0 \\ 0 & \sigma_{yy} & 0 \\ 0 & 0 & 0 \end{bmatrix} \quad (\text{B. 7})$$

At the elastic limit,  $D = 0 \rightarrow g(D) = 1$  and  $f = 0$ :

$$f(\tilde{\boldsymbol{\sigma}}) = \sqrt{\sigma_{yy}^2} + \sin\alpha \cdot \sigma_{yy} - K = |\sigma_{yy}| + \sin\alpha \cdot \sigma_{yy} - K = 0 \quad (\text{B. 8})$$

The unconfined compression value providing  $f = 0$  is the uniaxial compressive strength (*UCS*),  $\sigma_0$ . In particular, this corresponds to the *UCS* for  $\omega = 0$ , writing  $\sigma_{0,0^\circ}$ . In general, *UCS* for a generic inclination,  $\sigma_{0,\omega}$ , is defined positive for every  $\omega$ . Because of the rock mechanics' convention on variables signs (tensile stresses are positive and compressive stresses are negative),  $\sigma_{yy} < 0$  in Eq. B.8. If it represents a uniaxial compression state at failure,  $|\sigma_{yy}| = -\sigma_{yy}$  and, for what previously stated,  $\sigma_{0,0^\circ} = -\sigma_{yy}$ . Eq. B.8 can be rewritten as follows:

$$|\sigma_{yy}| + \sin\alpha \cdot \sigma_{yy} - K = -\sigma_{yy} + \sin\alpha \cdot \sigma_{yy} - K = \sigma_{0,0^\circ} - \sin\alpha \cdot \sigma_{0,0^\circ} - K = 0 \quad (\text{B. 9})$$

Eventually, *UCS* for  $\omega = 0$  writes:

$$\sigma_{0,0^\circ} = \frac{K}{(1 - \sin\alpha)} \quad (\text{B. 10})$$

Eq. B.10 corresponds to the classical *UCS* for an isotropic Drucker-Prager criterion. But, if the unconfined compression occurs again along  $y$ , for  $\omega = 90^\circ$  (perpendicular to bedding in Figure B.1), the modified stress tensor (Eq. B.6) writes:

$$\tilde{\boldsymbol{\sigma}} = \begin{bmatrix} 0 & 0 & 0 \\ 0 & (1+h)^2\sigma_{yy} & 0 \\ 0 & 0 & 0 \end{bmatrix} \quad (\text{B. 11})$$

At the elastic limit:

$$f(\tilde{\boldsymbol{\sigma}}) = \sqrt{(1+h)^4\sigma_{yy}^2} + \sin\alpha \cdot (1+h)^2\sigma_{yy} - K = (1+h)^2|\sigma_{yy}| + \sin\alpha \cdot (1+h)^2\sigma_{yy} - K = 0 \quad (\text{B. 12})$$

In analogy with  $\sigma_{0,0^\circ}$ , the UCS at  $\omega = 90^\circ$  writes:

$$\sigma_{0,90^\circ} = \frac{K}{(1+h)^2(1-\sin\alpha)} \quad (\text{B. 13})$$

It is finally possible to write the expression for the anisotropy scaling factor,  $h$ , as a function of the ratio between UCS at  $0^\circ$  and  $90^\circ$ , as reported in Chapter 3, Section 3.2:

$$\frac{\sigma_{0,0^\circ}}{\sigma_{0,90^\circ}} = \frac{\frac{K}{(1-\sin\alpha)}}{\frac{K}{(1+h)^2(1-\sin\alpha)}} = (1+h)^2 \rightarrow h = \sqrt{\frac{\sigma_{0,0^\circ}}{\sigma_{0,90^\circ}}} - 1 \quad (\text{B. 14})$$

*B.2 Mohr-Coulomb type failure criterion based on a second (II) order rotation tensor  
(neglecting the axial stress component  $\sigma_{zz}$ )*

In the following, this anisotropic criterion, as reported in Chapter 3, Section 3.4, is detailed and its analytical expressions derived from the failure function  $f$  are provided, for the cases of unconfined loading and loading confined with a stress  $p_C$ .

The unit normal vector  $\mathbf{n}$  defines the second order rotation tensor  $\mathbf{M}$  accounting for material anisotropy, as done in the previous 3d criterion:

$$\mathbf{n} = (\cos\omega \quad \sin\omega)^T \quad ; \quad \mathbf{M} = \delta_{ij} + h(\mathbf{n} \otimes \mathbf{n}) \quad (\text{B. 15a-b})$$

Similarly, a modified stress tensor  $\tilde{\boldsymbol{\sigma}}$  to identify the stress components at failure is written as:

$$\tilde{\boldsymbol{\sigma}} = \mathbf{M}^T \cdot \boldsymbol{\sigma} \cdot \mathbf{M} \quad (\text{B. 16})$$

Formalizing the 2d tensor  $\mathbf{M}$ :

$$\mathbf{M} = \begin{bmatrix} 1+h\cos^2\omega & h\sin\omega\cos\omega \\ h\sin\omega\cos\omega & 1+h\sin^2\omega \end{bmatrix} \quad (\text{B. 17})$$

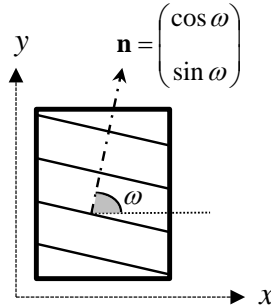


**Figure B.2:** volume element scheme for the anisotropic Mohr-Coulomb type failure criterion.

The final expression of  $\tilde{\boldsymbol{\sigma}}$  in two dimensions writes:

$$\begin{aligned}\tilde{\boldsymbol{\sigma}} &= \begin{bmatrix} 1+h\cos^2\omega & h\sin\omega\cos\omega \\ h\sin\omega\cos\omega & 1+h\sin^2\omega \end{bmatrix} \cdot \begin{bmatrix} \sigma_{xx} & \sigma_{xy} \\ \sigma_{xy} & \sigma_{yy} \end{bmatrix} \cdot \begin{bmatrix} 1+h\cos^2\omega & h\sin\omega\cos\omega \\ h\sin\omega\cos\omega & 1+h\sin^2\omega \end{bmatrix} \\ &= \begin{bmatrix} \tilde{\sigma}_{xx} & \tilde{\sigma}_{xy} \\ \tilde{\sigma}_{xy} & \tilde{\sigma}_{yy} \end{bmatrix}\end{aligned}\quad (\text{B. 18})$$

Adopting every component in Eq. B.18, the bi-dimensional failure criterion writes:

$$f(\tilde{\boldsymbol{\sigma}}, D) = \sqrt{(\tilde{\sigma}_{xx} - \tilde{\sigma}_{yy})^2 + 4\tilde{\sigma}_{xy}^2} + \sin\phi(\tilde{\sigma}_{xx} + \tilde{\sigma}_{yy}) - g(D)K \quad (\text{B. 19})$$

For uniaxial compression along the vertical axis  $y$  ( $\sigma_{xx} = \sigma_{xy} = 0$ ):

$$\boldsymbol{\sigma} = \begin{bmatrix} 0 & 0 \\ 0 & \sigma_{yy} \end{bmatrix} \quad (\text{B. 20})$$

The modified stress tensor writes:

$$\tilde{\boldsymbol{\sigma}} = \begin{bmatrix} h^2\sin^2\omega\cos^2\omega \cdot \sigma_{yy} & h\sin\omega\cos\omega(1+h\sin^2\omega) \cdot \sigma_{yy} \\ h\sin\omega\cos\omega(1+h\sin^2\omega) \cdot \sigma_{yy} & (1+h\sin^2\omega)^2 \sigma_{yy} \end{bmatrix} \quad (\text{B. 21})$$

In this configuration, the criterion when failure is firstly attained ( $D = 0$ ,  $g(D) = 1$ ) writes:

$$\begin{aligned}f(\tilde{\boldsymbol{\sigma}}, D) &= \sqrt{\left[h^2\sin^2\omega\cos^2\omega - (1+h\sin^2\omega)^2\right]^2 \sigma_{yy}^2 + 4h^2\sin^2\omega\cos^2\omega(1+h\sin^2\omega)^2 \sigma_{yy}^2} + \\ &+ \sin\phi \left[h^2\sin^2\omega\cos^2\omega + (1+h\sin^2\omega)^2\right] \sigma_{yy} - K \\ &= \sqrt{\left[h^2\sin^2\omega\cos^2\omega - (1+h\sin^2\omega)^2\right]^2 + 4h^2\sin^2\omega\cos^2\omega(1+h\sin^2\omega)^2} |\sigma_{yy}| + \\ &+ \sin\phi \left[h^2\sin^2\omega\cos^2\omega + (1+h\sin^2\omega)^2\right] \sigma_{yy} - K\end{aligned}\quad (\text{B. 22})$$

When  $f = 0$ , again, it is possible to write  $|\sigma_{yy}| = -\sigma_{yy}$  and  $\sigma_{0,\omega} = -\sigma_{yy}$  ( $\sigma_{0,\omega} \equiv$  unconfined compressive strength  $UCS$ ,  $\forall \omega$ ). The analytical expression of  $\sigma_{0,\omega}$  writes:

$$\sigma_{0,\omega} = \frac{K}{C_{\text{dev}} - C_{\text{sph}}} \quad (\text{B. 23})$$

In Eq. B.23, these coefficients are defined:

$$C_{\text{dev}} = \sqrt{\left[h^2\sin^2\omega\cos^2\omega - (1+h\sin^2\omega)^2\right]^2 + 4h^2\sin^2\omega\cos^2\omega(1+h\sin^2\omega)^2} \quad (\text{B. 24})$$

as a *deviatoric* coefficient, and:

$$C_{\text{sph}} = \sin\phi \left[h^2\sin^2\omega\cos^2\omega + (1+h\sin^2\omega)^2\right] \quad (\text{B. 25})$$

as a *spherical* coefficient.

The function of  $\sigma_{\theta,\omega}$ , periodical with  $\omega$ , is, traced in Figure B.3 for  $\varphi = 20^\circ$ ,  $K = 15$  MPa and  $h = 0.2$ . It is possible to select an appropriate interval of variation covering  $90^\circ$ , to evaluate different combinations of  $\sigma_{\theta,\omega}$  evolution with the bedding inclination (e.g., monotonic or not).

Back to Eq. B.19, a compression along vertical axis  $y$  with a confinement along  $x$  is now considered:  $\sigma_{xx} = p_C$ ,  $\sigma_{yy} > 0$ ,  $\sigma_{xy} = 0$ . The stress tensor writes:

$$\boldsymbol{\sigma} = \begin{bmatrix} p_C & 0 \\ 0 & \sigma_{yy} \end{bmatrix} \quad (\text{B. 26})$$

The modified stress tensor writes:

$$\tilde{\boldsymbol{\sigma}} = \begin{bmatrix} \tilde{\sigma}_{xx} & \tilde{\sigma}_{xy} \\ \tilde{\sigma}_{xy} & \tilde{\sigma}_{yy} \end{bmatrix} \quad (\text{B. 27})$$

With (applying Eq. B.16):

$$\tilde{\sigma}_{xx} = (1 + h \cos^2 \omega)^2 p_C + h^2 \sin^2 \omega \cos^2 \omega \cdot \sigma_{yy} \quad (\text{B. 28})$$

$$\tilde{\sigma}_{yy} = h^2 \sin^2 \omega \cos^2 \omega \cdot p_C + (1 + h \sin^2 \omega)^2 \sigma_{yy} \quad (\text{B. 29})$$

$$\tilde{\sigma}_{xy} = h \sin \omega \cos \omega [(1 + h \cos^2 \omega) \cdot p_C + (1 + h \sin^2 \omega) \cdot \sigma_{yy}] \quad (\text{B. 30})$$

The criterion at initial yielding ( $D = 0$ ,  $g(D) = 1$ ) writes:

$$\begin{aligned} f(\tilde{\boldsymbol{\sigma}}) = & \sqrt{\left[ (1 + h \cos^2 \omega)^2 p_C + h^2 \sin^2 \omega \cos^2 \omega (\sigma_{yy} - p_C) - (1 + h \sin^2 \omega)^2 \sigma_{yy} \right]^2 +} \\ & + \sqrt{4h^2 \sin^2 \omega \cos^2 \omega [(1 + h \cos^2 \omega) \cdot p_C + (1 + h \sin^2 \omega) \cdot \sigma_{yy}]^2} + \\ & + \sin \varphi \left[ (1 + h \cos^2 \omega)^2 p_C + h^2 \sin^2 \omega \cos^2 \omega (\sigma_{yy} + p_C) + (1 + h \sin^2 \omega)^2 \sigma_{yy} \right] - K = 0 \end{aligned} \quad (\text{B. 31})$$

It is possible to rewrite the criterion above separating, each time, respectively for  $p_C$  and  $\sigma_{yy}$ , their coefficients, expressed as function of  $h$  and  $\omega$ :

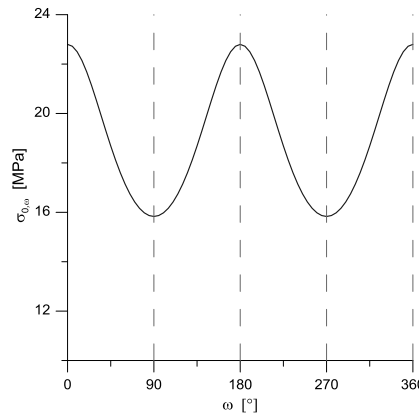


**Figure B.3:**  $\sigma_{\theta,\omega}$ , as a function of  $\omega$ , with  $\varphi = 20^\circ$ ,  $K = 15$  MPa and  $h = 0.2$ .

$$f(\tilde{\sigma}) = \sqrt{\left[ (1+h\cos^2\omega)^2 - h^2\sin^2\omega\cos^2\omega \right] p_C + \left[ h^2\sin^2\omega\cos^2\omega - (1+h\sin^2\omega)^2 \right] \sigma_{yy}}^2 + \sqrt{\left[ 2h\sin\omega\cos\omega(1+h\cos^2\omega) \cdot p_C + 2h\sin\omega\cos\omega(1+h\sin^2\omega) \cdot \sigma_{yy} \right]^2} + \quad (\text{B. 32})$$

$$+ \sin\varphi \left\{ \left[ (1+h\cos^2\omega)^2 + h^2\sin^2\omega\cos^2\omega \right] p_C + \left[ h^2\sin^2\omega\cos^2\omega + (1+h\sin^2\omega)^2 \right] \sigma_{yy} \right\} - K = 0$$

$$= \sqrt{(Ap_C + B\sigma_{yy})^2 + (Cp + D\sigma_{yy})^2} + \sin\varphi(Ep_C + F\sigma_{yy}) - K = 0 \quad (\text{B. 33})$$

In the following, the coefficients in Eq. B.33 are expressed:

$$A = \left[ (1+h\cos^2\omega)^2 - h^2\sin^2\omega\cos^2\omega \right] \quad ; \quad B = \left[ h^2\sin^2\omega\cos^2\omega - (1+h\sin^2\omega)^2 \right] \quad (\text{B. 34a})$$

$$C = 2h\sin\omega\cos\omega(1+h\cos^2\omega) \quad ; \quad D = 2h\sin\omega\cos\omega(1+h\sin^2\omega) \quad (\text{B. 34b})$$

$$E = \left[ (1+h\cos^2\omega)^2 + h^2\sin^2\omega\cos^2\omega \right] \quad ; \quad F = \left[ h^2\sin^2\omega\cos^2\omega + (1+h\sin^2\omega)^2 \right] \quad (\text{B. 34c})$$

Since the confinement  $p_C$  is a constant boundary condition, it is possible to write again:

$$A \cdot p_C = \bar{A} = \text{const.} \quad (\text{B. 35a})$$

$$C \cdot p_C = \bar{C} = \text{const.} \quad (\text{B. 35b})$$

$$\sin\varphi \cdot E \cdot p_C = \bar{E} = \text{const.} \quad ; \quad \sin\varphi \cdot F = \bar{F} = \text{const.} \quad (\text{B. 35c})$$

As a function of the vertical load,  $\sigma_{yy}$ , only, the criterion writes:

$$f(\sigma_{yy}) = \sqrt{(\bar{A} + B\sigma_{yy})^2 + (\bar{C} + D\sigma_{yy})^2} + \bar{E} + \bar{F}\sigma_{yy} = K \quad (\text{B. 36a})$$

$$= \sqrt{(\bar{A} + B\sigma_{yy})^2 + (\bar{C} + D\sigma_{yy})^2} = (K - \bar{E}) - \bar{F}\sigma_{yy} \quad (\text{B. 36b})$$

From Eq. B.36b, one derives:

$$(\bar{A} + B\sigma_{yy})^2 + (\bar{C} + D\sigma_{yy})^2 = \left[ (K - \bar{E}) - \bar{F}\sigma_{yy} \right]^2 = (K - \bar{E})^2 - 2(K - \bar{E})\bar{F}\sigma_{yy} + \bar{F}^2\sigma_{yy}^2 \quad (\text{B. 37})$$

It is possible, eventually, to reduce the entire equation to a second order polynomial:

$$(\mathbf{B}^2 + \mathbf{D}^2 - \bar{\mathbf{F}}^2)\sigma_{yy}^2 + 2[\bar{\mathbf{A}}\mathbf{B} + \bar{\mathbf{C}}\mathbf{D} + (K - \bar{\mathbf{E}})\bar{\mathbf{F}}]\sigma_{yy} + [\bar{\mathbf{A}}^2 + \bar{\mathbf{C}}^2 - (K - \bar{\mathbf{E}})^2] = 0 \quad (\text{B. 38})$$

Since, at failure,  $\sigma_0(p_C)_\omega = -\sigma_{yy}$ , the criterion writes:

$$a_1 \cdot \sigma_0^2(p_C)_\omega - a_2 \cdot \sigma_0(p_C)_\omega + a_3 = 0 \quad (\text{B. 39a})$$

with the following coefficients:

$$a_1 = (\mathbf{B}^2 + \mathbf{D}^2 - \bar{\mathbf{F}}^2) \quad (\text{B. 39b})$$

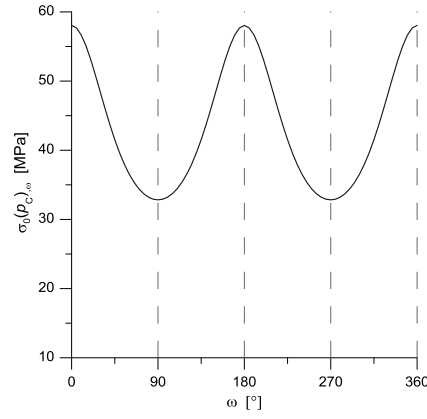


**Figure B.4:**  $\sigma_0(p_C = 12 \text{ MPa})_{,\omega}$  as a function of  $\omega$ , with  $\varphi = 20^\circ$ ,  $K = 15 \text{ MPa}$  and  $h = 0.2$ .

$$a_2 = 2[\bar{A}\bar{B} + \bar{C}\bar{D} + (K - \bar{E})\bar{F}] \quad (\text{B. 39c})$$

$$a_3 = [\bar{A}^2 + \bar{C}^2 - (K - \bar{E})^2] \quad (\text{B. 39d})$$

According to the analytical solution for second order polynomials, the expression of  $\sigma_0(p_C)_{,\omega}$  writes:

$$\sigma_0(p_C)_{,\omega} = \frac{a_2 \pm \sqrt{a_2^2 - 4 \cdot a_1 \cdot a_3}}{2a_1} \quad (\text{B. 40})$$

with  $a_1 > 0$ . In particular, it is possible to verify that, to obtain positive values of  $\sigma_0(p_C)_{,\omega}$ , the unique solution corresponds to:

$$\sigma_0(p_C)_{,\omega} = \frac{a_2 + \sqrt{a_2^2 - 4 \cdot a_1 \cdot a_3}}{2a_1} \quad (\text{B. 41})$$

Similarly to  $\sigma_{0,\omega}$ , the function  $\sigma_0(p_C)_{,\omega}$  is periodical with  $\omega$ . It is traced in Figure B.4 for the same failure parameters adopted in Figure B.3, with a confinement  $\sigma_{xx} = p_C = 12 \text{ MPa}$ . Again, in this case, an interval of inclination  $\omega$ , covering a variation of  $90^\circ$ , can be chosen to describe a monotonic or non-monotonic trend for  $\sigma_0(p_C)_{,\omega}$ , according to confined compression data at failure.

### B.3 Mohr-Coulomb type failure criterion based on a fourth (IV) order rotation tensor (neglecting the axial stress component $\sigma_{zz}$ )

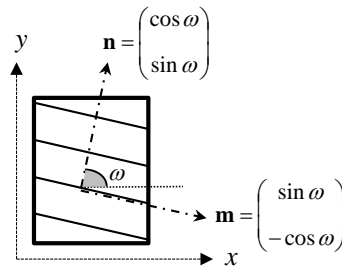


**Figure B.5:** volume element scheme for the IV order anisotropic Mohr-Coulomb type failure criterion.

The last anisotropic criterion proposed (Chapter 4, Section 4.3), is detailed here and its analytical expressions derived from the failure function  $f$  are provided, for unconfined loading and loading confined with a stress  $p_c$ . By the unit vectors  $\mathbf{n}$  and  $\mathbf{m}$  (Figure B.5), the fourth order rotation tensor  $\mathbf{H}$  accounting for material anisotropy is defined as:

$$\mathbf{n} = (\cos \omega \quad \sin \omega)^T \quad ; \quad \mathbf{m} = (\sin \omega \quad -\cos \omega)^T \quad (\text{B. 42a-b})$$

$$\begin{aligned} \mathbf{H} = & h_n (\mathbf{n} \otimes \mathbf{n}^T) \otimes (\mathbf{n} \otimes \mathbf{n}^T) + (\mathbf{m} \otimes \mathbf{m}^T) \otimes (\mathbf{m} \otimes \mathbf{m}^T) + \\ & + \frac{h_s}{2} [(\mathbf{m} \otimes \mathbf{n}^T + \mathbf{n} \otimes \mathbf{m}^T) \otimes (\mathbf{m} \otimes \mathbf{n}^T + \mathbf{n} \otimes \mathbf{m}^T)] \end{aligned} \quad (\text{B. 43})$$

$h_n$  and  $h_s$  are defined, respectively, the *normal* and *shear* anisotropic scaling factors. The modified stress tensor  $\tilde{\boldsymbol{\sigma}}$  is written as:

$$\tilde{\boldsymbol{\sigma}} = \mathbf{H} \cdot \boldsymbol{\sigma} \quad (\text{B. 44})$$

Eq. B.44 is explicitly formalized for a generic 2d stress state:

$$\tilde{\boldsymbol{\sigma}} = \begin{bmatrix} \tilde{\sigma}_{xx} \\ \tilde{\sigma}_{yy} \\ \tilde{\sigma}_{xy} \\ \tilde{\sigma}_{yx} \end{bmatrix} = \begin{bmatrix} H_{xxxx} & H_{xxyy} & H_{xxxy} & H_{xxyx} \\ H_{yyxx} & H_{yyyy} & H_{yyxy} & H_{yyyx} \\ H_{xyxx} & H_{xyyy} & H_{xyxy} & H_{xyyx} \\ H_{yxxx} & H_{yxyy} & H_{yxyx} & H_{yxyx} \end{bmatrix} \cdot \begin{bmatrix} \sigma_{xx} \\ \sigma_{yy} \\ \sigma_{xy} \\ \sigma_{yx} \end{bmatrix} \quad (\text{B. 45})$$

Since  $\tilde{\sigma}_{xy} = \tilde{\sigma}_{yx}$  and  $\sigma_{xy} = \sigma_{yx}$ , several simplifications occur in  $\mathbf{H}$  in Eq. B.45, in particular, referring to the matrix components,  $H_{33} = H_{44} = H_{34} = H_{43}$ . Moreover, the matrix is overall symmetric, i.e.  $H_{ij} = H_{ji}, \forall i, j$ . Thus, Eq. B.45 can be reduced to write  $\mathbf{H}$  as a 3x3 matrix as reported in Chapter 4, Section 4.3. According to Eq. B.42-B.43, the terms  $H_{ijkl}$  are written:

$$H_{xxxx} = H_{11} = h_n \cos^4 \omega + \sin^4 \omega + 2h_s \sin^2 \omega \cos^2 \omega \quad (\text{B. 46a})$$

$$H_{yyyy} = H_{22} = \cos^4 \omega + h_n \sin^4 \omega + 2h_s \sin^2 \omega \cos^2 \omega \quad (\text{B. 46b})$$

$$H_{xxyy} = H_{yyxx} = H_{12} = H_{21} = (1 + h_n) \sin^2 \omega \cos^2 \omega - 2h_s \sin^2 \omega \cos^2 \omega \quad (\text{B. 46c})$$

$$\begin{aligned} H_{xxxy} = H_{xxyx} = H_{xyxx} = H_{yxxx} = H_{13} = H_{14} = H_{31} = H_{41} = \\ h_n \cos^3 \omega \sin \omega - \sin^3 \omega \cos \omega + \frac{h_s}{2} [(2 \sin \omega \cos \omega)(\sin^2 \omega - \cos^2 \omega)] = \end{aligned} \quad (\text{B. 46d})$$

$$h_n \cos^3 \omega \sin \omega - \sin^3 \omega \cos \omega - \frac{h_s}{4} \sin 4\omega$$

$$H_{yyxy} = H_{yyyx} = H_{xyyy} = H_{yxyy} = H_{23} = H_{24} = H_{32} = H_{42} =$$

$$h_n \sin^3 \omega \cos \omega - \cos^3 \omega \sin \omega + \frac{h_s}{2} [(2 \sin \omega \cos \omega)(\cos^2 \omega - \sin^2 \omega)] =$$

$$= h_n \sin^3 \omega \cos \omega - \cos^3 \omega \sin \omega + \frac{h_s}{4} \sin 4\omega \quad (\text{B. 46e})$$

$$H_{xyxy} = H_{xyyx} = H_{yyxy} = H_{yyxxy} = H_{33} = H_{34} = H_{43} = H_{44} = (1 + h_n) \cos^2 \omega \sin^2 \omega + \frac{h_s}{2} (\sin^2 \omega - \cos^2 \omega)^2 = (1 + h_n) \cos^2 \omega \sin^2 \omega + \frac{h_s}{2} (\cos 2\omega)^2 \quad (\text{B. 46f})$$

It is possible to demonstrate that, if  $h_n = h_s = 1$ ,  $\mathbf{H}$  is a IV order identity matrix, i.e.  $\delta_{ijkl}$ . Neglecting the axial component  $\sigma_{zz}$ , the bi-dimensional failure criterion writes:

$$f(\tilde{\boldsymbol{\sigma}}, D) = \sqrt{(\tilde{\sigma}_{xx} - \tilde{\sigma}_{yy})^2 + 4\tilde{\sigma}_{xy}^2} + \sin \phi (\tilde{\sigma}_{xx} + \tilde{\sigma}_{yy}) - g(D)K \quad (\text{B. 47})$$

For uniaxial compression along the vertical axis  $y$  ( $\sigma_{xx} = \sigma_{xy} = 0$ ), the modified stress tensor writes:

$$\tilde{\boldsymbol{\sigma}} = \begin{bmatrix} H_{xyxy} \sigma_{yy} & H_{xyyx} \sigma_{yy} \\ H_{yyxy} \sigma_{yy} & H_{yyxxy} \sigma_{yy} \end{bmatrix} = \begin{bmatrix} H_{xyxy} & H_{xyyx} \\ H_{yyxy} & H_{yyxxy} \end{bmatrix} \sigma_{yy} \quad (\text{B. 48})$$

Eq. B.47 when failure is firstly attained ( $D = 0$ ,  $g(D) = 1$ ) writes:

$$\begin{aligned} f(\tilde{\boldsymbol{\sigma}}, D) &= \sqrt{(H_{xyxy} - H_{yyxxy})^2 \sigma_{yy}^2 + 4H_{xyyx}^2 \sigma_{yy}^2} + \sin \phi (H_{xyxy} + H_{yyxxy}) \sigma_{yy} - K \\ &= \sqrt{(H_{xyxy} - H_{yyxxy})^2 + 4H_{xyyx}^2} |\sigma_{yy}| + \sin \phi (H_{xyxy} + H_{yyxxy}) \sigma_{yy} - K = 0 \end{aligned} \quad (\text{B. 49})$$

Since it is possible to replace  $|\sigma_{yy}|$  with  $-\sigma_{yy}$  and  $\sigma_{0,\omega}$  with  $-\sigma_{yy}$  ( $\sigma_{0,\omega} \equiv$  unconfined compressive strength  $UCS$ ,  $\forall \omega$ ). The analytical expression of  $\sigma_{0,\omega}$  writes:

$$\sigma_{0,\omega} = \frac{K}{\sqrt{(H_{xyxy} - H_{yyxxy})^2 + 4H_{xyyx}^2} - \sin \phi (H_{xyxy} + H_{yyxxy})} \quad (\text{B. 50})$$

In Eq. B.50, as done in Paragraph B.2, Eq B.23-B.25, two coefficients can be defined:

$$C_{\text{dev}} = \sqrt{(H_{xyxy} - H_{yyxxy})^2 + 4H_{xyyx}^2} \quad (\text{B. 51})$$

as a *deviatoric* coefficient, and:

$$C_{\text{sph}} = \sin \phi (H_{xyxy} + H_{yyxxy}) \quad (\text{B. 52})$$

as a *spherical* coefficient. Eq. B.50, defined with these coefficients, allows to trace easily the periodical function of  $\sigma_{0,\omega}$  in the interval  $[0 ; \pi]$ . It is plotted in Figure B.6 for  $\phi = 20^\circ$ ,  $K = 15$  MPa and  $h_n = h_s = 1.44$ . The scaling coefficients were set to this value to obtain, for  $\omega = 0$  and  $90^\circ$ , the same  $\sigma_{0,\omega}$  values reported in Figure B.3 for the previous model for 2d anisotropic failure, based on the definition of the II order tensor  $\mathbf{M}$ . In the latter case, it was necessary the selection of an interval within  $90^\circ$  to reproduce a monotonic or non-monotonic behaviour. Here, it is possible to calibrate directly the scaling coefficients to  $h_n$  and  $h_s$ , for the same interval covering

90°, to evaluate different combinations of  $\sigma_{\theta,\omega}$  evolution with the bedding inclination (e.g., monotonic or not).

The analytic expression of material strength with  $\omega$  exists, similarly, if the compression along vertical axis  $y$  occurs with a confinement along  $x$ , i.e.  $\sigma_{xx} = p_C$ ,  $\sigma_{yy} > 0$ ,  $\sigma_{xy} = 0$ . The stress tensor writes:

$$\boldsymbol{\sigma} = \begin{bmatrix} p_C & 0 \\ 0 & \sigma_{yy} \end{bmatrix} \quad (\text{B. 53})$$

The modified stress tensor writes:

$$\tilde{\boldsymbol{\sigma}} = \begin{bmatrix} \tilde{\sigma}_{xx} & \tilde{\sigma}_{xy} \\ \tilde{\sigma}_{xy} & \tilde{\sigma}_{yy} \end{bmatrix} \quad (\text{B. 54})$$

With (applying Eq. B.45 and Eq. B.46a-f):

$$\tilde{\sigma}_{xx} = H_{xxxx} p_C + H_{xxyy} \sigma_{yy} \quad (\text{B. 55})$$

$$\tilde{\sigma}_{yy} = H_{yyxx} p_C + H_{yyyy} \sigma_{yy} \quad (\text{B. 56})$$

$$\begin{aligned} \tilde{\sigma}_{xy} &= H_{xyxx} p_C + H_{xyyy} \sigma_{yy} \\ &= H_{yxxx} p_C + H_{yxyy} \sigma_{yy} \end{aligned} \quad (\text{B. 57})$$

The criterion at yielding ( $D = 0$ ,  $g(D) = 1$ ) writes:

$$\begin{aligned} f(\tilde{\boldsymbol{\sigma}}) &= \sqrt{\left[ (H_{xxxx} p_C + H_{xxyy} \sigma_{yy}) - (H_{yyxx} p_C + H_{yyyy} \sigma_{yy}) \right]^2 + 4(H_{xyxx} p_C + H_{xyyy} \sigma_{yy})^2} + \\ &+ \sin \varphi \left[ (H_{xxxx} p_C + H_{xxyy} \sigma_{yy}) + (H_{yyxx} p_C + H_{yyyy} \sigma_{yy}) \right] - K = 0 \end{aligned} \quad (\text{B. 58})$$

As done for the precedent failure criterion, Eq. B.58 is rewritten to separate  $p_C$  from  $\sigma_{yy}$ :

$$\begin{aligned} f(\tilde{\boldsymbol{\sigma}}) &= \sqrt{\left[ (H_{xxxx} - H_{xxyy}) p_C - (H_{yyxx} + H_{yyyy}) \sigma_{yy} \right]^2 + 4(H_{xyxx} p_C + H_{xyyy} \sigma_{yy})^2} + \\ &+ \sin \varphi \left[ (H_{xxxx} + H_{yyxx}) p_C + (H_{xxyy} + H_{yyyy}) \sigma_{yy} \right] - K = 0 \end{aligned} \quad (\text{B. 59})$$

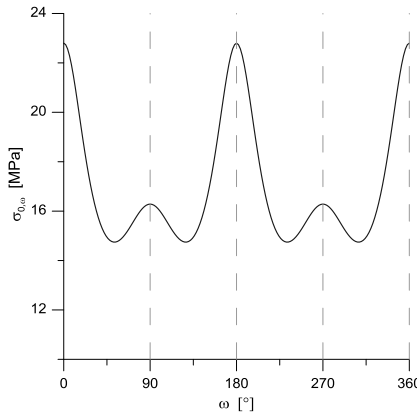


**Figure B.6:**  $\sigma_{\theta,\omega}$ , as a function of  $\omega$ , with  $\varphi = 20^\circ$ ,  $K = 15$  MPa and  $h_n = h_s = 1.44$ .

To simplify the notation in Eq. B.59:  $H_{xxxx} = a$ ;  $H_{yyyy} = b$ ;  $H_{xxyy} = H_{yyxx} = c$ ;  $H_{xyxx} = d$ ;  $H_{xyyy} = e$ . It is rewritten as follows:

$$f(\tilde{\sigma}) = \sqrt{[(a-c)p_c + (c-b)\sigma_{yy}]^2 + 4(dp_c + e\sigma_{yy})^2} + \sin\varphi[(a+c)p_c + (c+b)\sigma_{yy}] - K = 0 \quad (\text{B. 60})$$

$$\rightarrow (a-c)^2 p_c^2 + (c-b)^2 \sigma_{yy}^2 + 2(a-c)(c-b)p_c \sigma_{yy} + 4d^2 p_c^2 + 4e^2 \sigma_{yy}^2 + 8dep_c \sigma_{yy} = \{K - \sin\varphi[(a+c)p_c + (c+b)\sigma_{yy}]\}^2 \quad (\text{B. 61})$$

The left part of Eq. B.61 can be re-adjusted as:

$$[(a-c)^2 + 4d^2]p_c^2 + [(c-b)^2 + 4e^2]\sigma_{yy}^2 + 2[(a-c)(c-b) + 8de]p_c \sigma_{yy} \quad (\text{B. 62})$$

Confinement  $p_c$  is a constant boundary condition; new coefficients are defined for Eq. B.62:

$$[(a-c)^2 + 4d^2]p_c^2 = A \quad (\text{B. 63a})$$

$$[(c-b)^2 + 4e^2] = B \quad (\text{B. 63b})$$

$$2[(a-c)(c-b) + 8de]p_c = C \quad (\text{B. 63c})$$

Eq. B.61 can be rewritten as:

$$A + B\sigma_{yy}^2 + C\sigma_{yy} = [K - \sin\varphi(a+c)p_c - \sin\varphi(c+b)\sigma_{yy}]^2 \quad (\text{B. 64})$$

$$\rightarrow A + B\sigma_{yy}^2 + C\sigma_{yy} = (\bar{K} - D\sigma_{yy})^2$$

With:

$$\bar{K} = K - \sin\varphi(a+c)p_c \quad ; \quad D = \sin\varphi(c+b) \quad (\text{B. 65a-b})$$

The right part of Eq. B.64 can be developed and the entire equation, replacing  $\sigma_{yy}$  with  $\sigma_{\theta}(p_c)_{,\omega}$ , is re-adjusted as:

$$A + B\sigma_{yy}^2 + C\sigma_{yy} = \bar{K}^2 + D^2\sigma_{yy}^2 - 2\bar{K}D\sigma_{yy} \quad (\text{B. 66})$$

$$\rightarrow (B - D^2)\sigma_{yy}^2 + (C + 2\bar{K}D)\sigma_{yy} + (A - \bar{K}^2) = 0$$

Eq. B.66 corresponds to a second order polynomial with the following coefficients:

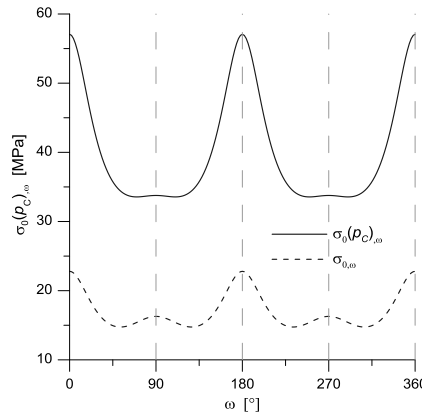


**Figure B.7:**  $\sigma_{\theta}(p_c = 12 \text{ MPa})_{,\omega}$  as a function of  $\omega$ , with  $\varphi = 20^\circ$ ,  $K = 15 \text{ MPa}$  and  $h_n = h_s = 1.44$ , compared with the precedent  $\sigma_{\theta,\omega}$ , with no confinement (e.g. Figure B.6).

$$b_1 = (\mathbf{B} - \mathbf{D}^2) \quad (\text{B. 67a})$$

$$b_2 = (\mathbf{C} + 2\bar{\mathbf{K}}\mathbf{D}) \quad (\text{B. 67b})$$

$$b_3 = (\mathbf{A} - \bar{\mathbf{K}}^2) \quad (\text{B. 67c})$$

It is verified, to obtain positive values of  $\sigma_0(p_C)_\omega$ , that the solution of Eq. B.66 corresponds to:

$$\sigma_0(p_C)_\omega = \frac{b_2 + \sqrt{b_2^2 - 4 \cdot b_1 \cdot b_3}}{2b_1} \quad (\text{B. 68})$$

Again, the function  $\sigma_0(p_C)_\omega$  is periodical with  $\omega$ . It is traced in Figure B.7 for the same failure parameters adopted in Figure B.6, with a confinement  $\sigma_{xx} = p_C = 12$  MPa. In Figure B.7, the plot of  $\sigma_0(p_C)_\omega$  is compared with the precedent, for unconfined loading.

#### B.4 Elastic-damage stiffness tensor with no damage expansion along $z$ accounting for a horizontal Young modulus $E_x = E_z > E_y$ (vertical Young modulus).

This formulation is based on the homogenisation of stiffness parameter related to solicitations along the axis of transverse isotropy, i.e. axis  $y$  Figure B.8. The horizontal stratification corresponds to a sequence of discontinuities with negligible thickness and equidistant  $d$  within the medium (*matrix*), which is characterized by isotropic elastic parameters  $E_{MAT} = E_x$  and  $\nu$ . Normal and shear stiffness of horizontal inclusions are identified by  $K_{nn}$  and  $K_{nt}$ . The ratio  $K_{nt}/K_{nn}$  is indicated by  $\kappa$ . Elastic-damage stiffness tensor is defined starting from the correspondent compliance matrix, for a 2d, plane strain problem including the axial stress  $\sigma_{zz}$  normal to  $\Gamma$  in Figure B.8, where damage  $D$  may occur. Based on the formulation proposed by Pouya et al. [75], the following compliance matrix can be written:

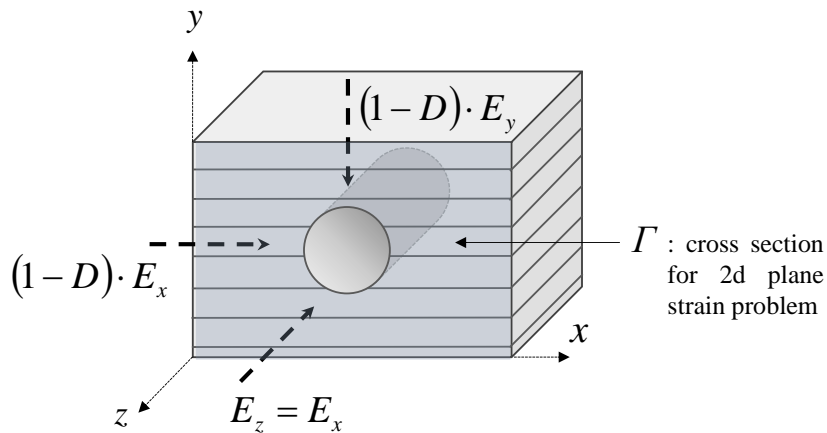


**Figure B.8:** 3d model for stratified formation behind the section  $\Gamma$  for 2d plane strain excavation problem.

$$\tilde{\mathbf{C}}^{-1} = \begin{bmatrix} \frac{1}{(1-D)E_x} & -\frac{\nu}{(1-D)E_x} & -\frac{\nu}{E_x} & 0 \\ -\frac{\nu}{(1-D)E_x} & \frac{1}{(1-D)E_y} & -\frac{\nu}{E_x} & 0 \\ -\frac{\nu}{E_x} & -\frac{\nu}{E_x} & \frac{1}{E_x} & 0 \\ 0 & 0 & 0 & \frac{1}{(1-D)\mu_{HOM}} \end{bmatrix} \quad (\text{B. 69})$$

In Eq. B.69, according to the approach described in Chapter 3, Section 3.3, the explicit parameters describing material's anisotropy for elasticity are  $E_x$  and  $E_y$ . Both  $E_y$  and the homogenized shear modulus  $\mu_{HOM}$  are related to  $K_{nn}$  and  $K_{tt}$  according to the following equations:

$$\frac{1}{E_y} = \frac{1}{E_{HOM}} = \frac{1}{E_x} + \frac{1}{dK_{nn}} \quad (\text{B. 70})$$

$$\frac{1}{\mu_{HOM}} = \frac{2(1+\nu)}{E_x} + \frac{1}{\kappa dK_{nn}} \quad (\text{B. 71})$$

From Eq. B.70:

$$dK_{nn} = \frac{E_x E_y}{E_x - E_y} \quad (\text{B. 72})$$

Eq. B.71 can be rewritten as:

$$\frac{1}{\mu_{HOM}} = \frac{2(1+\nu)}{E_x} + \frac{E_x - E_y}{\kappa E_x E_y} \quad (\text{B. 73})$$

From Eq. B.69 and B.73, the anisotropic elastic-damage compliance matrix, with damage on  $\Gamma$ , writes:

$$\tilde{\mathbf{C}}^{-1} = \begin{bmatrix} \frac{1}{(1-D)E_x} & -\frac{\nu}{(1-D)E_x} & -\frac{\nu}{E_x} & 0 \\ -\frac{\nu}{(1-D)E_x} & \frac{1}{(1-D)E_y} & -\frac{\nu}{E_x} & 0 \\ -\frac{\nu}{E_x} & -\frac{\nu}{E_x} & \frac{1}{E_x} & 0 \\ 0 & 0 & 0 & \frac{[2\kappa(1+\nu)-1]E_y + E_x}{\kappa(1-D)E_x E_y} \end{bmatrix} \quad (\text{B. 74})$$

The inversion of matrix in Eq. B.74, performed numerically, provides the elastic-damage stiffness tensor  $\tilde{\mathbf{C}}$  in Eq. B.75 and B.76a-g. These have been implemented in a FORTRAN subroutine, structured according to the procedure in Figure A.1, and processed in *POROFIS*.

$$\tilde{\mathbf{C}} = \frac{E_x(D-1)}{E_x[1+(D-1)\nu^2] + \nu^2 E_y[D+2\nu D-2(1+\nu)]} \cdot \begin{bmatrix} A_{11} & A_{12} & A_{13} & 0 \\ A_{12} & A_{22} & A_{32} & 0 \\ A_{13} & A_{32} & A_{33} & 0 \\ 0 & 0 & 0 & A_{44} \end{bmatrix} \quad (\text{B. 75})$$

In the following, each coefficient  $A_{ij}$  is reported:

$$A_{11} = E_x + E_y(1-D)\nu^2 \quad (\text{B. 76a})$$

$$A_{22} = E_y[(1-D)\nu^2 - 1] \quad (\text{B. 76b})$$

$$A_{33} = \frac{E_x - \nu^2 E_y}{(D-1)} \quad (\text{B. 76c})$$

$$A_{12} = -\nu E_y[1 + (1-D)\nu] \quad (\text{B. 76d})$$

$$A_{13} = -\nu(E_x + \nu E_y) \quad (\text{B. 76e})$$

$$A_{32} = -\nu E_y(1+\nu) \quad (\text{B. 76f})$$

$$A_{44} = \frac{(1-D)\kappa E_y \{E_x[1+(D-1)\nu^2] + \nu^2 E_y[D+2\nu D-2(1+\nu)]\}}{(D-1)\{E_x + E_y[2\kappa(1+\nu)-1]\}} \quad (\text{B. 76g})$$



